

Optimized Software for Theoretical Nonlinear Optical Calculations

by

Sean Martin Anderson

A thesis submitted in partial fulfillment of the requirements
for the degree of Doctor of Philosophy.

Advisor:
Dr. Bernardo Mendoza Santoyo

Centro de Investigaciones en Óptica, A.C.
Loma del Bosque 115, León, Guanajuato, 37150, México

June 3, 2016

The research presented in this thesis was carried out at the Centro de Investigaciones en Óptica, A.C., Loma del Bosque 115, León, Guanajuato, 37150, Mexico, in collaboration with the Laboratoire des Solides Irradiés, École Polytechnique, CNRS, CEA/DSM, 91128 Palaiseau, France, which is a part of the European Theoretical Spectroscopy Facility (ETSF), Palaiseau, France. Funding was provided by the CONACYT-México (Consejo Nacional de Ciencia y Tecnología), through scholarship N° 349278, and CONACYT-México Grant 153930.

Optimized Software for Theoretical Optical Calculations

by

Sean M. Anderson

Approved:

Dr. Bernardo Mendoza Santoyo
Thesis Advisor

Dr. Wolf Luis Mochán Bacal
External Reader

Dr. Ramón Carriles Jaimes
Reader

Centro de Investigaciones en Óptica, A.C.
Loma del Bosque 115, León, Guanajuato, 37150, México
June 3, 2016

“The purpose of computing is insight, not numbers.”

Richard Hamming

Abstract

In this thesis I formulate a theoretical approach of surface second-harmonic generation from semiconductor surfaces based on the length gauge and the electron density operator. Within the independent particle approximation the surface nonlinear second-order surface susceptibility tensor $\chi_{\text{surface}}^{\text{abc}}(-2\omega; \omega, \omega)$ is calculated, including in one unique formulation (i) the scissors correction, needed to have the correct value of the energy band gap, (ii) the contribution of the nonlocal part of the pseudopotentials, and (iii) the derivation for the inclusion of the cut function, used to extract the surface response. The first two contributions are described by spatially nonlocal quantum mechanical operators and are fully taken into account in the present formulation. I also revisit the three layer model for the SSHG yield and demonstrate that it provides more accurate results over several, more common, two layer models. This entire framework is implemented in the TINIBA software suite, which I helped develop over the course of this doctoral project. I apply this framework for the clean Si(001)2 \times 1 and Si(111)(1 \times 1):H surfaces, and compare with various experimental spectra from several different sources. I conclude that this new approach to the calculation of the second-harmonic spectra is versatile and accurate within this level of approximation. These surfaces provide an excellent platform for comparison with theory, and allows us to offer this study as an efficient benchmark for this type of calculation.

Contents

1	Introduction	1
1.1	A Review of Nonlinear Optics	1
1.1.1	Historical Overview	1
1.1.2	Nonlinear Polarization and Susceptibility	2
1.1.3	Symmetry Considerations for Centrosymmetric Materials	4
1.1.4	Bulk Quadrupolar and Other Contributions	6
1.1.5	SFG and SHG	6
1.2	The Nonlinear Surface Susceptibility	7
1.3	The SSHG yield	9
1.4	Other Optical Nonlinear Phenomena of Interest	10
1.4.1	Optical spin injection	10
1.4.2	Optical current injection	10
1.5	Outline	11
2	The Nonlinear Surface Susceptibility	12
2.1	The Nonlinear Surface Susceptibility	12
2.2	Time-dependent Perturbation Theory	14
2.3	Length Gauge	17
2.4	Layered Current Density	21
2.5	Microscopic surface susceptibility	24
2.6	About the code	26
2.7	Conclusions	27
3	Surface Second-Harmonic Generation Yield	28
3.1	The Three Layer Model for the SSHG Yield	29
3.1.1	Multiple SHG reflections	32
3.1.2	Multiple Reflections for the Linear Field	33
3.1.3	Deriving the SSHG yield	34
3.2	\mathcal{R}_{iF} for different polarization cases	36
3.2.1	\mathcal{R}_{pP} (<i>p</i> -in, <i>P</i> -out)	37
3.2.2	\mathcal{R}_{sP} (<i>s</i> -in, <i>P</i> -out)	39
3.2.3	\mathcal{R}_{pS} (<i>p</i> -in, <i>S</i> -out)	39
3.2.4	\mathcal{R}_{sS} (<i>s</i> -in, <i>S</i> -out)	40
3.3	Some Scenarios of Interest	40
3.3.1	The 3-layer Model Without Multiple Reflections	41

3.3.2	The two layer, or Fresnel (2-layer-fresnel) model	42
3.3.3	The 2-layer-bulk model: evaluating $\mathcal{P}(2\omega)$ and $\mathbf{E}(\omega)$ in the bulk	42
3.3.4	The 2-layer-vacuum model: evaluating $\mathcal{P}(2\omega)$ and $\mathbf{E}(\omega)$ in the vacuum	42
3.3.5	The 3-layer-hybrid model: evaluating $\mathcal{P}(2\omega)$ in ℓ and $\mathbf{E}(\omega)$ in the bulk	42
3.4	About the code	43
3.5	Conclusions	43
4	A SSHG Spectroscopic Study of Two Si Surfaces	44
4.1	Results for the Si(001)(2×1) surface	45
4.1.1	Calculating $\chi_{\text{surface}}^{xxx}(-2\omega; \omega, \omega)$	46
4.1.2	Overview of the calculated \mathcal{R} spectra	52
4.2	Results for the Si(111)(1×1):H surface	53
4.2.1	Calculating $\chi_{\text{surface}}^{xxx}(-2\omega; \omega, \omega)$	56
4.2.2	Comparing the theoretical \mathcal{R} to experiment	56
4.3	Conclusion	67
5	Final Remarks	70
A	Supplementary Derivations for the Nonlinear Surface Susceptibility	72
A.1	\mathbf{r}_e and \mathbf{r}_i	72
A.2	Matrix elements of $\mathbf{v}_{nm}^{\text{nl}}(\mathbf{k})$ and $\mathcal{V}_{nm}^{\text{nl},\ell}(\mathbf{k})$	75
A.3	Explicit expressions for $\mathcal{V}_{nm}^{a,\ell}(\mathbf{k})$ and $\mathcal{C}_{nm}^{\ell}(\mathbf{k})$	79
A.3.1	Time-reversal relations	80
A.4	$\mathcal{V}_{nm}^{\Sigma,a,\ell}$ and $(\mathcal{V}_{nm}^{\Sigma,a,\ell})_{;k^b}$	81
A.5	Generalized derivative $(\omega_n(\mathbf{k}))_{;\mathbf{k}}$	83
A.6	Expressions for $\chi_{\text{surface}}^{abc}$ in terms of $\mathcal{V}_{mn}^{\Sigma,a,\ell}$	83
A.6.1	Intraband Contributions	84
A.6.2	Interband Contributions	87
A.7	Generalized derivative $(\mathbf{r}_{nm}(\mathbf{k}))_{;\mathbf{k}}$ for nonlocal potentials	89
A.7.1	Case $n = m$	91
A.7.2	Case $n \neq m$	91
A.7.3	Layer Case	91
A.8	Matrix elements of $\tau_{nm}^{ab}(\mathbf{k})$	92
A.9	Scissors renormalization for $\mathcal{V}_{nm}^{\Sigma}$	94
B	Complete Derivations for the SSHG yield	95
B.1	Some useful expressions	96
B.1.1	2 ω terms	96
B.1.2	1 ω terms	97
B.1.3	Nonzero components of $\chi(-2\omega; \omega, \omega)$	98
B.2	\mathcal{R}_{pP}	99
B.2.1	For the (111) surface	100
B.2.2	For the (110) surface	103
B.2.3	For the (001) surface	104
B.3	\mathcal{R}_{ps}	105
B.3.1	For the (111) surface	106

B.3.2	For the (110) surface	107
B.3.3	For the (001) surface	107
B.4	\mathcal{R}_{sP}	107
B.4.1	For the (111) surface	108
B.4.2	For the (110) surface	109
B.4.3	For the (001) surface	110
B.5	\mathcal{R}_{ss}	110
B.5.1	For the (111) surface	111
B.5.2	For the (110) surface	111
B.5.3	For the (001) surface	111

List of Tables

1.1	Optical processes described by $\chi^{(n)}(-\omega; \omega_1, \dots, \omega_n)$	5
3.1	Polarization unit vectors for $\hat{\mathbf{e}}^F$ and $\hat{\mathbf{e}}^i$, and equations describing $\mathbf{e}_\ell^{2\omega, F}$ and $\mathbf{e}_\ell^{\omega, i} \mathbf{e}_\ell^{\omega, i}$ for each polarization case.	37
3.2	Components of χ for the (111), (110) and (001) crystallographic faces, belonging to the C_{3v} , C_{2v} , and C_{4v} , symmetry groups, respectively. For the (111) surface we choose the x and y axes along the $[11\bar{2}]$ and $[1\bar{1}0]$ directions, respectively. For the (110) and (001) we consider the y axis perpendicular to the plane of symmetry. [1] We remark that in general $\chi^{(111)} \neq \chi^{(110)} \neq \chi^{(001)}$.	37
3.3	Summary of the SSHG yield models used throughout this work. “Label” is the name used in subsequent figures, while the remaining columns show in which medium we will consider the specified quantity. ℓ is the thin layer below the surface of the material, v is the vacuum region, and b is the bulk region of the material. We use the following convention for the labels. Models with “3-layer” consider the presence of the thin layer ℓ , while “2-layer” models do not. The “fresnel”, “bulk”, “vacuum”, and “hybrid” tags refers to the configuration in which we evaluate the specific quantities. For instance, the 3-layer-hybrid model evaluates $\mathcal{P}(2\omega)$ in the thin layer ℓ , while the fundamental fields are evaluated in the bulk region b .	41
B.1	Polarization unit vectors for $\hat{\mathbf{e}}^{\text{out}}$ and $\hat{\mathbf{e}}^{\text{in}}$, and equations describing $\mathbf{e}_\ell^{2\omega}$ and $\mathbf{e}_\ell^\omega \mathbf{e}_\ell^\omega$ for each polarization case. When there are two equations to choose from, the former includes the effects of multiple reflections, and the latter neglects them.	98

List of Figures

2.1	Sketch of a semi-infinite system with a centrosymmetric bulk. The surface region is of width $\sim d$. The incoming photon of frequency ω is represented by a downward red arrow, whereas both the surface and bulk created second-harmonic photons of frequency 2ω are represented by upward green arrows. The red color suggests an incoming infrared photon with a green second-harmonic photon. The dipolar ($\chi_{\text{surface}}^{\text{abc}}$), and quadrupolar ($\chi_{\text{bulk}}^{\text{abcd}}$) susceptibility tensors are shown in the regions where they are nonzero. The z -axis is perpendicular to the surface and \mathbf{R} is parallel to it.	14
2.2	A sketch of the super-cell. The atomic slab corresponds to the circles representing the atoms of the system.	22
3.1	Sketch of the three layer model for SHG. The vacuum region (v) is on top with $\epsilon_v = 1$; the layer ℓ of thickness $d = d_1 + d_2$, is characterized with $\epsilon_\ell(\omega)$, and it is where the SH polarization sheet $\mathcal{P}_\ell(2\omega)$ is located at $z_\ell = d_1$. The bulk b is described with $\epsilon_b(\omega)$. The arrows point along the direction of propagation, and the p -polarization unit vector, $\hat{\mathbf{P}}_{\ell-(+)}$, along the downward (upward) direction is denoted with a thick arrow. The s -polarization unit vector $\hat{\mathbf{s}}$, points out of the page. The fundamental field $\mathbf{E}(\omega)$ is incident from the vacuum side along the $\kappa\hat{z}$ -plane, with θ_0 its angle of incidence and ν_{v-} its wave vector. $\Delta\varphi_i$ denotes the phase difference between the multiple reflected beams and the first layer-vacuum transmitted beam, denoted by the dashed-red arrow (of length L_2) followed by the solid black arrow (of length L_1). The dotted lines in the vacuum region are perpendicular to the beam extended from the solid black arrow (denoted by solid blue arrows of length L_6).	31
3.2	Sketch for the multiple reflected fundamental field $\mathbf{E}(\omega)$, which impinges from the vacuum side along the $\hat{\kappa}z$ -plane. θ_0 and ν_{v-} are the angle of incidence and wave vector, respectively. The arrows point along the direction of propagation. The p -polarization unit vectors $\hat{\mathbf{p}}_{\beta\pm}$, point along the downward (−) or upward (+) directions and are denoted with thick arrows, where $\beta = v$ or ℓ . The s -polarization unit vector $\hat{\mathbf{s}}$ points out of the page. $(1, 2, 3, \dots)\varphi$ denotes the phase difference for the multiple reflected beams with respect to the incident field, where the dotted line is perpendicular to this beam.	34
4.1	Several views of the slab used to represent the Si(001)(2×1) surface. This particular slab has 16 Si atomic layers (large blue balls) with two H atomic layers (small red balls).	46
4.2	The slab for the Si(001)(2×1) surface. The front (upper) surface is in a 2×1, clean reconstruction, and the rear (lower) surfaces is H-terminated, with “ideal” bulk-like atomic positions. The dangling bonds are H-saturated.	47

4.3	$ \chi_{\text{full-slab}}^{xxx} $ vs $\hbar\omega$ for the slab with 16, 24, 32, and 40 atomic Si layers. Adequate convergence is achieved after 32 layers. The spectra presented here use a scissors value of $\hbar\Delta = 0$ eV, and do not include the contribution from \mathbf{v}^{nl} .	48
4.4	$\chi_{\text{half-slab}}^{xxx}$ vs $\hbar\omega$ for the clean 2×1 and H-terminated surfaces, with $\hbar\Delta = 0.5$ eV and without the effects of \mathbf{v}^{nl} .	49
4.5	$\chi_{\text{half-slab}}^{xxx}$ and $\chi_{\text{full-slab}}^{xxx}$ vs $\hbar\omega$ for four different combinations: with and without the effects of \mathbf{v}^{nl} , and with two values for the scissors correction, $\hbar\Delta$.	50
4.6	$\chi_{\text{half-slab}}^{xxx}$ vs $\hbar\omega$, with and without the contribution from \mathbf{v}^{nl} . This spectrum has a scissors value of $\hbar\Delta = 0.5$ eV.	51
4.7	$\chi_{\text{half-slab}}^{xxx}$ vs $\hbar\omega$ for a slab with 32 atomic Si layers plus one H layer, for three different values of the scissors correction, $\hbar\Delta$.	52
4.8	\mathcal{R} for outgoing P polarization, versus the angle of incidence (θ_0) for the Si(001)(2×1) surface. The scissor shift used was $\hbar\Delta = 0.5$ eV. Both figures consider an azimuthal angle of $\phi = 45^\circ$.	53
4.9	\mathcal{R} for outgoing S polarized fields, versus the angle of incidence (θ_0) for the Si(001)(2×1) surface. The scissor shift used was $\hbar\Delta = 0.5$ eV. Both figures consider an azimuthal angle of $\phi = 45^\circ$.	54
4.10	Several views of the slab used to represent the Si(111)(1×1):H surface. This particular slab has 16 Si atomic layers (large blue balls) with two H atomic layers (small red balls).	55
4.11	Comparison of $\chi_{\text{surface}}^{xxx}$ calculated using relaxed and unrelaxed atomic positions, with the experimental data presented in Ref. [2]. The theoretical curves were calculated with a scissors shift of $\hbar\Delta = 0.7$ eV, and are broadened with $\sigma = 0.075$ eV. Experimental data was taken at 80 K.	57
4.12	\mathcal{R} for outgoing P polarization, versus the angle of incidence (θ_0) for the Si(111)(1×1):H surface. A scissors shift of $\hbar\Delta = 0.7$ eV is applied. The solid line represents $\theta_0 = 65^\circ$, and the dotted lines represent the E ₁ and E ₂ Si critical points. Both figures consider an azimuthal angle of $\phi = 30^\circ$.	58
4.13	\mathcal{R} for outgoing S polarized fields, versus the angle of incidence (θ_0) for the Si(111)(1×1):H surface. A scissors shift of $\hbar\Delta = 0.7$ eV is applied. The solid line represents $\theta_0 = 65^\circ$, and the dotted lines represent the E ₁ and E ₂ Si critical points. Both figures consider an azimuthal angle of $\phi = 30^\circ$.	58
4.14	Comparison between the three layer model with the effects of multiple reflections for two different values of the total layer thickness d , with the standard three layer model without the effects of multiple reflections, and the experimental data from Ref. [3]. We take $\theta = 65^\circ$, $\phi = 30^\circ$, and a scissors value of $\hbar\Delta = 0.7$ eV.	60
4.15	Comparison between including or neglecting the effects of multiple reflections for the fundamental fields. The theoretical spectra were produced for a layer thickness of $d = 10$ nm using the average value of \bar{R}_p^M .	61
4.16	Comparison between the three layer model with the effects of multiple reflections for two different values of d_2 , and the average value \bar{R}_p^M . All curves that include multiple reflections consider a layer ℓ thickness of $d = 10$ nm.	61
4.17	Comparison between theoretical models (see Table 3.3) and experiment for \mathcal{R}_{pP} , for $\theta = 65^\circ$, and a scissors value of $\hbar\Delta = 0.7$ eV. Experimental data taken from Ref. [3], measured at room temperature.	62

4.18 Comparison between the 2-layer-fresnel and 2-layer-vacuum models (see Table 3.3) and experiment for \mathcal{R}_{pP} , for $\theta = 65^\circ$, and a scissors value of $\hbar\Delta = 0.7 \text{ eV}$. Experimental data taken from Ref. [3], measured at room temperature.	63
4.19 Comparison between theoretical models (see Table 3.3) and experiment for \mathcal{R}_{pP} , for $\theta = 45^\circ$, and a scissors value of $\hbar\Delta = 0.7 \text{ eV}$. Experimental data taken from Ref. [4], measured at room temperature.	64
4.20 Comparison between theoretical models (see Table 3.3) and experiment for \mathcal{R}_{sP} , for $\theta = 65^\circ$, and a scissors value of $\hbar\Delta = 0.7 \text{ eV}$. Experimental data taken from Ref. [3], measured at room temperature.	65
4.21 Comparison between theoretical models (see Table 3.3) and experiment for \mathcal{R}_{pS} , for $\theta = 65^\circ$, and a scissors value of $\hbar\Delta = 0.7 \text{ eV}$. Experimental data taken from Ref. [3], measured at room temperature.	66
4.22 Comparison between theoretical models (see Table 3.3) and experiment for \mathcal{R}_{pS} , for $\theta = 45^\circ$. We use a scissors value of $\hbar\Delta = 0.7 \text{ eV}$. Experimental data taken from Ref. [4], measured at room temperature.	67
4.23 Calculated results for \mathcal{R}_{pS} for the different levels of approximation proposed in this article. All curves were calculated using the 3-layer model. We take $\theta = 65^\circ$ for this plot. See text for full details.	68

Chapter 1

Introduction

Outline

1.1	A Review of Nonlinear Optics	1
1.1.1	Historical Overview	1
1.1.2	Nonlinear Polarization and Susceptibility	2
1.1.3	Symmetry Considerations for Centrosymmetric Materials	4
1.1.4	Bulk Quadrupolar and Other Contributions	6
1.1.5	SFG and SHG	6
1.2	The Nonlinear Surface Susceptibility	7
1.3	The SSHG yield	9
1.4	Other Optical Nonlinear Phenomena of Interest	10
1.4.1	Optical spin injection	10
1.4.2	Optical current injection	10
1.5	Outline	11

1.1 A Review of Nonlinear Optics

1.1.1 Historical Overview

The discovery of the optical maser by Townes [5] and the construction of the laser by Maiman in the late 1950s and early 1960s ushered a new age of optical discoveries. The ability to produce optical beams with these devices automatically lead to very highly focused energies distributed over very small areas. These concentrated energies allowed scientists to finally move into the optical nonlinear regime for many different materials. The maser allowed for the first recorded observation of optical second-harmonic generation (SHG) by Franken et al. in 1961 [6]. They produced a second beam of light at twice the frequency of the original by exciting a piece of crystalline quartz. This frequency doubling effect was dubbed SHG and was observed to be much less intense than the exciting beam. There is a humorous anecdote about this experiment. Apparently, the editor of Physical Review Letters thought that the second harmonic dot on the photographic plate was a

speck of dust, which he edited out. The image found in the article has an arrow pointing at the empty spot where it should be. However, this did not detract from the importance of the find.

Other developments followed promptly. In 1962, Bloembergen et al. [7, 8] developed the mathematical framework to explain nonlinear optical phenomena. That same year, Terhune et al. [9] observed SHG in calcite. These discoveries were amongst others [10] that lead to further research into the geometrical dependence of nonlinear effects, and helped verify that the majority of the SHG signal produced in a centrosymmetric material comes from surface contribution, where inversion symmetry is broken. In the late 1960s, Bloembergen [11] and others [12] studied SHG in a variety of centrosymmetric materials and semiconductors. The advent of pulsed lasers during the 1970s [13] allowed for even greater intensities to be obtained. Dye lasers came to prominence during these years, offering very large bandwidths and relatively short picosecond pulses. However, these lasers were very difficult to maintain and the dyes used were typically very toxic and presented serious health risks. Interest began to form around using SHG to study surfaces and interfaces, since it had been proven [14] to be exclusive to the surface area of a centrosymmetric material in the dipole approximation. Shen et al. published [15] that there is also a quadrupole bulk contribution for this kind of material, and in 1989 [16] published a review article summarizing most of the trends in surface spectroscopy using SHG. Theoretical work also played an important role in the 1990s, with new theoretical models by Sipe [17] and others [18–21]. Downer et al. [22] and Lüpke [23] both produced very thorough and referenced texts on SHG surface spectroscopy of semiconductors in the late 1990s and early 2000s. This period of time provided the foundations for surface nonlinear optics today.

At around the same time, the first Ti:sapphire lasers were being produced and analyzed [24]. These early ultrafast lasers were capable of producing femtosecond pulses via mode-locked oscillators. Since the active medium is in solid state form, they present none of the risks of using dyes. These lasers were considerably more compact than dye lasers since they no longer needed external dye control systems. These lasers became commercial in the early 1990s. Chirped pulse amplification (CPA) was invented in 1985 by Mourou and Strickland [25]. This technique allowed Ti:sapphire lasers to achieve much higher peak energy without compromising the ultrashort pulse duration. During the 1990s, CPA became the prominent method for increasing energy output in Ti:sapphire lasers. At this point, Ti:sapphire lasers using the CPA technique were both compact, efficient, and cost effective. These factors would only improve over the following decade as the Ti:sapphire laser became the standard for high energy, ultrashort pulse applications.

1.1.2 Nonlinear Polarization and Susceptibility

So what happens when very intense light coincides on a given material? Let us talk about the dipole moment per unit volume, or polarization $\mathbf{P}(t)$. This polarization describes the effect light has on a material and vice versa; it represents the optical response of a material. Taking Maxwell's equations with the usual considerations of zero charge density ($\rho = 0$) and no free currents ($\mathbf{J} = 0$),

we have

$$\nabla \cdot \mathbf{D} = 0, \quad (1.1)$$

$$\nabla \cdot \mathbf{H} = 0, \quad (1.2)$$

$$\nabla \times \mathbf{E} = -\mu_0 \frac{\partial \mathbf{H}}{\partial t}, \quad (1.3)$$

$$\nabla \times \mathbf{H} = \frac{\partial \mathbf{D}}{\partial t}. \quad (1.4)$$

We take into account the nonlinearity of the material by relating the \mathbf{D} and \mathbf{E} fields with the total (linear and nonlinear) polarization \mathbf{P} ,

$$\mathbf{D} = \epsilon_0 \mathbf{E} + \mathbf{P}. \quad (1.5)$$

Proceeding in the usual manner for deriving the wave equation, we obtain

$$\nabla \times \nabla \times \mathbf{E} + \frac{1}{c^2} \frac{\partial^2}{\partial t^2} \mathbf{E} = -\frac{1}{\epsilon_0 c^2} \frac{\partial^2 \mathbf{P}}{\partial t^2}, \quad (1.6)$$

which can be considerably simplified thanks to the identity

$$\nabla \times \nabla \times \mathbf{E} = \nabla (\nabla \cdot \mathbf{E}) - \nabla^2 \mathbf{E}, \quad (1.7)$$

so we can finally express the inhomogenous wave equation as

$$\nabla^2 \mathbf{E} - \frac{1}{c^2} \frac{\partial^2}{\partial t^2} \mathbf{E} = \frac{1}{\epsilon_0 c^2} \frac{\partial^2 \mathbf{P}}{\partial t^2}. \quad (1.8)$$

In this form, it is clear that the polarization acts as a source for this differential equation, analogous to a simple harmonic oscillator. The polarization can be expressed by a power series of the form

$$P(t) = \epsilon_0 [\chi^{(1)} E(t) + \chi^{(2)} E^2(t) + \chi^{(3)} E^3(t) + \dots] \quad (1.9)$$

$$\equiv P^{(1)}(t) + P^{(2)}(t) + P^{(3)}(t) + \dots, \quad (1.10)$$

where $\chi^{(n)}$ is the n^{th} -order susceptibility of the material. We can define the susceptibility as a constant of proportionality that describes the degree of polarizability a material has in terms of the strength of an incoming optical electric field. The first term

$$P(t) = \epsilon_0 \chi^{(1)} E(t), \quad (1.11)$$

is the linear term that describes most everyday interactions between light and matter. When taking into account that the incoming fields are vectorial in nature, the linear susceptibility $\chi^{(1)}$ becomes a second-rank tensor. $\chi^{(2)}$, the second-order nonlinear optical susceptibility is a third-rank tensor [26]. The nonlinear susceptibilities are very small in nature. If $\chi^{(1)}$ is unity, $\chi^{(2)}$ is on the order of $\approx 10^{-12} \text{ m/V}$. This explains why such high intensity fields are needed to produce nonlinear interactions; each term in equation (1.9) depends on a higher power of the incoming field but has a much smaller value for the corresponding susceptibility.

A more general definition of the nonlinear polarization can be found when treating the input field as a superposition of plane waves. We assume that the electric field vector is of the form

$$\mathbf{E}(\mathbf{r}, t) = \sum_n \mathbf{E}_n(\mathbf{r}, t), \quad (1.12)$$

where

$$\mathbf{E}_n(\mathbf{r}, t) = \mathbf{E}_n(\mathbf{r})e^{-i\omega_n t} + \text{c.c..} \quad (1.13)$$

If we look at the form of equation (1.9), we can express the nonlinear polarization in its full form as

$$\mathbf{P}(\mathbf{r}, t) = \sum_n \mathbf{P}(\omega_n)e^{-i\omega_n t}. \quad (1.14)$$

Since we are only interested in second-order effects we can define the corresponding nonlinear polarization in terms of the second order susceptibility as

$$P^a(\omega_n + \omega_m) = \epsilon_0 \sum_{bc} \sum_{(nm)} \chi^{(2),abc}(\omega_n + \omega_m; \omega_n, \omega_m) E^b(\omega_n) E^c(\omega_m), \quad (1.15)$$

where the indices abc refer to the Cartesian components of the fields, and (nm) notes that n and m can be varied while the sum $\omega_n + \omega_m$ remains fixed. We can study the generalized case when we have two incoming fields with frequencies ω_1 and ω_2 . We can represent this in the following form

$$E(t) = E_1 e^{-i\omega_1 t} + E_2 e^{-i\omega_2 t} + \text{c.c.} \quad (1.16)$$

Assuming the form of equation (1.9)

$$P^{(2)} = \epsilon_0 \chi^{(2)} E^2(t), \quad (1.17)$$

and substituting expression (1.16) we get

$$\begin{aligned} P^{(2)}(t) &= \epsilon_0 \chi^{(2)} \left[E_1^2 e^{-i2\omega_1 t} + E_2^2 e^{-i2\omega_2 t} \right. \\ &\quad + 2E_1 E_2 e^{-i(\omega_1+\omega_2)t} + 2E_1 E_2^* e^{-i(\omega_1-\omega_2)t} + \text{c.c.} \left. \right] \\ &\quad + 2\epsilon_0 \chi^{(2)} [E_1 E_1^* + E_2 E_2^*]. \end{aligned} \quad (1.18)$$

We separate this expression into its components and the nonlinear effect that each represents in the following manner (abbreviations defined in table 1.1),

$$\begin{aligned} P(2\omega_1) &= \epsilon_0 \chi^{(2)} E_1^2 e^{-i2\omega_1 t} + \text{c.c.} \quad (\text{SHG}), \\ P(2\omega_2) &= \epsilon_0 \chi^{(2)} E_2^2 e^{-i2\omega_2 t} + \text{c.c.} \quad (\text{SHG}), \\ P(\omega_1 + \omega_2) &= 2\epsilon_0 \chi^{(2)} E_1 E_2 e^{-i(\omega_1+\omega_2)t} + \text{c.c.} \quad (\text{SFG}), \\ P(\omega_1 - \omega_2) &= 2\epsilon_0 \chi^{(2)} E_1 E_2^* e^{-i(\omega_1-\omega_2)t} + \text{c.c.} \quad (\text{DFG}), \\ P(0) &= 2\epsilon_0 \chi^{(2)} (E_1 E_1^* + E_2 E_2^*) + \text{c.c.} \quad (\text{OR}). \end{aligned} \quad (1.19)$$

Janner [27] has a wonderfully formatted table in her dissertation that summarizes the first few optical processes, which I reproduce here as follows. From this point forward we will only be concerned with second-order effects.

1.1.3 Symmetry Considerations for Centrosymmetric Materials

As mentioned previously, $\chi^{(2)}$ is a third-rank tensor with 27 elements. The amount of non-zero elements varies with the symmetry properties of the medium. SHG has intrinsic permutation

symmetry for the incoming fields, such that $\chi^{(2),abc} = \chi^{(2),acb}$; this reduces the total components from 27 to 18. Knowledge of the symmetry properties of the material can help us reduce the amount of unknown elements to calculate.

A centrosymmetric material, or a material with an inversion center, is a material that for every point at coordinates (x, y, z) , there is an identical point located at $(-x, -y, -z)$. For instance, many crystals are centrosymmetric. If we assume that we are in the bulk of a centrosymmetric material, we can write the nonlinear polarization as

$$P(t) = \epsilon_0 \chi^{(2)} E^2(t). \quad (1.20)$$

If the medium is centrosymmetric, a sign change must affect both the electric field and the polarization since they are polar vectors [28]. So,

$$-P(t) = \epsilon_0 \chi^{(2)} [-E(t)]^2, \quad (1.21)$$

$$= \epsilon_0 \chi^{(2)} E^2(t). \quad (1.22)$$

However, substituting (1.22) into (1.20) we get $P(t) = -P(t)$. We can finally deduce that

$$\chi^{(2)} = 0. \quad (1.23)$$

Therefore, all second-order processes are forbidden in the bulk of centrosymmetric materials in the dipole approximation. We will talk about the other important approximation in section 1.1.4. This property is broken at the surface since that region no longer presents an inversion center. This very special property is what enables second-order nonlinearities to be so effective for surface and interface measurements. Likewise, any other mechanism that breaks the symmetry, such as an electric field or mechanical stress will also allow a second-order signal to be produced. See Bloembergen's [29] excellent review about second-order effects for surface spectroscopy for further reading.

$\chi^{(n)}(-\omega; \omega_1, \dots, \omega_n)$	Process	Order
$-\omega ; \omega$	Linear absorption / emission and refractive index	1
$0 ; \omega, -\omega$	Optical rectification (OR)	2
$-\omega ; 0, \omega$	Pockels effect	2
$-2\omega ; \omega, \omega$	Second-harmonic generation (SHG)	2
$-(\omega_1 + \omega_2) ; \omega_1, \omega_2$	Sum-frequency generation (SFG)	2
$-(\omega_1 - \omega_2) ; \omega_1, \omega_2$	Difference-frequency generation (DFG) / Parametric amplification and oscillation	2
$-\omega ; 0, 0, \omega$	d.c. Kerr effect	3
$-2\omega ; 0, \omega, \omega$	Electric Field induced SHG (EFISH)	3
$-3\omega ; \omega, \omega, \omega$	Third-harmonic generation (THG)	3
$-\omega ; \omega, -\omega, \omega$	Degenerate four-wave mixing (DFWM)	3
$-\omega ; -\omega_2, \omega_2, \omega_1$	Two-photon absorption (TPA) / ionization / emission	3

Table 1.1: Optical processes described by $\chi^{(n)}(-\omega; \omega_1, \dots, \omega_n)$

1.1.4 Bulk Quadrupolar and Other Contributions

Everything that I have stated up to this point assumes what we call the *dipole approximation* that arises from assuming that the polarization can take the form of a multipole expansion. The dipole approximation simply assumes that the dipolar contribution is significantly greater than all the others. This is not necessarily the case in many materials. In particular, we find that there can be a non-negligible electric quadrupole contribution from the bulk of centrosymmetric materials. Bloembergen et al. [11] elaborate on this as early as the 1960s. This adds a severe complication to the use of second-order nonlinearities as surface probes since signal is actually produced from both surface and bulk. Sipe et al. [30] go into some detail about this problem, stating that it is very difficult to separate the surface and bulk contributions as the various nonlinear coefficients cannot be measured separately. Guyot-Sionnest and Shen [15] go one step further and state that the contributions are impossible to separate. They suggest that the best way to distinguish one from the other is by taking measurements before and after altering the surface and observing the overall changes to the produced signal. About a decade later, Shen et al. [31] state that bulk contributions not only come from the electric quadrupole, but also from the magnetic dipole, although the latter is typically much less intense than either of the former. They express the bulk polarization as a multipole series as follows,

$$\mathbf{P}^B(\omega) = \mathbf{P}_D(\omega) - \nabla \cdot \mathbf{Q}(\omega) - \left(\frac{c}{i\omega} \right) \nabla \times \mathbf{M}(\omega) + \dots, \quad (1.24)$$

where $\mathbf{P}_D(\omega)$ is the dipolar polarization, $\mathbf{Q}(\omega)$ is the electric quadrupole polarization, and $\mathbf{M}(\omega)$ is the magnetic dipole polarization. Indeed, if only the dipolar contribution is forbidden for centrosymmetric materials then there will be a contribution from the other two in addition to the dipolar contribution at the surface. The group does however go on to explain that there are a few experimental ways to help distinguish between surface and bulk contributions.

If $\mathbf{Q}(\omega)$ is assumed to take some form similar to

$$\mathbf{Q}(\omega) \approx \chi_q^{(2)}(\omega_1 + \omega_2) \mathbf{E}(\omega_1) \nabla \mathbf{E}(\omega_w), \quad (1.25)$$

then $\chi_q^{(2)}$ is a fourth-rank tensor with 81 independent elements. Clearly this adds some considerable complication to our problem and makes selecting the appropriate symmetry that much more important. In summary, bulk electric quadrupole and magnetic dipole contributions to second-order surface effects may not be negligible and need to be taken into account. However, in this thesis we study the nonlinear optical properties of Silicon, and it is known that the quadrupolar effects are quite small [1, 32–36]. Therefore, we will neglect these effects for the remainder of this thesis.

1.1.5 SFG and SHG

We call the third process in expression (1.19) Sum-frequency generation (SFG). It is a second-order process that involves two photons, of frequencies ω_1 and ω_2 that combine to form one photon of frequency $\omega_3 = \omega_1 + \omega_2$. This is represented mathematically in the previous expression

$$P(\omega_1 + \omega_2) = 2\epsilon_0 \chi^{(2)} E_1 E_2 e^{-i(\omega_1 + \omega_2)t} + \text{c.c.}, \quad (1.26)$$

where the term is explicitly stated in the exponential. A special case of sum-frequency generation is when both incoming frequencies are the same, i.e. $\omega_1 = \omega_2$; this case is also known as the degenerate case. The resulting frequency is then exactly double that of the input frequency.

As mentioned previously, second-order nonlinear processes are prohibited in the bulk of centrosymmetric materials (in the dipole approximation). Since it has a very strong surface contribution (where the inversion symmetry is broken), it can be used as a very precise diagnostic tool for surface and interface regions. The use of these second-order nonlinearities for surface studies had gained momentum in the 1990s. McGilp wrote a review about using SHG and SFG as surface and interface probes in 1996 [37]. He adds experimental confirmation to his theories in 1999 [38] in an extremely thorough review about using SHG on the surface of almost any material you can think of. Aktsipetrov et al. [39] followed a different approach by establishing what they call electric field induced second-harmonic generation, or EFISH. In this paper they elaborate how the sensitivity of SHG to surfaces can be enhanced by applying an electric field across the interface. More recently a book in the field of second-order nonlinear optics has been published with a wealth of useful information [40].

The theoretical side of things was further developed in a paper by Maytorena et al. [21] discussing the formalities of SFG from surfaces by finding the exact expressions for the susceptibility based on modeling conductors and dielectrics. These models include fluid based, classical dynamics in addition to the wave equation treatment. A couple of interesting review papers by Downer et al. [22] and Scheidt et al. [41] exist, where they report results of SHG spectroscopies from a variety of different surfaces and interfaces including nanocrystals.

1.2 The Nonlinear Surface Susceptibility

In recent years surface nonlinear optical spectroscopies, particularly surface second-harmonic generation (SSHG), have evolved as useful nondestructive and noninvasive tools to study surface and interface properties. These properties include atomic structure, phase transitions, adsorption of atoms, and many others. [2, 4, 34–36, 42–55] Nowadays, SSHG spectroscopy is a crucial tool for research and development in microelectronics [56], semiconductors [57], nanomaterials and bidimensional materials [58, 59], and many more recent areas of great scientific and commercial interest. [60] The high surface sensitivity of SSHG spectroscopy is due to the fact that within the dipole approximation the bulk SHG signal of centrosymmetric materials is identically zero. However, the SHG process can occur only at the surface where the inversion symmetry is broken. The bulk quadrupole contribution for centrosymmetric materials is different from zero, but usually it is very small [35], and could be neglected. Much of the foundation of surface science has been built from experiments involving emission or scattering of electrons from surfaces. These require ultrahigh vacuum (UHV) environments and provide no access to buried interfaces. However, SSHG is compatible with non-UHV conditions and has access to interfaces buried beneath transparent overlayers. Even when applied to surfaces in UHV, the light source and detectors can be aligned and used outside the vacuum chamber.

The usefulness of SSHG could be limited by the lack of microscopic theoretical understanding of the nonlinear spectra. The macroscopic phenomenological theory of SSHG, which relates the intensity, phase, and polarization of detected fields to nonlinear and linear susceptibilities at the material interface is now fully developed. [35] However, microscopic theory that relates electronic-level structure to the nonlinear source polarization is still being developed. [3, 51, 55, 61–72] Within the independent particle approximation (IPA) some frameworks for bulk SHG have been developed to study the nonlinear optical response of bulk materials. [51, 61–66] In this thesis we put forward an approach to calculate the microscopic second-harmonic surface susceptibility that encompasses

several theoretical features not taken into account before in the case of a surface.

The most used framework for *ab initio* calculations, Density Functional Theory (DFT) within the Local Density Approximation (LDA), [73] underestimates the energy band gap of semiconductors. It is well understood that one has to include the many-body interaction to correct for this underestimation of the gap. In this context, the so-called GW approximation [74] is known to correct the electronic gap of most semiconductors [75]. However this can be a very expensive calculation and thus one uses the much simpler scissors operator scheme. [76–78] This allows us to “open” the DFT-LDA gap to its correct experimental or GW value for most bulk semiconductors. This approximation has already been used in linear optical calculations for surfaces, [79] thus improving the agreement with experimental results. In this context, to correct for the underestimation of the energy band gap of semiconductors Nastos *et al.* [80] used the “length gauge” or “ $\mathbf{r} \cdot \mathbf{E}$ ” gauge to show how to correctly include the many-body corrections through the scissors operator in the SH susceptibility. Later, Cabellos *et al.* [81] elaborated a derivation of the “velocity gauge” or “ $\mathbf{A} \cdot \mathbf{v}$ ” gauge properly including the scissors operator and proved gauge invariance with respect to the length gauge. From these works it is clear the length gauge is a much better starting point to obtain the surface SH (SSH) susceptibility, as will be elaborated in this thesis. However, these considerations are only valid for bulk semiconductors.

Concerning the optical response of surfaces and interfaces, Reining *et al.* [82] introduced the concept of a cut function in order to obtain the surface SH susceptibility tensor. This cut function is required since one usually uses a slab approach when treating semi-infinite surface systems. [82] If the slab is centrosymmetric the susceptibility tensor will be identically zero. The cut function is such that it separates the nonlinear response for the two surfaces of the slab avoiding the destructive interference between them giving a finite value that one identifies with the SSH susceptibility tensor. If the slab is not centrosymmetric the cut function can be used to separate the different signals coming from either surface of the slab. Indeed, one of the main results of this thesis is to show that the SSH susceptibility tensor obtained by using the cut function is correctly extracted from the slab. After Reining *et al.*, [82] Refs. [3, 55, 68–70] followed upon this work and in particular Ref. [68] went into a detailed analysis of the different contributions to the SHG spectra of a surface and the nuanced relationship between bulk, surface, interband, intraband, 1ω and 2ω terms, and Ref. [71] developed a layer-by-layer analysis for the nonlinear responses of semiconductor systems, within a tight-binding framework. This model allows for obtaining results from selected regions of a system including the surface. However, in these references the scissors operator is either excluded or incorrectly implemented. In the works that include this operator, the velocity gauge was used to derive the expressions for the nonlinear second-order susceptibility, $\chi^{abc}(-2\omega; \omega, \omega)$. Nevertheless, a term in the time-dependent perturbation scheme necessary to satisfy the gauge invariance of $\chi^{abc}(-2\omega; \omega, \omega)$ was omitted. This was demonstrated in Ref. [81] where a comparison between the velocity and the length gauge was carried out.

Finally, DFT-LDA calculations are often based on the use of pseudopotentials. As it will be discussed in this thesis, the presence of a nonlocal part of the pseudopotential introduces corrections to the momentum operator of the electron that have to be included with care in the SSH susceptibility. For the bulk counterpart see for instance Refs. [83, 84]. Therefore, within the IPA the most complete approach for the calculation of the SSH susceptibility is one which includes (i) the scissors correction, (ii) the contribution of the nonlocal part of the pseudopotential, and (iii) the cut function. One of the goals of this thesis is to derive a new expression within the length gauge for the SSH susceptibility tensor $\chi^{abc}(-2\omega; \omega, \omega)$ that includes the aforementioned contributions. The

inclusion of these three contributions makes our scheme unprecedented and opens the possibility to study surface SHG with more versatility and providing accurate results.

1.3 The SSHG yield

For calculating the SSHG yield, we will use the nonlinear surface susceptibility tensor produced with the framework mentioned in the previous section, and featured in Ref. [85]. This formulation includes three features not previously found in a single formulation: (i) the scissors correction, (ii) the contribution of the nonlocal part of the pseudopotentials, and (iii) the cut function used to extract the surface response, all within the independent particle approximation. The inclusion of these three contributions opens the possibility to study SSHG with more versatility and accuracy than was previously available at this level of approximation. We also use the three layer (3-layer) model for the SSHG yield, which considers that the SH conversion takes place in a thin layer just below the surface that lies under the vacuum region and above the bulk of the material. Validating these improvements is difficult, however, without experimental data for comparison.

SSHG experiments focusing on semiconductor surfaces are available, but they are often reported over very limited energy ranges and lacking units and scale for the intensity. This lack of comprehensive experimental data has made comparison between theory and experiment difficult. However, the Si(111)(1×1):H surface offers some respite in this area. This surface can be prepared to a high degree of structural quality and has been experimentally characterized with SHG to a great degree of accuracy [3, 4]. The added H saturates the surface Si dangling bonds and eliminates any surface-related electronic states in the band gap. We consider that this surface represents an ideal benchmark for *ab initio* SSHG studies. More specifically, SSHG from the Si(111)(1×1):H surface was treated in detail in Ref. [3], and their approach yielded good qualitative results. However, the expressions presented for the nonlinear susceptibility tensor, $\chi(-2\omega; \omega, \omega)$, which is required for the SSHG yield, are derived in the velocity gauge. This method incorrectly implements the scissors quasiparticle correction and diverges for low energies [81]. We mention that the formulas presented in Ref. [3], where the 3-layer model was introduced for the first time, have some minor mistakes that have been corrected in Ref. [86]. They also propose a two layer (2-layer) model for SSHG which does not accurately represent the real physical process for surfaces. We consider that the theoretical and computational aspects of this subject have evolved considerably since then, making this topic ripe for revision.

In Chapter 4, I will present a comparison between theory and experiment by presenting the improved theoretical calculations against experimental SSHG spectra from several sources, namely Refs. [2–4, 87], with two-photon energies ranging from 2.5 eV to 5 eV covering both the E₁ and E₂ critical point transitions for bulk Si. These SHG experiments were carried out with different polarizations of incoming and outgoing beams which are taken into account in the theoretical analysis. We find that the new formalism compares favorably with experiment and permits insight into the physics behind SSHG. In spite of the advances mentioned, our treatment neglects local field and excitonic effects that are challenging from both a theoretical and a computational standpoint. This topic merits further review and may prove to be crucial for more accurate SSHG theory.

1.4 Other Optical Nonlinear Phenomena of Interest

Besides the phenomena mentioned above, there are several other nonlinear effects that have become particularly interesting with the advent of bidimensional materials, such as MoS₂, MoSe₂, WS₂, and WSe₂, and Graphene. In particular, Graphene is an allotrope of carbon with a planar, hexagonal, two-dimensional honeycomb structure with one carbon atom at each vertex. It has attracted a great deal of interest due to its distinctive properties, such as the fractional quantum Hall effect at room temperature, and excellent thermal transport properties [88–91]. It behaves like a metal, but can be modified to semiconductor behavior by tuning the band gap. This can be achieved by changing the surface area [92], applying an electric field [93], applying uniaxial strain [94], or by doping, amongst other methods. Previous works have explored doping with boron, nitrogen [95], and hydrogen [96–98]. Hydrogenated graphene can achieve different spatial configurations by varying the amount and location of the hydrogen bonds. When a hydrogen atom is bonded to a carbon atom in graphene, it draws the atom away from the plane. This modifies the carbon-carbon bond length resulting in an opening of the band gap [96,99]. In Ref. [100], I helped carry out a theoretical study of three optical nonlinear phenomena for two hydrogenated graphane structures: optical spin injection, optical current injection and second-harmonic generation (SHG). I describe the former two as follows.

1.4.1 Optical spin injection

The injection and detection of spin polarized electrons in nonmagnetic materials is at the core of spintronics [101, 102] and an important problem in condensed matter theory. The idea of creating and detecting spin polarized electrons from light originates in the 1960s with Ref. [103]. Following that work, it was later demonstrated that converting the angular momentum of light into electron spin is very efficient in III-IV semiconductors [104]. Optical spin injection is characterized through the dimensionless degree of spin polarization (DSP), $\mathcal{D}(\omega)$. DSP quantifies the fraction of injected electrons in the conduction bands that are spin polarized. This effect occurs when circularly polarized light is incident on a semiconducting material [104], thus allowing electrons to move from the valence to the conduction bands. The resulting polarization is produced by the interaction between the electron spin and its motion caused by the spin-orbit coupling in the material. DSP can be calculated with a full band structure method as shown in Refs. [81, 105]. There are theoretical reports of DSP calculations for bulk media [81, 105] and also for surfaces [106, 107].

1.4.2 Optical current injection

The optical current injection is a second-order optical nonlinear effect that has been the subject of research in recent years [107–111]. A photocurrent, $\mathbf{j}(\omega)$, can be injected with a single optical beam into noncentrosymmetric materials or at the surface of bulk centrosymmetric materials where the inversion symmetry has been broken [107]. This phenomenon results from the interference of one-photon absorption processes associated with different linear polarizations of light. In the process of current injection, the energy increase of the injected carriers is provided by the electromagnetic field, while the increase in momentum is provided by the crystal lattice [107]. One-photon current injection is characterized by the current injection tensor, $\eta^{abc}(\omega)$, and since it is generated with circularly polarized light, this phenomenon is also called the circular photovoltaic effect [112]. This effect has been studied in bulk semiconductors [110, 113], two-dimensional systems [114, 115], and

one-dimensional nanotubes [114]. Bidimensional materials are quite often noncentrosymmetric and present an optical current injection response.

1.5 Outline

This thesis is divided into 5 chapters including this introduction. Chapter 2 presents the derivation of explicit expressions for the nonlinear surface susceptibility, $\chi_{\text{surface}}(-2\omega; \omega, \omega)$, featuring the developments mentioned in Sec. 1.2. Chapter 3 presents the derivation of the expressions for the SSHG yield that utilize the calculated components of the nonlinear surface susceptibility. Chapter 4 presents the spectra for both $\chi_{\text{surface}}(-2\omega; \omega, \omega)$ and the SSHG yield for two surfaces, Si(001)(2×1) and Si(111)(1×1):H. I present comparisons with experimental data, and we will find that the results from the newly derived theory compares quite favorably to the experimental spectra. Chapter 5 is dedicated to the final observations and remarks. Appendix A contains the derivations for several necessary terms needed for $\chi_{\text{surface}}(-2\omega; \omega, \omega)$, and Appendix B presents the complete, step-by-step derivations for the SSHG yield. Finally, the complete bibliography is located at the end of the document for easy reference.

Chapter 2

The Nonlinear Surface Susceptibility

Outline

2.1	The Nonlinear Surface Susceptibility	12
2.2	Time-dependent Perturbation Theory	14
2.3	Length Gauge	17
2.4	Layered Current Density	21
2.5	Microscopic surface susceptibility	24
2.6	About the code	26
2.7	Conclusions	27

In this chapter we formulate a theoretical approach of surface second-harmonic generation from semiconductor surfaces based on the length gauge and the electron density operator. Within the independent particle approximation the nonlinear second-order surface susceptibility tensor $\chi^{abc}(-2\omega; \omega, \omega)$ is calculated, including in one unique formulation (i) the scissors correction, needed to have the correct value of the energy band gap, (ii) the contribution of the nonlocal part of the pseudopotentials, routinely used in *ab initio* band structure calculations, and (iii) the derivation for the inclusion of the cut function, used to extract the surface response. The first two contributions are described by spatially nonlocal quantum mechanical operators and are fully taken into account in the present formulation.

2.1 The Nonlinear Surface Susceptibility

In this section I will outline the general procedure to obtain the surface susceptibility tensor for SHG. We start with the nonlinear polarization $\mathbf{P}(\mathbf{r})$ of a bulk system, written as

$$P^a(\mathbf{r}, 2\omega) = \chi^{abc}(-2\omega; \omega, \omega)E^b(\mathbf{r}, \omega)E^c(\mathbf{r}, \omega) + \chi^{abcd}(-2\omega; \omega, \omega)E^b(\mathbf{r}, \omega)\nabla^c E^d(\mathbf{r}, \omega) + \dots, \quad (2.1)$$

where $\chi^{abc}(-2\omega; \omega, \omega)$ and $\chi^{abcd}(-2\omega; \omega, \omega)$ correspond to the dipolar and quadrupolar susceptibility tensors, and $\mathbf{E}(\mathbf{r})$ is the incoming electric field along the different Cartesian directions denoted by the roman superscripts. For ease of notation, I will drop the ω arguments from this point on.

At this point I introduce the units of the quantities above. For simplicity, we use the MKS system of units. The units of $\mathbf{E}(\mathbf{r})$ are $[\mathbf{E}] = \text{V/m}$, and the units of $\mathbf{P}(\mathbf{r})$ are $[\mathbf{P}] = \text{V/m}$ since $\mathbf{P}(\mathbf{r})$ is a *bulk* polarization. Therefore, the units of the bulk χ^{abc} are $[\chi^{abc}] = \text{m/V}$.

If we consider a semi-infinite system with a centrosymmetric bulk, we can obtain a bulk and a surface nonlinear polarization that differ from each other from symmetry considerations alone. To show this, we take

$$P^a(\mathbf{r}) = \chi^{abc} E^b(\mathbf{r}) E^c(\mathbf{r}) + \chi^{abcd} E^b(\mathbf{r}) \frac{\partial}{\partial r^c} E^d(\mathbf{r}) + \dots, \quad (2.2)$$

as the polarization with respect to the \mathbf{r} coordinate system, and

$$P^a(-\mathbf{r}) = \chi^{abc} E^b(-\mathbf{r}) E^c(-\mathbf{r}) + \chi^{abcd} E^b(-\mathbf{r}) \frac{\partial}{\partial (-r^c)} E^d(-\mathbf{r}) + \dots, \quad (2.3)$$

as the polarization in the inverted coordinate system, where we take \mathbf{r} to $-\mathbf{r}$. Note that we have kept the same susceptibility tensors as they must be invariant under $\mathbf{r} \rightarrow -\mathbf{r}$ since the system is centrosymmetric. Recalling that $\mathbf{P}(\mathbf{r})$ and $\mathbf{E}(\mathbf{r})$ are polar vectors [28], we have that Eq. (2.3) reduces to

$$\begin{aligned} -P^a(\mathbf{r}) &= \chi^{abc} (-E^b(\mathbf{r})) (-E^c(\mathbf{r})) + \chi^{abcd} (-E^b(\mathbf{r})) \left(-\frac{\partial}{\partial r^c} \right) (-E^d(\mathbf{r})) + \dots, \\ P^a(\mathbf{r}) &= -\chi^{abc} E^b(\mathbf{r}) E^c(\mathbf{r}) + \chi^{abcd} E^b(\mathbf{r}) \frac{\partial}{\partial r^c} E^d(\mathbf{r}) + \dots, \end{aligned} \quad (2.4)$$

that when compared with Eq. (2.2) leads to the conclusion that

$$\begin{aligned} \chi^{abc} &= 0, \\ &\quad (\text{centrosymmetric bulk}) \\ \chi^{abcd} &\neq 0, \end{aligned} \quad (2.5)$$

for a centrosymmetric bulk.

The surface of a centrosymmetric system necessarily breaks the centrosymmetry; thus, there are no symmetry restrictions imposed on the χ^{abc} produced from the surface region. Therefore, it is convenient to define the surface nonlinear polarization $\mathbf{P}_{\text{surface}}$ as follows,

$$P_{\text{surface}}^a \equiv \chi_{\text{surface}}^{abc} E^b E^c, \quad (2.6)$$

where $\chi_{\text{surface}}^{abc}$ is the surface nonlinear susceptibility. In this case, the MKS units of $[\mathbf{P}_{\text{surface}}]$ are V , and $[\chi_{\text{surface}}^{abc}]$ are m^2/V . The contribution from χ^{abcd} to the surface polarization is neglected as it originates from a higher order multipole. From Eq. (2.1) we have that for the bulk of a semi-infinite system,

$$P_{\text{bulk}}^a = \chi_{\text{bulk}}^{abcd} E^b \nabla^c E^d, \quad (2.7)$$

which is the bulk nonlinear polarization; in this case the dipolar contribution $\chi_{\text{bulk}}^{abc} = 0$ since we are in the centrosymmetric bulk. As it follows from Ref. [116], the surface nonlinear polarization is of dipolar electric order while the bulk polarization is of quadrupolar electric and dipolar magnetic order. The surface χ_{surface} and bulk χ_{bulk} susceptibilities are tensors of rank three and four, respectively.

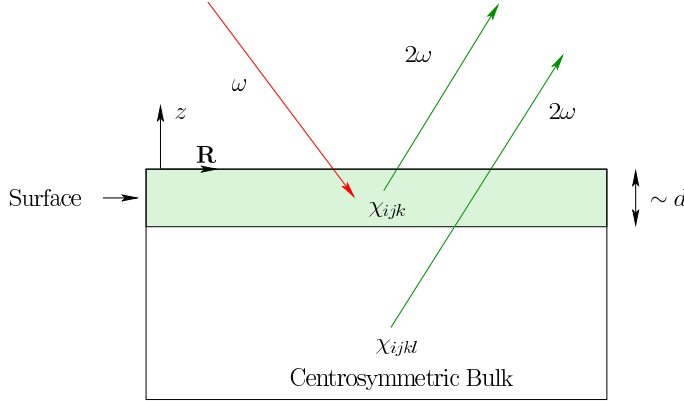


Figure 2.1: Sketch of a semi-infinite system with a centrosymmetric bulk. The surface region is of width $\sim d$. The incoming photon of frequency ω is represented by a downward red arrow, whereas both the surface and bulk created second-harmonic photons of frequency 2ω are represented by upward green arrows. The red color suggests an incoming infrared photon with a green second-harmonic photon. The dipolar ($\chi_{\text{surface}}^{\text{abc}}$), and quadrupolar ($\chi_{\text{bulk}}^{\text{abcd}}$) susceptibility tensors are shown in the regions where they are nonzero. The z -axis is perpendicular to the surface and \mathbf{R} is parallel to it.

In this work, we will only concentrate on SSHG, even though bulk-generated SH is also a very important optical phenomenon. To this end, we will neglect the contribution from Eq. (2.7) and only consider the surface term from Eq. (2.6). I will also exclude other interesting surface SH phenomena like, electric field induced second-harmonic (EFISH), which would be represented by a surface susceptibility tensor of quadrupolar origin. As mentioned in Chapter 1, in centrosymmetric systems for which the quadrupolar bulk response is much smaller than the dipolar surface response, SH is a very capable and powerful optical surface probe [35].

In the following sections of this chapter, we show the theoretical approach to derive the expressions for the surface susceptibility tensor $\chi_{\text{surface}}^{\text{abc}}$.

2.2 Time-dependent Perturbation Theory

We assume the IPA, a classical electromagnetic field, and quantum mechanical matter. We neglect local field and excitonic effects. We can describe the system using the one electron density operator ρ , with which we can calculate the expectation value of a single-particle observable \mathcal{O} as

$$\langle \mathcal{O} \rangle = \text{Tr}(\rho \mathcal{O}), \quad (2.8)$$

with \mathcal{O} the associated quantum mechanical operator and Tr the trace. The density operator satisfies

$$i\hbar \frac{d\rho}{dt} = [H, \rho], \quad (2.9)$$

with $H(t)$ as the total single electron Hamiltonian, written as

$$H(t) = H_0 + H_I(t),$$

where H_0 is the unperturbed time-independent Hamiltonian, and $H_I(t)$ is the time-dependent potential energy due to the interaction of the electron with the electromagnetic field. To proceed with the solution of ρ it is convenient to use the interaction picture, where a unitary operator

$$U = e^{iH_0 t/\hbar}, \quad (2.10)$$

transforms any operator \mathcal{O} into

$$\tilde{\mathcal{O}} = U\mathcal{O}U^\dagger. \quad (2.11)$$

Even if \mathcal{O} is time-independent, $\tilde{\mathcal{O}}$ is time-dependent through the explicit time dependence of U . The dynamical equation for $\tilde{\rho}$ is given by

$$i\hbar \frac{d\tilde{\rho}}{dt} = [-e\mathbf{r}(t) \cdot \mathbf{E}(t), \tilde{\rho}] = [\tilde{H}_I(t), \tilde{\rho}], \quad (2.12)$$

with solution

$$i\hbar\tilde{\rho}(t) = i\hbar\tilde{\rho}_0 + \int_{-\infty}^t [\tilde{H}_I(t'), \tilde{\rho}(t')] dt', \quad (2.13)$$

where $\tilde{\rho}_0 = \tilde{\rho}(t = -\infty)$ is the unperturbed density matrix.

We assume that the interaction is switched-on adiabatically and choose a time-periodic perturbing field, to write

$$\mathbf{E}(t) = \mathbf{E}e^{-i\omega t}e^{\eta t} = \mathbf{E}e^{-i\tilde{\omega}t}, \quad (2.14)$$

with

$$\tilde{\omega} = \omega + i\eta, \quad (2.15)$$

where $\eta > 0$ assures that at $t = -\infty$, the interaction is zero and has its full strength \mathbf{E} at $t = 0$. After computing the required time integrals one takes $\eta \rightarrow 0$. Also, $\tilde{\rho}(t = -\infty)$ should be time independent and thus $[\tilde{H}_I, \tilde{\rho}]_{t=-\infty} = 0$. This implies that $\tilde{\rho}(t = -\infty) \equiv \tilde{\rho}_0$, such that

$$\langle n\mathbf{k}|\tilde{\rho}_0|m\mathbf{k}'\rangle = f_n(\hbar\omega_n^\Sigma(\mathbf{k}))\delta_{nm}\delta(\mathbf{k} - \mathbf{k}'), \quad (2.16)$$

with $f_n(\hbar\omega_n^\Sigma(\mathbf{k})) = f_n$ as the Fermi-Dirac distribution function. For a clean, cold semiconductor $f_n = 1$ when n is a valence (v) or occupied band, and zero when n is a conduction (c) or empty band. We assume this for the remainder of this work. As we neglect spin-orbit coupling, the final expression for $\chi^{abc}(-2\omega; \omega, \omega)$ has to be multiplied by a factor of 2 to account for spin-degeneracy. The expectation values must always satisfy $\langle \mathcal{O} \rangle = \text{Tr}(\rho\mathcal{O}) = \text{Tr}(\tilde{\rho}\tilde{\mathcal{O}})$.

We solve Eq. (2.13) using the standard iterative solution, for which we write

$$\tilde{\rho} = \tilde{\rho}^{(0)} + \tilde{\rho}^{(1)} + \tilde{\rho}^{(2)} + \dots, \quad (2.17)$$

where $\tilde{\rho}^{(N)}$ where the superscript denotes the order (power) with which each term depends on the perturbation $H_I(t)$. Then, Eq. (2.13) reads

$$\tilde{\rho}^{(0)} + \tilde{\rho}^{(1)} + \tilde{\rho}^{(2)} + \dots = \tilde{\rho}_0 + \frac{1}{i\hbar} \int_{-\infty}^t [\tilde{H}_I(t'), \tilde{\rho}^{(0)} + \tilde{\rho}^{(1)} + \tilde{\rho}^{(2)} + \dots] dt', \quad (2.18)$$

where, by equating equal orders in the perturbation, we find

$$\tilde{\rho}^{(0)} \equiv \tilde{\rho}_0, \quad (2.19)$$

and the N th-order term

$$\tilde{\rho}^{(N)}(t) = \frac{1}{i\hbar} \int_{-\infty}^t [\tilde{H}_I(t'), \tilde{\rho}^{(N-1)}(t')] dt'. \quad (2.20)$$

It is simple to show that matrix elements of Eq. (2.20) satisfy $\langle n\mathbf{k}|\rho^{(N+1)}(t)|m\mathbf{k}'\rangle = \rho_{nm}^{(N+1)}(\mathbf{k})\delta(\mathbf{k}-\mathbf{k}')$, with

$$\rho_{nm}^{(N+1)}(\mathbf{k}; t) = \frac{e}{i\hbar} \int_{-\infty}^t \langle n\mathbf{k}| [\mathbf{r}(t'), \tilde{\rho}^{(N)}(t')] |m\mathbf{k}\rangle \cdot \mathbf{E}(t') dt'. \quad (2.21)$$

This shows that the $N+1$ solution is determined by the N th solution, which in turn is determined by the $N-1$ solution, and so on. Starting from the zeroth order solution given in Eq. (2.19), we can solve Eq. (2.21) for any desired order.

We will look for the expectation value of the microscopic current density, \mathbf{J} , given by

$$\mathbf{J} = \langle \mathbf{J} \rangle = \frac{e}{A} \text{Tr}(\rho \dot{\mathbf{r}}),$$

where $\dot{\mathbf{r}}$ is the time derivative of the position operator of the electron with charge e , defined as

$$\mathbf{v} \equiv \dot{\mathbf{r}} = \frac{1}{i\hbar} [\mathbf{r}, H_0], \quad (2.22)$$

with \mathbf{v} the velocity operator of the electron, and A the area of the unit cell. We calculate the polarization density \mathbf{P} , related to \mathbf{J} by $\mathbf{J} = d\mathbf{P}/dt$. We write the second-order nonlinear polarization as,

$$\mathcal{P}^a(2\omega) = \chi_{\text{surface}}^{abc}(-2\omega; \omega, \omega) E^b(\omega) E^c(\omega), \quad (2.23)$$

where $\chi^{abc}(-2\omega; \omega, \omega)$ is the nonlinear susceptibility responsible for surface second-harmonic generation (SSHG). The superscripts in Eq. (2.23) denote Cartesian components, and if repeated are to be summed over. Without loss of generality we will define $\chi_{\text{surface}}^{abc}(-2\omega; \omega, \omega)$ to satisfy intrinsic permutation symmetry, $\chi_{\text{surface}}^{abc}(-2\omega; \omega, \omega) = \chi_{\text{surface}}^{acb}(-2\omega; \omega, \omega)$.

The unperturbed Hamiltonian is used to solve the Kohn-Sham equations [73] of Density Functional Theory (DFT). It is convenient to work within the Local Density Approximation (LDA), so we label the hamiltonian with the corresponding LDA superscript. Any other approximation can be used (like the generalized gradient approximation) and our derivation remains the same. Then,

$$H_0^{\text{LDA}}(\mathbf{r}, \mathbf{p}) = \frac{p^2}{2m_e} + V(\mathbf{r}, \mathbf{p}) \quad (2.24)$$

with m_e the mass of the electron, $\mathbf{p} = -i\hbar\nabla$ its canonical momentum, and V the periodic crystal potential, where we neglect spin-orbit terms. To be more general in our derivation of $\chi^{abc}(-2\omega; \omega, \omega)$, we assume contribution as is customary for most pseudopotentials, and then we replace V with

$$V^{\text{ps}}(\mathbf{r}, \mathbf{p}) = V(\mathbf{r}) + V^{\text{nl}}(\mathbf{r}, \mathbf{p}), \quad (2.25)$$

where $V(\mathbf{r})$ and $V^{\text{nl}}(\mathbf{r}, \mathbf{p})$ are the local and nonlocal parts, respectively. The argument (\mathbf{r}, \mathbf{p}) is equivalent to the explicit $(\mathbf{r}, \mathbf{r}')$ nonlocal notation [83]. For this nonlocal part, we have that

$$V^{\text{nl}}(\mathbf{r}, \mathbf{r}') \equiv \langle \mathbf{r}|V^{\text{nl}}|\mathbf{r}' \rangle \neq 0 \quad \text{for } \mathbf{r} \neq \mathbf{r}', \quad (2.26)$$

where $V^{\text{nl}}(\mathbf{r}, \mathbf{r}')$ is a function of \mathbf{r} and \mathbf{r}' representing the nonlocal contribution of the pseudopotential. In case of a local potential, i.e. $V = V(\mathbf{r})$, like that of all-electron schemes, we simply omit the contribution of $V^{\text{nl}}(\mathbf{r}, \mathbf{p})$ from the results that we have derived.

It is well known that the use of the LDA leads to an underestimation of the band gap. A standard procedure to correct for this is to use the “scissors approximation”, where the conduction bands are rigidly shifted in energy so that the band gap corresponds to the accepted experimental electronic band gap. [76–78] This is often in fairly good agreement with the GW band gap based on a more sophisticated calculation. [117] The LDA wave functions are used since they produce band structures with dispersion relations similar to those predicted by the GW. Mathematically, the scissors (non-local) operator S is added to the unperturbed or unscissored Hamiltonian H_0^{LDA} ,

$$H_0^\Sigma(\mathbf{r}, \mathbf{p}) = H_0^{\text{LDA}}(\mathbf{r}, \mathbf{p}) + S(\mathbf{r}, \mathbf{p}) \quad (2.27)$$

where

$$S(\mathbf{r}, \mathbf{p}) = \hbar\Delta \sum_n \int (1 - f_n) |n\mathbf{k}\rangle \langle n\mathbf{k}| d^3k, \quad (2.28)$$

with $\hbar\Delta$ the rigid (\mathbf{k} -independent) energy correction to be applied. The unscissored and scissored Hamiltonians satisfy

$$H_0^{\text{LDA}}(\mathbf{r}, \mathbf{p})\psi_{n\mathbf{k}}(\mathbf{r}) = \hbar\omega_n^{\text{LDA}}(\mathbf{k})\psi_{n\mathbf{k}}(\mathbf{r}),$$

$$H_0^\Sigma(\mathbf{r}, \mathbf{p})\psi_{n\mathbf{k}}(\mathbf{r}) = \hbar\omega_n^\Sigma(\mathbf{k})\psi_{n\mathbf{k}}(\mathbf{r}),$$

where the scissor-shifted energies, $\omega_n^\Sigma(\mathbf{k})$, are given by

$$\omega_n^\Sigma(\mathbf{k}) = \omega_n^{\text{LDA}}(\mathbf{k}) + (1 - f_n)\Delta. \quad (2.29)$$

Lastly, the Schrödinger equation reads

$$\left(\frac{-\hbar^2}{2m_e} \nabla^2 + V(\mathbf{r}) \right) \psi_{n\mathbf{k}}(\mathbf{r}) + \int V^{\text{nl}}(\mathbf{r}, \mathbf{r}') \psi_{n\mathbf{k}}(\mathbf{r}') d\mathbf{r}' = E_i \psi_{n\mathbf{k}}(\mathbf{r}), \quad (2.30)$$

where $\psi_{n\mathbf{k}}(\mathbf{r}) = \langle \mathbf{r} | n\mathbf{k} \rangle = e^{i\mathbf{k}\cdot\mathbf{r}} u_{n\mathbf{k}}(\mathbf{r})$, are the real space representations of the Bloch states $|n\mathbf{k}\rangle$ labeled by the band index n and the crystal momentum \mathbf{k} , and $u_{n\mathbf{k}}(\mathbf{r})$ is cell periodic. We emphasize that the scissored and unscissored Hamiltonian have the same eigenfunctions.

2.3 Length Gauge

According to Ref. [83], we first start with the interaction Hamiltonian expressed in the velocity gauge, containing the nonlocal parts $V^{\text{nl}}(\mathbf{r}, \mathbf{p})$ and $S(\mathbf{r}, \mathbf{p})$. Within the dipole approximation and using a gauge transformation, it can be transformed into an effective Hamiltonian [118]

$$H_I(t) = -e\mathbf{r} \cdot \mathbf{E}(t). \quad (2.31)$$

The treatment of the position operator \mathbf{r} for extended Bloch states is problematic and has been discussed in Refs. [119, 120] and will be dealt with in Appendix A.1. The matrix elements of \mathbf{r} are split between the *intraband* (\mathbf{r}_i) and *interband* (\mathbf{r}_e) parts, where $\mathbf{r} = \mathbf{r}_i + \mathbf{r}_e$ [119, 120], and its matrix elements are [65]

$$\langle n\mathbf{k} | \mathbf{r}_i | m\mathbf{k}' \rangle = \delta_{nm} [\delta(\mathbf{k} - \mathbf{k}') \xi_{nn}(\mathbf{k}) + i\nabla_{\mathbf{k}} \delta(\mathbf{k} - \mathbf{k}')], \quad (2.32)$$

$$\langle n\mathbf{k} | \mathbf{r}_e | m\mathbf{k}' \rangle = (1 - \delta_{nm}) \delta(\mathbf{k} - \mathbf{k}') \xi_{nm}(\mathbf{k}), \quad (2.33)$$

such that $\mathbf{r}_{e,nm} = 0$ for $n = m$, and

$$\boldsymbol{\xi}_{nm}(\mathbf{k}) \equiv i \frac{(2\pi)^3}{\Omega} \int_{\Omega} u_{n\mathbf{k}}^*(\mathbf{r}) \nabla_{\mathbf{k}} u_{m\mathbf{k}}(\mathbf{r}) d\mathbf{r}, \quad (2.34)$$

where Ω is the unit cell volume. The interband part, \mathbf{r}_e , can be obtained as follows. We use H_0^Σ in Eq. (2.22) to obtain the velocity operator

$$\mathbf{v}^\Sigma = \frac{1}{i\hbar} [\mathbf{r}, H_0^\Sigma], \quad (2.35)$$

and calculating its matrix elements

$$i\hbar \langle n\mathbf{k} | \mathbf{v}^\Sigma | m\mathbf{k} \rangle = \langle n\mathbf{k} | [\mathbf{r}, H_0^\Sigma] | m\mathbf{k} \rangle = \langle n\mathbf{k} | \mathbf{r} H_0^\Sigma - H_0^\Sigma \mathbf{r} | m\mathbf{k} \rangle = (\hbar\omega_m^\Sigma(\mathbf{k}) - \hbar\omega_n^\Sigma(\mathbf{k})) \langle n\mathbf{k} | \mathbf{r} | m\mathbf{k} \rangle. \quad (2.36)$$

Defining $\omega_{nm}^\Sigma(\mathbf{k}) = \omega_n^\Sigma(\mathbf{k}) - \omega_m^\Sigma(\mathbf{k})$, we get

$$\mathbf{r}_{nm}(\mathbf{k}) = \frac{\mathbf{v}_{nm}^\Sigma(\mathbf{k})}{i\omega_{nm}^\Sigma(\mathbf{k})} \quad n \notin D_m, \quad (2.37)$$

which can be identified as $\mathbf{r}_{nm} = (1 - \delta_{nm})\boldsymbol{\xi}_{nm} \rightarrow \mathbf{r}_{e,nm}$. Here, D_m are all the possible degenerate m -states. For the intraband part, \mathbf{r}_i only appears in commutators during the derivation of the optical response. We use [65]

$$\langle n\mathbf{k} | [\mathbf{r}_i, \mathcal{O}] | m\mathbf{k}' \rangle = i\delta(\mathbf{k} - \mathbf{k}') (\mathcal{O}_{nm})_{;\mathbf{k}}, \quad (2.38)$$

where

$$(\mathcal{O}_{nm})_{;\mathbf{k}} = \nabla_{\mathbf{k}} \mathcal{O}_{nm}(\mathbf{k}) - i\mathcal{O}_{nm}(\mathbf{k}) (\boldsymbol{\xi}_{nn}(\mathbf{k}) - \boldsymbol{\xi}_{mm}(\mathbf{k})), \quad (2.39)$$

is the generalized derivative of the operator \mathcal{O} (see Appendix A.1). The vectors $\boldsymbol{\xi}_{nn}(\mathbf{k})$ are defined in Ref. [65] though they do not need to be calculated explicitly in what follows.

As can be seen from Eq. (2.27) and (2.24), both \mathcal{S} and V^{nl} are nonlocal potentials. Their contribution in the calculation of the optical response must be considered in order to get reliable results [83]. Before continuing, we derive a key result for the length gauge formulation. Then,

$$\begin{aligned} \mathbf{v}^\Sigma &= \mathbf{v} + \mathbf{v}^{\text{nl}} + \mathbf{v}^{\mathcal{S}} = \mathbf{v}^{\text{LDA}} + \mathbf{v}^{\mathcal{S}} \\ &= \frac{\mathbf{p}}{m_e} + \frac{1}{i\hbar} [\mathbf{r}, V^{\text{nl}}(\mathbf{r}, \mathbf{r}')] + \frac{1}{i\hbar} [\mathbf{r}, \mathcal{S}(\mathbf{r}, \mathbf{p})], \end{aligned} \quad (2.40)$$

where we have defined

$$\begin{aligned} \mathbf{v} &= \frac{\mathbf{p}}{m_e} \\ \mathbf{v}^{\text{nl}} &= \frac{1}{i\hbar} [\mathbf{r}, V^{\text{nl}}] \\ \mathbf{v}^{\mathcal{S}} &= \frac{1}{i\hbar} [\mathbf{r}, \mathcal{S}(\mathbf{r}, \mathbf{p})] \\ \mathbf{v}^{\text{LDA}} &= \mathbf{v} + \mathbf{v}^{\text{nl}} \end{aligned} \quad (2.41)$$

$\mathbf{p} = -i\hbar\nabla$ is the momentum operator, and using $[r^a, p^b] = i\hbar\delta_{ab}$, where δ_{ab} is the Kronecker delta. Using Eq. (2.28), we obtain that the matrix elements of $\mathbf{v}^{\mathcal{S}}$ are given by

$$\mathbf{v}_{nm}^{\mathcal{S}} = i\Delta f_{mn} \mathbf{r}_{nm}, \quad (2.42)$$

with $f_{nm} \equiv f_n - f_m$, where we see that $\mathbf{v}_{nn}^S = 0$. From Eqs. (2.37) and (2.40) it follows that

$$\begin{aligned}\mathbf{v}_{nm}^\Sigma &= \mathbf{v}_{nm}^{\text{LDA}} + i\Delta f_{mn} \mathbf{r}_{nm} \\ &= \mathbf{v}_{nm}^{\text{LDA}} + i\Delta f_{mn} \frac{\mathbf{v}_{nm}^\Sigma(\mathbf{k})}{i\omega_{nm}^\Sigma(\mathbf{k})} \\ \mathbf{v}_{nm}^\Sigma \frac{\omega_{nm}^\Sigma - \Delta f_{mn}}{\omega_{nm}^\Sigma} &= \mathbf{v}_{nm}^{\text{LDA}} \\ \mathbf{v}_{nm}^\Sigma \frac{\omega_{nm}^{\text{LDA}}}{\omega_{nm}^\Sigma} &= \mathbf{v}_{nm}^{\text{LDA}} \\ \frac{\mathbf{v}_{nm}^\Sigma}{\omega_{nm}^\Sigma} &= \frac{\mathbf{v}_{nm}^{\text{LDA}}}{\omega_{nm}^{\text{LDA}}},\end{aligned}\tag{2.43}$$

since $\omega_{nm}^\Sigma - \Delta f_{mn} = \omega_{nm}^{\text{LDA}}$. Therefore,

$$\mathbf{v}_{nm}^\Sigma(\mathbf{k}) = \frac{\omega_{nm}^\Sigma}{\omega_{nm}^{\text{LDA}}} \mathbf{v}_{nm}^{\text{LDA}}(\mathbf{k}) = \left(1 + \frac{\Delta}{\omega_c(\mathbf{k}) - \omega_v(\mathbf{k})}\right) \mathbf{v}_{nm}^{\text{LDA}}(\mathbf{k}) \quad n \notin D_m\tag{2.44}$$

$$\mathbf{v}_{nn}^\Sigma(\mathbf{k}) = \mathbf{v}_{nn}^{\text{LDA}}(\mathbf{k}),$$

and Eq. (2.37) gives

$$\mathbf{r}_{nm}(\mathbf{k}) = \frac{\mathbf{v}_{nm}^\Sigma(\mathbf{k})}{i\omega_{nm}^\Sigma(\mathbf{k})} = \frac{\mathbf{v}_{nm}^{\text{LDA}}(\mathbf{k})}{i\omega_{nm}^{\text{LDA}}(\mathbf{k})} \quad n \notin D_m.\tag{2.45}$$

The matrix elements of $\mathbf{r}_{nm}(\mathbf{k})$ are identical using either the LDA or scissored Hamiltonian, thus negating the need to label them. Of course, it is more convenient to calculate them through $\mathbf{v}_{nm}^{\text{LDA}}(\mathbf{k})$ which includes only the contribution of $\mathbf{v}_{nm}^{\text{nl}}(\mathbf{k})$. These can be readily calculated for fully separable nonlocal pseudopotentials in the Kleinman-Bylander form. [121–124] The advantage of using the electron density operator along with the length gauge formalism for calculating linear and nonlinear optical responses, for the scissored Hamiltonian, resides in the ease with which the scissors operator can be introduced into the calculation by simply using the unscissored LDA Hamiltonian, H_0^{LDA} , for the unperturbed system with $-e\mathbf{r} \cdot \mathbf{E}(t)$ as the interaction. We stress that within the length gauge, we need only replace ω_n^{LDA} with ω_n^Σ at the end of the derivation to obtain the scissored results for any susceptibility expression, whether linear or nonlinear [80]. In Appendix A.2 we outline how this is accomplished.

We also need to derive the matrix elements the density operator. In order to proceed, we must now work out the commutator of Eq. (2.21). Then,

$$\begin{aligned}\langle n\mathbf{k} | [\mathbf{r}(t), \tilde{\rho}^{(N)}(t)] | m\mathbf{k} \rangle &= \langle n\mathbf{k} | [U\mathbf{r}U^\dagger, U\rho^{(N)}(t)U^\dagger] | m\mathbf{k} \rangle \\ &= \langle n\mathbf{k} | U [\mathbf{r}, \rho^{(N)}(t)] U^\dagger | m\mathbf{k} \rangle \\ &= e^{i\omega_{nm}^\Sigma t} \left(\langle n\mathbf{k} | [\mathbf{r}_e, \rho^{(N)}(t)] + [\mathbf{r}_i, \rho^{(N)}(t)] | m\mathbf{k} \rangle \right),\end{aligned}\tag{2.46}$$

where the time dependence of the operator in the interaction picture is explicitly shown by the exponential factor, and the implicit dependence of $\rho^{(N)}$ inherited from Eq. (2.9) is given through

the t argument. We calculate the interband term first, so using Eq. (2.45) we obtain

$$\begin{aligned} \langle n\mathbf{k}| [\mathbf{r}_e, \tilde{\rho}^{(N)}(t)] |m\mathbf{k}\rangle &= \sum_q \left(\langle n\mathbf{k}|\mathbf{r}_e|q\mathbf{k}\rangle \langle q\mathbf{k}|\tilde{\rho}^{(N)}(t)|m\mathbf{k}\rangle - \langle n\mathbf{k}|\tilde{\rho}^{(N)}(t)|q\mathbf{k}\rangle \langle q\mathbf{k}|\mathbf{r}_e|m\mathbf{k}\rangle \right) \\ &= \sum_{q \neq n,m} \left(\mathbf{r}_{nq}(\mathbf{k}) \rho_{qm}^{(N)}(\mathbf{k}; t) - \rho_{nq}^{(N)}(\mathbf{k}; t) \mathbf{r}_{qm}(\mathbf{k}) \right) \\ &\equiv \mathbf{R}_e^{(N)}(\mathbf{k}; t), \end{aligned} \quad (2.47)$$

and from Eq. (2.38),

$$\langle n\mathbf{k}|[\mathbf{r}_i, \tilde{\rho}^{(N)}(t)]|m\mathbf{k}'\rangle = i\delta(\mathbf{k} - \mathbf{k}')(\rho_{nm}^{(N)}(t))_{;\mathbf{k}} \equiv \delta(\mathbf{k} - \mathbf{k}')\mathbf{R}_i^{(N)}(\mathbf{k}; t). \quad (2.48)$$

Then Eq. (2.21) becomes

$$\tilde{\rho}_{nm}^{(N+1)}(\mathbf{k}; t) = \frac{ie}{\hbar} \int_{-\infty}^t e^{i(\omega_{nm}^\Sigma - \tilde{\omega})t'} [R_e^{\text{b}(N)}(\mathbf{k}; t') + R_i^{\text{b}(N)}(\mathbf{k}; t')] E^{\text{b}} dt', \quad (2.49)$$

where the roman superindices abc denote Cartesian components that are summed over if repeated. Starting from the linear response and proceeding from Eq. (2.16) and (2.47),

$$\begin{aligned} R_e^{\text{b}(0)}(\mathbf{k}; t) &= \sum_q \left(r_{nq}^{\text{b}}(\mathbf{k}) \rho_{qm}^{(0)}(\mathbf{k}) - \rho_{nq}^{(0)}(\mathbf{k}) r_{qm}^{\text{b}}(\mathbf{k}) \right) \\ &= \sum_q \left(r_{nq}^{\text{b}}(\mathbf{k}) \delta_{qm} f_m(\hbar\omega_m^\Sigma(\mathbf{k})) - \delta_{nq} f_n(\hbar\omega_n^\Sigma(\mathbf{k})) r_{qm}^{\text{b}}(\mathbf{k}) \right) \\ &= f_{mn} r_{nm}^{\text{b}}(\mathbf{k}), \end{aligned} \quad (2.50)$$

where $f_{mn} = f_m - f_n$. From now on, it should be clear that the matrix elements of \mathbf{r}_{nm} imply $n \notin D_m$. We also have from Eq. (2.48) and Eq. (2.39) that

$$R_i^{\text{b}(0)}(\mathbf{k}) = i(\rho_{nm}^{(0)})_{;\mathbf{k}^{\text{b}}} = i\delta_{nm}(f_{n\mathbf{k}})_{;\mathbf{k}^{\text{b}}} = i\delta_{nm}\nabla_{k^{\text{b}}} f_{n\mathbf{k}}. \quad (2.51)$$

For a semiconductor at $T = 0$, $f_n = 1$ if the state $|n\mathbf{k}\rangle$ is a valence state and $f_n = 0$ if it is a conduction state. Thus, $\nabla_{\mathbf{k}} f_n = 0$, $\mathbf{R}_i^{(0)} = 0$ and the linear response has no contribution from the intraband transitions. Then,

$$\begin{aligned} \tilde{\rho}_{nm}^{(1)}(\mathbf{k}; t) &= \frac{ie}{\hbar} f_{mn} r_{nm}^{\text{b}}(\mathbf{k}) E^{\text{b}} \int_{-\infty}^t dt' e^{i(\omega_{nm}^\Sigma - \tilde{\omega})t'} \\ &= \frac{e}{\hbar} f_{mn} r_{nm}^{\text{b}}(\mathbf{k}) E^{\text{b}} \frac{e^{i(\omega_{nm}^\Sigma - \tilde{\omega})t}}{\omega_{nm}^\Sigma - \tilde{\omega}} \\ &= e^{i(\omega_{nm}^\Sigma - \tilde{\omega})t} B_{mn}^{\text{b}}(\mathbf{k}) E^{\text{b}}(t) \\ &= e^{i\omega_{nm}^\Sigma t} \rho_{nm}^{(1)}(\mathbf{k}; t), \end{aligned} \quad (2.52)$$

with

$$B_{nm}^{\text{b}}(\mathbf{k}, \omega) = \frac{e}{\hbar} \frac{f_{mn} r_{nm}^{\text{b}}(\mathbf{k})}{\omega_{nm}^\Sigma - \tilde{\omega}}, \quad (2.53)$$

and

$$\rho_{nm}^{(1)}(\mathbf{k}; t) = B_{mn}^{\text{b}}(\mathbf{k}, \omega) E^{\text{b}}(\omega) e^{-i\tilde{\omega}t}. \quad (2.54)$$

Now, we calculate the second-order response. Then, from Eq. (2.47)

$$\begin{aligned} R_e^{\text{b}(1)}(\mathbf{k}; t) &= \sum_q \left(r_{nq}^{\text{b}}(\mathbf{k}) \rho_{qm}^{(1)}(\mathbf{k}; t) - \rho_{nq}^{(1)}(\mathbf{k}; t) r_{qm}^{\text{b}}(\mathbf{k}) \right) \\ &= \sum_q \left(r_{nq}^{\text{b}}(\mathbf{k}) B_{qm}^{\text{c}}(\mathbf{k}, \omega) - B_{nq}^{\text{c}}(\mathbf{k}, \omega) r_{qm}^{\text{b}}(\mathbf{k}) \right) E^{\text{c}}(t), \end{aligned} \quad (2.55)$$

and from Eq. (2.48)

$$R_i^{\text{b}(1)}(\mathbf{k}; t) = i(\rho_{nm}^{(1)}(t))_{;k^{\text{b}}} = iE^{\text{c}}(t)(B_{nm}^{\text{c}}(\mathbf{k}, \omega))_{;k^{\text{b}}}. \quad (2.56)$$

Using Eqs. (2.55) and (2.56) in Eq. (2.49), we obtain

$$\begin{aligned} \tilde{\rho}_{nm}^{(2)}(\mathbf{k}; t) &= \frac{e}{i\hbar} \left[i \sum_q \left(r_{nq}^{\text{b}}(\mathbf{k}) B_{qm}^{\text{c}}(\mathbf{k}, \omega) - B_{nq}^{\text{c}}(\mathbf{k}, \omega) r_{qm}^{\text{b}}(\mathbf{k}) \right) \right. \\ &\quad \left. - \left(B_{nm}^{\text{c}}(\mathbf{k}, \omega) \right)_{;k^{\text{b}}} \right] E^{\text{b}}(\omega) E^{\text{c}}(\omega) \int_{-\infty}^t e^{i(\omega_{nm}^{\Sigma} - 2\tilde{\omega})t'} dt' \\ &= \frac{e}{i\hbar} \frac{1}{\omega_{nm}^{\Sigma} - 2\tilde{\omega}} \left[i \sum_q \left(r_{nq}^{\text{b}}(\mathbf{k}) B_{qm}^{\text{c}}(\mathbf{k}, \omega) - B_{nq}^{\text{c}}(\mathbf{k}, \omega) r_{qm}^{\text{b}}(\mathbf{k}) \right) \right. \\ &\quad \left. - \left(B_{nm}^{\text{c}}(\mathbf{k}, \omega) \right)_{;k^{\text{b}}} \right] E^{\text{b}}(\omega) E^{\text{c}}(\omega) e^{i(\omega_{nm}^{\Sigma} - 2\tilde{\omega})t} \\ &= e^{i\omega_{nm}^{\Sigma}t} \rho_{nm}^{(2)}(\mathbf{k}; t). \end{aligned} \quad (2.57)$$

Now, we write $\rho_{nm}^{(2)}(\mathbf{k}; t) = \rho_{nm}^{(2)}(\mathbf{k}; 2\omega) e^{-i2\tilde{\omega}t}$, with

$$\begin{aligned} \rho_{nm}^{(2)}(\mathbf{k}; 2\omega) &= \frac{e}{i\hbar} \frac{1}{\omega_{nm}^{\Sigma} - 2\tilde{\omega}} \left[i \sum_q \left(r_{nq}^{\text{b}} B_{qm}^{\text{c}}(\mathbf{k}, \omega) - B_{nq}^{\text{c}}(\mathbf{k}, \omega) r_{qm}^{\text{b}} \right) \right. \\ &\quad \left. - \left(B_{nm}^{\text{c}}(\mathbf{k}, \omega) \right)_{;k^{\text{b}}} \right] E^{\text{b}}(\omega) E^{\text{c}}(\omega) \end{aligned} \quad (2.58)$$

where $B_{qm}^{\text{a}}(\mathbf{k}, \omega)$ are given by Eq. (2.53). We remark that $\mathbf{r}_{nm}(\mathbf{k})$ are the same whether calculated with the LDA or the scissored Hamiltonian (see Eq. (2.45)). We chose the former in this thesis.

We have used the fact that for a cold semiconductor $\partial f_n / \partial \mathbf{k} = 0$ and thus the intraband contribution to the linear term vanishes identically. Note that the indices in Eq. (2.57) are all different from each other. This is due to the f_{nm} factor in Eq. (2.53), and therefore $B_{nn}^{\text{a}} = 0$. The dependence on \mathbf{k} of all quantities is implicitly understood from this point forward.

2.4 Layered Current Density

The approach we use to study the surface of a semi-infinite semiconductor crystal is as follows. Instead of using a semi-infinite system, we replace it by a super-cell that consists of a finite slab of atomic layers and a vacuum region (see Fig. 2.2). This super-cell is repeated to form a full three dimensional crystalline structure. The slab itself consists of front, back, and sub-surface regions, and in between these a region that is equivalent to the bulk of the system. In general the surface of a crystal reconstructs or relaxes as the atoms move to find equilibrium positions. This

is due to the fact that the otherwise balanced forces are disrupted when the surface atoms do not find their partner atoms that are now absent at the slab surface. To take the reconstruction or relaxation into account, we take “surface” to mean the true surface of the first layer of atoms and some of the atomic sub-layers adjacent to it. Since the front and the back surfaces of the slab are usually identical the total slab is centrosymmetric. This would imply that $\chi_{\text{slab}}^{\text{abc}} = 0$ so we must find a scheme in order to have a finite χ^{abc} representative of the surface. Even if the front and back surfaces of the slab are different, breaking the centrosymmetry and therefore giving an overall $\chi_{\text{slab}}^{\text{abc}} \neq 0$; we still need a procedure to extract the front surface $\chi_{\text{front}}^{\text{abc}}$ and the back surface $\chi_{\text{back}}^{\text{abc}}$ from the slab susceptibility. We have omitted the frequency dependence of χ^{abc} for convenience of notation.

A convenient way to accomplish the separation of the SH signal of either surface is to introduce a “cut function”, $\mathcal{C}(z)$, which is usually taken to be unity over one half of the slab and zero over the other half. [82] In this case $\mathcal{C}(z)$ will give the contribution of the side of the slab for which $\mathcal{C}(z) = 1$. As was done for the linear response, [125] we can generalize this simple choice for $\mathcal{C}(z)$ by a top-hat cut function $\mathcal{C}^\ell(z)$ that selects a given layer,

$$\mathcal{C}^\ell(z) = \Theta(z - z_\ell + \Delta_\ell^b)\Theta(z_\ell - z + \Delta_\ell^f), \quad (2.59)$$

where Θ is the Heaviside function. Here, $\Delta_\ell^{f/b}$ is the distance that the ℓ -th layer extends towards the front (f) or back (b) from its z_ℓ position. We take z_ℓ to be at the center of an atom that belongs to layer ℓ , so the previous equation would give the ℓ -th atomic-layer contribution to the nonlinear optical response. $\Delta_\ell^f + \Delta_\ell^b$ is the thickness of layer ℓ (see Fig. 2.2).

To introduce the cut function $\mathcal{C}(z)$ in the calculation of χ^{abc} , we start from the operator for the electron current, $\mathbf{j}(\mathbf{r}) = \frac{e}{2} (\mathbf{v}^\Sigma |\mathbf{r}\rangle\langle\mathbf{r}| + |\mathbf{r}\rangle\langle\mathbf{r}|\mathbf{v}^\Sigma)$, that leads to

$$\mathbf{j}^{(N)}(\mathbf{r}, t) = \text{Tr}(\mathbf{j}(\mathbf{r})\rho^{(N)}(t)) = \int \frac{d^3k}{8\pi^3} \sum_{nm} \rho_{nm}^{(N)}(\mathbf{k}; t) \mathbf{j}_{mn}(\mathbf{k}; \mathbf{r}). \quad (2.60)$$

We can derive the $\mathbf{j}_{mn}(\mathbf{k}; \mathbf{r})$ matrix elements as follows. The operator for the electron current is

$$\mathbf{j}(\mathbf{r}) = \frac{e}{2} (\mathbf{v}^\Sigma |\mathbf{r}\rangle\langle\mathbf{r}| + |\mathbf{r}\rangle\langle\mathbf{r}|\mathbf{v}^\Sigma), \quad (2.61)$$

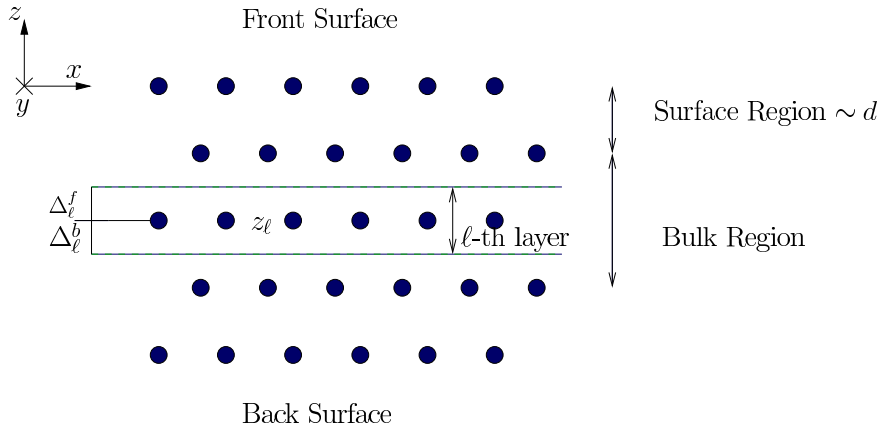


Figure 2.2: A sketch of the super-cell. The atomic slab corresponds to the circles representing the atoms of the system.

where \mathbf{v}^Σ is the electron's velocity operator to be dealt with below. We define $\hat{\mu} \equiv |\mathbf{r}\rangle\langle\mathbf{r}|$ and use the cyclic invariance of the trace to write

$$\begin{aligned} \text{Tr}(\mathbf{j}(\mathbf{r})\tilde{\rho}(t)) &= \text{Tr}(\tilde{\rho}(t)\hat{\mathbf{j}}(\mathbf{r})) \\ &= \frac{e}{2} (\text{Tr}(\tilde{\rho}\hat{\mathbf{v}}^\Sigma\hat{\mu}) + \text{Tr}(\tilde{\rho}\hat{\mu}\hat{\mathbf{v}}^\Sigma)) \\ &= \frac{e}{2} \sum_{n\mathbf{k}} (\langle n\mathbf{k}|\tilde{\rho}\mathbf{v}^\Sigma\hat{\mu}|n\mathbf{k}\rangle + \langle n\mathbf{k}|\tilde{\rho}\hat{\mu}\mathbf{v}^\Sigma|n\mathbf{k}\rangle) \\ &= \frac{e}{2} \sum_{nm} \langle n\mathbf{k}|\tilde{\rho}|m\mathbf{k}\rangle (\langle m\mathbf{k}|\mathbf{v}^\Sigma|\mathbf{r}\rangle\langle\mathbf{r}|n\mathbf{k}\rangle + \langle m\mathbf{k}|\mathbf{r}\rangle\langle\mathbf{r}|\mathbf{v}^\Sigma|n\mathbf{k}\rangle) \\ \mathbf{j}(\mathbf{r}, t) &= \sum_{nm} \rho_{nm}(\mathbf{k}; t) \mathbf{j}_{mn}(\mathbf{k}; \mathbf{r}), \end{aligned} \quad (2.62)$$

where

$$\mathbf{j}_{mn}(\mathbf{k}; \mathbf{r}) = \frac{e}{2} (\langle m\mathbf{k}|\mathbf{v}^\Sigma|\mathbf{r}\rangle\langle\mathbf{r}|n\mathbf{k}\rangle + \langle m\mathbf{k}|\mathbf{r}\rangle\langle\mathbf{r}|\mathbf{v}^\Sigma|n\mathbf{k}\rangle), \quad (2.63)$$

are the matrix elements of the microscopic current operator, and we have used the fact that the matrix elements between states $|n\mathbf{k}\rangle$ are diagonal in \mathbf{k} , i.e. proportional to $\delta(\mathbf{k} - \mathbf{k}')$. Integrating the microscopic current $\mathbf{j}(\mathbf{r}, t)$ over the entire slab gives the averaged microscopic current density, $\mathbf{J}(t)$. If we want the contribution from only one region of the unit cell towards the total current, we can integrate $\mathbf{j}(\mathbf{r}, t)$ over the desired region. Then the contribution to the current density from the chosen region of the slab is given by

$$\frac{1}{A} \int d^3r \mathcal{C}(z) \mathbf{J}^{(N)}(\mathbf{r}, t) \equiv \mathcal{J}^{(N)}(t),$$

where $\mathcal{J}^{(N)}(t)$ is the N -th order current induced in the region specified by $\mathcal{C}(z)$. Therefore we define

$$e\mathcal{V}_{mn}^\Sigma(\mathbf{k}) \equiv \int d^3r \mathcal{C}(z) \mathbf{j}_{mn}(\mathbf{k}; \mathbf{r}), \quad (2.64)$$

to write the Fourier transform of Eq. (2.60) as

$$\mathcal{J}^{(N)}(2\omega) = \frac{e}{A} \int \frac{d^3k}{8\pi^3} \sum_{mn} \mathcal{V}_{mn}^\Sigma(\mathbf{k}) \rho_{nm}^{(N)}(\mathbf{k}; 2\omega), \quad (2.65)$$

that gives the induced microscopic current of the chosen region, to order N in the external perturbation. From Eqs. (2.64) and (2.63) we obtain

$$\mathcal{V}_{mn}^{\Sigma,\ell}(\mathbf{k}) = \frac{1}{2} \int d^3r \mathcal{C}(z) \left[\langle m\mathbf{k}|\mathbf{v}^\Sigma|\mathbf{r}\rangle\langle\mathbf{r}|n\mathbf{k}\rangle + \langle m\mathbf{k}|\mathbf{r}\rangle\langle\mathbf{r}|\mathbf{v}^\Sigma|n\mathbf{k}\rangle \right], \quad (2.66)$$

and using the following property

$$\begin{aligned} \langle \mathbf{r}|\mathbf{v}^\Sigma(\mathbf{r}, \mathbf{r}')|n\mathbf{k}\rangle &= \int d^3r'' \langle \mathbf{r}|\mathbf{v}^\Sigma(\mathbf{r}, \mathbf{r}')|\mathbf{r}''\rangle\langle\mathbf{r}''|n\mathbf{k}\rangle \\ &= \mathbf{v}^\Sigma(\mathbf{r}, \mathbf{r}'') \int d^3r'' \langle \mathbf{r}|\mathbf{r}''\rangle\langle\mathbf{r}''|n\mathbf{k}\rangle \\ &= \mathbf{v}^\Sigma(\mathbf{r}, \mathbf{r}') \psi_{n\mathbf{k}}(\mathbf{r}), \end{aligned} \quad (2.67)$$

that stems from the fact that the operator $\mathbf{v}^\Sigma(\mathbf{r}, \mathbf{r}')$ does not act on \mathbf{r}'' , we can write

$$\begin{aligned}\mathcal{V}_{mn}^{\Sigma,\ell}(\mathbf{k}) &= \frac{1}{2} \int \mathcal{C}(z) \left[\psi_{n\mathbf{k}}(\mathbf{r}) \mathbf{v}^{\Sigma*} \psi_{m\mathbf{k}}^*(\mathbf{r}) + \psi_{m\mathbf{k}}^*(\mathbf{r}) \mathbf{v}^{\Sigma} \psi_{n\mathbf{k}}(\mathbf{r}) \right] d^3r \\ &= \int \psi_{m\mathbf{k}}^*(\mathbf{r}) \left[\frac{\mathcal{C}(z) \mathbf{v}^{\Sigma} + \mathbf{v}^{\Sigma} \mathcal{C}(z)}{2} \right] \psi_{n\mathbf{k}}(\mathbf{r}) d^3r \\ &= \int \psi_{m\mathbf{k}}^*(\mathbf{r}) \mathcal{V}^\Sigma \psi_{n\mathbf{k}}(\mathbf{r}) d^3r,\end{aligned}\quad (2.68)$$

where we used the hermitian property of \mathbf{v}^Σ and defined

$$\mathcal{V}^\Sigma = \frac{\mathcal{C}(z) \mathbf{v}^{\Sigma} + \mathbf{v}^{\Sigma} \mathcal{C}(z)}{2}, \quad (2.69)$$

We see that the replacement

$$\mathbf{V} \rightarrow \mathcal{V} = \frac{\mathcal{C}(z) \mathbf{V} + \mathbf{V} \mathcal{C}(z)}{2}, \quad (2.70)$$

is all that is needed to change any of the electron velocity operators \mathbf{V} to the new velocity operator \mathcal{V} that implicitly takes into account the contribution of the region of the slab given by $\mathcal{C}(z)$. We note that this modified operator is hermitian as it should. [126] The operator \mathbf{V} could be any of those given by Eq. (2.40), thus

$$\begin{aligned}\mathcal{V}^\Sigma &= \mathcal{V}^{\text{LDA}} + \mathcal{V}^S \\ \mathcal{V}^{\text{LDA}} &= \mathcal{V} + \mathcal{V}^{\text{nl}}.\end{aligned}\quad (2.71)$$

As shown in Appendix A.9, Eq. (2.43) is generalized to $\mathcal{V}_{nm}^\Sigma = (\omega_{nm}^\Sigma / \omega_{nm}^{\text{LDA}}) \mathcal{V}_{nm}^{\text{LDA}}$ from which \mathcal{V}_{nm}^Σ can be readily calculated. As a consistency test we have calculated the matrix elements of \mathcal{V}^{LDA} and \mathcal{V}^S separately, according to the derivation presented in Appendix A.4 and A.3, and confirm that both approaches yield identical results for $\chi_{\text{surface}}^{\text{abc}}$. If not stated differently, calligraphic letters correspond to layer quantities.

To limit the SHG response to one surface, Eq. (2.70) for \mathcal{V} was proposed in Ref. [82] and later used in Refs. [55], [69], [70], and [71] also in the context of SHG. The layer-by-layer analysis of Refs. [127] and [128] used Eq. (2.59), limiting the current response to a particular layer of the slab and used to obtain the anisotropic linear optical response of semiconductor surfaces. However, the first formal derivation of this scheme is presented in Ref. [125] for the linear response. In this thesis I formally introduce the cut function $\mathcal{C}(z)$ for the second-harmonic optical response of semiconductor surfaces, from an average of the second order polarization over the region of interest.

2.5 Microscopic surface susceptibility

In this section we obtain the expressions for the surface susceptibility tensor $\chi_{\text{surface}}^{\text{abc}}$. Using $\mathcal{J} = d\mathcal{P}/dt$ and Eq. (2.65) we obtain the SH polarization of a given region as

$$\mathcal{P}^{(2)}(2\omega) = \frac{ie}{2A\tilde{\omega}} \int \frac{d^3k}{8\pi^3} \sum_{mn} \mathcal{V}_{mn}^\Sigma(\mathbf{k}) \rho_{nm}^{(2)}(\mathbf{k}; 2\omega), \quad (2.72)$$

and using Eqs. (2.23) and (2.57) leads to

$$\chi^{abc}(-2\omega; \omega, \omega) = \frac{e^2}{2A\hbar\tilde{\omega}} \int \frac{d^3k}{8\pi^3} \sum_{mn} \frac{\mathcal{V}_{mn}^{\Sigma,a}(\mathbf{k})}{\omega_{nm}^\Sigma - 2\tilde{\omega}} \left[i \sum_q \left(r_{nq}^b B_{qm}^c(\mathbf{k}, \omega) - B_{nq}^c(\mathbf{k}, \omega) r_{qm}^b \right) - \left(B_{nm}^c(\mathbf{k}, \omega) \right)_{;k^b} \right], \quad (2.73)$$

which gives the susceptibility $\chi^{abc}(-2\omega; \omega, \omega)$ of the layers of the slab specified by $\mathcal{C}(z)$. We mention that the units of $\chi^{abc}(-2\omega; \omega, \omega)$ are m^2/V , as they should be for a surface SH susceptibility. Using Eq. (2.53) we split this equation into two contributions from the first and second terms on the right hand side of Eq. (2.73):

$$\chi_i^{abc}(-2\omega; \omega, \omega) = -\frac{e^3}{A\hbar^2 2\tilde{\omega}} \int \frac{d^3k}{8\pi^3} \sum_{mn} \frac{\mathcal{V}_{mn}^{\Sigma,a}}{\omega_{nm}^\Sigma - 2\tilde{\omega}} \left(\frac{f_{mn} r_{nm}^b}{\omega_{nm}^\Sigma - \tilde{\omega}} \right)_{;k^c}, \quad (2.74)$$

related to intraband transitions, and

$$\chi_e^{abc}(-2\omega; \omega, \omega) = \frac{ie^3}{A\hbar^2 2\tilde{\omega}} \int \frac{d^3k}{8\pi^3} \sum_{qmn} \frac{\mathcal{V}_{mn}^{\Sigma,a}}{\omega_{nm}^\Sigma - 2\tilde{\omega}} \left(\frac{r_{nq}^c r_{qm}^b f_{mq}}{\omega_{qm}^\Sigma - \tilde{\omega}} - \frac{r_{nq}^b r_{qm}^c f_{qn}}{\omega_{nq}^\Sigma - \tilde{\omega}} \right), \quad (2.75)$$

related to interband transitions. The generalized derivative in Eq. (2.74) is dealt with by the chain rule

$$\left(\frac{f_{mn} r_{nm}^b}{\omega_{nm}^\Sigma - \tilde{\omega}} \right)_{;k^c} = \frac{f_{mn}}{\omega_{nm}^\Sigma - \tilde{\omega}} \left(r_{nm}^b \right)_{;k^c} - \frac{f_{mn} r_{nm}^b \Delta_{nm}^c}{(\omega_{nm}^\Sigma - \tilde{\omega})^2}, \quad (2.76)$$

where substituting H_0^Σ into Eq. (2.38) and then Eq. (2.45) we obtain

$$\left(\omega_{nm}^\Sigma \right)_{;k^a} = \left(\omega_{nm}^{\text{LDA}} \right)_{;k^a} = v_{nn}^{\text{LDA},a} - v_{mm}^{\text{LDA},a} \equiv \Delta_{nm}^a. \quad (2.77)$$

The apparent divergence as $\tilde{\omega} \rightarrow 0$ in Eqs. (2.74) and (2.75), is removed by a partial fraction expansion over $\tilde{\omega}$. Using time-reversal symmetry, an integration by parts to remove the square in the denominator of the second term of Eq. (2.76), and taking the limit of $\eta \rightarrow 0$, we obtain the following expressions for the imaginary parts of Eqs. (2.74) and (2.75),

$$\text{Im}[\chi_{e,\omega}^{abc}] = \frac{\pi|e|^3}{2\hbar^2} \int \frac{d^3k}{8\pi^3} \sum_{vc} \sum_{q \neq (v,c)} \frac{1}{\omega_{cv}^\Sigma} \left[\frac{\text{Im}[\mathcal{V}_{qc}^{\Sigma,a}\{r_{cv}^b r_{vq}^c\}]}{(2\omega_{cv}^\Sigma - \omega_{cq}^\Sigma)} - \frac{\text{Im}[\mathcal{V}_{vq}^{\Sigma,a}\{r_{qc}^c r_{cv}^b\}]}{(2\omega_{cv}^\Sigma - \omega_{qv}^\Sigma)} \right] \delta(\omega_{cv}^\Sigma - \omega), \quad (2.78a)$$

$$\text{Im}[\chi_{i,\omega}^{abc}] = \frac{\pi|e|^3}{2\hbar^2} \int \frac{d^3k}{8\pi^3} \sum_{cv} \frac{1}{(\omega_{cv}^\Sigma)^2} \left[\text{Re} \left[\left\{ r_{cv}^b \left(\mathcal{V}_{vc}^{\Sigma,a} \right)_{;k^c} \right\} \right] + \frac{\text{Re} \left[\mathcal{V}_{vc}^{\Sigma,a} \left\{ r_{cv}^b \Delta_{cv}^c \right\} \right]}{\omega_{cv}^\Sigma} \right] \delta(\omega_{cv}^\Sigma - \omega), \quad (2.78b)$$

$$\text{Im}[\chi_{e,2\omega}^{abc}] = -\frac{\pi|e|^3}{2\hbar^2} \int \frac{d^3k}{8\pi^3} \sum_{vc} \frac{4}{\omega_{cv}^\Sigma} \left[\sum_{v' \neq v} \frac{\text{Im}[\mathcal{V}_{vc}^{\Sigma,a}\{r_{cv}^b r_{v'v}^c\}]}{2\omega_{cv'}^\Sigma - \omega_{cv}^\Sigma} - \sum_{c' \neq c} \frac{\text{Im}[\mathcal{V}_{vc}^{\Sigma,a}\{r_{cc'}^c r_{c'v}^b\}]}{2\omega_{c'v}^\Sigma - \omega_{cv}^\Sigma} \right] \delta(\omega_{cv}^\Sigma - 2\omega), \quad (2.78c)$$

$$\text{Im}[\chi_{i,2\omega}^{abc}] = \frac{\pi|e|^3}{2\hbar^2} \int \frac{d^3k}{8\pi^3} \sum_{vc} \frac{4}{(\omega_{cv}^\Sigma)^2} \left[\text{Re} \left[\mathcal{V}_{vc}^{\Sigma,a} \left\{ \left(r_{cv}^b \right)_{;k^c} \right\} \right] - \frac{2\text{Re} \left[\mathcal{V}_{vc}^{\Sigma,a} \left\{ r_{cv}^b \Delta_{cv}^c \right\} \right]}{\omega_{cv}^\Sigma} \right] \delta(\omega_{cv}^\Sigma - 2\omega), \quad (2.78d)$$

where we have split the interband and intraband 1ω and 2ω contributions and suppressed the ω arguments for convenience of notation. The factor of 2 for spin degeneracy is not included in Eq. (2.78). The real part of each contribution can be obtained through a Kramers-Kronig transformation [129] and $\chi^{abc} = \chi_{e,\omega}^{abc} + \chi_{e,2\omega}^{abc} + \chi_{i,\omega}^{abc} + \chi_{i,2\omega}^{abc}$. To fulfill the required intrinsic permutation symmetry, the $\{\}$ notation symmetrizes the bc Cartesian indices, i.e. $\{u^b s^c\} = (u^b s^c + u^c s^b)/2$, and thus $\chi^{abc} = \chi^{acb}$. The full expressions for $\chi^{abc}(-2\omega; \omega, \omega)$, along with the various quantities involved in Eq. (2.78) are given in the Appendix A.6. We mention that if we take $\mathcal{C}(z) = 1$ through out, the layered matrix elements \mathcal{V}_{nm}^Σ become standard bulk-like \mathbf{v}_{nm}^Σ matrix elements. We mention that in this case, Eq. (2.78) is equivalent to the expressions of Ref. [81], valid for bulk semiconductors. Finally, we could also calculate the nonlinear surface susceptibility as

$$\chi_{\text{surface}}(-2\omega; \omega, \omega) = \sum_{\{\ell\}} \chi^\ell(-2\omega; \omega, \omega), \quad (2.79)$$

where ℓ would denote a particular layer chosen through $\mathcal{C}^\ell(z)$ of Eq. (2.59) and $\{\ell\}$ is meant to be a chosen set of layers. For instance, one can take a single layer encompassing half of the slab, or take each atomic layer individually to the middle of the slab. For the first case there is a single summand in Eq. (2.79). For the second case there is a sum from $\ell = 1$, denoting the first layer right at the surface, to $\ell = N$, denoting the layer at the middle of the slab that behaves like a bulk layer. We remark that the value of N is not universal and the slab needs to have enough atomic layers in order to give converged results for $\chi_{\text{surface}}(-2\omega; \omega, \omega)$. We can use Eq. (2.79) for either the front or the back surface.

In Appendices A.7 and A.4 we demonstrate how to calculate the generalized derivatives of $(\mathbf{r}_{nm})_{;\mathbf{k}}$ and $(\mathcal{V}_{nm}^{\Sigma,a})_{;\mathbf{k}}$. From Appendix A.7 we find that T_{nm}^{ab} , given by

$$T_{nm}^{ab} = \frac{\hbar}{m_e} \delta_{ab} \delta_{nm} - \hbar L_{nm}^{ab}, \quad (2.80)$$

where

$$L_{nm}^{ab} = \frac{i}{\hbar} [r^b, v^{\text{nl},a}]_{nm}, \quad (2.81)$$

is the contribution to the generalized derivatives $(\mathbf{r}_{nm})_{;\mathbf{k}}$, and $(\mathcal{V}_{nm}^{\Sigma,a,\ell})_{;\mathbf{k}}$ coming from the nonlocal part of the pseudopotential, \mathbf{v}^{nl} . In Appendix A.8 we calculate L_{nm}^{ab} . It is shown in Ref. [118] that this term has a very small numerical value, and a computational time of at least an order of magnitude larger than for all the other terms involved in the expressions for χ^{abc} . Therefore, we neglect it throughout this thesis and take

$$T_{nm}^{ab} \approx \frac{\hbar}{m_e} \delta_{ab} \delta_{nm}. \quad (2.82)$$

2.6 About the code

The TINIBA code is a suite of scripts that work with the popular ABINIT package to run and calculate optical properties of crystalline semiconductors by parallelizing the computation of the different quantities involved in the procedure. I have created a [Github repository](#) with the user manual for the TINIBA code, along with a detailed manuscript on how we coded the expressions derived in this chapter.

2.7 Conclusions

I have presented a formulation to calculate the surface second-harmonic (SSH) susceptibility tensor $\chi_{\text{surface}}(-2\omega; \omega, \omega)$, using the length gauge formalism and within the independent particle approximation (IPA). It includes on equal footing: (i) the scissors correction, (ii) the contribution of the non-local part of the pseudopotentials, and (iii) the cut function. We have neglected local field and excitonic effects. Although these are important factors in the optical response of a semiconductor, their efficient calculation is theoretically and numerically challenging and still under debate [67]. This merits further study but is beyond the scope of this thesis. Nevertheless, the inclusion of aforementioned contributions in our scheme opens the unprecedented possibility to study surface SHG with more versatility and more accurate results.

Chapter 3

Surface Second-Harmonic Generation Yield

Outline

3.1	The Three Layer Model for the SSHG Yield	29
3.1.1	Multiple SHG reflections	32
3.1.2	Multiple Reflections for the Linear Field	33
3.1.3	Deriving the SSHG yield	34
3.2	\mathcal{R}_{iF} for different polarization cases	36
3.2.1	\mathcal{R}_{pP} (<i>p</i> -in, <i>P</i> -out)	37
3.2.2	\mathcal{R}_{sP} (<i>s</i> -in, <i>P</i> -out)	39
3.2.3	\mathcal{R}_{pS} (<i>p</i> -in, <i>S</i> -out)	39
3.2.4	\mathcal{R}_{sS} (<i>s</i> -in, <i>S</i> -out)	40
3.3	Some Scenarios of Interest	40
3.3.1	The 3-layer Model Without Multiple Reflections	41
3.3.2	The two layer, or Fresnel (2-layer-fresnel) model	42
3.3.3	The 2-layer-bulk model: evaluating $\mathcal{P}(2\omega)$ and $\mathbf{E}(\omega)$ in the bulk	42
3.3.4	The 2-layer-vacuum model: evaluating $\mathcal{P}(2\omega)$ and $\mathbf{E}(\omega)$ in the vacuum	42
3.3.5	The 3-layer-hybrid model: evaluating $\mathcal{P}(2\omega)$ in ℓ and $\mathbf{E}(\omega)$ in the bulk	42
3.4	About the code	43
3.5	Conclusions	43

In Chapter 2 we derived the expressions for the nonlinear surface susceptibility tensor including three features not previously found in a single formulation: (i) the scissors correction, (ii) the contribution of the nonlocal part of the pseudopotentials, and (iii) the cut function used to extract the surface response, all within the independent particle approximation. There are, of course, several other theoretical formalisms that describe the SHG process for surfaces with different approximations and varying levels of difficulty [3, 55, 64, 68–72]. However, I consider that this newly developed

framework, with the inclusion of these three contributions opens the possibility to study SSHG with more versatility and accuracy than was previously available at this level of approximation.

In this chapter, I will walk the reader through the considerations for developing the three layer (3-layer) model for the SSHG yield, that considers that the SH conversion takes place in a thin layer just below the surface that lies under the vacuum region and above the bulk of the material. We will then derive explicit expressions for each of the four polarization configurations for the incoming and outgoing fields. These expressions will be simplified by taking into account the symmetry relations for the (111), (110), and (001) surfaces. I have also included Appendix B that contains a wealth of supplementary derivations for all the work contained in this chapter.

3.1 The Three Layer Model for the SSHG Yield

In this section, we will derive the formulas required for the calculation of the SSHG yield, defined by

$$\mathcal{R}(\omega) = \frac{I(2\omega)}{I^2(\omega)}, \quad (3.1)$$

with the intensity given by [130, 131]

$$I(\omega) = \begin{cases} \frac{c}{2\pi} n(\omega) |E(\omega)|^2 & (\text{CGS units}) \\ 2\epsilon_0 c n(\omega) |E(\omega)|^2 & (\text{MKS units}) \end{cases}, \quad (3.2)$$

where $n(\omega) = \sqrt{\epsilon(\omega)}$ is the index of refraction with $\epsilon(\omega)$ as the dielectric function, ϵ_0 is the vacuum permittivity, and c the speed of light in vacuum.

There are several ways to calculate R , one of which is the procedure followed by Cini [132]. This approach calculates the nonlinear susceptibility and at the same time the radiated fields. However, I present an alternative derivation based on the work of Mizrahi and Sipe [133], since the derivation of the 3-layer model is straightforward. In this scheme, the surface is represented by three regions or layers. The first layer is the vacuum region (denoted by v) with a dielectric function $\epsilon_v(\omega) = 1$ from where the fundamental electric field $\mathbf{E}_v(\omega)$ impinges on the material. The second layer is a thin layer (denoted by ℓ) of thickness d characterized by a dielectric function $\epsilon_\ell(\omega)$. It is in this layer where the SHG takes place. The third layer is the bulk region denoted by b and characterized by $\epsilon_b(\omega)$. Both the vacuum and bulk layers are semi-infinite (see Fig. 3.1).

To model the electromagnetic response of the 3-layer model, we follow Ref. [133] and assume a polarization sheet of the form

$$\mathbf{P}(\mathbf{r}, t) = \mathcal{P} e^{i\kappa \cdot \mathbf{R}} e^{-i\omega t} \delta(z - z_\beta) + \text{c.c.}, \quad (3.3)$$

where $\mathbf{R} = (x, y)$, κ is the component of the wave vector ν_β parallel to the surface, and z_β is the position of the sheet within medium β , and \mathcal{P} is the position independent polarization. Ref. [134] demonstrates that the solution of the Maxwell equations for the radiated fields $E_{\beta,p\pm}$, and $E_{\beta,s}$ with $\mathbf{P}(\mathbf{r}, t)$ as a source at points $z \neq 0$, can be written as

$$(E_{\beta,p\pm}, E_{\beta,s}) = \left(\frac{\gamma i \tilde{\omega}^2}{\tilde{w}_\beta} \hat{\mathbf{p}}_{\beta\pm} \cdot \mathcal{P}, \frac{\gamma i \tilde{\omega}^2}{\tilde{w}_\beta} \hat{\mathbf{s}} \cdot \mathcal{P} \right), \quad (3.4)$$

where $\gamma = 2\pi$ in CGS units or $\gamma = 1/2\epsilon_0$ in MKS units, and $\tilde{\omega} = \omega/c$. Also, $\hat{\mathbf{s}}$ and $\hat{\mathbf{p}}_{\beta\pm}$ are the unitary vectors for the s and p polarizations of the radiated field, respectively. The \pm refers to

upward (+) or downward (−) direction of propagation within medium β , as shown in Fig. 3.1. Also, $\tilde{w}_\beta(\omega) = \tilde{\omega} w_\beta$, where

$$\hat{\mathbf{p}}_{\beta\pm}(\omega) = \frac{\kappa(\omega)\hat{\mathbf{z}} \mp \tilde{w}_\beta(\omega)\hat{\boldsymbol{\kappa}}}{\tilde{\omega}n_\beta(\omega)} = \frac{\sin\theta_0\hat{\mathbf{z}} \mp w_\beta(\omega)\hat{\boldsymbol{\kappa}}}{n_\beta(\omega)}, \quad (3.5)$$

with

$$w_\beta(\omega) = (\epsilon_\beta(\omega) - \sin^2\theta_0)^{1/2}, \quad (3.6)$$

θ_0 is the angle of incidence of $\mathbf{E}_v(\omega)$, $\kappa(\omega) = |\boldsymbol{\kappa}| = \tilde{\omega}\sin\theta_0$, $n_\beta(\omega) = \sqrt{\epsilon_\beta(\omega)}$ is the index of refraction of medium β , and z is the direction perpendicular to the surface that points towards the vacuum. If we consider the plane of incidence along the $\boldsymbol{\kappa}z$ plane, then

$$\hat{\boldsymbol{\kappa}} = \cos\phi\hat{\mathbf{x}} + \sin\phi\hat{\mathbf{y}}, \quad (3.7)$$

and

$$\hat{\mathbf{s}} = -\sin\phi\hat{\mathbf{x}} + \cos\phi\hat{\mathbf{y}}, \quad (3.8)$$

where ϕ is the azimuthal angle with respect to the x axis.

In the 3-layer model the nonlinear polarization responsible for the SHG is immersed in the thin layer ($\beta = \ell$), and is given by

$$\mathcal{P}_{\ell,i}(2\omega) = \begin{cases} \chi_{\text{surface}}^{abc}(-2\omega;\omega,\omega)E^b(\omega)E^c(\omega) & (\text{CGS units}) \\ \epsilon_0\chi_{\text{surface}}^{abc}(-2\omega;\omega,\omega)E^b(\omega)E^c(\omega) & (\text{MKS units}) \end{cases}, \quad (3.9)$$

where $\chi_{\text{surface}}(-2\omega;\omega,\omega)$ is the dipolar surface nonlinear susceptibility tensor that we derived in Chapter 2, and the Cartesian indices a, b, c are summed over if repeated. As we mentioned before, $\chi^{abc}(-2\omega;\omega,\omega) = \chi^{acb}(-2\omega;\omega,\omega)$ is the intrinsic permutation symmetry due to the fact that SHG is degenerate in $E_j(\omega)$ and $E_k(\omega)$. As in Ref. [133], we consider the polarization sheet (Eq. (3.3)) to be oscillating at some frequency ω in order to properly express Eqs. (3.4)-(3.8). However, in the following we find it convenient to use ω exclusively to denote the fundamental frequency and $\boldsymbol{\kappa}$ to denote the component of the incident wave vector parallel to the surface. The generated nonlinear polarization is oscillating at $\Omega = 2\omega$ and will be characterized by a wave vector parallel to the surface $\mathbf{K} = 2\boldsymbol{\kappa}$. We can carry over Eqs. (3.3)-(3.8) simply by replacing the lowercase symbols $(\omega, \tilde{\omega}, \boldsymbol{\kappa}, n_\beta, \tilde{w}_\beta, w_\beta, \hat{\mathbf{p}}_{\beta\pm}, \hat{\mathbf{s}})$ with uppercase symbols $(\Omega, \tilde{\Omega}, \mathbf{K}, N_\beta, \tilde{W}_\beta, W_\beta, \hat{\mathbf{P}}_{\beta\pm}, \hat{\mathbf{S}})$, all evaluated at 2ω . Of course, we always have that $\hat{\mathbf{S}} = \hat{\mathbf{s}}$.

From Fig. 3.1, we observe the propagation of the SH field as it is refracted at the layer-vacuum interface (ℓv), and reflected multiple times from the layer-bulk (ℓb) and layer-vacuum (ℓv) interfaces. Thus, we can define

$$\mathbf{T}^{\ell v} = \hat{\mathbf{s}}T_s^{\ell v}\hat{\mathbf{s}} + \hat{\mathbf{P}}_{v+}T_p^{\ell v}\hat{\mathbf{P}}_{\ell+}, \quad (3.10)$$

as the transmission tensor for the ℓv interface,

$$\mathbf{R}^{\ell b} = \hat{\mathbf{s}}R_s^{\ell b}\hat{\mathbf{s}} + \hat{\mathbf{P}}_{\ell+}R_p^{\ell b}\hat{\mathbf{P}}_{\ell-}, \quad (3.11)$$

as the reflection tensor for the ℓb interface, and

$$\mathbf{R}^{\ell v} = \hat{\mathbf{s}}R_s^{\ell v}\hat{\mathbf{s}} + \hat{\mathbf{P}}_{\ell-}R_p^{\ell v}\hat{\mathbf{P}}_{\ell+}, \quad (3.12)$$

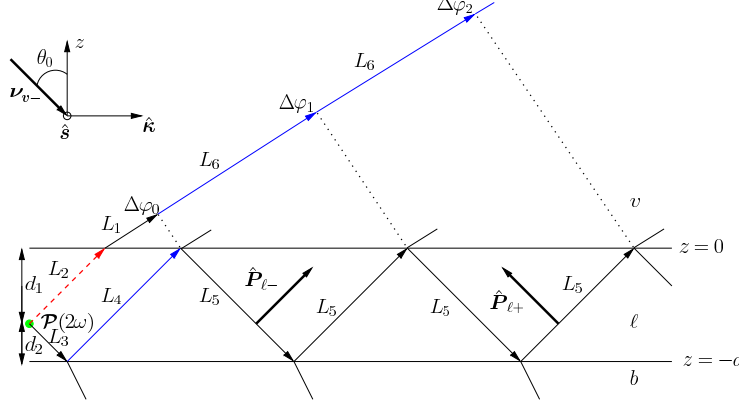


Figure 3.1: Sketch of the three layer model for SHG. The vacuum region (v) is on top with $\epsilon_v = 1$; the layer ℓ of thickness $d = d_1 + d_2$, is characterized with $\epsilon_\ell(\omega)$, and it is where the SH polarization sheet $\mathcal{P}_\ell(2\omega)$ is located at $z_\ell = d_1$. The bulk b is described with $\epsilon_b(\omega)$. The arrows point along the direction of propagation, and the p -polarization unit vector, $\hat{\mathbf{P}}_{\ell-(+)}$, along the downward (upward) direction is denoted with a thick arrow. The s -polarization unit vector $\hat{\mathbf{s}}$, points out of the page. The fundamental field $\mathbf{E}(\omega)$ is incident from the vacuum side along the $\kappa\hat{z}$ -plane, with θ_0 its angle of incidence and ν_{v-} its wave vector. $\Delta\varphi_i$ denotes the phase difference between the multiple reflected beams and the first layer-vacuum transmitted beam, denoted by the dashed-red arrow (of length L_2) followed by the solid black arrow (of length L_1). The dotted lines in the vacuum region are perpendicular to the beam extended from the solid black arrow (denoted by solid blue arrows of length L_6).

as the reflection tensor for the ℓv interface. The Fresnel factors in uppercase letters, $T_{s,p}^{ij}$ and $R_{s,p}^{ij}$, are evaluated at 2ω from the following well known formulas [28]

$$\begin{aligned} t_s^{ij}(\omega) &= \frac{2w_i(\omega)}{w_i(\omega) + w_j(\omega)}, & t_p^{ij}(\omega) &= \frac{2w_i(\omega)\sqrt{\epsilon_i(\omega)\epsilon_j(\omega)}}{w_i(\omega)\epsilon_j(\omega) + w_j(\omega)\epsilon_i(\omega)}, \\ r_s^{ij}(\omega) &= \frac{w_i(\omega) - w_j(\omega)}{w_i(\omega) + w_j(\omega)}, & r_p^{ij}(\omega) &= \frac{w_i(\omega)\epsilon_j(\omega) - w_j\epsilon_i(\omega)}{w_i(\omega)\epsilon_j(\omega) + w_j(\omega)\epsilon_i(\omega)}. \end{aligned} \quad (3.13)$$

With these expressions we easily derive the following useful relations,

$$\begin{aligned} 1 + r_s^{\ell b} &= t_s^{\ell b}, \\ 1 + r_p^{\ell b} &= \frac{n_b}{n_\ell} t_p^{\ell b}, \\ 1 - r_p^{\ell b} &= \frac{n_\ell}{n_b} \frac{w_b}{w_\ell} t_p^{\ell b}, \\ t_p^{\ell v} &= \frac{w_\ell}{w_v} t_p^{v\ell}, \\ t_s^{\ell v} &= \frac{w_\ell}{w_v} t_s^{v\ell}. \end{aligned} \quad (3.14)$$

3.1.1 Multiple SHG reflections

The SH field $\mathbf{E}(2\omega)$ radiated by the SH polarization $\mathcal{P}_\ell(2\omega)$ will radiate directly into the vacuum and the bulk, where it will be reflected back at the layer-bulk interface into the thin layer. This beam will be transmitted and reflected multiple times, as shown in Fig. 3.1. As the two beams propagate, a phase difference will develop between them according to

$$\begin{aligned}\Delta\varphi_m &= \tilde{\Omega}((L_3 + L_4 + 2mL_5)N_\ell - (L_2N_\ell + (L_1 + mL_6)N_v)) \\ &= \delta_0 + m\delta \quad m = 0, 1, 2, \dots,\end{aligned}\tag{3.15}$$

where

$$\delta_0 = 8\pi \left(\frac{d_2}{\lambda_0} \right) W_\ell, \tag{3.16}$$

and

$$\delta = 8\pi \left(\frac{d}{\lambda_0} \right) W_\ell, \tag{3.17}$$

where λ_0 is the wavelength of the fundamental field in the vacuum, d is the thickness of layer ℓ , and d_2 is the distance of $\mathcal{P}_\ell(2\omega)$ from the ℓb interface (see Fig. 3.1). We see that δ_0 is the phase difference of the first and second transmitted beams, and $m\delta$ that of the first and third ($m = 1$), first and fourth ($m = 2$), and so on. Note that the thickness d of the layer ℓ enters through the phase δ , and the position d_2 of the nonlinear polarization sheet $\mathbf{P}(\mathbf{r}, t)$ (Eq. (3.3)) enters through δ_0 . In particular, d_2 could be used as a variable to study the effects of multiple reflections on the SSHG yield $\mathcal{R}(2\omega)$.

To take into account the multiple reflections of the generated SH field in the layer ℓ , we proceed as follows. I include the algebra for the p -polarized SH field, and the s -polarized field could be worked out along the same steps. The p -polarized $\mathbf{E}_{\ell,p}(2\omega)$ field reflected multiple times is given by

$$\begin{aligned}\mathbf{E}_{\ell,p}(2\omega) &= E_{\ell,p+}(2\omega)\mathbf{T}^{\ell v} \cdot \hat{\mathbf{P}}_{\ell+} + E_{\ell,p-}(2\omega)\mathbf{T}^{\ell v} \cdot \mathbf{R}^{\ell b} \cdot \hat{\mathbf{P}}_{\ell-} e^{i\Delta\varphi_0} \\ &\quad + E_{\ell,p-}(2\omega)\mathbf{T}^{\ell v} \cdot \mathbf{R}^{\ell b} \cdot \mathbf{R}^{\ell v} \cdot \mathbf{R}^{\ell b} \cdot \hat{\mathbf{P}}_{\ell-} e^{i\Delta\varphi_1} \\ &\quad + E_{\ell,p-}(2\omega)\mathbf{T}^{\ell v} \cdot \mathbf{R}^{\ell b} \cdot \mathbf{R}^{\ell v} \cdot \mathbf{R}^{\ell b} \cdot \mathbf{R}^{\ell v} \cdot \mathbf{R}^{\ell b} \cdot \hat{\mathbf{P}}_{\ell-} e^{i\Delta\varphi_2} + \dots \\ &= E_{\ell,p+}(2\omega)\mathbf{T}^{\ell v} \cdot \hat{\mathbf{P}}_{\ell+} + E_{\ell,p-}(2\omega)\mathbf{T}^{\ell v} \cdot \sum_{m=0}^{\infty} (\mathbf{R}^{\ell b} \cdot \mathbf{R}^{\ell v} e^{i\delta})^m \cdot \mathbf{R}^{\ell b} \cdot \hat{\mathbf{P}}_{\ell-} e^{i\delta_0}.\end{aligned}\tag{3.18}$$

From Eqs. (3.10) - (3.12) it is easy to show that

$$\mathbf{T}^{\ell v} \cdot (\mathbf{R}^{\ell b} \cdot \mathbf{R}^{\ell v})^n \cdot \mathbf{R}^{\ell b} = \hat{\mathbf{s}} T_s^{\ell v} (R_s^{\ell b} R_s^{\ell v})^n R_s^{\ell b} \hat{\mathbf{s}} + \hat{\mathbf{P}}_{v+} T_p^{\ell v} (R_p^{\ell b} R_p^{\ell v})^n R_p^{\ell b} \hat{\mathbf{P}}_{\ell-},$$

then,

$$\mathbf{E}_{\ell,p}(2\omega) = \hat{\mathbf{P}}_{\ell+} T_p^{\ell v} \left(E_{\ell,p+}(2\omega) + \frac{R_p^{\ell b} e^{i\delta_0}}{1 + R_p^{\ell b} R_p^{\ell v} e^{i\delta}} E_{\ell,p-}(2\omega) \right), \tag{3.19}$$

where we used $R_{s,p}^{ij} = -R_{s,p}^{ji}$. Using Eq. (3.4) and (3.14), we can readily write

$$\mathbf{E}_{\ell,p}(2\omega) = \frac{\gamma i \tilde{\Omega}}{W_\ell} \mathbf{H}_\ell \cdot \mathcal{P}_\ell(2\omega), \tag{3.20}$$

where

$$\mathbf{H}_\ell = \frac{W_\ell}{W_v} \left[\hat{\mathbf{s}} T_s^{v\ell} \left(1 + R_s^M \right) \hat{\mathbf{s}} + \hat{\mathbf{P}}_{v+} T_p^{v\ell} \left(\hat{\mathbf{P}}_{\ell+} + R_p^M \hat{\mathbf{P}}_{\ell-} \right) \right], \quad (3.21)$$

and

$$R_i^M \equiv \frac{R_i^{\ell b} e^{i\delta_0}}{1 + R_i^{v\ell} R_i^{\ell b} e^{i\delta}}, \quad i = s, p, \quad (3.22)$$

is defined as the multiple (M) reflection coefficient. This coefficient depends on the thickness d of layer ℓ , and most importantly on the position d_2 of $\mathcal{P}_\ell(2\omega)$ within this layer. The final results will depend on both d and d_2 . However, using Eq. (3.16) we can also define an average \bar{R}_i^M as

$$\bar{R}_i^M \equiv \frac{1}{d} \int_0^d \frac{R_i^{\ell b} e^{i(8\pi W_\ell / \lambda_0)x}}{1 + R_i^{v\ell} R_i^{\ell b} e^{i\delta}} dx = \frac{R_i^{\ell b} e^{i\delta/2}}{1 + R_i^{v\ell} R_i^{\ell b} e^{i\delta}} \text{sinc}(\delta/2), \quad (3.23)$$

that only depends on d through the δ term from Eq. (3.17).

To connect with the work in Ref. [133], where $\mathcal{P}(2\omega)$ is located on top of the vacuum-surface interface and only the vacuum radiated beam and the first (and only) reflected beam need be considered, we take $\ell = v$ and $d_2 = 0$, then $T^{\ell v} = 1$, $R^{\ell v} = 0$ and $\delta_0 = 0$, with which $R_i^M = R_i^{vb}$. Thus, Eq. (3.21) coincides with Eq. (3.8) of Ref. [133].

3.1.2 Multiple Reflections for the Linear Field

For a more complete formulation, we must also consider the multiple reflections of the fundamental field $\mathbf{E}_\ell(\omega)$ inside the thin ℓ layer. In Fig. 3.2 I present the situation where $\mathbf{E}_v(\omega)$ impinges from the vacuum side with an angle of incidence θ_0 . As the first transmitted beam is multiply reflected from the ℓb and the ℓv interfaces, it accumulates a phase difference of $n\phi$, with $n = 1, 2, 3, \dots$, given by

$$\begin{aligned} \varphi &= \frac{\omega}{c} (2L_1 n_\ell - L_2 n_v) \\ &= 4\pi \left(\frac{d}{\lambda_0} \right) w_\ell, \end{aligned} \quad (3.24)$$

where $n_v = 1$. Besides the equivalent of Eqs. (3.11) and (3.12) for ω , we also need

$$\mathbf{t}^{v\ell} = \hat{\mathbf{s}} t_s^{v\ell} \hat{\mathbf{s}} + \hat{\mathbf{p}}_{\ell-} t_p^{v\ell} \hat{\mathbf{p}}_{v-}, \quad (3.25)$$

to write

$$\begin{aligned} \mathbf{E}(\omega) &= E_0 \left[\mathbf{t}^{v\ell} + \mathbf{r}^{\ell b} \cdot \mathbf{t}^{v\ell} e^{i\varphi} + \mathbf{r}^{\ell b} \cdot \mathbf{r}^{\ell v} \cdot \mathbf{r}^{\ell b} \cdot \mathbf{t}^{v\ell} e^{i2\varphi} + \mathbf{r}^{\ell b} \cdot \mathbf{r}^{\ell v} \cdot \mathbf{r}^{\ell b} \cdot \mathbf{r}^{\ell v} \cdot \mathbf{r}^{\ell b} \cdot \mathbf{t}^{v\ell} e^{i3\varphi} + \dots \right] \cdot \hat{\mathbf{e}}^i \\ &= E_0 \left[1 + \left(1 + \mathbf{r}^{\ell b} \cdot \mathbf{r}^{\ell v} e^{i\varphi} + (\mathbf{r}^{\ell b} \cdot \mathbf{r}^{\ell v})^2 e^{i2\varphi} + \dots \right) \cdot \mathbf{r}^{\ell b} e^{i\varphi} \right] \cdot \mathbf{t}^{v\ell} \cdot \hat{\mathbf{e}}^i \\ &= E_0 \left[\hat{\mathbf{s}} t_s^{v\ell} (1 + r_s^M) \hat{\mathbf{s}} + t_p^{v\ell} \left(\hat{\mathbf{p}}_{\ell-} + \hat{\mathbf{p}}_{\ell+} r_p^M \right) \hat{\mathbf{p}}_{v-} \right] \cdot \hat{\mathbf{e}}^i, \end{aligned} \quad (3.26)$$

where E_0 is the intensity of the fundamental field, and $\hat{\mathbf{e}}^i$ is the unit vector of the incoming polarization, with $i = s, p$, and then, $\hat{\mathbf{e}}^s = \hat{\mathbf{s}}$ and $\hat{\mathbf{e}}^p = \hat{\mathbf{p}}_{v-}$. Also,

$$r_i^M \equiv \frac{r_i^{\ell b} e^{i\varphi}}{1 + r_i^{v\ell} r_i^{\ell b} e^{i\varphi}}, \quad i = s, p. \quad (3.27)$$

r_i^M is defined as the multiple (M) reflection coefficient for the fundamental field. We define $\mathbf{E}_\ell^i(\omega) \equiv E_0 \mathbf{e}_\ell^{\omega,i}$ ($i = s, p$), where

$$\mathbf{e}_\ell^{\omega,i} = [\hat{\mathbf{s}} t_s^{v\ell} (1 + r_s^M) \hat{\mathbf{s}} + t_p^{v\ell} (\hat{\mathbf{p}}_{\ell-} + \hat{\mathbf{p}}_{\ell+} r_p^M) \hat{\mathbf{p}}_{v-}] \cdot \hat{\mathbf{e}}^i, \quad (3.28)$$

and using Eq. (3.5) we obtain that

$$\mathbf{e}_\ell^{\omega,p} = \frac{t_p^{v\ell}}{n_\ell} (r_p^{M+} \sin \theta_0 \hat{\mathbf{z}} + r_p^{M-} w_\ell \hat{\boldsymbol{\kappa}}), \quad (3.29)$$

for p -input polarization with $\hat{\mathbf{e}}^i = \hat{\mathbf{p}}_{v-}$, and

$$\mathbf{e}_\ell^{\omega,s} = t_s^{v\ell} r_s^{M+} \hat{\mathbf{s}}, \quad (3.30)$$

for s -input polarization with $\hat{\mathbf{e}}^i = \hat{\mathbf{s}}$, where

$$r_i^{M\pm} = 1 \pm r_i^M, \quad i = s, p. \quad (3.31)$$

3.1.3 Deriving the SSHG yield

The magnitude of the radiated field is given by $E(2\omega) = \hat{\mathbf{e}}^F \cdot \mathbf{E}_\ell(2\omega)$, where $\hat{\mathbf{e}}^F$ is the unit vector of the final, S or P SH polarization with $F = S, P$, where $\hat{\mathbf{e}}^S = \hat{\mathbf{s}}$ and $\hat{\mathbf{e}}^P = \hat{\mathbf{P}}_{v+}$. We expand the

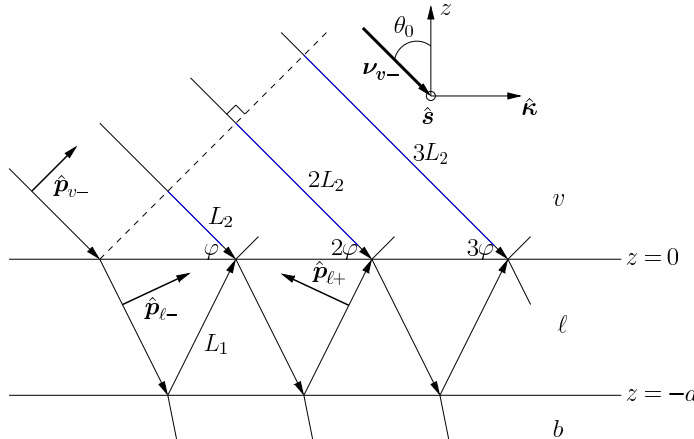


Figure 3.2: Sketch for the multiple reflected fundamental field $\mathbf{E}(\omega)$, which impinges from the vacuum side along the $\hat{\boldsymbol{\kappa}}z$ -plane. θ_0 and ν_{v-} are the angle of incidence and wave vector, respectively. The arrows point along the direction of propagation. The p -polarization unit vectors $\hat{\mathbf{p}}_{\beta\pm}$, point along the downward ($-$) or upward ($+$) directions and are denoted with thick arrows, where $\beta = v$ or ℓ . The s -polarization unit vector $\hat{\mathbf{s}}$ points out of the page. $(1, 2, 3, \dots)\varphi$ denotes the phase difference for the multiple reflected beams with respect to the incident field, where the dotted line is perpendicular to this beam.

rightmost term in parenthesis of Eq. (3.21) as

$$\begin{aligned}\hat{\mathbf{P}}_{\ell+} + R_p^M \hat{\mathbf{P}}_{\ell-} &= \frac{\sin \theta_0 \hat{\mathbf{z}} - W_\ell \hat{\boldsymbol{\kappa}}}{N_\ell} + R_p^M \frac{\sin \theta_0 \hat{\mathbf{z}} + W_\ell \hat{\boldsymbol{\kappa}}}{N_\ell} \\ &= \frac{1}{N_\ell} \left(\sin \theta_0 R_p^{M+} \hat{\mathbf{z}} - W_\ell R_p^{M-} \hat{\boldsymbol{\kappa}} \right),\end{aligned}\quad (3.32)$$

where

$$R_i^{M\pm} \equiv 1 \pm R_i^M, \quad i = s, p. \quad (3.33)$$

Using Eq. (3.14) we write Eq. (3.20) as

$$E(2\omega) = \frac{2\gamma i\omega}{cW_\ell} \hat{\mathbf{e}}^F \cdot \mathbf{H}_\ell \cdot \mathcal{P}_\ell(2\omega) = \frac{2\gamma i\omega}{cW_v} \mathbf{e}_\ell^{2\omega, F} \cdot \mathcal{P}_\ell(2\omega), \quad (3.34)$$

where

$$\mathbf{e}_\ell^{2\omega, F} = \hat{\mathbf{e}}^F \cdot \left[\hat{\mathbf{s}} T_s^{v\ell} R_s^{M+} \hat{\mathbf{s}} + \hat{\mathbf{P}}_{v+} \frac{T_p^{v\ell}}{N_\ell} \left(\sin \theta_0 R_p^{M+} \hat{\mathbf{z}} - W_\ell R_p^{M-} \hat{\boldsymbol{\kappa}} \right) \right]. \quad (3.35)$$

Replacing $\mathbf{E}(\omega) \rightarrow E_0 \mathbf{e}_\ell^{\omega, i}$, in Eq. (3.9), we obtain that

$$\mathcal{P}_\ell(2\omega) = \begin{cases} E_0^2 \chi_{\text{surface}} : \mathbf{e}_\ell^{\omega, i} \mathbf{e}_\ell^{\omega, i} & (\text{CGS units}) \\ \epsilon_0 E_0^2 \chi_{\text{surface}} : \mathbf{e}_\ell^{\omega, i} \mathbf{e}_\ell^{\omega, i} & (\text{MKS units}) \end{cases}, \quad (3.36)$$

where $\mathbf{e}_\ell^{\omega, i}$ is given by Eq. (3.28), and thus Eq. (3.34) reduces to ($W_v = \cos \theta_0$)

$$E_\ell(2\omega) = \frac{2\eta i\omega}{c \cos \theta_0} \mathbf{e}_\ell^{2\omega, F} \cdot \chi_{\text{surface}} : \mathbf{e}_\ell^{\omega, i} \mathbf{e}_\ell^{\omega, i}, \quad (3.37)$$

where $\eta = 2\pi$ in CGS units and $\eta = 1/2$ in MKS units. For ease of notation, we define

$$\Upsilon_{iF} \equiv \mathbf{e}_\ell^{2\omega, F} \cdot \chi_{\text{surface}} : \mathbf{e}_\ell^{\omega, i} \mathbf{e}_\ell^{\omega, i}, \quad (3.38)$$

where i stands for the incoming polarization of the fundamental electric field given by $\hat{\mathbf{e}}^i$ in Eq. (3.28), and F for the outgoing polarization of the SH electric field given by $\hat{\mathbf{e}}^F$ in Eq. (3.35). I purposely omitted the full $\chi(-2\omega; \omega, \omega)$ notation, and will do so from this point on.

From Eqs. (3.1) and (3.2) we obtain that in CGS units ($\eta = 2\pi$),

$$\begin{aligned}|E(2\omega)|^2 &= |E_0|^4 \frac{16\pi^2 \omega^2}{c^2 W_v^2} |\Upsilon_{iF}|^2 \\ \frac{c}{2\pi} |\sqrt{N_v} E(2\omega)|^2 &= \frac{32\pi^3 \omega^2}{c^3 \cos^2 \theta_0} \left| \frac{\sqrt{N_v}}{n_\ell^2} \Upsilon_{iF} \right|^2 \left(\frac{c}{2\pi} |\sqrt{n_\ell} E_0|^2 \right)^2 \\ I(2\omega) &= \frac{32\pi^3 \omega^2}{c^3 \cos^2 \theta_0} \left| \frac{\sqrt{N_v}}{n_\ell^2} \Upsilon_{iF} \right|^2 I^2(\omega) \\ \mathcal{R}_{iF}(2\omega) &= \frac{32\pi^3 \omega^2}{c^3 \cos^2 \theta_0} \left| \frac{1}{n_\ell} \Upsilon_{iF} \right|^2,\end{aligned}\quad (3.39)$$

and in MKS units ($\eta = 1/2$),

$$\begin{aligned} |E(2\omega)|^2 &= |E_0|^4 \frac{\omega^2}{c^2 W_v^2} \\ 2\epsilon_0 c |\sqrt{N_v} E(2\omega)|^2 &= \frac{2\epsilon_0 \omega^2}{c \cos^2 \theta_0} \left| \frac{\sqrt{N_v}}{n_\ell^2} \Upsilon_{\text{iF}} \right|^2 \frac{1}{4\epsilon_0^2 c^2} \left(2\epsilon_0 c |\sqrt{n_\ell} E_0|^2 \right)^2 \\ I(2\omega) &= \frac{\omega^2}{2\epsilon_0 c^3 \cos^2 \theta_0} \left| \frac{\sqrt{N_v}}{n_\ell^2} \Upsilon_{\text{iF}} \right|^2 I^2(\omega) \\ \mathcal{R}_{\text{iF}}(2\omega) &= \frac{\omega^2}{2\epsilon_0 c^3 \cos^2 \theta_0} \left| \frac{1}{n_\ell} \Upsilon_{\text{iF}} \right|^2. \end{aligned} \quad (3.40)$$

Finally, we condense these results and establish the SSHG yield as

$$\mathcal{R}_{\text{iF}}(2\omega) \begin{cases} \frac{32\pi^3 \omega^2}{c^3 \cos^2 \theta_0} \left| \frac{1}{n_\ell} \Upsilon_{\text{iF}} \right|^2 & (\text{CGS units}) \\ \frac{\omega^2}{2\epsilon_0 c^3 \cos^2 \theta_0} \left| \frac{1}{n_\ell} \Upsilon_{\text{iF}} \right|^2 & (\text{MKS units}) \end{cases}, \quad (3.41)$$

where $N_v = 1$ and $W_v = \cos \theta_0$. As mentioned in Chapter (2), χ_{surface} is given in m^2/V in the MKS unit system, since it is a surface second order nonlinear susceptibility, and \mathcal{R}_{iF} is given in m^2/W .

3.2 \mathcal{R}_{iF} for different polarization cases

We now have everything we need to derive explicit expressions for \mathcal{R}_{iF} , Eq. (3.41), for the most commonly used polarizations of incoming and outgoing fields (iF= pP , pS , sP , and sS). For this, we must expand Υ_{iF} from Eq. (3.38) for each case. By substituting Eqs. (3.7) and (3.8) into Eq. (3.35), we obtain

$$\mathbf{e}_\ell^{2\omega, P} = \frac{T_p^{v\ell}}{N_\ell} (\sin \theta_0 R_p^{M+} \hat{\mathbf{z}} - W_\ell R_p^{M-} \cos \phi \hat{\mathbf{x}} - W_\ell R_p^{M-} \sin \phi \hat{\mathbf{y}}), \quad (3.42)$$

for P ($\hat{\mathbf{e}}^F = \hat{\mathbf{P}}_{v+}$) outgoing polarization, and

$$\mathbf{e}_\ell^{2\omega, S} = T_s^{v\ell} R_s^{M+} (-\sin \phi \hat{\mathbf{x}} + \cos \phi \hat{\mathbf{y}}). \quad (3.43)$$

for S ($\hat{\mathbf{e}}^F = \hat{\mathbf{s}}$) outgoing polarization.

Following a similar procedure, we use Eqs. (3.7) and (3.8) with Eq. (3.29), and obtain

$$\begin{aligned} \mathbf{e}_\ell^{\omega, p} \mathbf{e}_\ell^{\omega, p} &= \left(\frac{t_p^{v\ell}}{n_\ell} \right)^2 \left((r_p^{M-})^2 w_\ell^2 \cos^2 \phi \hat{\mathbf{x}} \hat{\mathbf{x}} + 2(r_p^{M-})^2 w_\ell^2 \sin \phi \cos \phi \hat{\mathbf{x}} \hat{\mathbf{y}} \right. \\ &\quad + 2r_p^{M+} r_p^{M-} w_\ell \sin \theta_0 \cos \phi \hat{\mathbf{x}} \hat{\mathbf{z}} + (r_p^{M-})^2 w_\ell^2 \sin^2 \phi \hat{\mathbf{y}} \hat{\mathbf{y}} \\ &\quad \left. + 2r_p^{M+} r_p^{M-} w_\ell \sin \theta_0 \sin \phi \hat{\mathbf{y}} \hat{\mathbf{z}} + (r_p^{M+})^2 \sin^2 \theta_0 \hat{\mathbf{z}} \hat{\mathbf{z}} \right), \end{aligned} \quad (3.44)$$

for p incoming polarization ($\hat{\mathbf{e}}^i = \hat{\mathbf{p}}_{v-}$), and with Eq. (3.30),

$$\mathbf{e}_\ell^{\omega, s} \mathbf{e}_\ell^{\omega, s} = \left(t_s^{v\ell} r_s^{M+} \right)^2 (\sin^2 \phi \hat{\mathbf{x}} \hat{\mathbf{x}} + \cos^2 \phi \hat{\mathbf{y}} \hat{\mathbf{y}} - 2 \sin \phi \cos \phi \hat{\mathbf{x}} \hat{\mathbf{y}}). \quad (3.45)$$

Case	$\hat{\mathbf{e}}^F$	$\hat{\mathbf{e}}^i$	$\mathbf{e}_\ell^{2\omega,F}$	$\mathbf{e}_\ell^{\omega,i} \mathbf{e}_\ell^{\omega,i}$
\mathcal{R}_{pP}	$\hat{\mathbf{P}}_{v+}$	$\hat{\mathbf{p}}_{v-}$	Eq. (3.42)	Eq. (3.44)
\mathcal{R}_{pS}	$\hat{\mathbf{S}}$	$\hat{\mathbf{p}}_{v-}$	Eq. (3.43)	Eq. (3.44)
\mathcal{R}_{sP}	$\hat{\mathbf{P}}_{v+}$	$\hat{\mathbf{s}}$	Eq. (3.42)	Eq. (3.45)
\mathcal{R}_{sS}	$\hat{\mathbf{S}}$	$\hat{\mathbf{s}}$	Eq. (3.43)	Eq. (3.45)

Table 3.1: Polarization unit vectors for $\hat{\mathbf{e}}^F$ and $\hat{\mathbf{e}}^i$, and equations describing $\mathbf{e}_\ell^{2\omega,F}$ and $\mathbf{e}_\ell^{\omega,i} \mathbf{e}_\ell^{\omega,i}$ for each polarization case.

for s incoming polarization ($\hat{\mathbf{e}}^i = \hat{\mathbf{s}}$).

I have summarized the combination of equations needed to derive the expressions for all four polarization cases of \mathcal{R}_{iF} in Table 3.1. In the following subsections we will derive the explicit expressions for Υ_{iF} for the most general case where the surface has no symmetry other than that of noncentrosymmetry. We will then develop these expressions for particular cases of the most commonly investigated surfaces, the (111), (001), and (110) crystallographic faces. For ease of writing we split Υ_{iF} as

$$\Upsilon_{iF} = \Gamma_{iF} r_{iF}. \quad (3.46)$$

Lastly, in Table 3.2 I list the nonzero components of χ_{surface} for each surface symmetry [1, 135]. From this point on, I will omit the “surface” subscript for the χ^{abc} components for ease of notation.

I have provided the full, step-by-step derivation for all of these expressions in Appendix B, with and without the effects of multiple reflections. The avid reader should refer to that chapter if interested in deriving any of the expressions listed below.

3.2.1 \mathcal{R}_{pP} (*p*-in, *P*-out)

Per Table 3.1, \mathcal{R}_{pP} requires Eqs. (3.42) and (3.44). After some algebra, we obtain that

$$\Gamma_{pP} = \frac{T_p^{v\ell}}{N_\ell} \left(\frac{t_p^{v\ell}}{n_\ell} \right)^2, \quad (3.47)$$

(111)- C_{3v}	(110)- C_{2v}	(001)- C_{4v}
χ^{zzz}	χ^{zzz}	χ^{zzz}
$\chi^{zxx} = \chi^{zyy}$	$\chi^{zxx} \neq \chi^{zyy}$	$\chi^{zxx} = \chi^{zyy}$
$\chi^{xxz} = \chi^{yyz}$	$\chi^{xxz} \neq \chi^{yyz}$	$\chi^{xxz} = \chi^{yyz}$
$\chi^{xxx} = -\chi^{xyy} = -\chi^{yyx}$		

Table 3.2: Components of χ for the (111), (110) and (001) crystallographic faces, belonging to the C_{3v} , C_{2v} , and C_{4v} , symmetry groups, respectively. For the (111) surface we choose the x and y axes along the $[11\bar{2}]$ and $[1\bar{1}0]$ directions, respectively. For the (110) and (001) we consider the y axis perpendicular to the plane of symmetry. [1] We remark that in general $\chi^{(111)} \neq \chi^{(110)} \neq \chi^{(001)}$.

and

$$\begin{aligned}
r_{pP} = & -R_p^{M-} \left(r_p^{M-} \right)^2 w_\ell^2 W_\ell \cos^3 \phi \chi^{xxx} - 2R_p^{M-} \left(r_p^{M-} \right)^2 w_\ell^2 W_\ell \sin \phi \cos^2 \phi \chi^{xxy} \\
& - 2R_p^{M-} r_p^{M+} r_p^{M-} w_\ell W_\ell \sin \theta_0 \cos^2 \phi \chi^{xxz} - R_p^{M-} \left(r_p^{M-} \right)^2 w_\ell^2 W_\ell \sin^2 \phi \cos \phi \chi^{xyy} \\
& - 2R_p^{M-} r_p^{M+} r_p^{M-} w_\ell W_\ell \sin \theta_0 \sin \phi \cos \phi \chi^{xyz} - R_p^{M-} \left(r_p^{M+} \right)^2 W_\ell \sin^2 \theta_0 \cos \phi \chi^{xzz} \\
& - R_p^{M-} \left(r_p^{M-} \right)^2 w_\ell^2 W_\ell \sin \phi \cos^2 \phi \chi^{yxx} - 2R_p^{M-} \left(r_p^{M-} \right)^2 w_\ell^2 W_\ell \sin^2 \phi \cos \phi \chi^{yxy} \\
& - 2R_p^{M-} r_p^{M+} r_p^{M-} w_\ell W_\ell \sin \theta_0 \sin \phi \cos \phi \chi^{yxz} - R_p^{M-} \left(r_p^{M-} \right)^2 w_\ell^2 W_\ell \sin^3 \phi \chi^{yyy} \quad (3.48) \\
& - 2R_p^{M-} r_p^{M+} r_p^{M-} w_\ell W_\ell \sin \theta_0 \sin^2 \phi \chi^{yyz} - R_p^{M-} \left(r_p^{M+} \right)^2 W_\ell \sin^2 \theta_0 \sin \phi \chi^{yzz} \\
& + R_p^{M+} \left(r_p^{M-} \right)^2 w_\ell^2 \sin \theta_0 \cos^2 \phi \chi^{zxx} + 2R_p^{M+} r_p^{M+} r_p^{M-} w_\ell \sin^2 \theta_0 \cos \phi \chi^{zxx} \\
& + 2R_p^{M+} \left(r_p^{M-} \right)^2 w_\ell^2 \sin \theta_0 \sin \phi \cos \phi \chi^{zxy} + R_p^{M+} \left(r_p^{M-} \right)^2 w_\ell^2 \sin \theta_0 \sin^2 \phi \chi^{zyy} \\
& + 2R_p^{M+} r_p^{M+} r_p^{M-} w_\ell \sin^2 \theta_0 \sin \phi \chi^{zzy} + R_p^{M+} \left(r_p^{M+} \right)^2 \sin^3 \theta_0 \chi^{zzz},
\end{aligned}$$

where all 18 independent components of χ for a surface with no symmetries, contribute to \mathcal{R}_{pP} . Recall that $\chi^{abc} = \chi^{acb}$. We will derive the expressions for each of the three surfaces being considered here, referring to Table 3.2. For the (111) surface we obtain

$$\begin{aligned}
r_{pP}^{(111)} = & R_p^{M+} \sin \theta_0 \left[\left(r_p^{M+} \right)^2 \sin^2 \theta_0 \chi^{zzz} + \left(r_p^{M-} \right)^2 w_\ell^2 \chi^{zxx} \right] \quad (3.49) \\
& - R_p^{M-} w_\ell W_\ell \left[2r_p^{M+} r_p^{M-} \sin \theta_0 \chi^{xxz} + \left(r_p^{M-} \right)^2 w_\ell \chi^{xxx} \cos 3\phi \right],
\end{aligned}$$

where the three-fold azimuthal symmetry of the SHG signal that is typical of the C_{3v} symmetry group, is seen in the 3ϕ argument of the cosine function. For the (110) surface, we have that

$$\begin{aligned}
r_{pP}^{(110)} = & R_p^{M+} \sin \theta_0 \left[\left(r_p^{M+} \right)^2 \sin^2 \theta_0 \chi^{zzz} + \left(r_p^{M-} \right)^2 w_\ell^2 \left(\frac{\chi^{zyy} + \chi^{zxx}}{2} + \frac{\chi^{zyy} - \chi^{zxx}}{2} \cos 2\phi \right) \right] \\
& - 2R_p^{M-} r_p^{M+} r_p^{M-} w_\ell W_\ell \sin \theta_0 \left(\frac{\chi^{yyz} + \chi^{xxz}}{2} + \frac{\chi^{yyz} - \chi^{xxz}}{2} \cos 2\phi \right). \quad (3.50)
\end{aligned}$$

The two-fold azimuthal symmetry of the SHG signal that is typical of the C_{2v} symmetry group, is seen in the 2ϕ argument of the cosine function. For the (001) surface we simply make $\chi^{xxx} = \chi^{zyy}$ and $\chi^{xxz} = \chi^{yyz}$ as seen in Table 3.2, and the previous expression reduces to

$$\begin{aligned}
r_{pP}^{(001)} = & R_p^{M+} \sin \theta_0 \left[\left(r_p^{M+} \right)^2 \sin^2 \theta_0 \chi^{zzz} + \left(r_p^{M-} \right)^2 w_\ell^2 \chi^{zxx} \right] \quad (3.51) \\
& - 2R_p^{M-} r_p^{M+} r_p^{M-} w_\ell W_\ell \sin \theta_0 \chi^{xxz}.
\end{aligned}$$

This time, the azimuthal 4ϕ symmetry for the C_{4v} group of the (001) surface is absent in this expression since this contribution is only related to the bulk nonlinear quadrupolar SH term, Eq. (2.7) [1], that we neglect in this work.

3.2.2 \mathcal{R}_{sP} (*s*-in, *P*-out)

Per Table 3.1, \mathcal{R}_{sP} requires Eqs. (3.42) and (3.45). After some algebra, we obtain that

$$\Gamma_{sP} = \frac{T_p^{v\ell}}{N_\ell} \left(t_s^{v\ell} r_s^{M+} \right)^2, \quad (3.52)$$

and

$$\begin{aligned} r_{sP} = & R_p^{M-} W_\ell (-\sin^2 \phi \cos \phi \chi^{xxx} + 2 \sin \phi \cos^2 \phi \chi^{xxy} - \cos^3 \phi \chi^{xyy}) \\ & R_p^{M-} W_\ell (-\sin^3 \phi \chi^{yxx} + 2 \sin^2 \phi \cos \phi \chi^{yxy} - \sin \phi \cos^2 \phi \chi^{yyy}) \\ & R_p^{M+} \sin \theta_0 (\sin^2 \phi \chi^{zxx} - 2 \sin \phi \cos \phi \chi^{zxy} + \cos^2 \phi \chi^{zyy}). \end{aligned} \quad (3.53)$$

In this case, 9 out of the 18 components of χ for a surface with no symmetries, contribute to \mathcal{R}_{sP} . This is because there is no $E_z(\omega)$ component, as the incoming polarization is *s*. From Table 3.2 we get,

$$r_{sP}^{(111)} = R_p^{M+} \sin \theta_0 \chi^{zxx} + R_p^{M-} W_\ell \chi^{xxx} \cos 3\phi, \quad (3.54)$$

for the (111) surface,

$$r_{sP}^{(110)} = R_p^{M+} \sin \theta_0 \left(\frac{\chi^{zxx} + \chi^{zyy}}{2} + \frac{\chi^{zyy} - \chi^{zxx}}{2} \cos 2\phi \right), \quad (3.55)$$

for the (110) surface, and

$$r_{sP}^{(001)} = R_p^{M+} \sin \theta_0 \chi^{zxx}, \quad (3.56)$$

for the (001) surface.

3.2.3 \mathcal{R}_{pS} (*p*-in, *S*-out)

Per Table 3.1, \mathcal{R}_{pS} requires Eqs. (3.43) and (3.44). After some algebra, we obtain that

$$\Gamma_{pS} = T_s^{v\ell} R_s^{M+} \left(\frac{t_p^{v\ell}}{n_\ell} \right)^2, \quad (3.57)$$

and

$$\begin{aligned} r_{pS} = & - \left(r_p^{M-} \right)^2 w_\ell^2 \sin \phi \cos^2 \phi \chi^{xxx} - 2 \left(r_p^{M-} \right)^2 w_\ell^2 \sin^2 \phi \cos \phi \chi^{xxy} \\ & - 2 r_p^{M+} r_p^{M-} w_\ell \sin \theta_0 \sin \phi \cos \phi \chi^{xxz} - \left(r_p^{M-} \right)^2 w_\ell^2 \sin^3 \phi \chi^{xyy} \\ & - 2 r_p^{M+} r_p^{M-} w_\ell \sin \theta_0 \sin^2 \phi \chi^{xzy} - \left(r_p^{M+} \right)^2 \sin^2 \theta_0 \sin \phi \chi^{xzz} \\ & + \left(r_p^{M-} \right)^2 w_\ell^2 \cos^3 \phi \chi^{yxx} + 2 \left(r_p^{M-} \right)^2 w_\ell^2 \sin \phi \cos^2 \phi \chi^{yxy} \\ & + 2 r_p^{M+} r_p^{M-} w_\ell \sin \theta_0 \cos^2 \phi \chi^{yxz} + \left(r_p^{M-} \right)^2 w_\ell^2 \sin^2 \phi \cos \phi \chi^{yyy} \\ & + 2 r_p^{M+} r_p^{M-} w_\ell \sin \theta_0 \sin \phi \cos \phi \chi^{zyy} + \left(r_p^{M+} \right)^2 \sin^2 \theta_0 \cos \phi \chi^{yzz}. \end{aligned} \quad (3.58)$$

In this case, 12 out of the 18 components of χ for a surface with no symmetries, contribute to \mathcal{R}_{pS} . This is because there is no $\mathcal{P}_z(2\omega)$ component, as the outgoing polarization is S . From Table 3.2 we obtain,

$$r_{pS}^{(111)} = - \left(r_p^{M-} \right)^2 w_\ell^2 \chi^{xxx} \sin 3\phi, \quad (3.59)$$

for the (111) surface,

$$r_{sP}^{(110)} = r_p^{M+} r_p^{M-} w_\ell \sin \theta_0 (\chi^{yyz} - \chi^{xxz}) \sin 2\phi, \quad (3.60)$$

for the (110) surface, finally,

$$r_{pS}^{(001)} = 0, \quad (3.61)$$

for the (001) surface, where the zero value is only surface related as we neglect the bulk nonlinear quadrupolar contribution [1].

3.2.4 \mathcal{R}_{sS} (*s*-in, *S*-out)

Per Table 3.1, \mathcal{R}_{sS} requires Eqs. (3.43) and (3.45). After some algebra, we obtain that

$$\Gamma_{sS} = T_s^{v\ell} R_s^{M+} \left(t_s^{v\ell} r_s^{M+} \right)^2, \quad (3.62)$$

and

$$r_{sS} = - \sin^3 \phi \chi^{xxx} + 2 \sin^2 \phi \cos \phi \chi^{xxy} - \sin \phi \cos^2 \phi \chi^{xyy} \\ + \sin^2 \phi \cos \phi \chi^{yxx} + \cos^3 \phi \chi^{yyy} - 2 \sin \phi \cos^2 \phi \chi^{xyy}. \quad (3.63)$$

In this case, only 6 out of the 18 components of χ for a surface with no symmetries, contribute to \mathcal{R}_{sS} . This is because there is neither an $E_z(\omega)$ component as the incoming polarization is s , nor a $\mathcal{P}_z(2\omega)$ component as the outgoing polarization is S . From Table 3.2, we get

$$r_{sS}^{(111)} = \chi^{xxx} \sin 3\phi, \quad (3.64)$$

for the (111) surface,

$$r_{sS}^{(110)} = 0, \quad (3.65)$$

and

$$r_{sS}^{(001)} = 0, \quad (3.66)$$

for the (110) and (001) surfaces, respectively, both being zero as the bulk nonlinear quadrupolar contribution is not considered here [1].

3.3 Some Scenarios of Interest

In this section we present five different scenarios for placing the nonlinear polarization $\mathcal{P}(2\omega)$ and the fundamental electric field $\mathbf{E}(\omega)$, which are alternatives to the three-layer model presented above. In what follows, we confine ourselves only to the (111) surface and the *p*-in *P*-out combination polarizations. This is the case where the proposed scenarios differ the most as the SHG yield depends on all the finite χ^{abc} components for this surface. However, the other *pS*, *sP*, and *sS* polarization cases, or the (110) or (001) surfaces could be worked out along the same lines described below. For all the scenarios we omit the multiple SH reflections by taking $R_p^{M\pm} \rightarrow 1 \pm R_p^{\ell b}$ (Eq.

(3.33)) and the linear multiple reflections by taking $r_p^{M\pm} \rightarrow 1 \pm r_p^{\ell b}$ (Eq. (3.31)). Using the expressions in Eq. (3.14), we obtain the following useful relationships

$$\begin{aligned} r_p^{M+} &\rightarrow \frac{n_b}{n_\ell} t_p^{\ell b} \\ r_p^{M-} &\rightarrow \frac{n_\ell}{n_b} \frac{w_b}{w_\ell} t_p^{\ell b}, \end{aligned} \quad (3.67)$$

which will come in handy for expressing Γ_{pP} and $r_{pP}^{(111)}$ in the forms presented below. Recall that these expressions are valid for the 2ω terms by simply capitalizing the relevant quantities as explained in Sec. 3.1. We summarize these scenarios in Table 3.3 for quick reference.

3.3.1 The 3-layer Model Without Multiple Reflections

Using Eq. (3.67) in Eq. (3.49) with Eq. (3.47), we obtain

$$\Gamma_{pP} = \frac{T_p^{\ell v} T_p^{\ell b}}{N_\ell^2 N_b} \left(\frac{t_p^{v\ell} t_p^{\ell b}}{n_\ell^2 n_b} \right)^2, \quad (3.68)$$

and

$$\begin{aligned} r_{pP}^{(111)} &= N_b^2 \sin \theta_0 \left(n_b^4 \sin^2 \theta_0 \chi^{zzz} + n_\ell^4 w_b^2 \chi^{zxx} \right) \\ &\quad - N_\ell^2 n_\ell^2 w_b W_b \left(2n_b^2 \sin \theta_0 \chi^{xxz} + n_\ell^2 w_b \chi^{xxx} \cos(3\phi) \right). \end{aligned} \quad (3.69)$$

Now that we have neglected multiple SH reflections, we can use these two expressions for Γ_{pP} and r_{pP} to obtain the next four scenarios by using the choices described in each subsection below. Note that by neglecting the multiple reflections, the thickness d of layer ℓ disappears from the formulation, and the location of the nonlinear polarization sheet $\mathbf{P}(\mathbf{r}, t)$ (Eq. (3.3)) at d_2 (see Fig. 3.1) is immaterial.

Label	$\mathcal{P}(2\omega)$	$\mathbf{E}(\omega)$
3-layer	ℓ	ℓ
3-layer-hybrid	ℓ	b
2-layer-bulk	b	b
2-layer-fresnel	v	b
2-layer-vacuum	v	v

Table 3.3: Summary of the SSHG yield models used throughout this work. “Label” is the name used in subsequent figures, while the remaining columns show in which medium we will consider the specified quantity. ℓ is the thin layer below the surface of the material, v is the vacuum region, and b is the bulk region of the material. We use the following convention for the labels. Models with “3-layer” consider the presence of the thin layer ℓ , while “2-layer” models do not. The “fresnel”, “bulk”, “vacuum”, and “hybrid” tags refers to the configuration in which we evaluate the specific quantities. For instance, the 3-layer-hybrid model evaluates $\mathcal{P}(2\omega)$ in the thin layer ℓ , while the fundamental fields are evaluated in the bulk region b .

3.3.2 The two layer, or Fresnel (2-layer-fresnel) model

Historically, this is the model most used in the literature. In Chap. 4, we will see how the 3-layer model, presented in the previous sections, offers a significant improvement over this model.

In the 2-layer-fresnel model, we consider that $\mathcal{P}(2\omega)$ is evaluated in the vacuum region, while the fundamental fields are evaluated in the bulk region [1, 133]. To do this, we evaluate the 2ω radiations factors in the vacuum by taking $\ell = v$, thus $\epsilon_\ell(2\omega) = 1$, $T_p^{\ell v} = 1$, and $T_p^{\ell b} = T_p^{vb}$. We also evaluate the fundamental field inside medium b by taking $\ell = b$, thus $\epsilon_\ell(\omega) = \epsilon_b(\omega)$, $t_p^{v\ell} = t_p^{vb}$, and $t_p^{\ell b} = 1$. With these choices, Eqs. (3.68) and (3.69) reduce to

$$\Gamma_{pP} = \frac{T_p^{vb}(t_p^{vb})^2}{n_b^2 N_b}, \quad (3.70)$$

and

$$r_{pP}^{(111)} = N_b^2 \sin \theta_0 \left(\sin^2 \theta_0 \chi^{zzz} + w_b^2 \chi^{zxx} \right) - w_b W_b \left(2 \sin \theta_0 \chi^{xxz} + w_b \chi^{xxx} \cos(3\phi) \right). \quad (3.71)$$

These expressions are in perfect agreement with Refs. [1] and [133].

3.3.3 The 2-layer-bulk model: evaluating $\mathcal{P}(2\omega)$ and $\mathbf{E}(\omega)$ in the bulk

We follow the same procedure as above considering that both the 2ω and 1ω terms will be evaluated in the bulk, by taking $\ell = b$. Thus, $\epsilon_\ell(2\omega) = \epsilon_b(2\omega)$, $T_p^{v\ell} = T_p^{vb}$, $T_p^{\ell b} = 1$, and $\epsilon_\ell(\omega) = \epsilon_b(\omega)$, $t_p^{v\ell} = t_p^{vb}$, and $t_p^{\ell b} = 1$. With these choices Eqs. (3.68) and (3.69) reduce to

$$\Gamma_{pP} = \frac{T_p^{vb} (t_p^{vb})^2}{n_b^2 N_b}, \quad (3.72)$$

and

$$r_{pP}^{(111)} = \sin^3 \theta_0 \chi^{zzz} + w_b^2 \sin \theta_0 \chi^{zxx} - 2w_b W_b \sin \theta_0 \chi^{xxz} - w_b^2 W_b \chi^{xxx} \cos 3\phi. \quad (3.73)$$

3.3.4 The 2-layer-vacuum model: evaluating $\mathcal{P}(2\omega)$ and $\mathbf{E}(\omega)$ in the vacuum

We consider both $\mathcal{P}(2\omega)$ and the fundamental fields to be evaluated in the vacuum. We take $\ell = v$, thus $\epsilon_\ell(2\omega) = 1$, $T_p^{\ell v} = 1$, $T_p^{\ell b} = T_p^{vb}$, and $\epsilon_\ell(\omega) = 1$, $t_p^{v\ell} = 1$, and $t_p^{\ell b} = t_p^{vb}$. With these choices Eqs. (3.68) and (3.69) reduce to

$$\Gamma_{pP} = \frac{T_p^{vb} (t_p^{vb})^2}{n_b^2 N_b}, \quad (3.74)$$

and

$$r_{pP}^{(111)} = n_b^4 N_b^2 \sin^3 \theta_0 \chi^{zzz} + N_b^2 w_b^2 \sin \theta_0 \chi^{zxx} - 2n_b^2 w_b W_b \sin \theta_0 \chi^{xxz} - w_b^2 W_b \chi^{xxx} \cos 3\phi. \quad (3.75)$$

3.3.5 The 3-layer-hybrid model: evaluating $\mathcal{P}(2\omega)$ in ℓ and $\mathbf{E}(\omega)$ in the bulk

Again, we follow the same procedure as above considering that 2ω terms are evaluated in the thin layer ℓ , and the 1ω terms will be evaluated in the bulk by taking $\ell = b$, thus $\epsilon_\ell(\omega) = \epsilon_b(\omega)$, $t_p^{v\ell} = t_p^{vb}$,

and $t_p^{\ell b} = 1$. With these choices Eqs. (3.68) and (3.69) reduce to

$$\Gamma_{pP}^{\ell b} = \frac{T_p^{v\ell} T_p^{\ell b} \left(t_p^{vb}\right)^2}{N_\ell^2 n_b^2 N_b}, \quad (3.76)$$

and

$$r_{pP}^{(111)} = N_b^2 \sin^3 \theta_0 \chi^{zzz} + N_b^2 k_b^2 \sin \theta_0 \chi^{zxx} - 2N_\ell^2 w_b W_b \sin \theta_0 \chi^{xxz} - N_\ell^2 w_b^2 W_b \chi^{xxx} \cos 3\phi. \quad (3.77)$$

3.4 About the code

SHGyield is a python script designed to calculate the nonlinear reflection coefficient for semiconductor surfaces. It works in conjunction with the matrix elements calculated with ABINIT and TINIBA, our in-house optical calculation software. I have created a [Github repository](#) with the code. Like all free and open-source software, it can be freely downloaded, modified, and shared. The script reads an input file that specifies all the necessary filenames, angles, broadening, and other variables. It allows the user to include the effects of multiple reflections if desired, and select several parameters for calculating these effects. It will automatically try to read all 18 independent components of the nonlinear susceptibility (for SHG), but the user can easily limit which components it will attempt to read if the total number can be reduced due to symmetry relations.

3.5 Conclusions

In this chapter, we derived the complete expressions for the SSHG radiation using the three layer model to describe the radiating system. Our derivation yields the full expressions for the radiation that include all required components of χ^{abc} , regardless of symmetry considerations. Thus, these expressions can be applied to any surface symmetry. We also reduce them according to the most commonly used surface symmetries, the (111), (110), and (100) cases.

In the next chapter, I will present the results obtained from using the theory developed here and in Chapter 2 applied to the Si(001)(2×1) and the Si(111)(1×1):H surfaces. In particular, we will compare the theoretical SSHG yield for the latter surface with experimental data from several sources. This is an excellent way to test the validity of this approach, and will provide a benchmark for future calculations using the theory developed here.

Chapter 4

A SSHG Spectroscopic Study of Two Si Surfaces

Outline

4.1	Results for the Si(001)(2×1) surface	45
4.1.1	Calculating $\chi_{\text{surface}}^{xxx}(-2\omega; \omega, \omega)$	46
4.1.1.1	Full-slab results	47
4.1.1.2	Half-slab vs full-slab	48
4.1.1.3	Half-slab results	51
4.1.2	Overview of the calculated \mathcal{R} spectra	52
4.2	Results for the Si(111)(1×1):H surface	53
4.2.1	Calculating $\chi_{\text{surface}}^{xxx}(-2\omega; \omega, \omega)$	56
4.2.2	Comparing the theoretical \mathcal{R} to experiment	56
4.2.2.1	Overview of the calculated \mathcal{R} spectra	57
4.2.2.2	$\mathcal{R}_{pP}(p\text{-in}, P\text{-out})$	59
4.2.2.3	Calculated \mathcal{R}_{sP} compared to experiment	63
4.2.2.4	Calculated \mathcal{R}_{pS} compared to experiment	64
4.3	Conclusion	67

In this chapter, I will present the results for the calculation of the nonlinear susceptibility, χ_{surface} , and the SSHG yield, \mathcal{R}_{iF} , for the Si(001)(2×1) and the Si(111)(1×1):H surfaces. These results are the direct product of all the theory derived in Chapters 2 and 3. These example surfaces provide the perfect testbed for the theory developed in this work, and the resulting spectra yield insight into the various key aspects of the theory.

The first part focuses on using the Si(001)(2×1) surface to review and compare the enhancements that we have added to the framework for calculating χ . This surface is presented in a special configuration that allows us to test each improvement made on the theory; namely, the use of the cut function for extracting the surface susceptibility, the effect of the scissors operator, and the

addition of \mathbf{v}^{nl} . I will also present a very brief overview of the calculated SSHG yield, but with no comparison to experimental data as there is very little available for this surface.

The second part features the Si(111)(1×1):H, which is experimentally well-characterized, and thus provides an excellent platform with which to test our robust formulation for the SSHG yield. We will first compare the calculated χ^{xxx} component with experimental data from Ref. [2]. This will provide a nice confirmation of everything we learned from the Si(001)(2×1) surface. We will then review the calculated spectra for different polarization cases of the incoming fields, and compare them to experimental data from Refs. [3, 4, 87], over a wide energy range covering both the E₁ and E₂ critical point transitions for bulk Si. We will find that this new formalism, that is developed from the 3-layer model and includes the effect of multiple reflections in the material, compares quite favorably with the experimental data. The quality of these calculations affords us some insight into how the SSHG spectrum can be affected by several physical factors.

4.1 Results for the Si(001)(2×1) surface

In this section, let us review the characteristics of the Si(001)(2×1) surface we will be using for the subsequent calculations. This surface provides an excellent test case to check the consistency of our approach for calculating χ with the new elements described in Chap. 2. For this, I have selected a clean Si(001) surface with a 2×1 surface reconstruction. The slab for such a surface could be made centrosymmetric by creating the front and back surfaces with the same 2×1 reconstruction. However, this particular slab has the lower surface terminated with hydrogen, producing a terminated, “ideal” bulk Si surface. The H atoms saturate the dangling bonds of the bulk-like Si atoms at the surface, as seen in Fig. 4.1. Consider the z coordinate pointing out of the surface with the x coordinate along the crystallographic [011] direction, parallel to the dimers.

The self-consistent ground state and the Kohn-Sham states were calculated in the DFT-LDA framework using the plane-wave ABINIT code [136, 137], using Troullier-Martins pseudopotentials [138] that are fully separable nonlocal pseudopotentials in the Kleinman-Bylander form [123]. The contribution of \mathbf{v}^{nl} and \mathcal{V}^{nl} to Eq. (2.78) was carried out using the DP code [139], which is implemented in our in the TINIBA code [140] developed at the Centro de Investigaciones en Óptica, A.C. The surface was studied with the experimental lattice constant of 5.43 Å. Structural optimizations were also performed with the ABINIT code. The geometry optimization was carried out in slabs of 12 atomic layers, where the central four layers were fixed at the bulk positions. The structures were relaxed until the Cartesian force components were less than 5 meV/Å. The geometry optimization for the clean surface gives a dimer buckling of 0.721 Å, and a dimer length of 2.301 Å. For the dihydride surface, the obtained Si-H bond distance was 1.48 Å. These results are in good agreement with previous theoretical studies [125, 141]. The vacuum size is equivalent to one quarter the size of the slab, avoiding the effects produced by possible wave-function tunneling from the contiguous surfaces of the full crystal formed by the repeated super-cell scheme [125]. Note that all spectra for χ^{xxx} presented in this section were calculated with a Gaussian broadening of 0.15 eV.

Spin-orbit, local field, and electron-hole attraction [67] effects on the SHG process are all neglected. Although these are important factors in the optical response of a semiconductor, their efficient calculation is still theoretically and numerically challenging and under debate. This merits further study but is beyond the scope of this thesis. For a given slab size, I found the converged spectra to obtain the relevant parameters. The most important of these are: an energy cutoff of

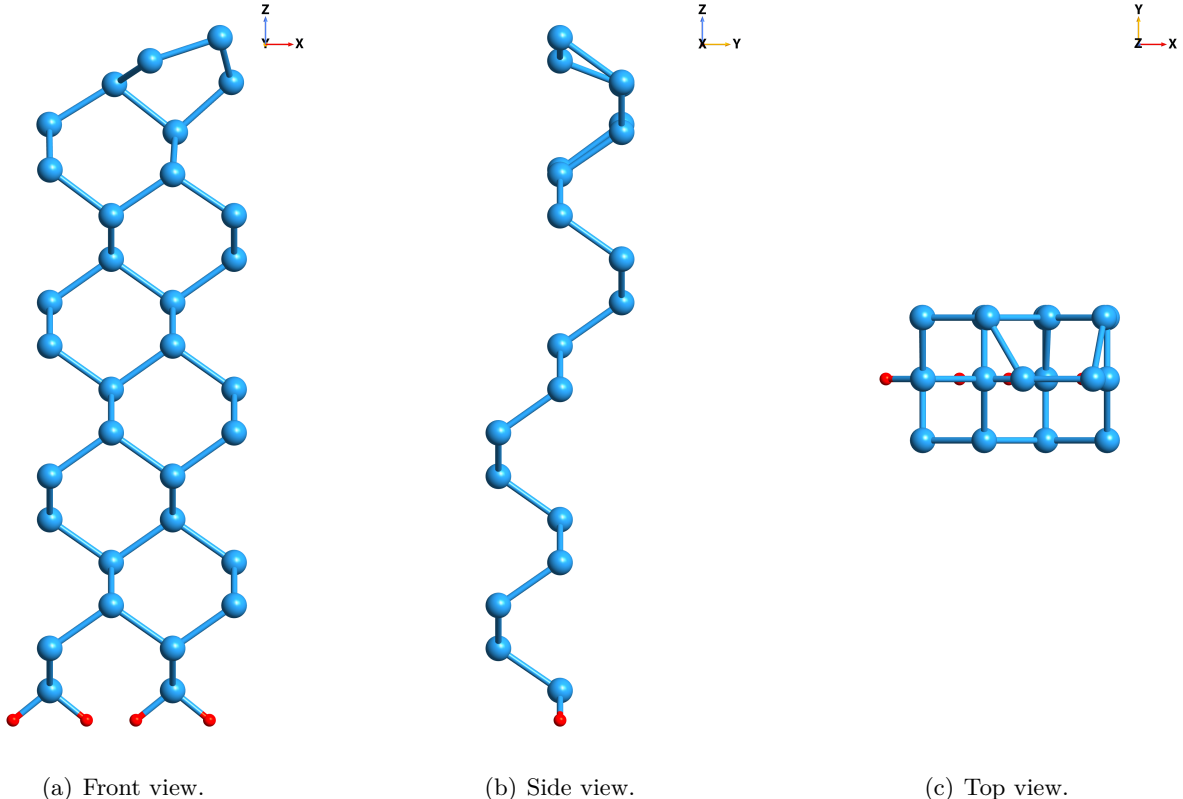


Figure 4.1: Several views of the slab used to represent the Si(001)(2×1) surface. This particular slab has 16 Si atomic layers (large blue balls) with two H atomic layers (small red balls).

10 Ha for the 16, 24, and 32 layered slabs and 13 Ha for the 40 layer slab, an equal number of conduction and valence bands, and a set of 244 \mathbf{k} points in the irreducible Brillouin zone, which are equivalent to 1058 \mathbf{k} points when disregarding symmetry relations. The \mathbf{k} points are used for the linear analytic tetrahedron method for evaluating the 3D Brillouin Zone (BZ) integrals, where special care was taken to examine the double resonances of Eq. (2.78) [80]. Note that the Brillouin zone for the slab geometry collapses to a 2D-zone, with only one \mathbf{k} -point along the z -axis.

4.1.1 Calculating $\chi_{\text{surface}}^{xxx}(-2\omega; \omega, \omega)$

The idea behind the special slab configuration, pictured in Fig. 4.2, is that the crystalline symmetry of the H terminated surface imposes that $\chi_H^{xxx} = 0$. The 2×1 surface has no such restrictions, so naturally $\chi_{2 \times 1}^{xxx} \neq 0$. This is due to the fact that along the y direction there is a mirror plane for the H-saturated surface (causing centrosymmetry), whereas for the 2×1 surface this mirror is lost as the dimers are asymmetric along x . Thus, calculating χ^{xxx} for the full-slab, or the upper half-slab containing the 2×1 surface [142] should yield the same result, since the contribution from the H saturated surface is zero either way. The following relationship must be satisfied for this particular slab,

$$\chi_{\text{half-slab}}^{xxx} = \chi_{\text{full-slab}}^{xxx},$$

where $\chi_{\text{half-slab}}^{xxx}$ is calculated using $\mathcal{C}(z) = 1$ for the upper half containing the 2×1 surface reconstruction (see Fig. 4.2), and $\chi_{\text{full-slab}}^{xxx}$ is calculated using $\mathcal{C}(z) = 1$ for the entire slab. Again, the dihydride surface on the lower half of the slab must have $\chi_{\text{half-slab}}^{xxx} = 0$.

$$2 \times 1 \text{ reconstruction} \Rightarrow \chi_{2 \times 1}^{xxx} \neq 0$$

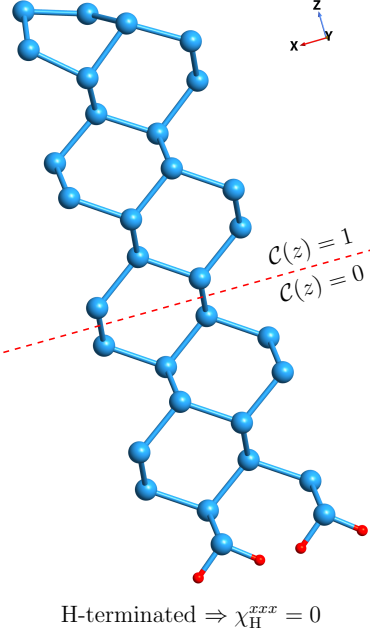


Figure 4.2: The slab for the Si(001)(2×1) surface. The front (upper) surface is in a 2×1 , clean reconstruction, and the rear (lower) surfaces is H-terminated, with “ideal” bulk-like atomic positions. The dangling bonds are H-saturated.

4.1.1.1 Full-slab results

Fig. 4.3 shows $|\chi_{\text{full-slab}}^{xxx}|$ for the slab with 16, 24, 32, and 40 Si atomic layers, without the contribution of \mathbf{v}^{nl} , and with no scissors correction. Since the clean Si(001) surface is in a 2×1 reconstruction there are two atoms per atomic layer. Thus, the total number of atoms per slab is twice the number of atomic layers of the slab. The slabs were extended in the z directions in steps of 8 layers of bulk-like atomic positions. Note that the response differs substantially for 16 and 24 layers but is quite similar for 32 and 40 layers. As explained above, the calculation of the \mathbf{v}^{nl} contribution is computationally expensive, so it is crucial to minimize the number of atoms in the calculation. I consider a slab with 32 Si atomic layers as a good compromise between the convergence of $\chi_{\text{full-slab}}^{xxx}$ as a function of the number of layers in the slab, and the computational expense.

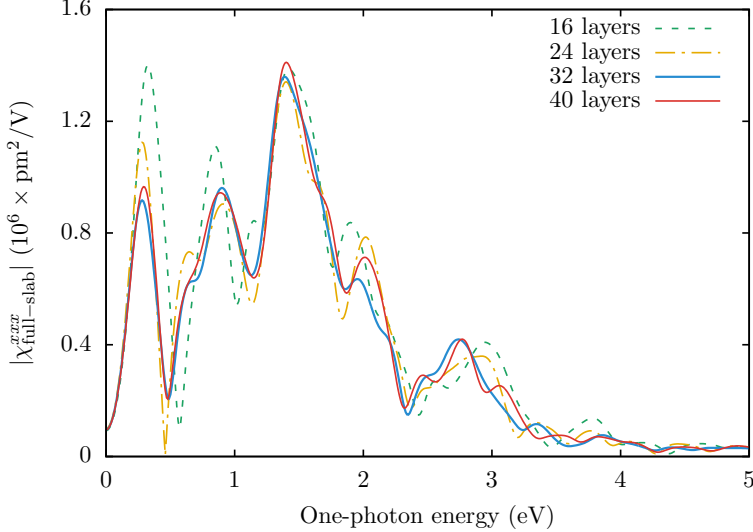


Figure 4.3: $|\chi_{\text{full-slab}}^{xxx}|$ vs $\hbar\omega$ for the slab with 16, 24, 32, and 40 atomic Si layers. Adequate convergence is achieved after 32 layers. The spectra presented here use a scissors value of $\hbar\Delta = 0$ eV, and do not include the contribution from \mathbf{v}^{nl} .

4.1.1.2 Half-slab vs full-slab

Now that we have established an adequate number of layers to attain convergence, we can proceed to study the spectra produced from the slab with 32 atomic layers. Fig. 4.5 presents a comparison between $\chi_{\text{half-slab}}^{xxx}$ and $\chi_{\text{full-slab}}^{xxx}$ for four different scenarios: with and without the effects of \mathbf{v}^{nl} , and with two values for the scissors correction, $\hbar\Delta$. I have chosen a scissors value of $\hbar\Delta = 0.5$ eV, that is the GW gap reported in Refs. [143, 144]. This is justified by the fact that the surface states from the clean 2×1 surface are rigidly shifted and maintain their dispersion relation with respect to the LDA value, according to the GW calculations of Ref. [143].

We can appreciate that the difference between the half-slab and full-slab responses is quite small for all four scenarios. Indeed, when the value $|\chi^{xxx}|$ is large, the difference between the two is quite small; when $|\chi^{xxx}|$ is small, the difference increases slightly but the spectra is so close to zero that it is negligible. Of course, the difference between the two would decrease as the number of atomic layers increases. Note how 32 layers in the slab is more than enough to confirm that the extraction of the surface second-harmonic susceptibility from the 2×1 surface is readily possible using the formalism contained in Eq. (2.78). Calculating the response from the lower half of the slab substantiates that $|\chi_{\text{half-slab}}^{xxx}| \approx 0$ for the dihydride surface, shown in Fig. 4.4.

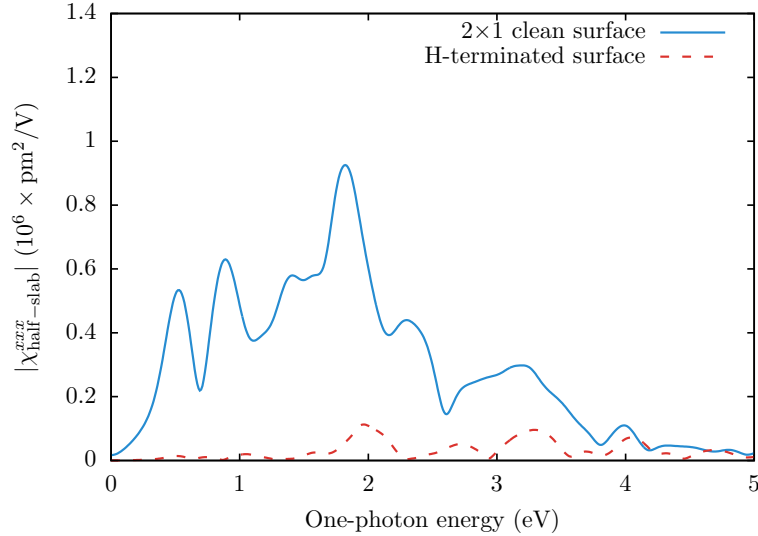


Figure 4.4: $\chi_{\text{half-slab}}^{xxx}$ vs $\hbar\omega$ for the clean 2×1 and H-terminated surfaces, with $\hbar\Delta = 0.5$ eV and without the effects of \mathbf{v}^{nl} .

This confirms the validity of the theory developed in Chapter 2 and is an important result of this work. Through the proposed layer formalism, we can calculate the surface χ^{abc} component including the contribution from the nonlocal part of the pseudopotentials, and part of the many-body effects through the scissors correction. Therefore, this scheme is robust and versatile and should work for any crystalline surface.

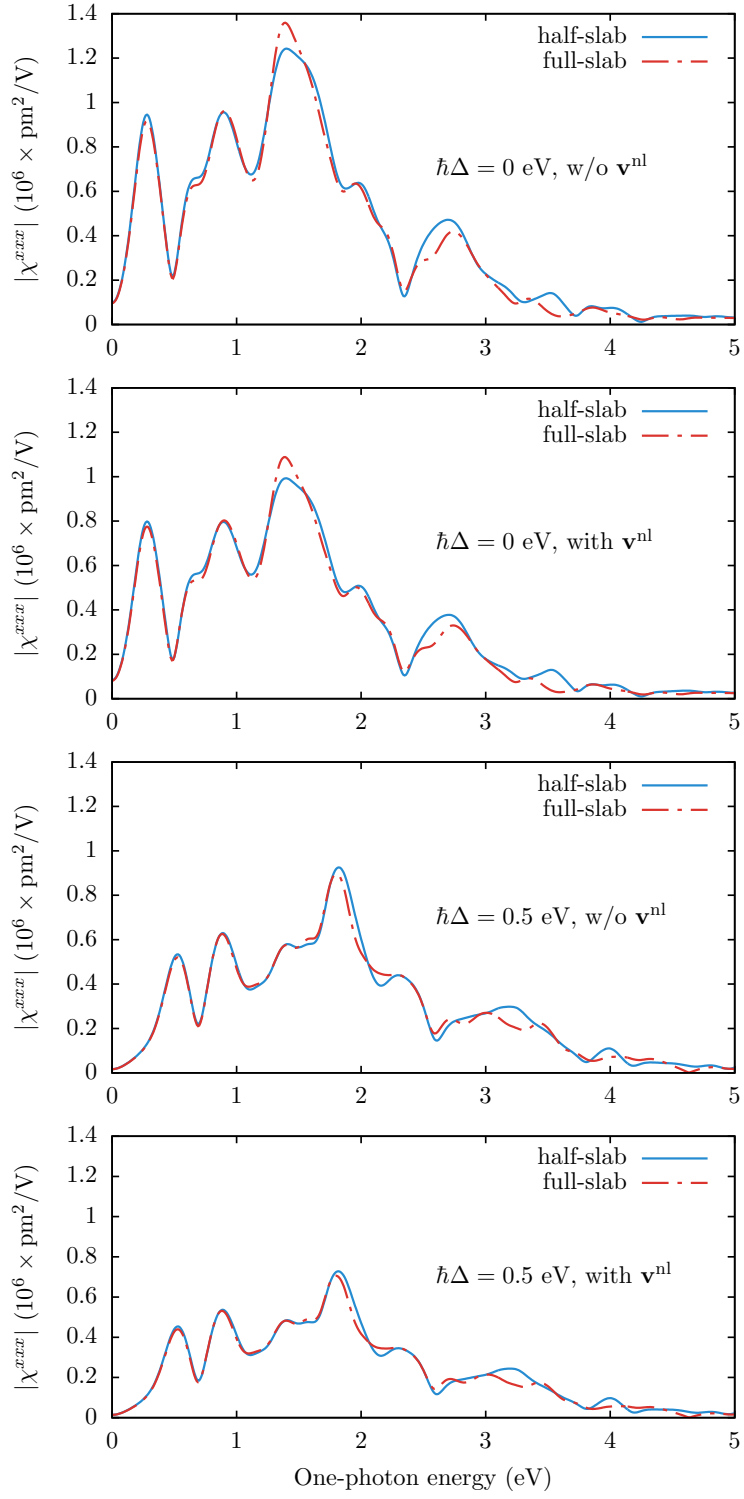


Figure 4.5: $\chi_{\text{half-slab}}^{xxx}$ and $\chi_{\text{full-slab}}^{xxx}$ vs $\hbar\omega$ for four different combinations: with and without the effects of \mathbf{v}^{nl} , and with two values for the scissors correction, $\hbar\Delta$.

4.1.1.3 Half-slab results

I proceed to explain some of the features seen in $|\chi_{\text{half-slab}}^{xxx}|$ that is obtained when setting $\mathcal{C}(z) = 1$ for the upper half containing the 2×1 surface reconstruction, as seen in Fig. 4.2. From Fig. 4.5, we note a series of resonances that derive from the 1ω and 2ω terms in Eq. (2.78). Notice that the 2ω resonances start below $E_g/2$, where E_g is the band gap (0.53 eV for LDA, and 1.03 eV if the scissor is used with $\hbar\Delta = 0.5$ eV). These resonances come from the electronic states of the 2×1 surface, that lie inside the bulk band gap of Si and are the well known electronic surface states [143].

Fig. 4.6 shows that the inclusion of \mathbf{v}^{nl} reduces the value of $|\chi_{\text{half-slab}}^{xxx}|$ by 15-20%. This demonstrates the importance of this contribution for a fully correct SSHG calculation. This is in agreement with the analysis for bulk semiconductors [84]. However, the inclusion of \mathbf{v}^{nl} does not change the spectral shape of $|\chi_{\text{half-slab}}^{xxx}|$. We can confirm that this is not unique for this specific scissors shift, as we can appreciate from the upper two panels of Fig. 4.5, with $\hbar\Delta = 0$ eV.

To demonstrate the effect of the scissors correction, I considered two different finite values for $\hbar\Delta$. The first, with a value of $\hbar\Delta = 0.5$ eV that is used in the previous results, is the “average” GW gap taken from Ref. [143] that is in agreement with Ref. [144]. The second, with a value of $\hbar\Delta = 0.63$ eV is the “average” gap taken from Ref. [145], where more \mathbf{k} points in the Brillouin zone were used to calculate the GW value. Fig. 4.7 shows that the scissors correction shifts the spectra from its LDA value to higher energies, as expected. However, contrary to the case of linear optics [81], the shift introduced by the scissors correction is not rigid, which is consistent with the work of Ref. [80]. This is because the second-harmonic optical response mixes 1ω and 2ω transitions (see Eq. (2.78)), and accounts for the non-rigid shift. The reduction of the spectral strength is in agreement with previous calculations for bulk systems [80, 146, 147]. When comparing $|\chi_{\text{half-slab}}^{xxx}|$ for the two finite values of $\hbar\Delta$, it is clear that the first two peaks are almost rigidly shifted with a small difference in height while the rest of the peaks are modified substantially. This behavior comes from the fact that the first two peaks are almost exclusively related to the 2ω resonances of

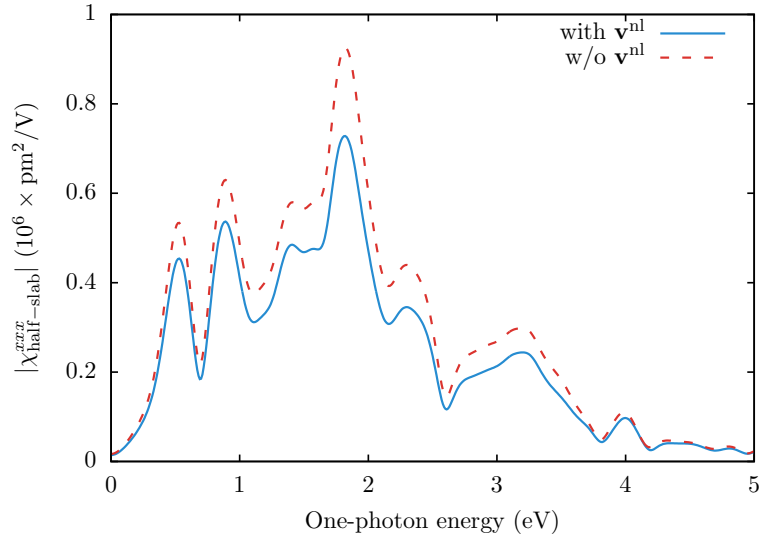


Figure 4.6: $\chi_{\text{half-slab}}^{xxx}$ vs $\hbar\omega$, with and without the contribution from \mathbf{v}^{nl} . This spectrum has a scissor value of $\hbar\Delta = 0.5$ eV.

Eq. (2.78). The other peaks are a combination of 1ω and 2ω resonances and yield a more varied spectrum. Note that for large-gap materials the 1ω and 2ω resonances would be split, producing a small interference effect. The 2ω resonances would still strongly depend on the surface states. Thus, small changes in the scissors shift can affect the SSH susceptibility spectrum quite dramatically. In Ref. [148], the authors already noted that the nonlinear optical response of bulk materials is more influenced by the electronic structure of the material than the linear case. For the case of semiconductor surfaces, the problem is even more intricate due to the presence of electronic surface states.

The high sensitivity of SSHG to the energy position of surface states, as seen in Fig. 4.7, makes SSHG a good benchmark tool for spectroscopically testing the validity of the inclusion of many-body effects, and in particular the quasi-particle correction to the electronic states. Although local fields are neglected, in principle they should be quite small parallel to the interface as the electric field is continuous. χ^{xxx} should have a relatively small influence from these local fields. Excitonic effects should also be explored, but their efficient calculation is theoretically and numerically challenging [67] and far beyond the scope of this work. Unfortunately the experimental measurement of the χ^{xxx} component is difficult as the SH radiated intensity would be proportional not only to this component but also to the other components of χ . However, I will present this comparison later on in Sec. 4.2.1 for the Si(111)(1×1):H surface.

4.1.2 Overview of the calculated \mathcal{R} spectra

In Figs. 4.8 and 4.9, I present the results for the calculation of the SSHG yield for our test surface. The 2×1 surface reconstruction yields a Class 1, primitive triclinic system with all 18 components independent from each other [135]. We cannot take advantage of any symmetry relations for this surface. However, this is no problem for the robust formulation we derived in Chapter 3 that can accommodate all 18 components disregarding any surface symmetries. Calculating all 18

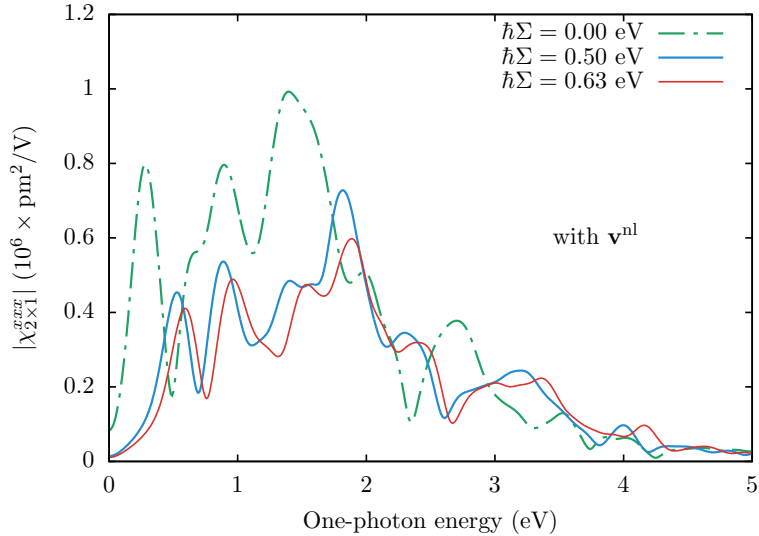


Figure 4.7: $\chi_{\text{half-slab}}^{xxx}$ vs $\hbar\omega$ for a slab with 32 atomic Si layers plus one H layer, for three different values of the scissors correction, $\hbar\Delta$.

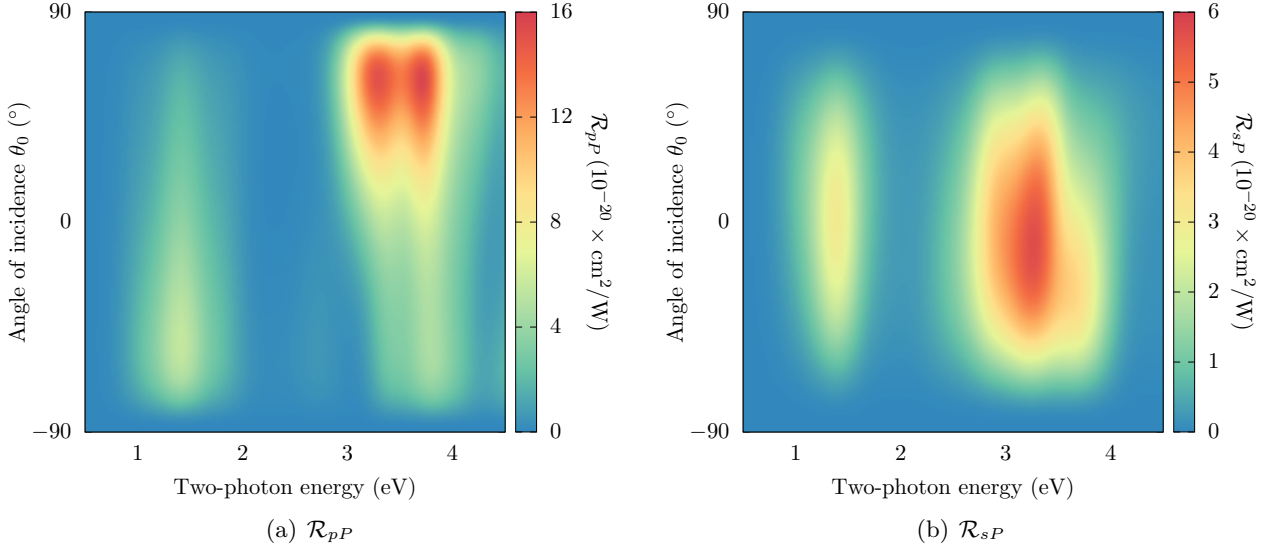


Figure 4.8: \mathcal{R} for outgoing P polarization, versus the angle of incidence (θ_0) for the Si(001)(2×1) surface. The scissor shift used was $\hbar\Delta = 0.5$ eV. Both figures consider an azimuthal angle of $\phi = 45^{\circ}$.

components is obviously more time consuming, but this calculation can be parallelized in order to calculate all components at once, so very little time is actually lost.

Fig. 4.8 presents the results for the SSHG yield with outgoing P polarization. I set a fixed azimuthal angle of $\phi = 45^{\circ}$ and then varied the incoming angle θ_0 from -90° to 90° . We can clearly see that the surface states associated with the 2×1 reconstruction produce significant intensity between 1-2 eV in the two-photon energy range. This is consistent with the findings presented in the previous section and in Ref. [85]. The intensity of the peak related to the surface states is significantly lower than the peaks produced in the 2.5-4 eV two-photon energy range. The spectrum for \mathcal{R}_{pP} is very consistent with other calculations of this type [149], and even with some limited experimental data [45].

Fig. 4.9 presents the results for the SSHG yield with outgoing S polarization. They are quite similar to what we observed in Fig. 4.8, with a peak related to the surface states between 1-2 eV, and a larger set of peaks between 2.4-4 eV in the two-photon energy range. These spectra have a clear maxima around $\theta_0 = 0^{\circ}$. These plots are presented for mainly illustrative purposes, as there is little experimental data to compare with the theoretical spectrum. However, these kinds of plots will be quite useful to the experimentalist interested in this kind of spectroscopy. Excellent intensity for all polarization cases can be obtained for small beam angles, such as $\theta_0 = 30^{\circ}$.

4.2 Results for the Si(111)(1×1):H surface

We will now focus our attention on the Si(111)(1×1):H surface. This surface is a C_{3v} , primitive hexagonal system with only 4 nonzero components independent from each other, as shown in Table 3.2 [1, 133, 135]. It is composed of stacked layers with one Si atom each, with one H atom terminating each surface. The added H saturates the surface Si dangling bonds and eliminates any

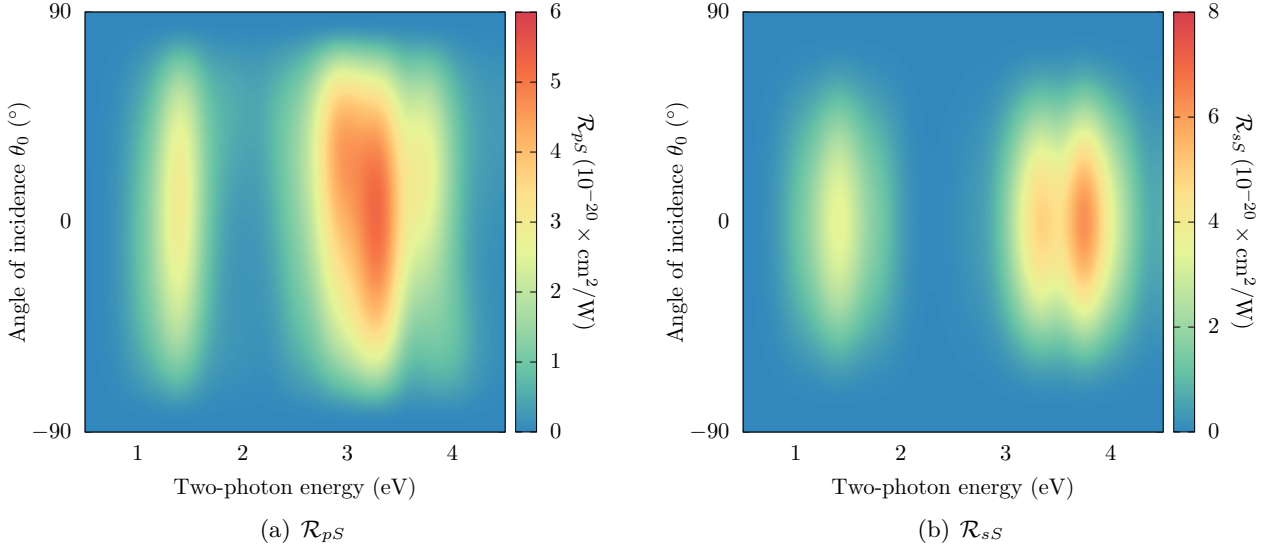


Figure 4.9: \mathcal{R} for outgoing S polarized fields, versus the angle of incidence (θ_0) for the Si(001)(2×1) surface. The scissor shift used was $\hbar\Delta = 0.5$ eV. Both figures consider an azimuthal angle of $\phi = 45^{\circ}$.

surface-related electronic states in the band gap. Here, the top and bottom surfaces are mirror images (see Fig. 4.10); this provides the centrosymmetry that necessitates the use of the cut function to extract the nonzero surface response. In Sec. 4.2.1 we will compare the spectrum produced by using relaxed and unrelaxed coordinates, so it is worth reviewing this concept here. The specifics of this process are as follows.

The relaxation process was done by my colleague, Nicolas Tancogne-Dejean [149]. The structure was initially constructed with the experimental lattice constant of 5.43 Å, and then performed structural optimizations with the ABINIT [136, 137] code. It was then relaxed until the Cartesian force components were less than 5 meV/Å, yielding a final Si-H bond distance of 1.50 Å. The energy cutoff used was 20 Ha, and Troullier-Martin LDA pseudopotentials were used [138]. The resulting atomic positions are in good agreement with previous theoretical studies [3, 150–153], as well as the experimental value for the Si-H distance [154].

I also evaluated the number of layers required for convergence (like Sec. 4.1.1.1) and settled on a slab with 48 atomic Si planes. The geometric optimizations mentioned above are therefore carried out on slabs of 48 atomic layers without fixing any atoms to the bulk positions. Fig. 4.10 depicts a sample slab with 16 layers of Si. The surface susceptibilities must be extracted from only half of the slab. This encompasses 24 layers of Si and the single layer of H that terminates the top surface. The vacuum size is equivalent to one quarter the size of the slab, avoiding the effects produced by possible wave-function tunneling from the contiguous surfaces of the full crystal formed by the repeated super-cell scheme [125].

The electronic wave-functions, $\psi_{n\mathbf{k}}(\mathbf{r})$, were also calculated with the ABINIT code using a planewave basis set with an energy cutoff of 15 Hartrees. $\chi^{abc}_{\text{surface}}$ was properly converged with 576 \mathbf{k} points in the irreducible Brillouin zone, which are equivalent to 1250 \mathbf{k} points when disregarding symmetry relations. The contribution of \mathbf{v}^{nl} in Eq. (2.78) was carried out using the DP [139] code

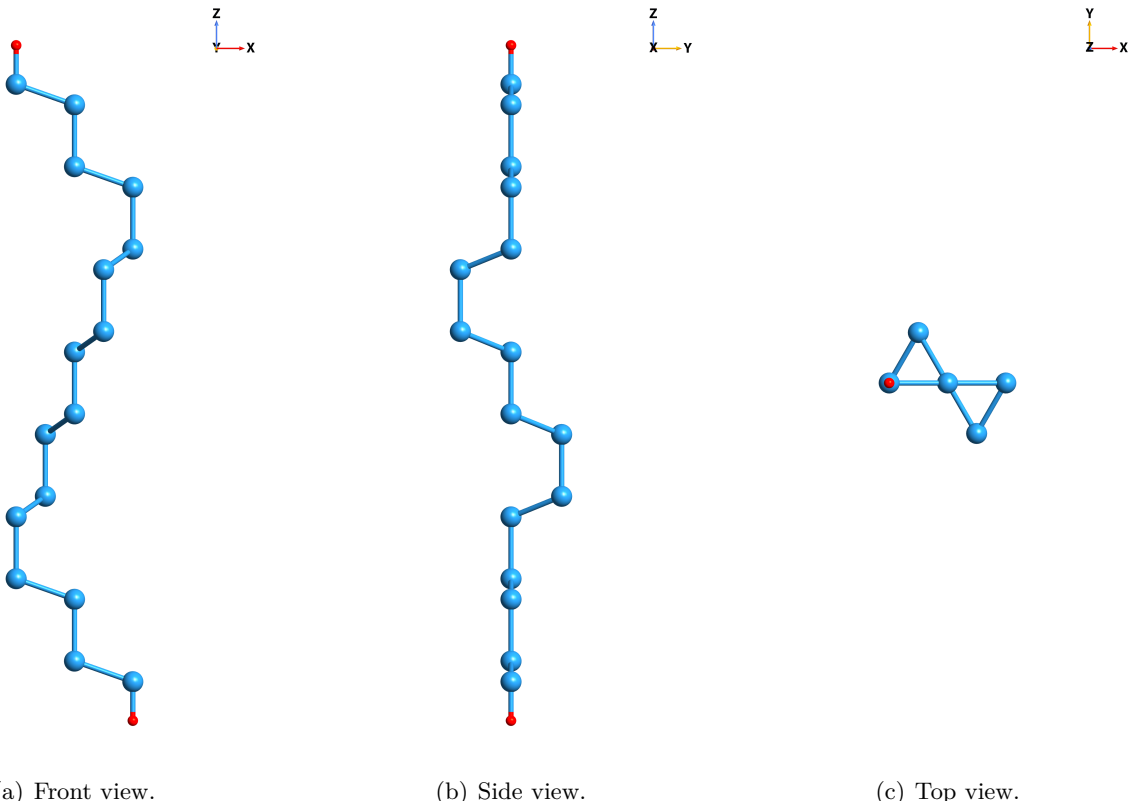


Figure 4.10: Several views of the slab used to represent the Si(111)(1×1):H surface. This particular slab has 16 Si atomic layers (large blue balls) with two H atomic layers (small red balls).

implemented in TINIBA [140], with a basis set of 3000 planewaves. Convergence for the number of bands was achieved at 200, which includes 97 occupied bands and 103 unoccupied bands. All spectra were produced using a scissors value of 0.7 eV in the $\chi^{\text{abc}_{\text{surface}}}$ and $\epsilon_{\ell}(\omega)$ calculations. This value was obtained from Ref. [155], in which the authors carry out a G_0W_0 calculation on this surface for increasing numbers of layers. They calculated the LDA and G_0W_0 band gaps, and found that the difference between the two tends towards ~ 0.7 eV as more layers are added, culminating in a value of 0.68 eV for bulk Si. This calculation is completely *ab-initio*, so I consider 0.7 eV to be a very reasonable value for the scissors correction.

It is important to mention that we must also calculate the bulk and surface dielectric functions, $\epsilon_b(\omega)$ and $\epsilon_\ell(\omega)$. For this, we follow the method presented in Ref. [125]. For the bulk, the tensor components are equal in all three directions due to the cubic symmetry,

$$\varepsilon_b(\omega) = \epsilon_b^{xx}(\omega) = \epsilon_b^{yy}(\omega) = \epsilon_b^{zz}(\omega).$$

For the purpose of this calculation, we introduce the average value for the surface dielectric function, $\varepsilon_\ell(\omega)$. This entails that $\epsilon_\ell^{xx}(\omega) = \epsilon_\ell^{yy}(\omega) \approx \epsilon_\ell^{zz}(\omega)$, since symmetry is broken in the zz direction because of the surface. We find the average in the conventional way,

$$\varepsilon_\ell(\omega) = \frac{\epsilon_\ell^{xx}(\omega) + \epsilon_\ell^{yy}(\omega) + \epsilon_\ell^{zz}(\omega)}{3},$$

and use that quantity in the equations for the SSHG yield. In order to obtain a result which does not depend on the size of the vacuum region [156], we have normalized the surface dielectric function to the volume of the slab, instead of the volume of the super-cell. We remark that we could calculate $\epsilon_{\text{half-slab}}^{\text{ab}}(\omega)$ using $\mathcal{C}(z) = 1$ for the upper half of our slab and normalize to the volume of the half-slab. Nevertheless, $\epsilon_{\ell}^{\text{ab}}(\omega)$ and $\epsilon_{\text{half-slab}}^{\text{ab}}(\omega)$ give the same result [127, 128, 156].

4.2.1 Calculating $\chi_{\text{surface}}^{xxx}(-2\omega; \omega, \omega)$

The pioneering work presented in Ref. [3] showed the effect of artificially moving the atomic position on the resulting SSHG spectra. In this section, I will address the more practical and relevant case of atomic relaxation. More precisely, I compare the fully relaxed structure described above with an unrelaxed structure where all the Si atoms are at the ideal bulk positions. Note that in both cases, the Si-H bond distance is the same 1.5 Å. The unrelaxed coordinates use the same parameters mentioned above. Fortunately, there exists experimental data that can be compared to the calculated $\chi_{\text{surface}}^{xxx}$ for this surface, taken from Ref. [2]. This data provides an excellent point of comparison as it was presented in absolute units and was measured at a very low temperature of 80 K.

Fig. 4.11 depicts the spectra from the relaxed and unrelaxed coordinates compared to experiment. The theoretical curves were calculated with a scissors shift of $\hbar\Delta = 0.7$ eV, as mentioned in the previous section. The relaxed coordinates have a peak position that is very slightly blueshifted with respect to the experimental peak near 1.7 eV. In contrast, the unrelaxed coordinates have a peak that is redshifted close to 0.05 eV from experiment. There is also a feature between 1.5 eV and 1.6 eV that appears in the relaxed spectrum that coincides partially with the experimental data. Both theoretical curves have half the intensity of the experimental peak. It is important to note that this data was taken at low temperature (80 K); this further favors the comparison, as the theory neglects the effects of temperature. As is shown in Ref. [2], the peaks in the spectrum redshift as the temperature increases. Intensity for both the relaxed and unrelaxed curves are roughly half the intensity of the experimental spectrum. I have converted the units of the experimental data from CGS to MKS units for easier comparison.

We can conclude that the most accurate theoretical results are produced by using relaxed atomic positions for the calculation of χ_{surface} . Although this process can be very time consuming for large numbers of atoms, this should be considered a crucial step. This also further demonstrates that SSHG is very sensitive to the surface atomic positions. In particular, these results show that a correct value of the Si-H bond length is not enough to obtain the most accurate SSHG spectra, and that a full relaxation of the structure is required. Additionally, it seems that the theory may coincide better with experiments that are conducted under very low temperature conditions.

4.2.2 Comparing the theoretical \mathcal{R} to experiment

All calculations presented from this point on were done using the relaxed atomic positions described in the the previous section. I will now present the theoretical SSHG yield for the Si(111)(1×1):H surface compared to experiments from Refs. [3, 4, 87]. These comparisons are good benchmarks to test the complete formalism for calculating the SSHG yield.

The method of calculation is as follows. I first calculated $\varepsilon_b(\omega)$, $\varepsilon_\ell(\omega)$, and then $\chi_{\text{surface}}^{\text{abc}}$ from Eq. (2.78). I used these for the Fresnel factors and in Eqs. (3.49), (3.59), and (3.54), and finally, those into Eq. (3.41) to obtain the theoretical SSHG yield for different polarizations that can then

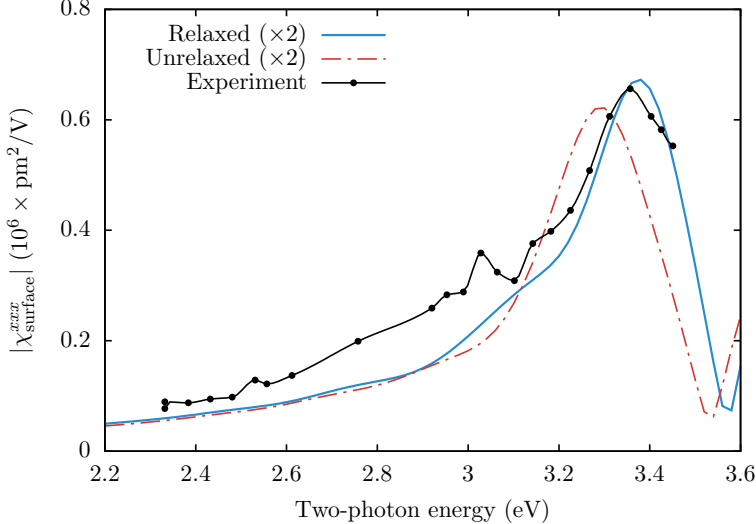


Figure 4.11: Comparison of $\chi_{\text{surface}}^{xxx}$ calculated using relaxed and unrelaxed atomic positions, with the experimental data presented in Ref. [2]. The theoretical curves were calculated with a scissors shift of $\hbar\Delta = 0.7$ eV, and are broadened with $\sigma = 0.075$ eV. Experimental data was taken at 80 K.

be compared with the experimental data. Remember that a scissors shift of $\hbar\Delta = 0.7$ eV is used for all the $\chi_{\text{surface}}^{\text{abc}}$ components. These components and the calculated \mathcal{R} spectra were also broadened with a Gaussian broadening of $\sigma = 0.075$ eV. These values were selected so that the theoretical calculation best represents the lineshape of the experimental spectrum.

4.2.2.1 Overview of the calculated \mathcal{R} spectra

We will carefully explain and compare the calculated \mathcal{R} for each different polarization case in the following sections. However, I first want to present a general overview of the theoretical SSHG yield, as I did in Sec. 4.1.2. In Figs. 4.12 and 4.13, I present these results over a two-photon energy range of 2.5-5 eV. This range corresponds to the experimental measurements featured in Refs. [3] and [87]. Note that the SSHG yield drops to zero very rapidly before for energy values under 3 eV. This is because of the lack of surface states due to the surface H-saturation.

I have included some helpful markers in these figures. First, the solid black line represents an angle incidence of $\theta_0 = 65^\circ$. This is one of two angles that we will consider for the remainder of this chapter; in particular, this is the angle used in the experiment from Ref. Refs. [3]. It is clear that they chose this particular angle to maximize the \mathcal{R}_{PP} output. Second, the dashed black lines represent the $E_1 = 3.4$ eV and $E_2 = 4.3$ eV critical points of bulk Si [157]. For the outgoing P polarization in Fig. 4.12, we can see that the calculated SSHG yield does have peaks around those energy values. We will review this in much further detail below. We see similar characteristics, for Fig. 4.13 with the outgoing S polarization cases. Indeed, the theoretical peak values seem to match quite well with the critical points. Again, we will review these findings in much more detail below. Note that I will omit \mathcal{R}_{SS} from this point forward, as I do not have any experimental data to compare it with.

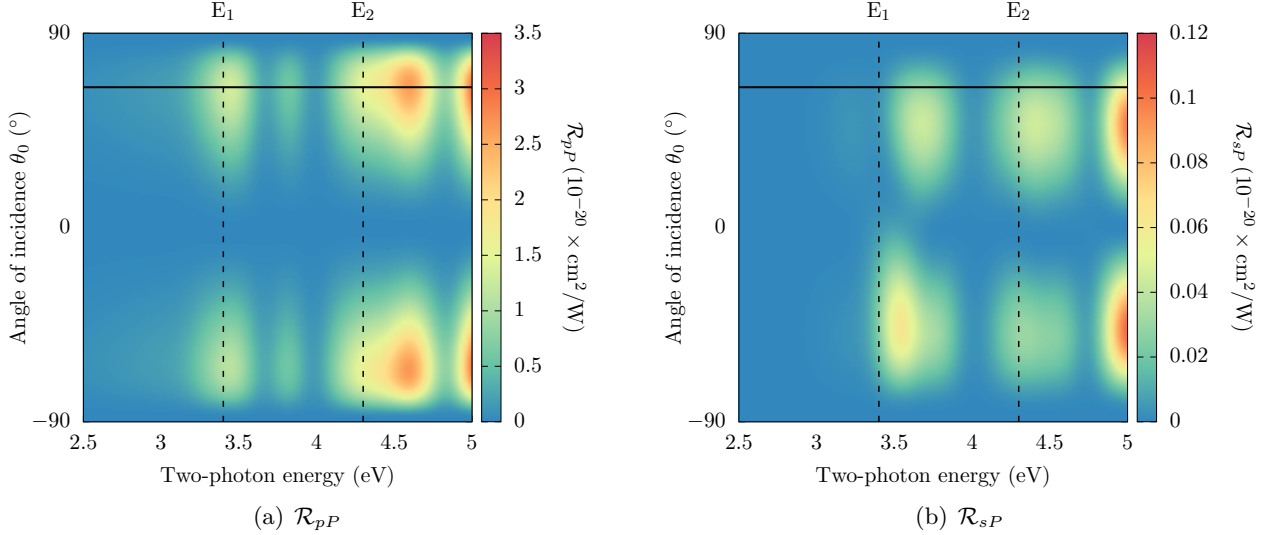


Figure 4.12: \mathcal{R} for outgoing P polarization, versus the angle of incidence (θ_0) for the Si(111)(1×1):H surface. A scissors shift of $\hbar\Delta = 0.7$ eV is applied. The solid line represents $\theta_0 = 65^\circ$, and the dotted lines represent the E_1 and E_2 Si critical points. Both figures consider an azimuthal angle of $\phi = 30^\circ$.

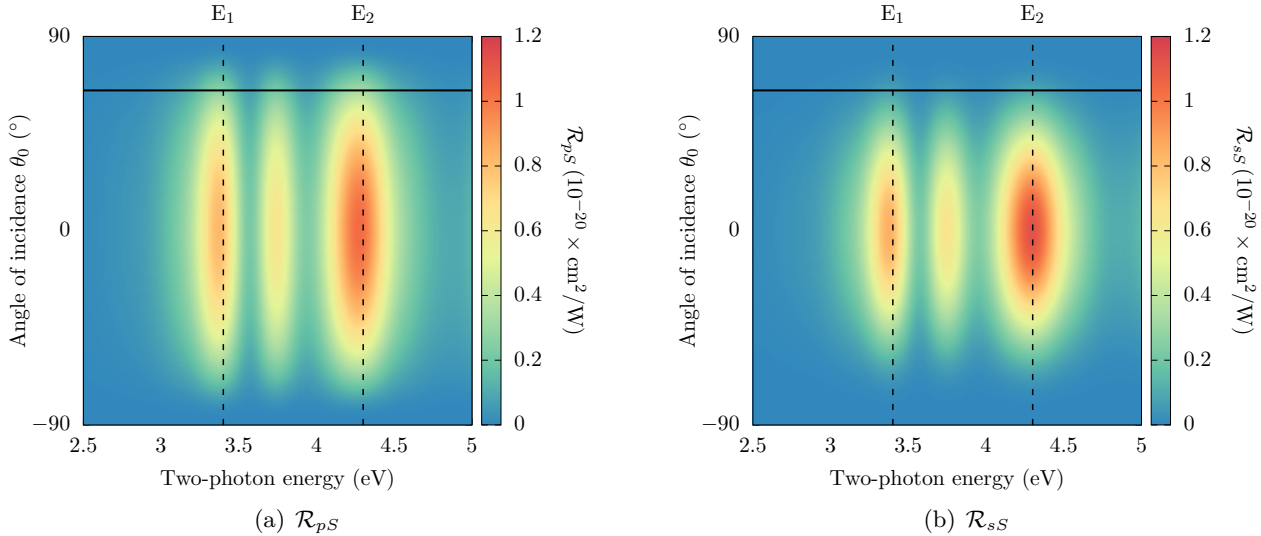


Figure 4.13: \mathcal{R} for outgoing S polarized fields, versus the angle of incidence (θ_0) for the Si(111)(1×1):H surface. A scissors shift of $\hbar\Delta = 0.7$ eV is applied. The solid line represents $\theta_0 = 65^\circ$, and the dotted lines represent the E_1 and E_2 Si critical points. Both figures consider an azimuthal angle of $\phi = 30^\circ$.

4.2.2.2 \mathcal{R}_{pP} (*p*-in, *P*-out)

We first analyze how the inclusion of multiple reflections affects the calculated SSHG yield. I will conduct this study for \mathcal{R}_{pP} as it is typically associated with the strongest signal output. It is also by far the most involved calculation out of the four different polarization cases, since it includes all four nonzero components. We are interested in finding the thickness of the layer ℓ where $\chi_{\text{surface}}^{\text{abc}} \neq 0$. As mentioned above, we found reasonable converged results for this surface using a slab of 48 atomic layers. This corresponds to a thickness of ~ 5 nm, that is equivalent to the 24 atomic sheets of Si along the (111) direction, corresponding to the half-slab. As this represents only the upper half of the slab, we find it reasonable to choose the thickness of the layer ℓ to be between $d \sim 5 - 10$ nm, as in this range of values $\chi_{\text{surface}}^{\text{abc}}$ will be well converged.

We begin our comparisons in Fig. 4.14, in which we compare the theoretical results for the SHG radiation with the experimental results from Ref. [3]. First, we note that the experimental spectrum shows two very well defined resonances which come from electronic transitions from the valence to the conduction bands around the well known $E_1 \sim 3.4$ eV and $E_2 \sim 4.3$ eV critical points of Si [157]. We mention that the experimental results were produced with an angle of incidence of $\theta = 65^\circ$, and an azimuthal angle of $\phi = 30^\circ$, which eliminates the contribution from $\chi_{\text{surface}}^{xxx}$ from Eq. (3.49). The theoretical curves that include multiple reflections are featured with the average value \bar{R}_p^M , Eq. (3.23), with two values for the total thickness, d , and Eqs. (3.47) and (3.49). We contrast these with the standard three layer model excluding the effects of multiple reflections from Sec. 3.3.1. We see that the E_2 peak is blueshifted by around 0.3 eV, and the yield does not go to zero after 4.75 eV. We can attribute these shortcomings to the fact that both $\chi_{\text{surface}}^{zzz}$ and $\chi_{\text{surface}}^{xxz}$ include out-of-plane incoming fields. These are affected by local field effects that can change both intensity and peak position [149]. Including these effects is computationally very expensive and is beyond the scope of this work. We speculate that the components of $\chi_{\text{surface}}^{\text{abc}}$ necessary for \mathcal{R}_{pP} require the proper inclusion of these effects in order to accurately describe the experimental peaks. Additionally, Ref. [47] shows that low temperature measurements of \mathcal{R}_{pP} will blueshift the spectrum away from room temperature measurements such as those shown in Figs. 4.17 and 4.19, and towards the theoretical results.

We can see that including the effects of multiple reflections enhances the E_2 peak significantly, and that the enhancement increases with the thickness d of the thin layer ℓ . This should be quite obvious from 3.1; as the layer thickness increases, so does the total contribution from the multiple reflections. Since we have already established that using a layer thickness of 10 nm is reasonable for this surface, I will use this value from this point on.

In Fig. 4.15, I present the results from calculating the spectra with and without the multiple reflections from the 1ω fields. The difference between the two lines is almost negligible for energies below 4 eV. After 4 eV, the spectrum without the 1ω multiple reflections is less intense. The difference in intensity between the two curves is most noticeable at E_2 . We can conclude that the 1ω multiple reflections contribute only slightly to the region around E_2 , and are almost negligible elsewhere. This is clear since the phase shift of Eq. (3.24) is not only a factor of 2 smaller than that of Eqs. (3.16) and (3.17), but also $w_\ell < W_\ell$. However, including them is indeed necessary in order to have the most complete formulation, and calculating r_p^M comes at no additional computational expense.

We can analyze the effects of moving the polarization sheet to different depths within the layer ℓ in Fig. 4.16. As mentioned above, we consider a layer thickness of $d = 10$ nm. We compare the theoretical SSHG yield for $d_2 = 0$ nm and $d_2 = 10$ nm, with the SSHG yield that neglects multiple

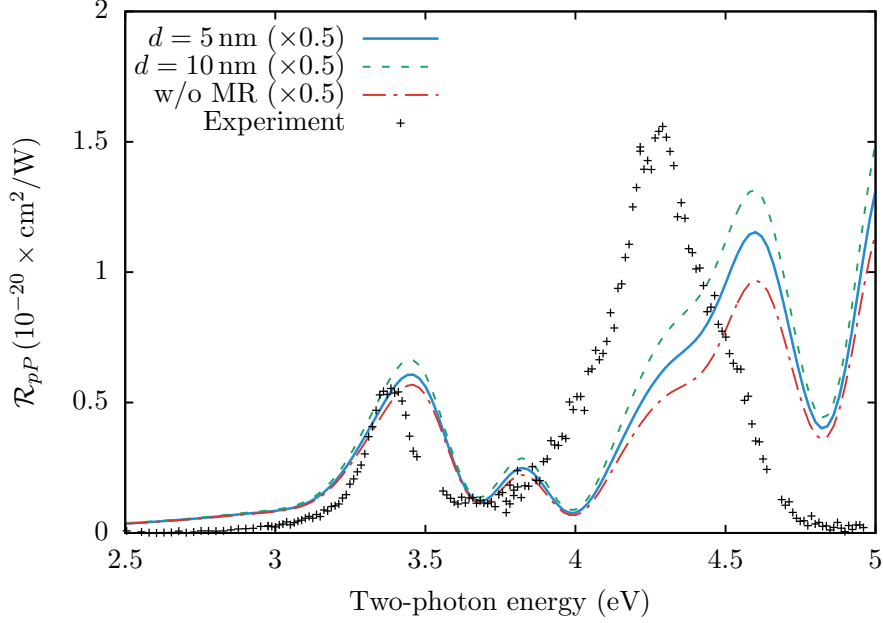


Figure 4.14: Comparison between the three layer model with the effects of multiple reflections for two different values of the total layer thickness d , with the standard three layer model without the effects of multiple reflections, and the experimental data from Ref. [3]. We take $\theta = 65^\circ$, $\phi = 30^\circ$, and a scissors value of $\hbar\Delta = 0.7 \text{ eV}$.

reflections. When $d_2 = 0 \text{ nm}$, we have placed the polarization sheet at the bottom of the layer region. This minimizes the effect of the multiple reflections, and thus the curve is very similar to the three layer model that neglects multiple reflections entirely. When $d_2 = 10 \text{ nm}$, the polarization sheet is placed at the top of the layer region. This maximizes the effect of the multiple reflections and therefore leads to the largest yield. We also notice that the average value obtained by using \bar{R}_p^M (Eq. (3.23)) is intermediate between $d_2 = 0$ and $d_2 = 10 \text{ nm}$, as expected. This is very similar to selecting $d_2 = d/2$, which can be interpreted as placing the nonlinear polarization sheet $\mathbf{P}(\mathbf{r}, t)$ at the middle of the thin layer ℓ .

As before, these enhancements are larger for E_2 than for E_1 . This can be understood from the fact that the corresponding λ_0 for E_1 is larger than that of E_2 . From Eqs. (3.16), (3.17), and (3.24), we see that the phase shifts are larger for E_2 than for E_1 , producing a larger enhancement of the SSHG yield at E_2 from the multiple reflections. As the phase shifts grow with d , so does the enhancement caused by the multiple reflections. From this figure, it becomes evident that the inclusion of multiple reflections is crucial to obtain a better agreement between the theoretical SSHG yield and the experimental spectrum. This is particularly true for larger energies, such as E_2 , as λ_0 becomes smaller and the multiple reflection effects become more noticeable. The selected value for $d \ll \lambda_0$, that comes naturally from the *ab initio* calculation of $\chi_{\text{surface}}^{\text{abc}}$ is thus very reasonable in order to model a thin surface layer below the vacuum region where the nonlinear SH conversion takes place. From this point on, we will always include the effects of multiple reflections in the 3-layer model, with a layer thickness of $d = 10 \text{ nm}$ and the average value of \bar{R}_p^M .

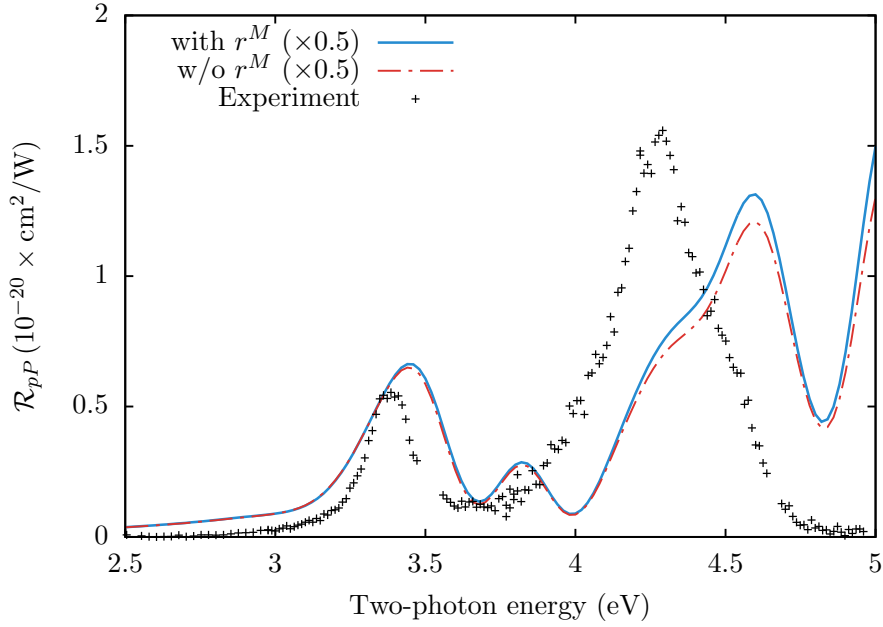


Figure 4.15: Comparison between including or neglecting the effects of multiple reflections for the fundamental fields. The theoretical spectra were produced for a layer thickness of $d = 10$ nm using the average value of \bar{R}_p^M .

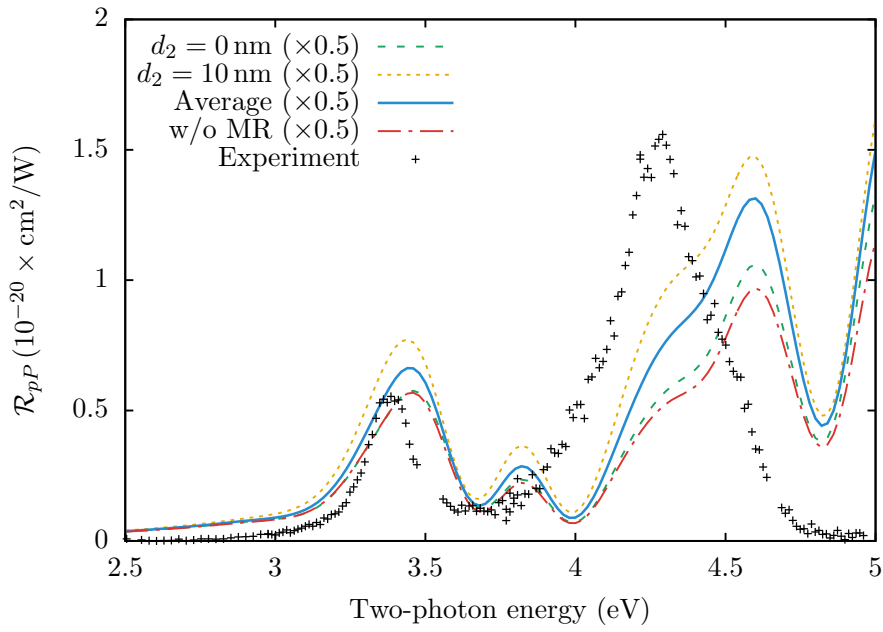


Figure 4.16: Comparison between the three layer model with the effects of multiple reflections for two different values of d_2 , and the average value \bar{R}_p^M . All curves that include multiple reflections consider a layer ℓ thickness of $d = 10$ nm.

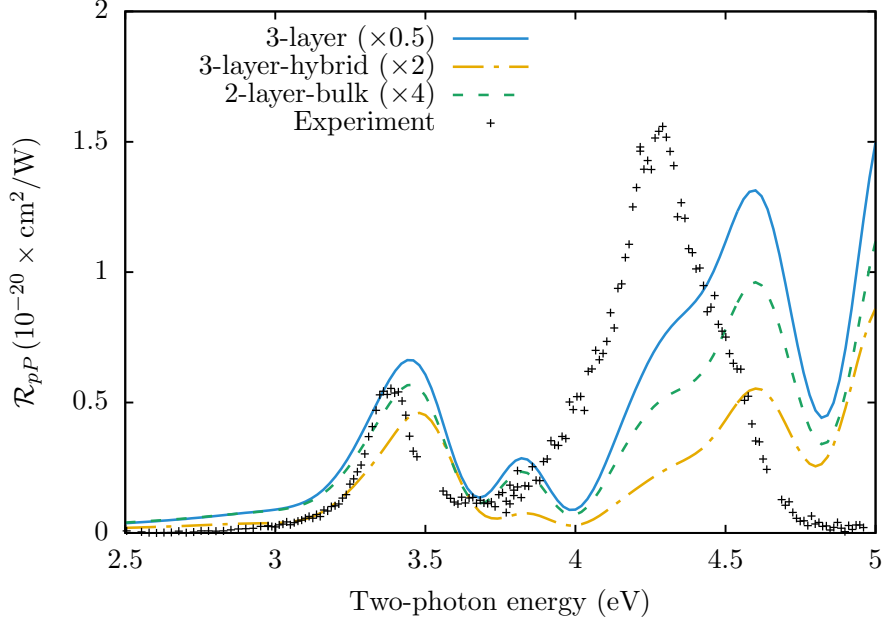


Figure 4.17: Comparison between theoretical models (see Table 3.3) and experiment for \mathcal{R}_{pP} , for $\theta = 65^\circ$, and a scissors value of $\hbar\Delta = 0.7 \text{ eV}$. Experimental data taken from Ref. [3], measured at room temperature.

I will now present an overview of the different models from Sec. 3.3, and summarized in Table 3.3. Namely, we will compare the 3-layer model with multiple reflections, the 2-layer-fresnel, 2-layer-bulk, 2-layer-vacuum, and 3-layer hybrid models. In Fig. 4.17, I present a comparison between the 3-layer, 3-layer-hybrid, and 2-layer-bulk models with experiment. The peak position for the 3-layer model compares quite nicely to the experimental peaks, with an overall intensity that is only two times larger. The 2-layer-bulk model is almost identical in lineshape to the 3-layer model, but with four times less intensity than the experiment. The 3-layer-hybrid model is also similar in lineshape with a less pronounced E_2 peak, and is half as intense as the experiment. All these observations are consistent as ϵ_b and ϵ_ℓ differ mostly in intensity; each model is screened with either ϵ_b (2-layer-bulk), ϵ_ℓ (3-layer), or a combination of the two (3-layer-hybrid). Ultimately, the 3-layer model has better peak proportions and good intensity, but the other two models are interesting alternatives.

The two remaining models from Sec. 3.3 are presented in Fig. 4.18. The 2-layer-fresnel model produces a spectrum with peak positions that are close to the experiment, but are around 40 times more intense. The calculated E_2 peak is similar, but the E_1 peak lacks the sharpness present in the experiment, with poor proportional intensity between the peaks. On the other hand, the 2-layer-vacuum model has the most extreme intensity difference with the experiment, over 5 orders of magnitude higher. The lineshape reproduces the E_2 peak quite well, but lacks a sharp E_1 peak with poor peak position. Clearly, the screening provided by ϵ_b and ϵ_ℓ are necessary for accurate results. From Eq. (3.49), it is clear that \mathcal{R}_{pP} has several 2ω terms that will change between models; this will have a deep effect on the lineshape. Additionally, Γ_{pP}^ℓ also has $\epsilon_\ell(2\omega)$ in the denominator, and so we have a significant difference in both lineshape and intensity between these models and the rest.

From this point forward, we will only consider the 3-layer (with multiple reflections), the 2-layer-fresnel (the historically popular model), and the 2-layer bulk models. These three models give an interesting overview of the different possibilities available and add some insight into the physics behind the SSHG yield.

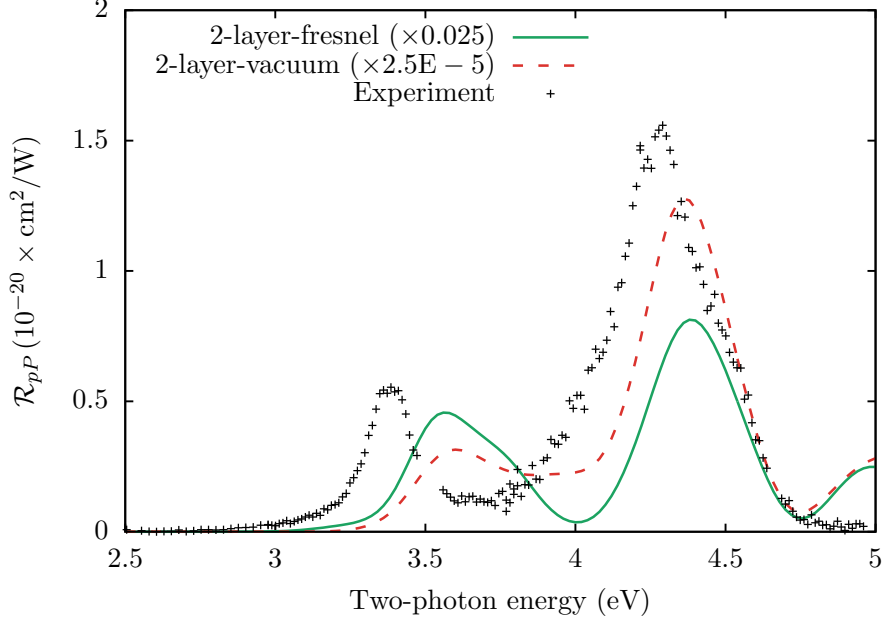


Figure 4.18: Comparison between the 2-layer-fresnel and 2-layer-vacuum models (see Table 3.3) and experiment for \mathcal{R}_{pP} , for $\theta = 65^\circ$, and a scissors value of $\hbar\Delta = 0.7 \text{ eV}$. Experimental data taken from Ref. [3], measured at room temperature.

In Fig. 4.19, I compare the theoretical spectra to results from Ref. [4]. The 3-layer model is, as before, close to the experiment in both peak position and intensity. Intensity is almost the same the experimental value. This provides a more compelling argument against the 2-layer-fresnel model than Fig. 4.17. The 2-layer-fresnel model is 20 times more intense and blueshifted by around 0.1 eV. As mentioned above, this surface is of very high quality with measurements taken shortly after surface preparation. The 2-layer-bulk model is intermediate between the other two models in both intensity and lineshape. Under these conditions, the 3-layer model very accurately reproduces the E₁ peak over the 2-layer-fresnel and 2-layer-bulk models.

4.2.2.3 Calculated \mathcal{R}_{sP} compared to experiment

Next, we will compare the calculated \mathcal{R}_{sP} spectra with experimental data from Ref. [3]. The calculation adheres to the experimental setup by taking an angle of incidence $\theta = 65^\circ$ and an azimuthal angle $\phi = 30^\circ$. As seen in Fig. 4.20, the overall intensity of \mathcal{R}_{sP} is one order of magnitude lower than \mathcal{R}_{pS} . The experimental data is far noisier than in the other cases but the E₁ and E₂ peaks are still discernible. As with the previous comparisons, the 3-layer model is the closest match in both intensity and lineshape to the experimental spectrum. It produces a curve that is very close to the experimental intensity with good proportional heights for the calculated

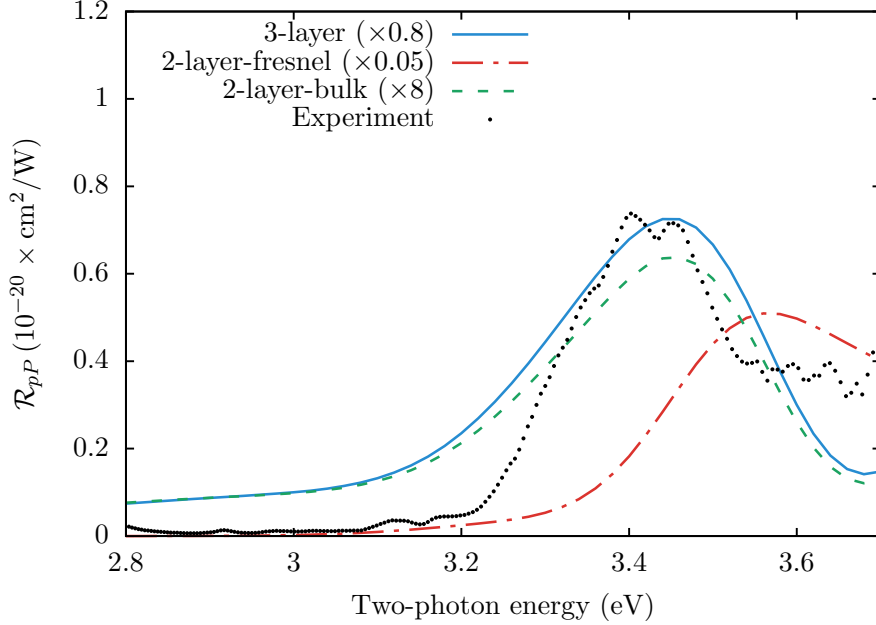


Figure 4.19: Comparison between theoretical models (see Table 3.3) and experiment for \mathcal{R}_{pP} , for $\theta = 45^\circ$, and a scissors value of $\hbar\Delta = 0.7$ eV. Experimental data taken from Ref. [4], measured at room temperature.

E_1 and E_2 peaks. In contrast, the 2-layer-fresnel model is 100 times more intense than experiment and produces an enlarged E_2 peak. The 2-layer-bulk model is ten times smaller with a very similar lineshape to the 3-layer model.

The differences between the 2-layer-fresnel and 2-layer-bulk models are not derived from Eq. (3.54), as the $\varepsilon_b(2\omega)$ does not change and the second term vanishes for this azimuthal angle of $\phi = 30$. However, Γ_{sP}^ℓ does cause a significant change in the intensity as there is an $\varepsilon_\ell(2\omega)$ term in the denominator. This will become $\varepsilon_v(2\omega) = 1$ for the 2-layer-fresnel model, and $\varepsilon_b(2\omega)$ in the bulk model. This accounts for the significant difference between the intensity of the two models, while the lineshape remains mostly consistent. At higher energies, the theoretical curve is blueshifted as compared to the experiment. The best explanation for this is the inclusion of the scissor operator, which does not adequately correct the transitions occurring at these higher energies. A full GW calculation would be well suited for this task, but is well beyond the scope of this work.

4.2.2.4 Calculated \mathcal{R}_{pS} compared to experiment

We will now compare the \mathcal{R}_{pS} spectra with room temperature experimental data from Ref. [3]. Adhering to the experimental setup, I set an angle of incidence $\theta = 65^\circ$ and an azimuthal angle of $\phi = 30^\circ$ with respect to the x -axis. This azimuthal angle maximizes r_{pS} , as shown in Eq. (3.59). Fig. 4.21, shows that all three models reproduce the lineshape of the experimental spectrum which includes the peaks corresponding to both the E_1 and E_2 critical points of bulk silicon, and a smaller feature at around 3.8 eV. The calculated E_1 and E_2 peaks are redshifted by 0.1 eV and 0.06 eV, respectively, compared with the experimental peaks. The proportional peak intensity is quite good and compares favorably with the experimental peaks. Any minor discrepancy in the peak intensity

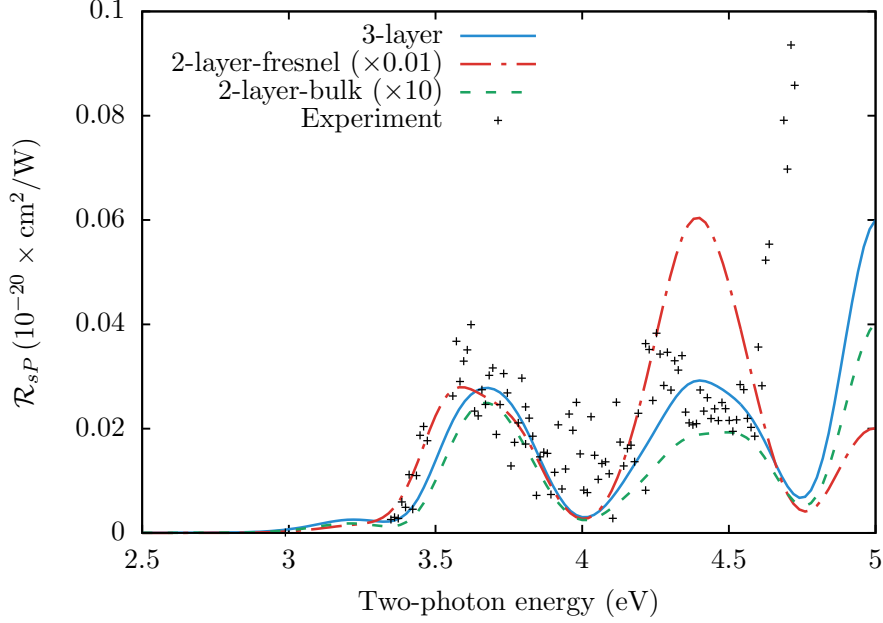


Figure 4.20: Comparison between theoretical models (see Table 3.3) and experiment for \mathcal{R}_{sP} , for $\theta = 65^\circ$, and a scissors value of $\hbar\Delta = 0.7$ eV. Experimental data taken from Ref. [3], measured at room temperature.

could be due to the effects of oxidation on the surface. Ref. [87] features similar data to those of Ref. [3] but focuses on the effects of surface oxidation. From Ref. [87] it is clear that as time passes during the experiment, the surface becomes more oxidized and the E_1 peak diminishes substantially, as shown by the experimental data taken 5 hours after initial H-termination. This may be enough time to slightly reduce the E_1 peak intensity in the experimental data.

In Fig. 4.22, I compare the theoretical \mathcal{R}_{pS} with experimental data from Ref. [4]. This calculation uses an angle of incidence $\theta = 45^\circ$ and an azimuthal angle $\phi = 30^\circ$ to match the experimental conditions. As in the previous comparison, the E_1 peak is slightly redshifted compared to experiment. The intensity of the theoretical yield is smaller than the experimental yield for all three models. The measurements presented in Ref. [4] were taken very shortly after the surface had been prepared, and the surface itself was prepared with a high degree of quality and measured at room temperature. Peak position compared to theory is slightly improved under these conditions. As before, the 3-layer model is closer in intensity to the experimental spectrum.

From Fig. 4.11, I presented that our calculation for $\chi_{\text{surface}}^{xxx}$ coincides with the measurement taken at a low temperature of 80 K. It is well known that temperature causes shifting in the peak position of SSHG spectra [47]. As \mathcal{R}_{pS} only depends on this component (see Eq. (3.59)), the position of the theoretical peak should be correct in Figs. 4.21 and 4.22. Thus, the difference in peak position should stem from the higher temperature at which the experiments were measured.

Both the 2-layer-fresnel and 2-layer-bulk models are identical and roughly three times smaller than the experiment. It is clear from Eq. (3.59) that \mathcal{R}_{pS} only has 1ω terms ($\varepsilon_\ell(\omega)$ and k_b). For both of these models, the fundamental fields are evaluated in the bulk, which means that the only change to Eq. (3.59) is that $\varepsilon_\ell(\omega) \rightarrow \varepsilon_b(\omega)$. Additionally, Γ_{pS}^ℓ also remains identical between the two models and has no 2ω terms in the denominator. Therefore, r_{pS} is identical between these two

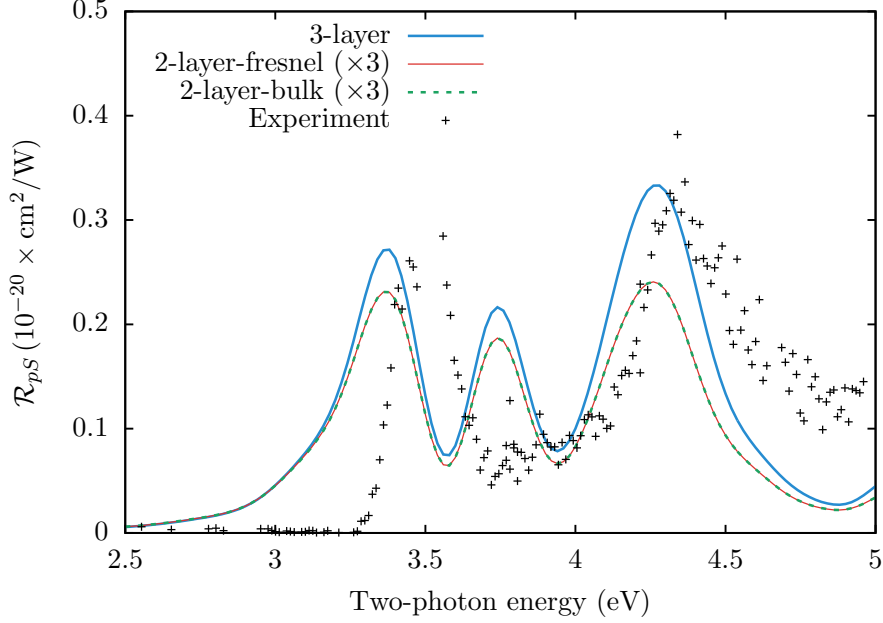


Figure 4.21: Comparison between theoretical models (see Table 3.3) and experiment for \mathcal{R}_{pS} , for $\theta = 65^\circ$, and a scissors value of $\hbar\Delta = 0.7 \text{ eV}$. Experimental data taken from Ref. [3], measured at room temperature.

models. Ultimately, the intensity of the 3-layer model is the closest to the experiment.

Per Eq. (3.59), the intensity of \mathcal{R}_{pS} depends only on $\chi_{\text{surface}}^{xxx}$, which is not affected by local field effects [149]. These effects are neglected in this calculation, but \mathcal{R}_{pS} maintains an accurate lineshape and provides a good quantitative description of the experimental SSHG yield. Note that both the calculated and experimental spectra show two-photon resonances at the energies corresponding to the critical point transitions of bulk Si. Note also that the SSHG yield drops rapidly to zero below E_1 , which is consistent with the absence of surface states due to the H saturation on the surface. This observation holds true for all three polarization cases studied for this surface.

In Fig. 4.23 I provide an overview of the different levels of approximation proposed in this article. All curves here were calculated using the 3-layer model. The long dashed line depicts the effect of excluding the contribution from the nonlocal part of the pseudopotentials. This is consistent with the results reported in Ref. [85], where the exclusion of this term increases the intensity of the components of χ_{surface} by approximately 15% to 20%. Note that the E_1 peak is larger than the E_2 peak, contrasting with the experiment, where the E_1 peak is smaller than E_2 . The thin solid line depicts the full calculation with a scissors value of $\hbar\Delta = 0$. The spectrum is almost rigidly redshifted as this H-saturated surface has no electronic surface states [85], in contrast to the Si(001)(2×1) surface presented in the first part of this chapter. Thus, this demonstrates the importance of including the scissors correction to accurately reproduce the experimental spectrum. In summary, the inclusion of the contribution from the nonlocal part of the pseudopotentials and the scissors operator on top of the 3-layer model produces spectra with a lineshape and intensity that compare favorably with the experimental data.

Lastly, GW transition energies are needed for linear optics and SHG. Doing a Bethe-Salpeter calculation for SSHG will undoubtedly improve the position and the amplitude of the peaks, but is

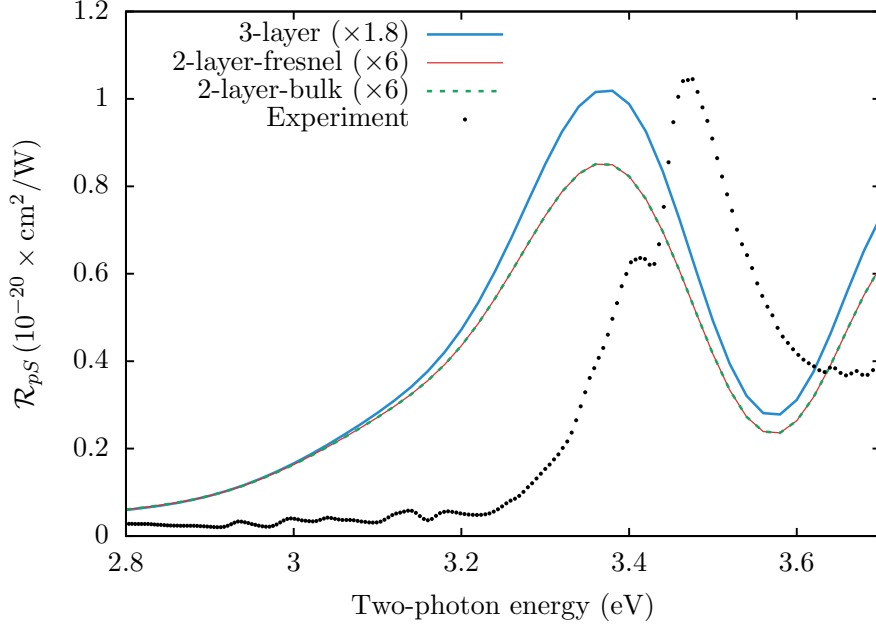


Figure 4.22: Comparison between theoretical models (see Table 3.3) and experiment for \mathcal{R}_{pS} , for $\theta = 45^\circ$. We use a scissors value of $\hbar\Delta = 0.7$ eV. Experimental data taken from Ref. [4], measured at room temperature.

far beyond current capabilities [158]. I kept the scissors shift constant throughout these calculations as I want to keep this calculation at the *ab initio* level. Remember that the choice of $\hbar\Delta = 0.7$ eV for the scissors shift comes from a *GW* calculation [155]. I have checked that it is not possible to have a single scissors value that can reproduce the energy positions of both the E_1 and the E_2 peaks. Of course, the experimental temperature at which the spectra is measured should be taken into account in a more complete formulation. However, these calculations are always restricted to $T = 0$ K. As mentioned before, it is important to consider the local field effects on the components of $\chi_{\text{surface}}^{abc}$. For this surface in particular, $\chi_{\text{surface}}^{zzz}$ and $\chi_{\text{surface}}^{xxz}$ include out-of-plane incoming fields. These are affected by local field effects [149] that reveal the inhomogeneities in the material, which are much more prevalent perpendicular to the surface than in the surface plane. This can be evidenced for Si, as Reflectance Anisotropy Spectroscopy (RAS) measurements are well described by *ab initio* calculations neglecting local field effects [159, 160]. It is therefore expected that the out-of-plane components will be more sensitive to the inclusion of local fields. These will not change the transition energies, only their relative weights of the resonant peaks [149]. Including these effects is challenging to compute [156], and beyond the scope of this thesis. These effects would mostly affect \mathcal{R}_{pP} since it includes all four nonzero components. We speculate that \mathcal{R}_{pP} requires the proper inclusion of these effects in order to accurately describe the experimental peaks.

4.3 Conclusion

We have used the formulation to calculate the surface nonlinear susceptibility tensor $\chi_{\text{surface}}(-2\omega; \omega, \omega)$, using the length gauge formalism and within the independent particle approximation (IPA). It in-

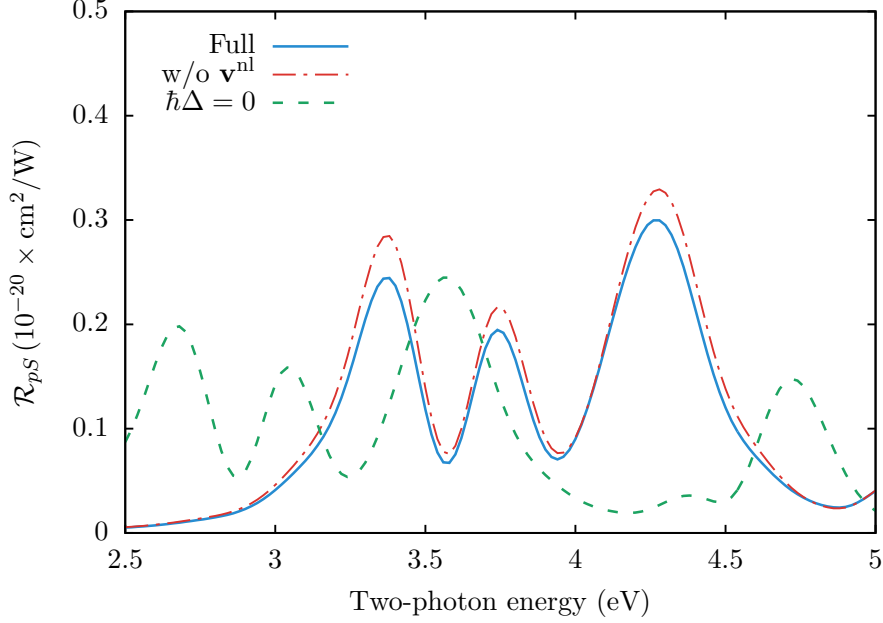


Figure 4.23: Calculated results for \mathcal{R}_{pS} for the different levels of approximation proposed in this article. All curves were calculated using the 3-layer model. We take $\theta = 65^\circ$ for this plot. See text for full details.

cludes on equal footing: (i) the scissors correction, (ii) the contribution of the non-local part of the pseudopotentials, and (iii) the cut function. We have used a Si(001) 2×1 surface to confirm that our scheme correctly obtains the surface response as we confirm that $\chi_{\text{half-slab}}^{xxx}(-2\omega; \omega, \omega) \approx \chi_{\text{full-slab}}^{xxx}(-2\omega; \omega, \omega)$. Although one can in principle increase the number of atomic layers, \mathbf{k} -points, etc. to improve even further on the similarity of the half-slab and full-slab results, we have chosen a good compromise between accuracy and the burden and time of the computations. We describe the effect of the independent inclusion of the three effects mentioned above in the calculation of $\chi(-2\omega; \omega, \omega)$. The scissors correction shifts the spectrum to higher energies though the shifting is not rigid and mixes the 1ω and 2ω resonances, and has a strong influence in the line-shape, as for the case of bulk semiconductors. [146, 147, 161] The cut function allows us to extract unequivocally $\chi_{2 \times 1}^{xxx}(-2\omega; \omega, \omega)$. The effects of the nonlocal part of the pseudopotentials keeps the same line-shape of $|\chi_{2 \times 1}^{xxx}(-2\omega; \omega, \omega)|$, but reduces the value of by 15–20%. The xxx component of $\chi_{2 \times 1}(-2\omega; \omega, \omega)$, can not be experimentally isolated, however in a forthcoming publication we will compare our formulation against experimental results. We have neglected local field and excitonic effects. Although these are important factors in the optical response of a semiconductor, their efficient calculation is theoretically and numerically challenging and still under debate [67]. This merits further study but is beyond the scope of this paper. Nevertheless, the inclusion of aforementioned contributions in our scheme opens the unprecedented possibility to study SSHG with more versatility and more accurate results.

I also revised the 3-layer model for the SSHG yield where the nonlinear polarization, $\mathcal{P}(2\omega)$, and the fundamental fields are taken within a small layer ℓ below the surface of the material. This model reproduces key spectral features and yields an intensity closer to the experiment for all cases of \mathcal{R}_{iF} . We consider it an upgrade over the much reviewed 2-layer model [133], and it comes with

very little added computational expense. Additionally, we have compared these to other models that change the placement of $\mathcal{P}(2\omega)$ and the fundamental fields. Ultimately we consider that the 3-layer model offers the closest comparison to experiment.

This study affords us an interesting view of both the theoretical and experimental aspects of SSHG studies. On the theoretical side, we have shown the importance of using relaxed atomic positions to more accurately calculate the nonlinear susceptibility tensor. The intensity of these spectra is greatly improved when compared to previous works. [3] We also postulate that the lack of local field effects in the theory is a shortcoming, but in this case, it only affects two of the $\chi_{\text{surface}}(-2\omega; \omega, \omega)$ components. Concerning the experiments, we show that surface preparation and quality are important for better results. The approach for calculating the SSHG yield presented here finds closer agreement with surfaces that are freshly prepared with little or no oxidation, and with measurements taken at low temperatures. Overall, this newly implemented framework for calculating $\chi_{\text{surface}}(-2\omega; \omega, \omega)$ and \mathcal{R} focused on the Si(001)2 × 1 and Si(111)(1×1):H surfaces provides a compelling benchmark for SSHG studies. We are confident that this work can be applied directly to many other surfaces of interest.

Chapter 5

Final Remarks

I have presented a formulation to calculate the surface second-harmonic (SSH) susceptibility tensor $\chi_{\text{surface}}(-2\omega; \omega, \omega)$, using the length gauge formalism and within the independent particle approximation (IPA). It includes on equal footing: (i) the scissors correction, (ii) the contribution of the non-local part of the pseudopotentials, and (iii) the cut function. I also revised the 3-layer model for the SSHG yield including the effects of multiple reflections from both the SH and fundamental fields. In this 3-layer model, the nonlinear polarization, $\mathcal{P}(2\omega)$, and the fundamental fields are taken within a small layer ℓ below the surface of the material. This model reproduces key spectral features and yields an intensity closer to the experiment for all cases of \mathcal{R}_{iF} . I consider it an improvement over the much reviewed 2-layer model [133], and it comes with very little added computational expense. Additionally, we have compared these two models with other models where both $\mathcal{P}(2\omega)$ and the fundamental fields are evaluated at different regions inside the material.

We have used a Si(001)2 \times 1 surface to confirm that our scheme correctly obtains the surface response as we confirm that $\chi_{\text{half-slab}}^{xxx}(-2\omega; \omega, \omega) \approx \chi_{\text{full-slab}}^{xxx}(-2\omega; \omega, \omega)$. Although one can in principle increase the number of atomic layers, \mathbf{k} -points, etc. to improve even further on the similarity of the half-slab and full-slab results, we have chosen a good compromise between accuracy and the burden and time of the computations. We describe the effect of the independent inclusion of the three effects mentioned above in the calculation of $\chi_{\text{surface}}(-2\omega; \omega, \omega)$. The scissors correction shifts the spectrum to higher energies though the shifting is not rigid and mixes the 1ω and 2ω resonances, and has a strong influence in the line-shape, as for the case of bulk semiconductors [146, 147, 161]. The cut function allows us to extract unequivocally $\chi_{2\times 1}^{xxx}(-2\omega; \omega, \omega)$. The effects of the nonlocal part of the pseudopotentials keeps the same line-shape of $|\chi_{2\times 1}^{xxx}(-2\omega; \omega, \omega)|$, but reduces the value of by 15-20%.

I then calculated the SSHG yield for the Si(111)(1 \times 1):H surface, which is experimentally well characterized. This study affords us an interesting view of both the theoretical and experimental aspects of SSHG studies. On the theoretical side, we have shown the importance of using relaxed atomic positions to more accurately calculate the nonlinear susceptibility tensor. The intensity of these spectra is greatly improved when compared to previous works [3]. Concerning the experiments, we show that surface preparation and quality are important for better results. The approach for calculating the SSHG yield presented here finds closer agreement with surfaces that are freshly prepared with little or no oxidation, and with measurements taken at low temperatures. We have neglected local field and excitonic effects. Although these are important factors in the optical response of a semiconductor, their efficient calculation is theoretically and numer-

ically challenging and still under debate [67]. This merits further study but is beyond the scope of this thesis. Nevertheless, the inclusion of aforementioned contributions in our scheme opens the unprecedented possibility to study surface SHG with more versatility and more accurate results. Overall, this newly implemented framework for calculating $\chi_{\text{surface}}(-2\omega; \omega, \omega)$ and \mathcal{R} focused on the Si(001)2 × 1 and Si(111)(1×1):H surfaces provides a compelling benchmark for SSHG studies. I am confident that this work can be applied directly to many other surfaces of interest.

Appendix A

Supplementary Derivations for the Nonlinear Surface Susceptibility

Outline

A.1	\mathbf{r}_e and \mathbf{r}_i	72
A.2	Matrix elements of $\mathbf{v}_{nm}^{\text{nl}}(\mathbf{k})$ and $\mathcal{V}_{nm}^{\text{nl},\ell}(\mathbf{k})$	75
A.3	Explicit expressions for $\mathcal{V}_{nm}^{a,\ell}(\mathbf{k})$ and $\mathcal{C}_{nm}^{\ell}(\mathbf{k})$	79
A.3.1	Time-reversal relations	80
A.4	$\mathcal{V}_{nm}^{\Sigma,a,\ell}$ and $(\mathcal{V}_{nm}^{\Sigma,a,\ell})_{;k^b}$	81
A.5	Generalized derivative $(\omega_n(\mathbf{k}))_{;\mathbf{k}}$	83
A.6	Expressions for $\chi_{\text{surface}}^{\text{abc}}$ in terms of $\mathcal{V}_{mn}^{\Sigma,a,\ell}$	83
A.6.1	Intraband Contributions	84
A.6.2	Interband Contributions	87
A.7	Generalized derivative $(\mathbf{r}_{nm}(\mathbf{k}))_{;\mathbf{k}}$ for nonlocal potentials	89
A.7.1	Case $n = m$	91
A.7.2	Case $n \neq m$	91
A.7.3	Layer Case	91
A.8	Matrix elements of $\tau_{nm}^{\text{ab}}(\mathbf{k})$	92
A.9	Scissors renormalization for $\mathcal{V}_{nm}^{\Sigma}$	94

A.1 \mathbf{r}_e and \mathbf{r}_i

In this appendix, we derive the expressions for the matrix elements of the electron position operator \mathbf{r} . The r representation of the Bloch states is given by

$$\psi_{n\mathbf{k}}(\mathbf{r}) = \langle \mathbf{r} | n\mathbf{k} \rangle = \sqrt{\frac{\Omega}{8\pi^3}} e^{i\mathbf{k}\cdot\mathbf{r}} u_{n\mathbf{k}}(\mathbf{r}), \quad (\text{A.1})$$

where $u_{n\mathbf{k}}(\mathbf{r}) = u_{n\mathbf{k}}(\mathbf{r} + \mathbf{R})$ is cell periodic, and

$$\int_{\Omega} u_{n\mathbf{k}}^*(\mathbf{r}) u_{m\mathbf{k}'}(\mathbf{r}) d^3r = \delta_{nm} \delta_{\mathbf{k}, \mathbf{k}'}, \quad (\text{A.2})$$

and Ω is the unit cell volume.

The key ingredient in the calculation are the matrix elements of the position operator \mathbf{r} . We start from the basic relation

$$\langle n\mathbf{k}|m\mathbf{k}' \rangle = \delta_{nm} \delta(\mathbf{k} - \mathbf{k}'), \quad (\text{A.3})$$

and take its derivative with respect to \mathbf{k} as follows. On one hand,

$$\frac{\partial}{\partial \mathbf{k}} \langle n\mathbf{k}|m\mathbf{k}' \rangle = \delta_{nm} \frac{\partial}{\partial \mathbf{k}} \delta(\mathbf{k} - \mathbf{k}'), \quad (\text{A.4})$$

and on the other,

$$\frac{\partial}{\partial \mathbf{k}} \langle n\mathbf{k}|m\mathbf{k}' \rangle = \frac{\partial}{\partial \mathbf{k}} \int \langle n\mathbf{k}|\mathbf{r} \rangle \langle \mathbf{r}|m\mathbf{k}' \rangle d\mathbf{r} = \int \left(\frac{\partial}{\partial \mathbf{k}} \psi_{n\mathbf{k}}^*(\mathbf{r}) \right) \psi_{m\mathbf{k}'}(\mathbf{r}) d\mathbf{r}. \quad (\text{A.5})$$

The derivative of the wavefunction is simply given by

$$\frac{\partial}{\partial \mathbf{k}} \psi_{n\mathbf{k}}^*(\mathbf{r}) = \sqrt{\frac{\Omega}{8\pi^3}} \left(\frac{\partial}{\partial \mathbf{k}} u_{n\mathbf{k}}^*(\mathbf{r}) \right) e^{-i\mathbf{k}\cdot\mathbf{r}} - i\mathbf{r} \psi_{n\mathbf{k}}^*(\mathbf{r}). \quad (\text{A.6})$$

Substituting into Eq. (A.5), we obtain

$$\begin{aligned} \frac{\partial}{\partial \mathbf{k}} \langle n\mathbf{k}|m\mathbf{k}' \rangle &= \sqrt{\frac{\Omega}{8\pi^3}} \int \left(\frac{\partial}{\partial \mathbf{k}} u_{n\mathbf{k}}^*(\mathbf{r}) \right) e^{-i\mathbf{k}\cdot\mathbf{r}} \psi_{m\mathbf{k}'}(\mathbf{r}) d\mathbf{r} - i \int \psi_{n\mathbf{k}}^*(\mathbf{r}) \mathbf{r} \psi_{m\mathbf{k}'}(\mathbf{r}) d\mathbf{r} \\ &= \frac{\Omega}{8\pi^3} \int e^{-i(\mathbf{k}-\mathbf{k}')\cdot\mathbf{r}} \left(\frac{\partial}{\partial \mathbf{k}} u_{n\mathbf{k}}^*(\mathbf{r}) \right) u_{m\mathbf{k}'}(\mathbf{r}) d\mathbf{r} - i \langle n\mathbf{k}|\hat{\mathbf{r}}|m\mathbf{k}' \rangle. \end{aligned} \quad (\text{A.7})$$

Restricting \mathbf{k} and \mathbf{k}' to the first Brillouin zone, we use the following result that is valid for any periodic function $f(\mathbf{r}) = f(\mathbf{r} + \mathbf{R})$,

$$\int e^{i(\mathbf{q}-\mathbf{k})\cdot\mathbf{r}} f(\mathbf{r}) d^3r = \frac{8\pi^3}{\Omega} \delta(\mathbf{q} - \mathbf{k}) \int_{\Omega} f(\mathbf{r}) d^3r, \quad (\text{A.8})$$

to finally write [120]

$$\frac{\partial}{\partial \mathbf{k}} \langle n\mathbf{k}|m\mathbf{k}' \rangle = \delta(\mathbf{k} - \mathbf{k}') \int_{\Omega} \left(\frac{\partial}{\partial \mathbf{k}} u_{n\mathbf{k}}^*(\mathbf{r}) \right) u_{m\mathbf{k}}(\mathbf{r}) d\mathbf{r} - i \langle n\mathbf{k}|\hat{\mathbf{r}}|m\mathbf{k}' \rangle. \quad (\text{A.9})$$

From

$$\int_{\Omega} u_{m\mathbf{k}} u_{n\mathbf{k}}^* d\mathbf{r} = \delta_{nm}, \quad (\text{A.10})$$

we easily find that

$$\int_{\Omega} \left(\frac{\partial}{\partial \mathbf{k}} u_{m\mathbf{k}}(\mathbf{r}) \right) u_{n\mathbf{k}}^*(\mathbf{r}) d\mathbf{r} = - \int_{\Omega} u_{m\mathbf{k}}(\mathbf{r}) \left(\frac{\partial}{\partial \mathbf{k}} u_{n\mathbf{k}}^*(\mathbf{r}) \right) d\mathbf{r}. \quad (\text{A.11})$$

Therefore, we define

$$\boldsymbol{\xi}_{nm}(\mathbf{k}) \equiv i \int_{\Omega} u_{n\mathbf{k}}^*(\mathbf{r}) \nabla_{\mathbf{k}} u_{m\mathbf{k}}(\mathbf{r}) d\mathbf{r}, \quad (\text{A.12})$$

with $\nabla_{\mathbf{k}} = \partial/\partial\mathbf{k}$. Now, from Eqs. (A.4), (A.7), and (A.12), we have that the matrix elements of the position operator of the electron are given by

$$\langle n\mathbf{k} | \hat{\mathbf{r}} | m\mathbf{k}' \rangle = \delta(\mathbf{k} - \mathbf{k}') \boldsymbol{\xi}_{nm}(\mathbf{k}) + i\delta_{nm} \nabla_{\mathbf{k}} \delta(\mathbf{k} - \mathbf{k}'), \quad (\text{A.13})$$

Then, from Eq. (A.13) and writing $\hat{\mathbf{r}} = \hat{\mathbf{r}}_e + \hat{\mathbf{r}}_i$, with $\hat{\mathbf{r}}_e$ ($\hat{\mathbf{r}}_i$) the interband (intraband) part, we obtain that

$$\langle n\mathbf{k} | \hat{\mathbf{r}}_i | m\mathbf{k}' \rangle = \delta_{nm} [\delta(\mathbf{k} - \mathbf{k}') \boldsymbol{\xi}_{nn}(\mathbf{k}) + i\nabla_{\mathbf{k}} \delta(\mathbf{k} - \mathbf{k}')], \quad (\text{A.14})$$

$$\langle n\mathbf{k} | \hat{\mathbf{r}}_e | m\mathbf{k}' \rangle = (1 - \delta_{nm}) \delta(\mathbf{k} - \mathbf{k}') \boldsymbol{\xi}_{nm}(\mathbf{k}). \quad (\text{A.15})$$

To proceed, we relate Eq. (A.15) to the matrix elements of the momentum operator as follows. For the intraband part, we derive the following general result,

$$\begin{aligned} \langle n\mathbf{k} | [\hat{\mathbf{r}}_i, \hat{O}] | m\mathbf{k}' \rangle &= \sum_{\ell, \mathbf{k}''} \left(\langle n\mathbf{k} | \hat{\mathbf{r}}_i | \ell\mathbf{k}'' \rangle \langle \ell\mathbf{k}'' | \hat{O} | m\mathbf{k}' \rangle - \langle n\mathbf{k} | \hat{O} | \ell\mathbf{k}'' \rangle \langle \ell\mathbf{k}'' | \hat{\mathbf{r}}_i | m\mathbf{k}' \rangle \right) \\ &= \sum_{\ell} \left(\langle n\mathbf{k} | \hat{\mathbf{r}}_i | \ell\mathbf{k}' \rangle \mathcal{O}_{\ell m}(\mathbf{k}') - \mathcal{O}_{n\ell}(\mathbf{k}) \langle \ell\mathbf{k} | \hat{\mathbf{r}}_i | m\mathbf{k}' \rangle \right), \end{aligned} \quad (\text{A.16})$$

where we have taken $\langle n\mathbf{k} | \hat{O} | \ell\mathbf{k}'' \rangle = \delta(\mathbf{k} - \mathbf{k}'') \mathcal{O}_{n\ell}(\mathbf{k})$. We substitute Eq. (A.14) to obtain

$$\begin{aligned} \sum_{\ell} (\delta_{n\ell} [\delta(\mathbf{k} - \mathbf{k}') \boldsymbol{\xi}_{nn}(\mathbf{k}) + i\nabla_{\mathbf{k}} \delta(\mathbf{k} - \mathbf{k}')]) \mathcal{O}_{\ell m}(\mathbf{k}') - \mathcal{O}_{n\ell}(\mathbf{k}) \delta_{\ell m} [\delta(\mathbf{k} - \mathbf{k}') \boldsymbol{\xi}_{mm}(\mathbf{k}) + i\nabla_{\mathbf{k}} \delta(\mathbf{k} - \mathbf{k}')] \\ = ([\delta(\mathbf{k} - \mathbf{k}') \boldsymbol{\xi}_{nn}(\mathbf{k}) + i\nabla_{\mathbf{k}} \delta(\mathbf{k} - \mathbf{k}')]) \mathcal{O}_{nm}(\mathbf{k}') - \mathcal{O}_{nm}(\mathbf{k}) [\delta(\mathbf{k} - \mathbf{k}') \boldsymbol{\xi}_{mm}(\mathbf{k}) + i\nabla_{\mathbf{k}} \delta(\mathbf{k} - \mathbf{k}')] \\ = \delta(\mathbf{k} - \mathbf{k}') \mathcal{O}_{nm}(\mathbf{k}) (\boldsymbol{\xi}_{nn}(\mathbf{k}) - \boldsymbol{\xi}_{mm}(\mathbf{k})) + i\mathcal{O}_{nm}(\mathbf{k}') \nabla_{\mathbf{k}} \delta(\mathbf{k} - \mathbf{k}') \\ + i\delta(\mathbf{k} - \mathbf{k}') \nabla_{\mathbf{k}} \mathcal{O}_{nm}(\mathbf{k}) - i\mathcal{O}_{nm}(\mathbf{k}') \nabla_{\mathbf{k}} \delta(\mathbf{k} - \mathbf{k}') \\ = i\delta(\mathbf{k} - \mathbf{k}') (\nabla_{\mathbf{k}} \mathcal{O}_{nm}(\mathbf{k}) - i\mathcal{O}_{nm}(\mathbf{k}) (\boldsymbol{\xi}_{nn}(\mathbf{k}) - \boldsymbol{\xi}_{mm}(\mathbf{k}))) \\ \equiv i\delta(\mathbf{k} - \mathbf{k}') (\mathcal{O}_{nm})_{;\mathbf{k}}. \end{aligned} \quad (\text{A.17})$$

Then,

$$\langle n\mathbf{k} | [\hat{\mathbf{r}}_i, \hat{O}] | m\mathbf{k}' \rangle = i\delta(\mathbf{k} - \mathbf{k}') (\mathcal{O}_{nm})_{;\mathbf{k}}, \quad (\text{A.18})$$

where

$$(\mathcal{O}_{nm})_{;\mathbf{k}} = \nabla_{\mathbf{k}} \mathcal{O}_{nm}(\mathbf{k}) - i\mathcal{O}_{nm}(\mathbf{k}) (\boldsymbol{\xi}_{nn}(\mathbf{k}) - \boldsymbol{\xi}_{mm}(\mathbf{k})), \quad (\text{A.19})$$

is the generalized derivative of \mathcal{O}_{nm} with respect to \mathbf{k} . Note that the highly singular term $\nabla_{\mathbf{k}} \delta(\mathbf{k} - \mathbf{k}')$ cancels in Eq. (A.17), thus giving a well defined commutator of the intraband position operator with any arbitrary operator \hat{O} .

A.2 Matrix elements of $\mathbf{v}_{nm}^{\text{nl}}(\mathbf{k})$ and $\mathcal{V}_{nm}^{\text{nl},\ell}(\mathbf{k})$

From Eq. (2.41), we have that

$$\begin{aligned}\mathbf{v}_{nm}^{\text{nl}}(\mathbf{k}) &= \langle n\mathbf{k} | \hat{\mathbf{v}}^{\text{nl}} | m\mathbf{k}' \rangle = \frac{i}{\hbar} \langle n\mathbf{k} | [\hat{V}^{\text{nl}}, \hat{\mathbf{r}}] | m\mathbf{k}' \rangle \\ &= \frac{i}{\hbar} \int \langle n\mathbf{k} | \mathbf{r} \rangle \langle \mathbf{r} | [\hat{V}^{\text{nl}}, \hat{\mathbf{r}}] | \mathbf{r}' \rangle \langle \mathbf{r}' | m\mathbf{k}' \rangle d\mathbf{r} d\mathbf{r}' \\ &= \frac{i}{\hbar} \delta(\mathbf{k} - \mathbf{k}') \int \psi_{n\mathbf{k}}^*(\mathbf{r}) \langle \mathbf{r} | [\hat{V}^{\text{nl}}, \hat{\mathbf{r}}] | \mathbf{r}' \rangle \psi_{m\mathbf{k}'}(\mathbf{r}') d\mathbf{r} d\mathbf{r}',\end{aligned}\quad (\text{A.20})$$

where $\mathbf{k} = \mathbf{k}'$ due to the fact that the integrand is periodic in real space, and \mathbf{k} is restricted to the Brillouin Zone. Now,

$$\begin{aligned}\langle \mathbf{r} | [\hat{V}^{\text{nl}}, \hat{\mathbf{r}}] | \mathbf{r}' \rangle &= \langle \mathbf{r} | \hat{V}^{\text{nl}} \hat{\mathbf{r}} - \hat{\mathbf{r}} \hat{V}^{\text{nl}} | \mathbf{r}' \rangle = \langle \mathbf{r} | \hat{V}^{\text{nl}} \hat{\mathbf{r}} | \mathbf{r}' \rangle - \langle \mathbf{r} | \hat{\mathbf{r}} \hat{V}^{\text{nl}} | \mathbf{r}' \rangle \\ &= \langle \mathbf{r} | \hat{V}^{\text{nl}} \mathbf{r}' | \mathbf{r}' \rangle - \langle \mathbf{r} | \mathbf{r} \hat{V}^{\text{nl}} | \mathbf{r}' \rangle = \langle \mathbf{r} | \hat{V}^{\text{nl}} | \mathbf{r}' \rangle (\mathbf{r}' - \mathbf{r}) = V^{\text{nl}}(\mathbf{r}, \mathbf{r}') (\mathbf{r}' - \mathbf{r}),\end{aligned}\quad (\text{A.21})$$

where we used $\hat{r}\langle \mathbf{r} | = r\langle \mathbf{r} |$, $\langle \mathbf{r}' | \hat{r} = \langle \mathbf{r}' | r'$, and $V^{\text{nl}}(\mathbf{r}, \mathbf{r}') = \langle \mathbf{r} | \hat{V}^{\text{nl}} | \mathbf{r}' \rangle$ (Eq. (2.26)). Also, we have the following identity which will be used shortly,

$$\begin{aligned}(\nabla_{\mathbf{K}} + \nabla_{\mathbf{K}'}) \frac{1}{\Omega} \int e^{-i\mathbf{K}\cdot\mathbf{r}} V^{\text{nl}}(\mathbf{r}, \mathbf{r}') e^{i\mathbf{K}'\cdot\mathbf{r}'} d\mathbf{r} d\mathbf{r}' &= -i \frac{1}{\Omega} \int e^{-i\mathbf{K}\cdot\mathbf{r}} \left(\mathbf{r} V^{\text{nl}}(\mathbf{r}, \mathbf{r}') - V^{\text{nl}}(\mathbf{r}, \mathbf{r}') \mathbf{r} \right) e^{i\mathbf{K}'\cdot\mathbf{r}'} d\mathbf{r} d\mathbf{r}' \\ (\nabla_{\mathbf{K}} + \nabla_{\mathbf{K}'}) \langle \mathbf{K} | V^{\text{nl}} | \mathbf{K}' \rangle &= \frac{i}{\Omega} \int e^{-i\mathbf{K}\cdot\mathbf{r}} V^{\text{nl}}(\mathbf{r}, \mathbf{r}') (\mathbf{r}' - \mathbf{r}) e^{i\mathbf{K}'\cdot\mathbf{r}'} d\mathbf{r} d\mathbf{r}',\end{aligned}\quad (\text{A.22})$$

where Ω is the volume of the unit cell, and we defined

$$V^{\text{nl}}(\mathbf{K}, \mathbf{K}') \equiv \langle \mathbf{K} | V^{\text{nl}} | \mathbf{K}' \rangle = \frac{1}{\Omega} \int e^{-i\mathbf{K}\cdot\mathbf{r}} V^{\text{nl}}(\mathbf{r}, \mathbf{r}') e^{i\mathbf{K}'\cdot\mathbf{r}'} d\mathbf{r} d\mathbf{r}',\quad (\text{A.23})$$

where $V^{\text{nl}}(\mathbf{K}', \mathbf{K}) = V^{\text{nl}*}(\mathbf{K}, \mathbf{K}')$, since $V^{\text{nl}}(\mathbf{r}', \mathbf{r}) = V^{\text{nl}*}(\mathbf{r}, \mathbf{r}')$ due to the fact that \hat{V}^{nl} is a hermitian operator. Using the plane wave expansion

$$\langle \mathbf{r} | n\mathbf{k} \rangle = \psi_{n\mathbf{k}}(\mathbf{r}) = \frac{1}{\sqrt{\Omega}} \sum_{\mathbf{G}} A_{n\mathbf{k}}(\mathbf{G}) e^{i\mathbf{K}\cdot\mathbf{r}},\quad (\text{A.24})$$

with $\mathbf{K} = \mathbf{k} + \mathbf{G}$, we obtain from Eq. (A.20) and Eq. (A.22), that

$$\begin{aligned}\mathbf{v}_{nm}^{\text{nl}}(\mathbf{k}) &= \frac{i}{\hbar} \delta(\mathbf{k} - \mathbf{k}') \sum_{\mathbf{G}, \mathbf{G}'} A_{n\mathbf{k}}^*(\mathbf{G}) A_{m\mathbf{k}'}(\mathbf{G}') \frac{1}{\Omega} \int d\mathbf{r} d\mathbf{r}' e^{-i\mathbf{K}\cdot\mathbf{r}} \langle \mathbf{r} | [\hat{V}^{\text{nl}}, \hat{\mathbf{r}}] | \mathbf{r}' \rangle e^{i\mathbf{K}'\cdot\mathbf{r}'} \\ &= \frac{1}{\hbar} \delta(\mathbf{k} - \mathbf{k}') \sum_{\mathbf{G}, \mathbf{G}'} A_{n\mathbf{k}}^*(\mathbf{G}) A_{m\mathbf{k}'}(\mathbf{G}') \frac{i}{\Omega} \int d\mathbf{r} d\mathbf{r}' e^{-i\mathbf{K}\cdot\mathbf{r}} V^{\text{nl}}(\mathbf{r}, \mathbf{r}') (\mathbf{r}' - \mathbf{r}) e^{i\mathbf{K}'\cdot\mathbf{r}'} \\ &= \frac{1}{\hbar} \delta(\mathbf{k} - \mathbf{k}') \sum_{\mathbf{G}, \mathbf{G}'} A_{n\mathbf{k}}^*(\mathbf{G}) A_{m\mathbf{k}'}(\mathbf{G}') (\nabla_{\mathbf{K}} + \nabla_{\mathbf{K}'}) V^{\text{nl}}(\mathbf{K}, \mathbf{K}').\end{aligned}\quad (\text{A.25})$$

For fully separable pseudopotentials in the Kleinman-Bylander (KB) form, [122–124] the matrix elements $\langle \mathbf{K} | V^{\text{nl}} | \mathbf{K}' \rangle = V^{\text{nl}}(\mathbf{K}, \mathbf{K}')$ can be readily calculated. [122] Indeed, the Fourier representa-

tion assumes the form, [124, 162, 163]

$$\begin{aligned} V_{\text{KB}}^{\text{nl}}(\mathbf{K}, \mathbf{K}') &= \sum_s e^{i(\mathbf{K}-\mathbf{K}') \cdot \boldsymbol{\tau}_s} \sum_{l=0}^{l_s} \sum_{m=-l}^l E_l F_{lm}^s(\mathbf{K}) F_{lm}^{s*}(\mathbf{K}') \\ &= \sum_s \sum_{l=0}^{l_s} \sum_{m=-l}^l E_l f_{lm}^s(\mathbf{K}) f_{lm}^{s*}(\mathbf{K}'), \end{aligned} \quad (\text{A.26})$$

with $f_{lm}^s(\mathbf{K}) = e^{i\mathbf{K} \cdot \boldsymbol{\tau}_s} F_{lm}^s(\mathbf{K})$, and

$$F_{lm}^s(\mathbf{K}) = \int d\mathbf{r} e^{-i\mathbf{K} \cdot \mathbf{r}} \delta V_l^S(\mathbf{r}) \Phi_{lm}^{\text{ps}}(\mathbf{r}). \quad (\text{A.27})$$

Here $\delta V_l^S(\mathbf{r})$ is the non-local contribution of the ionic pseudopotential centered at the atomic position $\boldsymbol{\tau}_s$ located in the unit cell, $\Phi_{lm}^{\text{ps}}(\mathbf{r})$ is the pseudo-wavefunction of the corresponding atom, while E_l is the so called Kleinman-Bylander energy. Further details can be found in Ref. [163]. From Eq. (A.26) we find

$$\begin{aligned} (\nabla_{\mathbf{K}} + \nabla_{\mathbf{K}'}) V_{\text{KB}}^{\text{nl}}(\mathbf{K}, \mathbf{K}') &= \sum_s \sum_{l=0}^{l_s} \sum_{m=-l}^l E_l (\nabla_{\mathbf{K}} + \nabla_{\mathbf{K}'}) f_{lm}^s(\mathbf{K}) f_{lm}^{s*}(\mathbf{K}') \\ &= \sum_s \sum_{l=0}^{l_s} \sum_{m=-l}^l E_l ([\nabla_{\mathbf{K}} f_{lm}^s(\mathbf{K})] f_{lm}^{s*}(\mathbf{K}') + f_{lm}^s(\mathbf{K}) [\nabla_{\mathbf{K}'} f_{lm}^{s*}(\mathbf{K}')]), \end{aligned} \quad (\text{A.28})$$

and using this in Eq. (A.25) leads to

$$\begin{aligned} \mathbf{v}_{nm}^{\text{nl}}(\mathbf{k}) &= \frac{1}{\hbar} \sum_s \sum_{l=0}^{l_s} \sum_{m=-l}^l E_l \sum_{\mathbf{G}\mathbf{G}'} A_{n,\vec{k}}^*(\mathbf{G}) A_{n',\vec{k}}(\mathbf{G}') \times (\nabla_{\mathbf{K}} f_{lm}^s(\mathbf{K}) f_{lm}^{s*}(\mathbf{K}') + f_{lm}^s(\mathbf{K}) \nabla_{\mathbf{K}'} f_{lm}^{s*}(\mathbf{K}')) \\ &= \frac{1}{\hbar} \sum_s \sum_{l=0}^{l_s} \sum_{m=-l}^l E_l \left[\left(\sum_{\mathbf{G}} A_{n,\vec{k}}^*(\mathbf{G}) \nabla_{\mathbf{K}} f_{lm}^s(\mathbf{K}) \right) \left(\sum_{\mathbf{G}'} A_{n',\vec{k}}(\mathbf{G}') f_{lm}^{s*}(\mathbf{K}') \right) \right. \\ &\quad \left. + \left(\sum_{\mathbf{G}} A_{n,\vec{k}}^*(\mathbf{G}) f_{lm}^s(\mathbf{K}) \right) \left(\sum_{\mathbf{G}'} A_{n',\vec{k}}(\mathbf{G}') \nabla_{\mathbf{K}'} f_{lm}^{s*}(\mathbf{K}') \right) \right], \end{aligned} \quad (\text{A.29})$$

where there are only single sums over \mathbf{G} . The above equation is implemented in the DP code [139].

Now we derive $\mathbf{v}_{nm}^{\text{nl},\ell}(\mathbf{k})$. First we prove that

$$\sum_{\mathbf{G}} |\mathbf{k} + \mathbf{G}\rangle \langle \mathbf{k} + \mathbf{G}| = 1. \quad (\text{A.30})$$

Proof:

$$\langle n\mathbf{k}|1|n'\mathbf{k}\rangle = \delta_{nn'}, \quad (\text{A.31})$$

take

$$\begin{aligned}
\sum_{\mathbf{G}} \langle n\mathbf{k} || \mathbf{k} + \mathbf{G} \rangle \langle \mathbf{k} + \mathbf{G} || n'\mathbf{k} \rangle &= \int d\mathbf{r} d\mathbf{r}' \sum_{\mathbf{G}} \langle n\mathbf{k} || \mathbf{r} \rangle \langle \mathbf{r} || \mathbf{k} + \mathbf{G} \rangle \langle \mathbf{k} + \mathbf{G} || \mathbf{r}' \rangle \langle \mathbf{r}' || n'\mathbf{k} \rangle \\
&= \int d\mathbf{r} d\mathbf{r}' \sum_{\mathbf{G}} \psi_{n\mathbf{k}}^*(\mathbf{r}) \frac{1}{\sqrt{\Omega}} e^{i(\mathbf{k}+\mathbf{G}) \cdot \mathbf{r}} \frac{1}{\sqrt{\Omega}} e^{-i(\mathbf{k}+\mathbf{G}) \cdot \mathbf{r}'} \psi_{m\mathbf{k}}(\mathbf{r}') \\
&= \int d\mathbf{r} d\mathbf{r}' \psi_{n\mathbf{k}}^*(\mathbf{r}) \psi_{m\mathbf{k}}(\mathbf{r}') \frac{1}{V} \sum_{\mathbf{G}} e^{i(\mathbf{k}+\mathbf{G}) \cdot (\mathbf{r}-\mathbf{r}')} \\
&= \int d\mathbf{r} d\mathbf{r}' \psi_{n\mathbf{k}}^*(\mathbf{r}) \psi_{m\mathbf{k}}(\mathbf{r}') \delta(\mathbf{r} - \mathbf{r}') = \int d\mathbf{r} \psi_{n\mathbf{k}}^*(\mathbf{r}) \psi_{m\mathbf{k}}(\mathbf{r}) = \delta_{nn'},
\end{aligned} \tag{A.32}$$

and thus Eq. (A.30) follows. We used

$$\langle \mathbf{r} | \mathbf{k} + \mathbf{G} \rangle = \frac{1}{\sqrt{\Omega}} e^{i(\mathbf{k}+\mathbf{G}) \cdot \mathbf{r}}. \tag{A.33}$$

From Eq. (2.69), we would like to calculate

$$\mathcal{V}_{nm}^{\text{nl},\ell}(\mathbf{k}) = \frac{1}{2} \langle n\mathbf{k} | C^\ell(z) \mathbf{v}^{\text{nl}} + \mathbf{v}^{\text{nl}} C^\ell(z) | m\mathbf{k} \rangle. \tag{A.34}$$

We work out the first term on the right hand side,

$$\begin{aligned}
\langle n\mathbf{k} | C^\ell(z) \mathbf{v}^{\text{nl}} | m\mathbf{k} \rangle &= \sum_{\mathbf{G}} \langle n\mathbf{k} | C^\ell(z) | \mathbf{k} + \mathbf{G} \rangle \langle \mathbf{k} + \mathbf{G} | \mathbf{v}^{\text{nl}} | m\mathbf{k} \rangle \\
&= \sum_{\mathbf{G}} \int d\mathbf{r} \int d\mathbf{r}' \langle n\mathbf{k} || \mathbf{r} \rangle \langle \mathbf{r} | C^\ell(z) | \mathbf{r}' \rangle \langle \mathbf{r}' || \mathbf{k} + \mathbf{G} \rangle \\
&\quad \times \int d\mathbf{r}'' \int d\mathbf{r}''' \langle \mathbf{k} + \mathbf{G} | \mathbf{r}'' \rangle \langle \mathbf{r}'' | \mathbf{v}^{\text{nl}} | \mathbf{r}''' \rangle \langle \mathbf{r}''' || m\mathbf{k} \rangle \\
&= \sum_{\mathbf{G}} \int d\mathbf{r} \int d\mathbf{r}' \langle n\mathbf{k} | \mathbf{r} \rangle C^\ell(z) \delta(\mathbf{r} - \mathbf{r}') \langle \mathbf{r}' | \mathbf{k} + \mathbf{G} \rangle \\
&\quad \times \int d\mathbf{r}'' \int d\mathbf{r}''' \langle \mathbf{k} + \mathbf{G} | \mathbf{r}'' \rangle \langle \mathbf{r}'' | \mathbf{v}^{\text{nl}} | \mathbf{r}''' \rangle \langle \mathbf{r}''' || m\mathbf{k} \rangle \\
&= \sum_{\mathbf{G}} \int d\mathbf{r} \langle n\mathbf{k} | \mathbf{r} \rangle C^\ell(z) \langle \mathbf{r} | \mathbf{k} + \mathbf{G} \rangle \\
&\quad \times \frac{i}{\hbar} \int d\mathbf{r}'' \int d\mathbf{r}''' \langle \mathbf{k} + \mathbf{G} | \mathbf{r}'' \rangle V^{\text{nl}}(\mathbf{r}'', \mathbf{r}''') (\mathbf{r}''' - \mathbf{r}'') \langle \mathbf{r}''' || m\mathbf{k} \rangle,
\end{aligned} \tag{A.35}$$

where we used Eq. (A.21) and (2.41). We use Eq. (A.24), (A.33) and (A.22) to obtain

$$\begin{aligned}
\langle n\mathbf{k} | C^\ell(z) \mathbf{v}^{\text{nl}} | m\mathbf{k} \rangle &= \sum_{\mathbf{G}} \sum_{\mathbf{G}'} A_{n\mathbf{k}}^*(\mathbf{G}') \frac{1}{\Omega} \int d\mathbf{r} e^{-i(\mathbf{k}+\mathbf{G}') \cdot \mathbf{r}} C^\ell(z) e^{i(\mathbf{k}+\mathbf{G}) \cdot \mathbf{r}} \\
&\quad \times \sum_{\mathbf{G}''} A_{m\mathbf{k}}(\mathbf{G}'') \frac{i}{\hbar \Omega} \int d\mathbf{r}'' \int d\mathbf{r}''' e^{-i(\mathbf{k}+\mathbf{G}) \cdot \mathbf{r}''} V^{\text{nl}}(\mathbf{r}'', \mathbf{r}''') (\mathbf{r}''' - \mathbf{r}'') e^{i(\mathbf{k}+\mathbf{G}'') \cdot \mathbf{r}'''} \\
&= \frac{1}{\hbar} \sum_{\mathbf{G}} \sum_{\mathbf{G}'} A_{n\mathbf{k}}^*(\mathbf{G}') \delta_{\mathbf{G}\parallel\mathbf{G}'\parallel} f_\ell(\mathbf{G}_\perp - \mathbf{G}'_\perp) \sum_{\mathbf{G}''} A_{m\mathbf{k}}(\mathbf{G}'') (\nabla_{\mathbf{K}} + \nabla_{\mathbf{K}''}) V^{\text{nl}}(\mathbf{K}, \mathbf{K}''),
\end{aligned} \tag{A.36}$$

where

$$\frac{1}{\Omega} \int d\mathbf{r} C^\ell(z) e^{i(\mathbf{G}-\mathbf{G}') \cdot \mathbf{r}} = \delta_{\mathbf{G}_\parallel \mathbf{G}'_\parallel} f_\ell(\mathbf{G}_\perp - \mathbf{G}'_\perp), \quad (\text{A.37})$$

and

$$f_\ell(g) = \frac{1}{L} \int_{z_\ell - \Delta_\ell^b}^{z_\ell + \Delta_\ell^f} e^{igz} dz, \quad (\text{A.38})$$

where $f^*(g) = f(-g)$. We define

$$\mathcal{F}_{n\mathbf{k}}^\ell(\mathbf{G}) = \sum_{\mathbf{G}'} A_{n\mathbf{k}}(\mathbf{G}') \delta_{\mathbf{G}_\parallel \mathbf{G}'_\parallel} f_\ell(\mathbf{G}'_\perp - \mathbf{G}_\perp), \quad (\text{A.39})$$

and

$$\mathcal{H}_{n\mathbf{k}}(\mathbf{G}) = \sum_{\mathbf{G}'} A_{n\mathbf{k}}(\mathbf{G}') (\nabla_{\mathbf{K}} + \nabla_{\mathbf{K}'}) V^{\text{nl}}(\mathbf{K}, \mathbf{K}'), \quad (\text{A.40})$$

thus we can compactly write,

$$\langle n\mathbf{k}|C^\ell(z)\mathbf{v}^{\text{nl}}|m\mathbf{k}\rangle = \frac{1}{\hbar} \sum_{\mathbf{G}} \mathcal{F}_{n\mathbf{k}}^{\ell*}(\mathbf{G}) \mathcal{H}_{m\mathbf{k}}(\mathbf{G}). \quad (\text{A.41})$$

Now, the second term of Eq. (A.34)

$$\begin{aligned} \langle n\mathbf{k}|\mathbf{v}^{\text{nl}}C^\ell(z)|m\mathbf{k}\rangle &= \sum_{\mathbf{G}} \langle n\mathbf{k}|\mathbf{v}^{\text{nl}}|\mathbf{k} + \mathbf{G}\rangle \langle \mathbf{k} + \mathbf{G}|C^\ell(z)|m\mathbf{k}\rangle \\ &= \sum_{\mathbf{G}} \int d\mathbf{r}'' \int d\mathbf{r}''' \langle n\mathbf{k}||\mathbf{r}''\rangle \langle \mathbf{r}''|\mathbf{v}^{\text{nl}}|\mathbf{r}'''\rangle \langle \mathbf{r}'''||\mathbf{k} + \mathbf{G}\rangle \\ &\quad \times \int d\mathbf{r} \int d\mathbf{r}' \langle \mathbf{k} + \mathbf{G}||\mathbf{r}\rangle \langle \mathbf{r}|C^\ell(z)|\mathbf{r}'\rangle \langle \mathbf{r}'||m\mathbf{k}\rangle \\ &= \sum_{\mathbf{G}} \frac{i}{\hbar} \int d\mathbf{r}'' \int d\mathbf{r}''' \langle n\mathbf{k}|\mathbf{r}''\rangle V^{\text{nl}}(\mathbf{r}'', \mathbf{r}''') (\mathbf{r}''' - \mathbf{r}'') \langle \mathbf{r}'''|\mathbf{k} + \mathbf{G}\rangle \\ &\quad \times \int d\mathbf{r} \langle \mathbf{k} + \mathbf{G}|\mathbf{r}\rangle C^\ell(z) \langle \mathbf{r}|m\mathbf{k}\rangle \\ &= \sum_{\mathbf{G}} \sum_{\mathbf{G}'} A_{n\mathbf{k}}^*(\mathbf{G}') \frac{i}{\hbar\Omega} \int d\mathbf{r}'' \int d\mathbf{r}''' e^{-i(\mathbf{k}+\mathbf{G}') \cdot \mathbf{r}''} V^{\text{nl}}(\mathbf{r}'', \mathbf{r}''') (\mathbf{r}''' - \mathbf{r}'') e^{i(\mathbf{k}+\mathbf{G}') \cdot \mathbf{r}''''} \\ &\quad \times \sum_{\mathbf{G}''} A_{m\mathbf{k}}(\mathbf{G}'') \frac{1}{\Omega} \int d\mathbf{r} e^{-i(\mathbf{k}+\mathbf{G}) \cdot \mathbf{r}} C^\ell(z) e^{i(\mathbf{k}+\mathbf{G}'') \cdot \mathbf{r}} \\ &= \frac{1}{\hbar} \sum_{\mathbf{G}} \sum_{\mathbf{G}'} A_{n\mathbf{k}}^*(\mathbf{G}') (\nabla_{\mathbf{K}} + \nabla_{\mathbf{K}'}) V^{\text{nl}}(\mathbf{K}', \mathbf{K}) \\ &\quad \times \sum_{\mathbf{G}''} A_{m\mathbf{k}}(\mathbf{G}'') \delta_{\mathbf{G}_\parallel \mathbf{G}''_\parallel} f_\ell(\mathbf{G}''_\perp - \mathbf{G}_\perp) \\ &= \frac{1}{\hbar} \sum_{\mathbf{G}} \mathcal{H}_{n\mathbf{k}}^*(\mathbf{G}) \mathcal{F}_{m\mathbf{k}}^\ell(\mathbf{G}). \end{aligned} \quad (\text{A.42})$$

Therefore Eq. (A.34) is compactly given by

$$\mathcal{V}_{nm}^{\text{nl},\ell}(\mathbf{k}) = \frac{1}{2\hbar} \sum_{\mathbf{G}} \left(\mathcal{F}_{n\mathbf{k}}^{\ell*}(\mathbf{G}) \mathcal{H}_{m\mathbf{k}}(\mathbf{G}) + \mathcal{H}_{n\mathbf{k}}^*(\mathbf{G}) \mathcal{F}_{m\mathbf{k}}^{\ell}(\mathbf{G}) \right). \quad (\text{A.43})$$

For fully separable pseudopotentials in the Kleinman-Bylander (KB) form [122–124], we can use Eq. (A.28) and evaluate above expression, that we have implemented in the DP code [139]. Explicitly,

$$\begin{aligned} \mathcal{V}_{nm}^{\text{nl},\ell}(\mathbf{k}) &= \frac{1}{2\hbar} \sum_s \sum_{l=0}^{l_s} \sum_{m=-l}^l E_l \\ &\left[\left(\sum_{\mathbf{G}''} \nabla_{\mathbf{G}''} f_{lm}^s(\mathbf{G}'') \sum_{\mathbf{G}} A_{n\mathbf{k}}^*(\mathbf{G}) \delta_{\mathbf{G}'' \parallel \mathbf{G}'' \parallel} f_\ell(G_z - G_z'') \right) \left(\sum_{\mathbf{G}'} A_{m\mathbf{k}}(\mathbf{G}') f_{lm}^{s*}(\mathbf{K}') \right) \right. \\ &+ \left(\sum_{\mathbf{G}''} f_{lm}^s(\mathbf{G}'') \sum_{\mathbf{G}} A_{n\mathbf{k}}^*(\mathbf{G}) \delta_{\mathbf{G}'' \parallel \mathbf{G}'' \parallel} f_\ell(G_z - G_z'') \right) \left(\sum_{\mathbf{G}'} A_{m\mathbf{k}}(\mathbf{G}') \nabla_{\mathbf{K}'} f_{lm}^{s*}(\mathbf{K}') \right) \\ &+ \left(\sum_{\mathbf{G}} A_{n\mathbf{k}}^*(\mathbf{G}) \nabla_{\mathbf{G}} f_{lm}^s(\mathbf{G}) \right) \left(\sum_{\mathbf{G}''} f_{lm}^{s*}(\mathbf{G}'') \sum_{\mathbf{G}'} A_{m\mathbf{k}}(\mathbf{G}') \delta_{\mathbf{G}' \parallel \mathbf{G}'' \parallel} f_\ell(G_z'' - G_z') \right) \\ &\left. + \left(\sum_{\mathbf{G}} A_{n\mathbf{k}}^*(\mathbf{G}) f_{lm}^s(\mathbf{G}) \right) \left(\sum_{\mathbf{G}''} \nabla_{\mathbf{G}''} f_{lm}^{s*}(\mathbf{G}'') \sum_{\mathbf{G}'} A_{m\mathbf{k}}(\mathbf{G}') \delta_{\mathbf{G}' \parallel \mathbf{G}'' \parallel} f_\ell(G_z'' - G_z') \right) \right]. \end{aligned} \quad (\text{A.44})$$

For a full slab calculation, equivalent to a bulk calculation, $C^\ell(z) = 1$ and then $f_\ell(g) = \delta_{g0}$, and Eq. (A.44) reduces to Eq. (A.29).

A.3 Explicit expressions for $\mathcal{V}_{nm}^{a,\ell}(\mathbf{k})$ and $\mathcal{C}_{nm}^\ell(\mathbf{k})$

Expanding the wave function in planewaves, we obtain

$$\psi_{n\mathbf{k}}(\mathbf{r}) = \sum_{\mathbf{G}} A_{n\mathbf{k}}(\mathbf{G}) e^{i(\mathbf{k}+\mathbf{G}) \cdot \mathbf{r}}, \quad (\text{A.45})$$

where $\{\mathbf{G}\}$ are the reciprocal basis vectors satisfying $e^{\mathbf{R} \cdot \mathbf{G}} = 1$, $\{\mathbf{R}\}$ are the translation vectors in real space, and $A_{n\mathbf{k}}(\mathbf{G})$ are the expansion coefficients. Using $m_e \mathbf{v} = -i\hbar \nabla$ into Eqs. (2.70) and (2.68) we obtain [125],

$$\mathcal{V}_{nm}^\ell(\mathbf{k}) = \frac{\hbar}{2m_e} \sum_{\mathbf{G}, \mathbf{G}'} A_{n\mathbf{k}}^*(\mathbf{G}') A_{m\mathbf{k}}(\mathbf{G}) (2\mathbf{k} + \mathbf{G} + \mathbf{G}') \delta_{\mathbf{G} \parallel \mathbf{G}' \parallel} f_\ell(G_\perp - G'_\perp), \quad (\text{A.46})$$

with

$$f_\ell(g) = \frac{1}{L} \int_{z_\ell - \Delta_\ell^b}^{z_\ell + \Delta_\ell^f} e^{igz} dz, \quad (\text{A.47})$$

where the reciprocal lattice vectors \mathbf{G} are decomposed into components parallel to the surface \mathbf{G}_{\parallel} , and perpendicular to the surface $G_{\perp}\hat{z}$, so that $\mathbf{G} = \mathbf{G}_{\parallel} + G_{\perp}\hat{z}$. Likewise we obtain that

$$\begin{aligned}\mathcal{C}_{nm}(\mathbf{k}) &= \int \psi_{n\mathbf{k}}^*(\mathbf{r}) f(z) \psi_{m\mathbf{k}}(\mathbf{r}) d\mathbf{r} \\ &= \sum_{\mathbf{G}, \mathbf{G}'} A_{n\mathbf{k}}^*(\mathbf{G}') A_{m\mathbf{k}}(\mathbf{G}) \int f(z) e^{-i(\mathbf{G}-\mathbf{G}') \cdot \mathbf{r}} d\mathbf{r} \\ &= \sum_{\mathbf{G}, \mathbf{G}'} A_{n\mathbf{k}}^*(\mathbf{G}') A_{m\mathbf{k}}(\mathbf{G}) \underbrace{\int e^{-i(\mathbf{G}_{\parallel}-\mathbf{G}'_{\parallel}) \cdot \mathbf{R}_{\parallel}} d\mathbf{R}_{\parallel}}_{\delta_{\mathbf{G}_{\parallel} \mathbf{G}'_{\parallel}}} \underbrace{\int e^{-i(g-g')z} f(z) dz}_{f_{\ell}(G_{\perp}-G'_{\perp})},\end{aligned}$$

which we can express compactly as,

$$\mathcal{C}_{nm}^{\ell}(\mathbf{k}) = \sum_{\mathbf{G}, \mathbf{G}'} A_{n\mathbf{k}}^*(\mathbf{G}') A_{m\mathbf{k}}(\mathbf{G}) \delta_{\mathbf{G}_{\parallel} \mathbf{G}'_{\parallel}} f_{\ell}(G_{\perp} - G'_{\perp}). \quad (\text{A.48})$$

The double summation over the \mathbf{G} vectors can be efficiently done by creating a pointer array to identify all the plane-wave coefficients associated with the same G_{\parallel} . We take z_{ℓ} at the center of an atom that belongs to layer ℓ , so the equations above give the ℓ -th atomic-layer contribution to the optical response [125].

If $\mathcal{C}^{\ell}(z) = 1$ from Eqs. (A.46) and (A.48), we recover the well known results

$$\begin{aligned}v_{nm}(\mathbf{k}) &= \frac{\hbar}{m_e} \sum_{\mathbf{G}} A_{n\mathbf{k}}^*(\mathbf{G}) A_{m\mathbf{k}}(\mathbf{G})(\mathbf{k} + \mathbf{G}), \\ \mathcal{C}_{nm}^{\ell} &= \delta_{nm},\end{aligned} \quad (\text{A.49})$$

since for this case, $f_{\ell}(g) = \delta_{g0}$.

A.3.1 Time-reversal relations

The following relations hold for time-reversal symmetry.

$$\begin{aligned}A_{n\mathbf{k}}^*(\mathbf{G}) &= A_{n-\mathbf{k}}(\mathbf{G}), \\ \mathbf{P}_{n\ell}(-\mathbf{k}) &= \hbar \sum_{\mathbf{G}} A_{n-\mathbf{k}}^*(\mathbf{G}) A_{\ell-\mathbf{k}}(\mathbf{G})(-\mathbf{k} + \mathbf{G}), \\ (\mathbf{G} \rightarrow -\mathbf{G}) &= -\hbar \sum_{\mathbf{G}} A_{n\mathbf{k}}(\mathbf{G}) A_{\ell\mathbf{k}}^*(\mathbf{G})(\mathbf{k} + \mathbf{G}) = -\mathbf{P}_{\ell n}(\mathbf{k}), \\ \mathcal{C}_{nm}(L; -\mathbf{k}) &= \sum_{\mathbf{G}_{\parallel}, g, g'} A_{n-\mathbf{k}}^*(\mathbf{G}_{\parallel}, g) A_{m-\mathbf{k}}(\mathbf{G}_{\parallel}, g') f_{\ell}(g - g') \\ &= \sum_{\mathbf{G}_{\parallel}, g, g'} A_{n\mathbf{k}}(\mathbf{G}_{\parallel}, g) A_{m\mathbf{k}}^*(\mathbf{G}_{\parallel}, g') f_{\ell}(g - g') \\ &= \mathcal{C}_{mn}(L; \mathbf{k}).\end{aligned}$$

A.4 $\mathcal{V}_{nm}^{\Sigma,a,\ell}$ and $(\mathcal{V}_{nm}^{\Sigma,a,\ell})_{;k^b}$

From Eq. (2.71)

$$(\mathcal{V}_{nm}^{\Sigma,a,\ell})_{;k^b} = (\mathcal{V}_{nm}^{\text{LDA},a,\ell})_{;k^b} + (\mathcal{V}_{nm}^{S,a,\ell})_{;k^b}. \quad (\text{A.50})$$

For the LDA term we have

$$\mathcal{V}_{nm}^{\text{LDA},a,\ell} = \frac{1}{2} (v^{\text{LDA},a} \mathcal{C}^\ell + \mathcal{C}^\ell v^{\text{LDA},a})_{nm} = \frac{1}{2} \sum_q (v_{nq}^{\text{LDA},a} \mathcal{C}_{qm}^\ell + \mathcal{C}_{nq}^\ell v_{qm}^{\text{LDA},a}) \quad (\text{A.51})$$

and

$$\begin{aligned} (\mathcal{V}_{nm}^{\text{LDA},a})_{;k^b} &= \frac{1}{2} \sum_q (v_{nq}^{\text{LDA},a} \mathcal{C}_{qm}^\ell + \mathcal{C}_{nq}^\ell v_{qm}^{\text{LDA},a})_{;k^b} \\ &= \frac{1}{2} \sum_q ((v_{nq}^{\text{LDA},a})_{;k^b} \mathcal{C}_{qm}^\ell + v_{nq}^{\text{LDA},a} (\mathcal{C}_{qm}^\ell)_{;k^b} + (\mathcal{C}_{nq}^\ell)_{;k^b} v_{qm}^{\text{LDA},a} + \mathcal{C}_{nq}^\ell (v_{qm}^{\text{LDA},a})_{;k^b}), \end{aligned} \quad (\text{A.52})$$

where we omit the \mathbf{k} argument in all terms. From Eq. (A.25) we know that $\mathbf{v}_{nm}^{\text{nl}}(\mathbf{k})$ can be readily calculated, and from Sec. A.3, both v_{nm}^a and \mathcal{C}_{nm}^ℓ are also known quantities. Thus, $\mathbf{v}_{nm}^{\text{LDA}}(\mathbf{k})$ is known, and in turn $\mathcal{V}_{nm}^{\text{LDA},a,\ell}$ is also known. For the generalized derivative $(\mathbf{v}_{nm}^{\text{LDA}}(\mathbf{k}))_{;\mathbf{k}}$ we use Eq. (2.45) to write

$$\begin{aligned} (v_{nm}^{\text{LDA},a})_{;k^b} &= i m_e (\omega_{nm}^{\text{LDA}} r_{nm}^a)_{;k^b} \\ &= i m_e (\omega_{nm}^{\text{LDA}})_{;k^b} r_{nm}^a + i m_e \omega_{nm}^{\text{LDA}} (r_{nm}^a)_{;k^b} \\ &= i m_e \Delta_{nm}^b r_{nm}^a + i m_e \omega_{nm}^{\text{LDA}} (r_{nm}^a)_{;k^b} \quad \text{for } n \neq m, \end{aligned} \quad (\text{A.53})$$

where we used Eq (2.77) and $(r_{nm}^a)_{;k^b}$, from Eq. (A.103).

Likewise for the scissored term,

$$\mathcal{V}_{nm}^{S,a,\ell} = \frac{1}{2} (v^S a \mathcal{C}^\ell + \mathcal{C}^\ell v^S a)_{nm} = \frac{1}{2} \sum_q (v_{nq}^S \mathcal{C}_{qm}^\ell + \mathcal{C}_{nq}^\ell v_{qm}^S) \quad (\text{A.54})$$

and

$$\begin{aligned} (\mathcal{V}_{nm}^S)_{;k^b} &= \frac{1}{2} \sum_q (v_{nq}^S \mathcal{C}_{qm}^\ell + \mathcal{C}_{nq}^\ell v_{qm}^S)_{;k^b} \\ &= \frac{1}{2} \sum_q ((v_{nq}^S)_{;k^b} \mathcal{C}_{qm}^\ell + v_{nq}^S (\mathcal{C}_{qm}^\ell)_{;k^b} + (\mathcal{C}_{nq}^\ell)_{;k^b} v_{qm}^S + \mathcal{C}_{nq}^\ell (v_{qm}^S)_{;k^b}), \end{aligned} \quad (\text{A.55})$$

where $v_{nm}^S(\mathbf{k})$ is given in Eq. (2.42) and $(v_{nm}^S)_{;k^b}$ is given in Eq. (A6) of Ref. [81] as

$$(v_{nm}^S)_{;k^b} = i \Delta f_{mn} (r_{nm}^a)_{;k^b}. \quad (\text{A.56})$$

To evaluate $(\mathcal{C}_{nm}^\ell)_{;k^a}$, we use the fact that as $\mathcal{C}^\ell(z)$ is only a function of the z coordinate, its commutator with \mathbf{r} is zero. Then,

$$\langle n\mathbf{k}| [r^a, \mathcal{C}^\ell(z)] |m\mathbf{k}'\rangle = \langle n\mathbf{k}| [r_e^a, \mathcal{C}^\ell(z)] |m\mathbf{k}'\rangle + \langle n\mathbf{k}| [r_i^a, \mathcal{C}^\ell(z)] |m\mathbf{k}'\rangle = 0. \quad (\text{A.57})$$

The interband part reduces to,

$$\begin{aligned}
[r_e^a, \mathcal{C}^\ell(z)]_{nm} &= \sum_{q\mathbf{k}''} \left(\langle n\mathbf{k}|r_e^a|q\mathbf{k}''\rangle \langle q\mathbf{k}''|\mathcal{C}^\ell(z)|m\mathbf{k}'\rangle - \langle n\mathbf{k}|\mathcal{C}^\ell(z)|q\mathbf{k}''\rangle \langle q\mathbf{k}''|r_e^a|m\mathbf{k}'\rangle \right) \\
&= \sum_{q\mathbf{k}''} \delta(\mathbf{k} - \mathbf{k}'') \delta(\mathbf{k}' - \mathbf{k}'') \left((1 - \delta_{qn}) \xi_{nq}^a \mathcal{C}_{qm}^\ell - (1 - \delta_{qm}) \mathcal{C}_{nq}^\ell \xi_{qm}^a \right) \\
&= \delta(\mathbf{k} - \mathbf{k}') \left(\sum_q \left(\xi_{nq}^a \mathcal{C}_{qm}^\ell - \mathcal{C}_{nq}^\ell \xi_{qm}^a \right) + \mathcal{C}_{nm}^\ell (\xi_{mm}^a - \xi_{nn}^a) \right), \tag{A.58}
\end{aligned}$$

where we used Eq. (A.15), and the \mathbf{k} and z dependence is implicitly understood. From Eq. (A.18) the intraband part is,

$$\langle n\mathbf{k}| [\hat{\mathbf{r}}_i, \mathcal{C}^\ell(z)] |m\mathbf{k}'\rangle = i\delta(\mathbf{k} - \mathbf{k}') (\mathcal{C}_{nm}^\ell)_{;\mathbf{k}}, \tag{A.59}$$

then from Eq. (A.57)

$$\left((\mathcal{C}_{nm}^\ell)_{;\mathbf{k}} - i \sum_q \left(\xi_{nq}^a \mathcal{C}_{qm}^\ell - \mathcal{C}_{nq}^\ell \xi_{qm}^a \right) - i\mathcal{C}_{nm}^\ell (\xi_{mm}^a - \xi_{nn}^a) \right) i\delta(\mathbf{k} - \mathbf{k}') = 0, \tag{A.60}$$

which we can simplify,

$$\begin{aligned}
(\mathcal{C}_{nm}^\ell)_{;\mathbf{k}} &= i \sum_q \left(\xi_{nq}^a \mathcal{C}_{qm}^\ell - \mathcal{C}_{nq}^\ell \xi_{qm}^a \right) + i\mathcal{C}_{nm}^\ell (\xi_{mm}^a - \xi_{nn}^a) \\
&= i \sum_{q \neq nm} \left(\xi_{nq}^a \mathcal{C}_{qm}^\ell - \mathcal{C}_{nq}^\ell \xi_{qm}^a \right) + i \left(\xi_{nn}^a \mathcal{C}_{nm}^\ell - \mathcal{C}_{nn}^\ell \xi_{nm}^a \right)_{q=n} \\
&\quad + i \left(\xi_{nm}^a \mathcal{C}_{mm}^\ell - \mathcal{C}_{nm}^\ell \xi_{mm}^a \right)_{q=m} + i\mathcal{C}_{nm}^\ell (\xi_{mm}^a - \xi_{nn}^a) \\
&= i \sum_{q \neq nm} \left(\xi_{nq}^a \mathcal{C}_{qm}^\ell - \mathcal{C}_{nq}^\ell \xi_{qm}^a \right) + i\xi_{nm}^a (\mathcal{C}_{mm}^\ell - \mathcal{C}_{nn}^\ell) \\
&= i \sum_{q \neq nm} \left(r_{nq}^a \mathcal{C}_{qm}^\ell - \mathcal{C}_{nq}^\ell r_{qm}^a \right) + ir_{nm}^a (\mathcal{C}_{mm}^\ell - \mathcal{C}_{nn}^\ell) \\
&= i \left(\sum_{q \neq n} r_{nq}^a \mathcal{C}_{qm}^\ell - \sum_{q \neq m} \mathcal{C}_{nq}^\ell r_{qm}^a \right) + ir_{nm}^a (\mathcal{C}_{mm}^\ell - \mathcal{C}_{nn}^\ell), \tag{A.61}
\end{aligned}$$

since in ξ_{nm}^a we have that $n \neq m$, and we can replace it with r_{nm}^a . The matrix elements $\mathcal{C}_{nm}^\ell(\mathbf{k})$ are calculated in Sec. A.3.

For the general case of

$$\langle n\mathbf{k}| [\hat{r}^a, \hat{\mathcal{G}}(\mathbf{r}, \mathbf{p})] |m\mathbf{k}'\rangle = \mathcal{U}_{nm}(\mathbf{k}), \tag{A.62}$$

we can generalize our result to a more general expression,

$$(\mathcal{G}_{nm}(\mathbf{k}))_{;\mathbf{k}^a} = \mathcal{U}_{nm}(\mathbf{k}) + i \sum_{q \neq (nm)} \left(r_{nq}^a(\mathbf{k}) \mathcal{G}_{qm}(\mathbf{k}) - \mathcal{G}_{nq}(\mathbf{k}) r_{qm}^a(\mathbf{k}) \right) + ir_{nm}^a(\mathbf{k}) (\mathcal{G}_{mm}(\mathbf{k}) - \mathcal{G}_{nn}(\mathbf{k})). \tag{A.63}$$

A.5 Generalized derivative $(\omega_n(\mathbf{k}))_{;\mathbf{k}}$

We obtain the generalized derivative $(\omega_n(\mathbf{k}))_{;\mathbf{k}}$. We start from

$$\langle n\mathbf{k} | \hat{H}_0^\Sigma | m\mathbf{k}' \rangle = \delta_{nm} \delta(\mathbf{k} - \mathbf{k}') \hbar \omega_m^\Sigma(\mathbf{k}), \quad (\text{A.64})$$

then for $n = m$, Eq. (A.19) yields

$$\begin{aligned} (H_{0,nn}^\Sigma)_{;\mathbf{k}} &= \nabla_{\mathbf{k}} H_{0,nn}^\Sigma(\mathbf{k}) - i H_{0,nn}^\Sigma(\mathbf{k}) (\boldsymbol{\xi}_{nn}(\mathbf{k}) - \boldsymbol{\xi}_{nn}(\mathbf{k})) \\ &= \hbar \nabla_{\mathbf{k}} \omega_m^\Sigma(\mathbf{k}), \end{aligned} \quad (\text{A.65})$$

and from Eq. (A.18),

$$\langle n\mathbf{k} | [\hat{\mathbf{r}}_i, \hat{H}_0] | m\mathbf{k} \rangle = i \delta_{nm} \hbar (\omega_m^\Sigma(\mathbf{k}))_{;\mathbf{k}} = i \delta_{nm} \hbar \nabla_{\mathbf{k}} \omega_m^\Sigma(\mathbf{k}), \quad (\text{A.66})$$

so

$$(\omega_n^\Sigma(\mathbf{k}))_{;\mathbf{k}} = \nabla_{\mathbf{k}} \omega_n^\Sigma(\mathbf{k}). \quad (\text{A.67})$$

From Eq. (2.35),

$$\langle n\mathbf{k} | [\hat{\mathbf{r}}, \hat{H}_0^\Sigma] | m\mathbf{k} \rangle = i \hbar \mathbf{v}_{nm}^\Sigma(\mathbf{k}), \quad (\text{A.68})$$

and substituting Eqs. (A.66) and (A.68) into

$$\langle n\mathbf{k} | [\hat{\mathbf{r}}, \hat{H}_0^\Sigma] | m\mathbf{k} \rangle = \langle n\mathbf{k} | [\hat{\mathbf{r}}_i, \hat{H}_0^\Sigma] | m\mathbf{k} \rangle + \langle n\mathbf{k} | [\hat{\mathbf{r}}_e, \hat{H}_0^\Sigma] | m\mathbf{k} \rangle, \quad (\text{A.69})$$

we get

$$i \hbar \mathbf{v}_{nm}^\Sigma(\mathbf{k}) = i \delta_{nm} \hbar \nabla_{\mathbf{k}} \omega_m^\Sigma(\mathbf{k}) + \omega_{mn}^\Sigma \mathbf{r}_{e,nm}(\mathbf{k}). \quad (\text{A.70})$$

For $m = n$, we have that

$$\begin{aligned} \nabla_{\mathbf{k}} \omega_n^\Sigma(\mathbf{k}) &= \mathbf{v}_{nn}^\Sigma(\mathbf{k}) \\ \nabla_{\mathbf{k}} (\omega^{\text{LDA}}_n(\mathbf{k}) + \frac{\Sigma}{\hbar} (1 - f_n)) &= \nabla_{\mathbf{k}} \omega^{\text{LDA}}_n(\mathbf{k}) \\ \nabla_{\mathbf{k}} \omega^{\text{LDA}}_n(\mathbf{k}) &= \mathbf{v}_{nn}^\Sigma(\mathbf{k}), \end{aligned} \quad (\text{A.71})$$

where we use Eq. (2.29). However, from Eq. (2.42), $v_{nn}^\mathcal{S} = 0$ so $\mathbf{v}_{nn}^\Sigma = v^{\text{LDA}}_{nn}$. Thus, from Eq. (A.67)

$$(\omega_n^\Sigma(\mathbf{k}))_{;k^a} = (\omega^{\text{LDA}}_n(\mathbf{k}))_{;k^a} = v_{nn}^{\text{LDA},a}(\mathbf{k}), \quad (\text{A.72})$$

which is the same for the LDA and scissored Hamiltonians; $\mathbf{v}_{nn}^{\text{LDA}}(\mathbf{k})$ are the LDA velocities of the electron in state $|n\mathbf{k}\rangle$.

A.6 Expressions for $\chi_{\text{surface}}^{\text{abc}}$ in terms of $\mathcal{V}_{mn}^{\Sigma,a,\ell}$

The prefactor of Eqs. (2.74) and (2.75) diverges as $\tilde{\omega} \rightarrow 0$. To remove this apparent divergence of χ , we perform a partial fraction expansion in $\tilde{\omega}$.

A.6.1 Intraband Contributions

For the intraband term of Eq. (2.74), we obtain

$$I = C \left[-\frac{1}{2(\omega_{nm}^\Sigma)^2} \frac{1}{\omega_{nm}^\Sigma - \tilde{\omega}} + \frac{2}{(\omega_{nm}^\Sigma)^2} \frac{1}{\omega_{nm}^\Sigma - 2\tilde{\omega}} + \frac{1}{2(\omega_{nm}^\Sigma)^2} \frac{1}{\tilde{\omega}} \right] \\ - D \left[-\frac{3}{2(\omega_{nm}^\Sigma)^3} \frac{1}{\omega_{nm}^\Sigma - \tilde{\omega}} + \frac{4}{(\omega_{nm}^\Sigma)^3} \frac{1}{\omega_{nm}^\Sigma - 2\tilde{\omega}} + \frac{1}{2(\omega_{nm}^\Sigma)^3} \frac{1}{\tilde{\omega}} - \frac{1}{2(\omega_{nm}^\Sigma)^2} \frac{1}{(\omega_{nm}^\Sigma - \tilde{\omega})^2} \right], \quad (\text{A.73})$$

where $C = f_{mn} \mathcal{V}_{mn}^{\Sigma,a}(r_{nm}^{\text{LDA},b})_{;k^c}$, and $D = f_{mn} \mathcal{V}_{mn}^{\Sigma,a} r_{nm}^b \Delta_{nm}^c$.

Time-reversal symmetry leads to the following relationships:

$$\begin{aligned} \mathbf{r}_{mn}(\mathbf{k})|_{-\mathbf{k}} &= \mathbf{r}_{nm}(\mathbf{k})|_{\mathbf{k}}, \\ (\mathbf{r}_{mn})_{;\mathbf{k}}(\mathbf{k})|_{-\mathbf{k}} &= (-\mathbf{r}_{nm})_{;\mathbf{k}}(\mathbf{k})|_{\mathbf{k}}, \\ \mathcal{V}_{mn}^{\Sigma,a,\ell}(\mathbf{k})|_{-\mathbf{k}} &= -\mathcal{V}_{nm}^{\Sigma,a,\ell}(\mathbf{k})|_{\mathbf{k}}, \\ (\mathcal{V}_{mn}^{\Sigma,a,\ell})_{;\mathbf{k}}(\mathbf{k})|_{-\mathbf{k}} &= (\mathcal{V}_{nm}^{\Sigma,a,\ell})_{;\mathbf{k}}(\mathbf{k})|_{\mathbf{k}}, \\ \omega_{mn}^\Sigma(\mathbf{k})|_{-\mathbf{k}} &= \omega_{mn}^\Sigma(\mathbf{k})|_{\mathbf{k}}, \\ \Delta_{nm}^a(\mathbf{k})|_{-\mathbf{k}} &= -\Delta_{nm}^a(\mathbf{k})|_{\mathbf{k}}. \end{aligned} \quad (\text{A.74})$$

For a clean, cold semiconductor, $f_n = 1$ for an occupied or valence ($n = v$) band, and $f_n = 0$ for an empty or conduction ($n = c$) band independent of \mathbf{k} , and $f_{nm} = -f_{mn}$. Using the relationships above, we can show that the $1/\omega$ terms cancel each other out. Therefore, all the remaining nonzero terms in expressions (A.73) are simple ω and 2ω resonant denominators that are well behaved at $\omega = 0$.

To apply time-reversal invariance, we notice that the energy denominators are invariant under $\mathbf{k} \rightarrow -\mathbf{k}$, so we only need to review the numerators. So,

$$\begin{aligned} C \rightarrow f_{mn} \mathcal{V}_{mn}^{\Sigma,a,\ell} (r_{nm}^{\text{LDA},b})_{;k^c} |_{\mathbf{k}} + f_{mn} \mathcal{V}_{mn}^{\Sigma,a,\ell} (r_{nm}^{\text{LDA},b})_{;k^c} |_{-\mathbf{k}} \\ = f_{mn} \left[\mathcal{V}_{mn}^{\Sigma,a,\ell} (r_{nm}^{\text{LDA},b})_{;k^c} |_{\mathbf{k}} + (-\mathcal{V}_{nm}^{\Sigma,a,\ell}) (-r_{mn}^{\text{LDA},b})_{;k^c} |_{\mathbf{k}} \right] \\ = f_{mn} \left[\mathcal{V}_{mn}^{\Sigma,a,\ell} (r_{nm}^{\text{LDA},b})_{;k^c} + \mathcal{V}_{nm}^{\Sigma,a,\ell} (r_{mn}^{\text{LDA},b})_{;k^c} \right] \\ = f_{mn} \left[\mathcal{V}_{mn}^{\Sigma,a,\ell} (r_{nm}^{\text{LDA},b})_{;k^c} + \left(\mathcal{V}_{mn}^{\Sigma,a,\ell} (r_{nm}^{\text{LDA},b})_{;k^c} \right)^* \right] \\ = 2f_{mn} \text{Re} \left[\mathcal{V}_{mn}^{\Sigma,a,\ell} (r_{nm}^{\text{LDA},b})_{;k^c} \right], \end{aligned} \quad (\text{A.75})$$

and likewise,

$$\begin{aligned} D \rightarrow f_{mn} \mathcal{V}_{mn}^{\Sigma,a,\ell} r_{nm}^{\text{LDA},b} \Delta_{nm}^c |_{\mathbf{k}} + f_{mn} \mathcal{V}_{mn}^{\Sigma,a,\ell} r_{nm}^{\text{LDA},b} \Delta_{nm}^c |_{-\mathbf{k}} \\ = f_{mn} \left[\mathcal{V}_{mn}^{\Sigma,a,\ell} r_{nm}^{\text{LDA},b} \Delta_{nm}^c |_{\mathbf{k}} + (-\mathcal{V}_{nm}^{\Sigma,a,\ell}) r_{mn}^{\text{LDA},b} (-\Delta_{nm}^c) |_{\mathbf{k}} \right] \\ = f_{mn} \left[\mathcal{V}_{mn}^{\Sigma,a,\ell} r_{nm}^{\text{LDA},b} + \mathcal{V}_{nm}^{\Sigma,a,\ell} r_{mn}^{\text{LDA},b} \right] \Delta_{nm}^c \\ = f_{mn} \left[\mathcal{V}_{mn}^{\Sigma,a,\ell} r_{nm}^{\text{LDA},b} + \left(\mathcal{V}_{mn}^{\Sigma,a,\ell} r_{nm}^{\text{LDA},b} \right)^* \right] \Delta_{nm}^c \\ = 2f_{mn} \text{Re} \left[\mathcal{V}_{mn}^{\Sigma,a,\ell} r_{nm}^{\text{LDA},b} \right] \Delta_{nm}^c. \end{aligned} \quad (\text{A.76})$$

The last term in the second line of Eq. (A.73) is dealt with as follows,

$$\begin{aligned} \frac{D}{2(\omega_{nm}^\Sigma)^2} \frac{1}{(\omega_{nm}^\Sigma - \tilde{\omega})^2} &= \frac{f_{mn}}{2} \frac{\mathcal{V}_{mn}^{\Sigma,a} r_{nm}^b}{(\omega_{nm}^\Sigma)^2} \frac{\Delta_{nm}^c}{(\omega_{nm}^\Sigma - \tilde{\omega})^2} = -\frac{f_{mn}}{2} \frac{\mathcal{V}_{mn}^{\Sigma,a} r_{nm}^b}{(\omega_{nm}^\Sigma)^2} \left(\frac{1}{\omega_{nm}^\Sigma - \tilde{\omega}} \right)_{;k^c} \\ &= \frac{f_{mn}}{2} \left(\frac{\mathcal{V}_{mn}^{\Sigma,a} r_{nm}^b}{(\omega_{nm}^\Sigma)^2} \right)_{;k^c} \frac{1}{\omega_{nm}^\Sigma - \tilde{\omega}}, \end{aligned} \quad (\text{A.77})$$

where we used Eq. (2.77). For the last line, we performed an integration by parts over the Brillouin zone where the contribution from the edges vanishes [164]. Now, we apply the chain rule, to get

$$\left(\frac{\mathcal{V}_{mn}^{\Sigma,a,\ell} r_{nm}^{\text{LDA},b}}{(\omega_{nm}^\Sigma)^2} \right)_{;k^c} = \frac{r_{nm}^{\text{LDA},b}}{(\omega_{nm}^\Sigma)^2} \left(\mathcal{V}_{mn}^{\Sigma,a,\ell} \right)_{;k^c} + \frac{\mathcal{V}_{mn}^{\Sigma,a,\ell}}{(\omega_{nm}^\Sigma)^2} \left(r_{nm}^{\text{LDA},b} \right)_{;k^c} - \frac{2\mathcal{V}_{mn}^{\Sigma,a,\ell} r_{nm}^{\text{LDA},b}}{(\omega_{nm}^\Sigma)^3} \left(\omega_{nm}^\Sigma \right)_{;k^c}, \quad (\text{A.78})$$

and work the time-reversal on each term. The first term is reduced to

$$\begin{aligned} \frac{r_{nm}^{\text{LDA},b}}{(\omega_{nm}^\Sigma)^2} \left(\mathcal{V}_{mn}^{\Sigma,a,\ell} \right)_{;k^c} |_{\mathbf{k}} + \frac{r_{nm}^{\text{LDA},b}}{(\omega_{nm}^\Sigma)^2} \left(\mathcal{V}_{mn}^{\Sigma,a,\ell} \right)_{;k^c} |_{-\mathbf{k}} &= \frac{r_{nm}^{\text{LDA},b}}{(\omega_{nm}^\Sigma)^2} \left(\mathcal{V}_{mn}^{\Sigma,a,\ell} \right)_{;k^c} |_{\mathbf{k}} + \frac{r_{mn}^{\text{LDA},b}}{(\omega_{nm}^\Sigma)^2} \left(\mathcal{V}_{nm}^{\Sigma,a,\ell} \right)_{;k^c} |_{\mathbf{k}} \\ &= \frac{1}{(\omega_{nm}^\Sigma)^2} \left[r_{nm}^{\text{LDA},b} \left(\mathcal{V}_{mn}^{\Sigma,a,\ell} \right)_{;k^c} + \left(r_{nm}^{\text{LDA},b} \left(\mathcal{V}_{mn}^{\Sigma,a,\ell} \right)_{;k^c} \right)^* \right] \\ &= \frac{2}{(\omega_{nm}^\Sigma)^2} \text{Re} \left[r_{nm}^{\text{LDA},b} \left(\mathcal{V}_{mn}^{\Sigma,a,\ell} \right)_{;k^c} \right], \end{aligned} \quad (\text{A.79})$$

the second term is reduced to

$$\begin{aligned} \frac{\mathcal{V}_{mn}^{\Sigma,a,\ell}}{(\omega_{nm}^\Sigma)^2} \left(r_{nm}^{\text{LDA},b} \right)_{;k^c} |_{\mathbf{k}} + \frac{\mathcal{V}_{mn}^{\Sigma,a,\ell}}{(\omega_{nm}^\Sigma)^2} \left(r_{nm}^{\text{LDA},b} \right)_{;k^c} |_{-\mathbf{k}} &= \frac{\mathcal{V}_{mn}^{\Sigma,a,\ell}}{(\omega_{nm}^\Sigma)^2} \left(r_{nm}^{\text{LDA},b} \right)_{;k^c} |_{\mathbf{k}} + \frac{\mathcal{V}_{nm}^{\Sigma,a,\ell}}{(\omega_{nm}^\Sigma)^2} \left(r_{mn}^{\text{LDA},b} \right)_{;k^c} |_{\mathbf{k}} \\ &= \frac{1}{(\omega_{nm}^\Sigma)^2} \left[\mathcal{V}_{mn}^{\Sigma,a,\ell} \left(r_{nm}^{\text{LDA},b} \right)_{;k^c} + \left(\mathcal{V}_{mn}^{\Sigma,a,\ell} \left(r_{nm}^{\text{LDA},b} \right)_{;k^c} \right)^* \right] \\ &= \frac{2}{(\omega_{nm}^\Sigma)^2} \text{Re} \left[\mathcal{V}_{mn}^{\Sigma,a,\ell} \left(r_{nm}^{\text{LDA},b} \right)_{;k^c} \right], \end{aligned} \quad (\text{A.80})$$

and by using (2.77), the third term is reduced to

$$\begin{aligned} \frac{2\mathcal{V}_{mn}^{\Sigma,a,\ell} r_{nm}^{\text{LDA},b}}{(\omega_{nm}^\Sigma)^3} \left(\omega_{nm}^\Sigma \right)_{;k^c} |_{\mathbf{k}} + \frac{2\mathcal{V}_{mn}^{\Sigma,a,\ell} r_{nm}^{\text{LDA},b}}{(\omega_{nm}^\Sigma)^3} \left(\omega_{nm}^\Sigma \right)_{;k^c} |_{-\mathbf{k}} &= \frac{2\mathcal{V}_{mn}^{\Sigma,a,\ell} r_{nm}^{\text{LDA},b}}{(\omega_{nm}^\Sigma)^3} \Delta_{nm}^c |_{\mathbf{k}} + \frac{2\mathcal{V}_{mn}^{\Sigma,a,\ell} r_{nm}^{\text{LDA},b}}{(\omega_{nm}^\Sigma)^3} \Delta_{nm}^c |_{-\mathbf{k}} \\ &= \frac{2\mathcal{V}_{nm}^{\Sigma,a,\ell} r_{mn}^{\text{LDA},b}}{(\omega_{nm}^\Sigma)^3} \Delta_{nm}^c |_{\mathbf{k}} + \frac{2\mathcal{V}_{mn}^{\Sigma,a,\ell} r_{nm}^{\text{LDA},b}}{(\omega_{nm}^\Sigma)^3} \Delta_{nm}^c |_{\mathbf{k}} \\ &= \frac{2}{(\omega_{nm}^\Sigma)^3} \left[\mathcal{V}_{nm}^{\Sigma,a,\ell} r_{mn}^{\text{LDA},b} + \left(\mathcal{V}_{nm}^{\Sigma,a,\ell} r_{mn}^{\text{LDA},b} \right)^* \right] \Delta_{nm}^c \\ &= \frac{4}{(\omega_{nm}^\Sigma)^3} \text{Re} \left[\mathcal{V}_{nm}^{\Sigma,a,\ell} r_{mn}^{\text{LDA},b} \right] \Delta_{nm}^c. \end{aligned} \quad (\text{A.81})$$

Combining the results from (A.79), (A.80), and (A.81) into (A.78),

$$\begin{aligned} \frac{f_{mn}}{2} \left[\left(\frac{\mathcal{V}_{mn}^{\Sigma,a,\ell} r_{nm}^{\text{LDA},b}}{(\omega_{nm}^\Sigma)^2} \right)_{;k^c} |_{\mathbf{k}} + \left(\frac{\mathcal{V}_{mn}^{\Sigma,a,\ell} r_{nm}^{\text{LDA},b}}{(\omega_{nm}^\Sigma)^2} \right)_{;k^c} |_{-\mathbf{k}} \right] \frac{1}{\omega_{nm}^\Sigma - \tilde{\omega}} = \\ \left(2 \text{Re} \left[r_{nm}^{\text{LDA},b} \left(\mathcal{V}_{mn}^{\Sigma,a,\ell} \right)_{;k^c} \right] + 2 \text{Re} \left[\mathcal{V}_{mn}^{\Sigma,a,\ell} \left(r_{nm}^{\text{LDA},b} \right)_{;k^c} \right] - \frac{4}{\omega_{nm}^\Sigma} \text{Re} \left[\mathcal{V}_{nm}^{\Sigma,a,\ell} r_{mn}^{\text{LDA},b} \right] \Delta_{nm}^c \right) \frac{f_{mn}}{2(\omega_{nm}^\Sigma)^2} \frac{1}{\omega_{nm}^\Sigma - \tilde{\omega}}. \end{aligned} \quad (\text{A.82})$$

We substitute (A.75), (A.76), and (A.82) in (A.73),

$$I = \left[-\frac{2f_{mn} \operatorname{Re} \left[\mathcal{V}_{mn}^{\Sigma, a, \ell} \left(r_{nm}^{\text{LDA}, b} \right)_{;k^c} \right]}{2(\omega_{nm}^\Sigma)^2} \frac{1}{\omega_{nm}^\Sigma - \tilde{\omega}} + \frac{4f_{mn} \operatorname{Re} \left[\mathcal{V}_{mn}^{\Sigma, a, \ell} \left(r_{nm}^{\text{LDA}, b} \right)_{;k^c} \right]}{(\omega_{nm}^\Sigma)^2} \frac{1}{\omega_{nm}^\Sigma - 2\tilde{\omega}} \right. \\ + \left[\frac{6f_{mn} \operatorname{Re} \left[\mathcal{V}_{mn}^{\Sigma, a, \ell} r_{nm}^{\text{LDA}, b} \right] \Delta_{nm}^c}{2(\omega_{nm}^\Sigma)^3} \frac{1}{\omega_{nm}^\Sigma - \tilde{\omega}} - \frac{8f_{mn} \operatorname{Re} \left[\mathcal{V}_{mn}^{\Sigma, a, \ell} r_{nm}^{\text{LDA}, b} \right] \Delta_{nm}^c}{(\omega_{nm}^\Sigma)^3} \frac{1}{\omega_{nm}^\Sigma - 2\tilde{\omega}} \right. \\ \left. + \frac{f_{mn} \left(2 \operatorname{Re} \left[r_{nm}^{\text{LDA}, b} \left(\mathcal{V}_{mn}^{\Sigma, a, \ell} \right)_{;k^c} \right] + 2 \operatorname{Re} \left[\mathcal{V}_{mn}^{\Sigma, a, \ell} \left(r_{nm}^{\text{LDA}, b} \right)_{;k^c} \right] - \frac{4}{\omega_{nm}^\Sigma} \operatorname{Re} \left[\mathcal{V}_{mn}^{\Sigma, a, \ell} r_{mn}^{\text{LDA}, b} \right] \Delta_{nm}^c \right)}{2(\omega_{nm}^\Sigma)^2} \frac{1}{\omega_{nm}^\Sigma - \tilde{\omega}} \right].$$

If we simplify,

$$I = -\frac{2f_{mn} \operatorname{Re} \left[\mathcal{V}_{mn}^{\Sigma, a, \ell} \left(r_{nm}^{\text{LDA}, b} \right)_{;k^c} \right]}{2(\omega_{nm}^\Sigma)^2} \frac{1}{\omega_{nm}^\Sigma - \tilde{\omega}} + \frac{4f_{mn} \operatorname{Re} \left[\mathcal{V}_{mn}^{\Sigma, a, \ell} \left(r_{nm}^{\text{LDA}, b} \right)_{;k^c} \right]}{(\omega_{nm}^\Sigma)^2} \frac{1}{\omega_{nm}^\Sigma - 2\tilde{\omega}} \\ + \frac{6f_{mn} \operatorname{Re} \left[\mathcal{V}_{mn}^{\Sigma, a, \ell} r_{nm}^{\text{LDA}, b} \right] \Delta_{nm}^c}{2(\omega_{nm}^\Sigma)^3} \frac{1}{\omega_{nm}^\Sigma - \tilde{\omega}} - \frac{8f_{mn} \operatorname{Re} \left[\mathcal{V}_{mn}^{\Sigma, a, \ell} r_{nm}^{\text{LDA}, b} \right] \Delta_{nm}^c}{(\omega_{nm}^\Sigma)^3} \frac{1}{\omega_{nm}^\Sigma - 2\tilde{\omega}} \\ + \frac{2f_{mn} \operatorname{Re} \left[r_{nm}^{\text{LDA}, b} \left(\mathcal{V}_{mn}^{\Sigma, a, \ell} \right)_{;k^c} \right]}{2(\omega_{nm}^\Sigma)^2} \frac{1}{\omega_{nm}^\Sigma - \tilde{\omega}} \\ + \frac{2f_{mn} \operatorname{Re} \left[\mathcal{V}_{mn}^{\Sigma, a, \ell} \left(r_{nm}^{\text{LDA}, b} \right)_{;k^c} \right]}{2(\omega_{nm}^\Sigma)^2} \frac{1}{\omega_{nm}^\Sigma - \tilde{\omega}} \\ - \frac{4f_{mn} \operatorname{Re} \left[\mathcal{V}_{mn}^{\Sigma, a, \ell} r_{mn}^{\text{LDA}, b} \right] \Delta_{nm}^c}{2(\omega_{nm}^\Sigma)^3} \frac{1}{\omega_{nm}^\Sigma - \tilde{\omega}}, \quad (\text{A.83})$$

we conveniently collect the terms in columns of ω and 2ω . We can now express the susceptibility in terms of ω and 2ω . Separating the 2ω terms and substituting in the equation above,

$$I_{2\omega} = -\frac{e^3}{\hbar^2} \sum_{mnk} \left[\frac{4f_{mn} \operatorname{Re} \left[\mathcal{V}_{mn}^{\Sigma, a, \ell} \left(r_{nm}^{\text{LDA}, b} \right)_{;k^c} \right]}{(\omega_{nm}^\Sigma)^2} - \frac{8f_{mn} \operatorname{Re} \left[\mathcal{V}_{mn}^{\Sigma, a, \ell} r_{nm}^{\text{LDA}, b} \right] \Delta_{nm}^c}{(\omega_{nm}^\Sigma)^3} \right] \frac{1}{\omega_{nm}^\Sigma - 2\tilde{\omega}} \\ = -\frac{e^3}{\hbar^2} \sum_{mnk} \frac{4f_{mn}}{(\omega_{nm}^\Sigma)^2} \left[\operatorname{Re} \left[\mathcal{V}_{mn}^{\Sigma, a, \ell} \left(r_{nm}^{\text{LDA}, b} \right)_{;k^c} \right] - \frac{2 \operatorname{Re} \left[\mathcal{V}_{mn}^{\Sigma, a, \ell} r_{nm}^{\text{LDA}, b} \right] \Delta_{nm}^c}{\omega_{nm}^\Sigma} \right] \frac{1}{\omega_{nm}^\Sigma - 2\tilde{\omega}}. \quad (\text{A.84})$$

We can express the energies in terms of transitions between bands. Therefore, $\omega_{nm}^\Sigma = \omega_{cv}^\Sigma$ for transitions between conduction and valence bands. To take the limit $\eta \rightarrow 0$, we use

$$\lim_{\eta \rightarrow 0} \frac{1}{x \pm i\eta} = P \frac{1}{x} \mp i\pi\delta(x), \quad (\text{A.85})$$

and can finally rewrite (A.84) in the desired form,

$$\text{Im}[\chi_{i,a,\ell bc,2\omega}^{s,\ell}] = -\frac{\pi|e|^3}{2\hbar^2} \sum_{vc\mathbf{k}} \frac{4}{(\omega_{cv}^\Sigma)^2} \left(\text{Re} \left[\mathcal{V}_{vc}^{\Sigma,a,\ell} (r_{cv}^{\text{LDA},b})_{;k^c} \right] - \frac{2 \text{Re} [\mathcal{V}_{vc}^{\Sigma,a,\ell} r_{cv}^{\text{LDA},b}] \Delta_{cv}^c}{\omega_{cv}^\Sigma} \right) \delta(\omega_{cv}^\Sigma - 2\omega). \quad (\text{A.86})$$

where we added a $1/2$ from the sum over $\mathbf{k} \rightarrow -\mathbf{k}$. We do the same for the $\tilde{\omega}$ terms in (A.83) to obtain

$$I_\omega = -\frac{e^3}{2\hbar^2} \sum_{nm\mathbf{k}} \left[-\frac{2f_{mn} \text{Re} [\mathcal{V}_{mn}^{\Sigma,a,\ell} (r_{nm}^{\text{LDA},b})_{;k^c}]}{(\omega_{nm}^\Sigma)^2} + \frac{6f_{mn} \text{Re} [\mathcal{V}_{mn}^{\Sigma,a,\ell} r_{nm}^{\text{LDA},b}] \Delta_{nm}^c}{(\omega_{nm}^\Sigma)^3} \right. \\ \left. + \frac{2f_{mn} \text{Re} [\mathcal{V}_{mn}^{\Sigma,a,\ell} (r_{nm}^{\text{LDA},b})_{;k^c}]}{(\omega_{nm}^\Sigma)^2} - \frac{4f_{mn} \text{Re} [\mathcal{V}_{nm}^{\Sigma,a,\ell} r_{mn}^{\text{LDA},b}] \Delta_{nm}^c}{(\omega_{nm}^\Sigma)^3} \right. \\ \left. + \frac{2f_{mn} \text{Re} [r_{nm}^{\text{LDA},b} (\mathcal{V}_{mn}^{\Sigma,a,\ell})_{;k^c}]}{(\omega_{nm}^\Sigma)^2} \right] \frac{1}{\omega_{nm}^\Sigma - \tilde{\omega}}. \quad (\text{A.87})$$

We reduce in the same way as (A.84),

$$I_\omega = -\frac{e^3}{2\hbar^2} \sum_{nm\mathbf{k}} \frac{f_{mn}}{(\omega_{nm}^\Sigma)^2} \left[2 \text{Re} \left[r_{nm}^{\text{LDA},b} (\mathcal{V}_{mn}^{\Sigma,a,\ell})_{;k^c} \right] + \frac{2 \text{Re} [\mathcal{V}_{mn}^{\Sigma,a,\ell} r_{nm}^{\text{LDA},b}] \Delta_{nm}^c}{\omega_{nm}^\Sigma} \right] \frac{1}{\omega_{nm}^\Sigma - \tilde{\omega}}, \quad (\text{A.88})$$

and using (A.85) we obtain our final form,

$$\text{Im}[\chi_{i,a,\ell bc,\omega}^{s,\ell}] = -\frac{\pi|e|^3}{2\hbar^2} \sum_{cv} \frac{1}{(\omega_{cv}^\Sigma)^2} \left(\text{Re} \left[r_{cv}^{\text{LDA},b} (\mathcal{V}_{vc}^{\Sigma,a,\ell})_{;k^c} \right] + \frac{\text{Re} [\mathcal{V}_{vc}^{\Sigma,a,\ell} r_{cv}^{\text{LDA},b}] \Delta_{cv}^c}{\omega_{cv}^\Sigma} \right) \delta(\omega_{cv}^\Sigma - \omega), \quad (\text{A.89})$$

where again we added a $1/2$ from the sum over $\mathbf{k} \rightarrow -\mathbf{k}$.

A.6.2 Interband Contributions

We follow an equivalent procedure for the interband contribution. From Eq. (2.75) we have

$$E = A \left[-\frac{1}{2\omega_{lm}^\Sigma (2\omega_{lm}^\Sigma - \omega_{nm}^\Sigma)} \frac{1}{\omega_{lm}^\Sigma - \tilde{\omega}} + \frac{2}{\omega_{nm}^\Sigma (2\omega_{lm}^\Sigma - \omega_{nm}^\Sigma)} \frac{1}{\omega_{nm}^\Sigma - 2\tilde{\omega}} + \frac{1}{2\omega_{lm}^\Sigma \omega_{nm}^\Sigma} \frac{1}{\tilde{\omega}} \right] \\ - B \left[-\frac{1}{2\omega_{nl}^\Sigma (2\omega_{nl}^\Sigma - \omega_{nm}^\Sigma)} \frac{1}{\omega_{nl}^\Sigma - \tilde{\omega}} + \frac{2}{\omega_{nm}^\Sigma (2\omega_{nl}^\Sigma - \omega_{nm}^\Sigma)} \frac{1}{\omega_{nm}^\Sigma - 2\tilde{\omega}} + \frac{1}{2\omega_{nl}^\Sigma \omega_{nm}^\Sigma} \frac{1}{\tilde{\omega}} \right], \quad (\text{A.90})$$

where $A = f_{ml} \mathcal{V}_{mn}^{\Sigma,a} r_{nl}^c r_{lm}^b$ and $B = f_{ln} \mathcal{V}_{mn}^{\Sigma,a} r_{nl}^b r_{lm}^c$.

Just as above, the $\frac{1}{\tilde{\omega}}$ terms cancel out. We multiply out the A and B terms,

$$E = \left[-\frac{A}{2\omega_{lm}^\Sigma (2\omega_{lm}^\Sigma - \omega_{nm}^\Sigma)} \frac{1}{\omega_{lm}^\Sigma - \tilde{\omega}} + \frac{2A}{\omega_{nm}^\Sigma (2\omega_{lm}^\Sigma - \omega_{nm}^\Sigma)} \frac{1}{\omega_{nm}^\Sigma - 2\tilde{\omega}} \right] \\ + \left[\frac{B}{2\omega_{nl}^\Sigma (2\omega_{nl}^\Sigma - \omega_{nm}^\Sigma)} \frac{1}{\omega_{nl}^\Sigma - \tilde{\omega}} - \frac{2B}{\omega_{nm}^\Sigma (2\omega_{nl}^\Sigma - \omega_{nm}^\Sigma)} \frac{1}{\omega_{nm}^\Sigma - 2\tilde{\omega}} \right]. \quad (\text{A.91})$$

As before, we notice that the energy denominators are invariant under $\mathbf{k} \rightarrow -\mathbf{k}$ so we need only to review the numerators. Starting with A ,

$$\begin{aligned}
A &\rightarrow f_{ml} \mathcal{V}_{mn}^{\Sigma,a,\ell} r_{nl}^c r_{lm}^b |_{\mathbf{k}} + f_{ml} \mathcal{V}_{mn}^{\Sigma,a,\ell} r_{nl}^c r_{lm}^b |_{-\mathbf{k}} \\
&= f_{ml} \left[\mathcal{V}_{mn}^{\Sigma,a,\ell} r_{nl}^c r_{lm}^b |_{\mathbf{k}} + \left(-\mathcal{V}_{nm}^{\Sigma,a,\ell} \right) r_{ln}^c r_{ml}^b |_{\mathbf{k}} \right] \\
&= f_{ml} \left[\mathcal{V}_{mn}^{\Sigma,a,\ell} r_{nl}^c r_{lm}^b - \mathcal{V}_{nm}^{\Sigma,a,\ell} r_{ln}^c r_{ml}^b \right] \\
&= f_{ml} \left[\mathcal{V}_{mn}^{\Sigma,a,\ell} r_{nl}^c r_{lm}^b - \left(\mathcal{V}_{mn}^{\Sigma,a,\ell} r_{nl}^c r_{lm}^b \right)^* \right] \\
&= -2f_{ml} \operatorname{Im} \left[\mathcal{V}_{mn}^{\Sigma,a,\ell} r_{nl}^c r_{lm}^b \right],
\end{aligned}$$

then B ,

$$\begin{aligned}
B &\rightarrow f_{ln} \mathcal{V}_{mn}^{\Sigma,a,\ell} r_{nl}^b r_{lm}^c |_{\mathbf{k}} + f_{ln} \mathcal{V}_{mn}^{\Sigma,a,\ell} r_{nl}^b r_{lm}^c |_{-\mathbf{k}} \\
&= f_{ln} \left[\mathcal{V}_{mn}^{\Sigma,a,\ell} r_{nl}^b r_{lm}^c |_{\mathbf{k}} + \left(-\mathcal{V}_{nm}^{\Sigma,a,\ell} \right) r_{ln}^b r_{ml}^c |_{\mathbf{k}} \right] \\
&= f_{ln} \left[\mathcal{V}_{mn}^{\Sigma,a,\ell} r_{nl}^b r_{lm}^c - \mathcal{V}_{nm}^{\Sigma,a,\ell} r_{ln}^b r_{ml}^c \right] \\
&= f_{ln} \left[\mathcal{V}_{mn}^{\Sigma,a,\ell} r_{nl}^b r_{lm}^c - \left(\mathcal{V}_{mn}^{\Sigma,a,\ell} r_{nl}^b r_{lm}^c \right)^* \right] \\
&= -2f_{ln} \operatorname{Im} \left[\mathcal{V}_{mn}^{\Sigma,a,\ell} r_{nl}^b r_{lm}^c \right].
\end{aligned}$$

We then substitute in (A.91),

$$E = \left[\frac{2f_{ml} \operatorname{Im} \left[\mathcal{V}_{mn}^{\Sigma,a,\ell} r_{nl}^c r_{lm}^b \right]}{2\omega_{lm}^{\Sigma} (2\omega_{lm}^{\Sigma} - \omega_{nm}^{\Sigma})} \frac{1}{\omega_{lm}^{\Sigma} - \tilde{\omega}} - \frac{4f_{ml} \operatorname{Im} \left[\mathcal{V}_{mn}^{\Sigma,a,\ell} r_{nl}^c r_{lm}^b \right]}{\omega_{nm}^{\Sigma} (2\omega_{lm}^{\Sigma} - \omega_{nm}^{\Sigma})} \frac{1}{\omega_{nm}^{\Sigma} - 2\tilde{\omega}} \right. \\
\left. - \frac{2f_{ln} \operatorname{Im} \left[\mathcal{V}_{mn}^{\Sigma,a,\ell} r_{nl}^b r_{lm}^c \right]}{2\omega_{nl}^{\Sigma} (2\omega_{nl}^{\Sigma} - \omega_{nm}^{\Sigma})} \frac{1}{\omega_{nl}^{\Sigma} - \tilde{\omega}} + \frac{4f_{ln} \operatorname{Im} \left[\mathcal{V}_{mn}^{\Sigma,a,\ell} r_{nl}^b r_{lm}^c \right]}{\omega_{nm}^{\Sigma} (2\omega_{nl}^{\Sigma} - \omega_{nm}^{\Sigma})} \frac{1}{\omega_{nm}^{\Sigma} - 2\tilde{\omega}} \right].$$

We manipulate indices and simplify,

$$\begin{aligned}
E &= \left[\frac{f_{ml} \operatorname{Im} \left[\mathcal{V}_{mn}^{\Sigma,a,\ell} r_{nl}^c r_{lm}^b \right]}{\omega_{lm}^{\Sigma} (2\omega_{lm}^{\Sigma} - \omega_{nm}^{\Sigma})} \frac{1}{\omega_{lm}^{\Sigma} - \tilde{\omega}} - \frac{f_{ln} \operatorname{Im} \left[\mathcal{V}_{mn}^{\Sigma,a,\ell} r_{nl}^b r_{lm}^c \right]}{\omega_{nl}^{\Sigma} (2\omega_{nl}^{\Sigma} - \omega_{nm}^{\Sigma})} \frac{1}{\omega_{nl}^{\Sigma} - \tilde{\omega}} \right] \\
&\quad + \left[\frac{f_{ln} \operatorname{Im} \left[\mathcal{V}_{mn}^{\Sigma,a,\ell} r_{nl}^b r_{lm}^c \right]}{2\omega_{nl}^{\Sigma} - \omega_{nm}^{\Sigma}} - \frac{f_{ml} \operatorname{Im} \left[\mathcal{V}_{mn}^{\Sigma,a,\ell} r_{nl}^c r_{lm}^b \right]}{2\omega_{lm}^{\Sigma} - \omega_{nm}^{\Sigma}} \right] \frac{4}{\omega_{nm}^{\Sigma}} \frac{1}{\omega_{nm}^{\Sigma} - 2\tilde{\omega}} \\
&= \left[\frac{f_{mn} \operatorname{Im} \left[\mathcal{V}_{ml}^{\Sigma,a,\ell} r_{ln}^c r_{nm}^b \right]}{2\omega_{nm}^{\Sigma} - \omega_{lm}^{\Sigma}} - \frac{f_{mn} \operatorname{Im} \left[\mathcal{V}_{ln}^{\Sigma,a,\ell} r_{nm}^b r_{ml}^c \right]}{2\omega_{nm}^{\Sigma} - \omega_{nl}^{\Sigma}} \right] \frac{1}{\omega_{nm}^{\Sigma}} \frac{1}{\omega_{nm}^{\Sigma} - \tilde{\omega}} \\
&\quad + \left[\frac{f_{ln} \operatorname{Im} \left[\mathcal{V}_{mn}^{\Sigma,a,\ell} r_{nl}^b r_{lm}^c \right]}{2\omega_{nl}^{\Sigma} - \omega_{nm}^{\Sigma}} - \frac{f_{ml} \operatorname{Im} \left[\mathcal{V}_{mn}^{\Sigma,a,\ell} r_{nl}^c r_{lm}^b \right]}{2\omega_{lm}^{\Sigma} - \omega_{nm}^{\Sigma}} \right] \frac{4}{\omega_{nm}^{\Sigma}} \frac{1}{\omega_{nm}^{\Sigma} - 2\tilde{\omega}},
\end{aligned}$$

and substitute in (2.75),

$$I = -\frac{e^3}{2\hbar^2} \sum_{nm} \frac{1}{\omega_{nm}^\Sigma} \left[\frac{f_{mn} \operatorname{Im} [\mathcal{V}_{ml}^{\Sigma,a,\ell} \{r_{ln}^c r_{nm}^b\}]}{2\omega_{nm}^\Sigma - \omega_{lm}^\Sigma} - \frac{f_{mn} \operatorname{Im} [\mathcal{V}_{ln}^{\Sigma,a,\ell} \{r_{nm}^b r_{ml}^c\}]}{2\omega_{nm}^\Sigma - \omega_{nl}^\Sigma} \right] \frac{1}{\omega_{nm}^\Sigma - \tilde{\omega}} + 4 \left[\frac{f_{ln} \operatorname{Im} [\mathcal{V}_{mn}^{\Sigma,a,\ell} \{r_{nl}^b r_{lm}^c\}]}{2\omega_{nl}^\Sigma - \omega_{nm}^\Sigma} - \frac{f_{ml} \operatorname{Im} [\mathcal{V}_{mn}^{\Sigma,a,\ell} \{r_{nl}^c r_{lm}^b\}]}{2\omega_{lm}^\Sigma - \omega_{nm}^\Sigma} \right] \frac{1}{\omega_{nm}^\Sigma - 2\tilde{\omega}}.$$

Finally, we take $n = c$, $m = v$, and $l = q$ and substitute,

$$\begin{aligned} I &= -\frac{e^3}{2\hbar^2} \sum_{cv} \frac{1}{\omega_{cv}^\Sigma} \left(\left[\frac{f_{vc} \operatorname{Im} [\mathcal{V}_{vq}^{\Sigma,a,\ell} \{r_{qc}^c r_{cv}^b\}]}{2\omega_{cv}^\Sigma - \omega_{qv}^\Sigma} - \frac{f_{vc} \operatorname{Im} [\mathcal{V}_{qc}^{\Sigma,a,\ell} \{r_{cv}^b r_{vq}^c\}]}{2\omega_{cv}^\Sigma - \omega_{cq}^\Sigma} \right] \frac{1}{\omega_{cv}^\Sigma - \tilde{\omega}} \right. \\ &\quad \left. + 4 \left[\frac{f_{qc} \operatorname{Im} [\mathcal{V}_{vc}^{\Sigma,a,\ell} \{r_{cq}^b r_{qv}^c\}]}{2\omega_{cq}^\Sigma - \omega_{cv}^\Sigma} - \frac{f_{vq} \operatorname{Im} [\mathcal{V}_{vc}^{\Sigma,a,\ell} \{r_{cq}^c r_{qv}^b\}]}{2\omega_{qv}^\Sigma - \omega_{cv}^\Sigma} \right] \frac{1}{\omega_{cv}^\Sigma - 2\tilde{\omega}} \right) \\ &= \frac{e^3}{2\hbar^2} \sum_{cv} \frac{1}{\omega_{cv}^\Sigma} \left(\left[\frac{\operatorname{Im} [\mathcal{V}_{qc}^{\Sigma,a,\ell} \{r_{cv}^b r_{vq}^c\}]}{2\omega_{cv}^\Sigma - \omega_{cq}^\Sigma} - \frac{\operatorname{Im} [\mathcal{V}_{vq}^{\Sigma,a,\ell} \{r_{qc}^c r_{cv}^b\}]}{2\omega_{cv}^\Sigma - \omega_{qv}^\Sigma} \right] \frac{1}{\omega_{cv}^\Sigma - \tilde{\omega}} \right. \\ &\quad \left. - 4 \left[\frac{f_{qc} \operatorname{Im} [\mathcal{V}_{vc}^{\Sigma,a,\ell} \{r_{cq}^b r_{qv}^c\}]}{2\omega_{cq}^\Sigma - \omega_{cv}^\Sigma} - \frac{f_{vq} \operatorname{Im} [\mathcal{V}_{vc}^{\Sigma,a,\ell} \{r_{cq}^c r_{qv}^b\}]}{2\omega_{qv}^\Sigma - \omega_{cv}^\Sigma} \right] \frac{1}{\omega_{cv}^\Sigma - 2\tilde{\omega}} \right). \end{aligned}$$

We use (A.85),

$$\begin{aligned} I &= \frac{\pi|e^3|}{2\hbar^2} \sum_{cv} \frac{1}{\omega_{cv}^\Sigma} \left(\left[\frac{\operatorname{Im} [\mathcal{V}_{qc}^{\Sigma,a,\ell} \{r_{cv}^b r_{vq}^c\}]}{2\omega_{cv}^\Sigma - \omega_{cq}^\Sigma} - \frac{\operatorname{Im} [\mathcal{V}_{vq}^{\Sigma,a,\ell} \{r_{qc}^c r_{cv}^b\}]}{2\omega_{cv}^\Sigma - \omega_{qv}^\Sigma} \right] \delta(\omega_{cv}^\Sigma - \omega) \right. \\ &\quad \left. - 4 \left[\frac{f_{qc} \operatorname{Im} [\mathcal{V}_{vc}^{\Sigma,a,\ell} \{r_{cq}^b r_{qv}^c\}]}{2\omega_{cq}^\Sigma - \omega_{cv}^\Sigma} - \frac{f_{vq} \operatorname{Im} [\mathcal{V}_{vc}^{\Sigma,a,\ell} \{r_{cq}^c r_{qv}^b\}]}{2\omega_{qv}^\Sigma - \omega_{cv}^\Sigma} \right] \delta(\omega_{cv}^\Sigma - 2\omega) \right), \end{aligned}$$

and recognize that for the 1ω terms, $q \neq (v, c)$, and for the 2ω q can have two distinct values such that,

$$\begin{aligned} I &= \frac{\pi|e^3|}{2\hbar^2} \sum_{cv} \frac{1}{\omega_{cv}^\Sigma} \left(\sum_{q \neq (v,c)} \left[\frac{\operatorname{Im} [\mathcal{V}_{qc}^{\Sigma,a,\ell} \{r_{cv}^b r_{vq}^c\}]}{2\omega_{cv}^\Sigma - \omega_{cq}^\Sigma} - \frac{\operatorname{Im} [\mathcal{V}_{vq}^{\Sigma,a,\ell} \{r_{qc}^c r_{cv}^b\}]}{2\omega_{cv}^\Sigma - \omega_{qv}^\Sigma} \right] \delta(\omega_{cv}^\Sigma - \omega) \right. \\ &\quad \left. - 4 \left[\sum_{v' \neq v} \frac{\operatorname{Im} [\mathcal{V}_{vc}^{\Sigma,a,\ell} \{r_{cv'}^b r_{v'v}^c\}]}{2\omega_{cv'}^\Sigma - \omega_{cv}^\Sigma} - \sum_{c' \neq c} \frac{\operatorname{Im} [\mathcal{V}_{vc}^{\Sigma,a,\ell} \{r_{cc'}^c r_{c'v}^b\}]}{2\omega_{c'v}^\Sigma - \omega_{cv}^\Sigma} \right] \delta(\omega_{cv}^\Sigma - 2\omega) \right). \end{aligned}$$

A.7 Generalized derivative $(\mathbf{r}_{nm}(\mathbf{k}))_{;\mathbf{k}}$ for nonlocal potentials

We will derive the generalized derivative $(\mathbf{r}_{nm}(\mathbf{k}))_{;\mathbf{k}}$ for the case of a nonlocal potential in the Hamiltonian. We start from Eq. (2.41),

$$[r^a, v^{\text{LDA,b}}] = [r^a, v^b] + [r^a, v^{\text{nl,b}}] = \frac{i\hbar}{m_e} \delta_{ab} + [r^a, v^{\text{nl,b}}] \equiv \tau^{ab}, \quad (\text{A.92})$$

where we used the fact that $[r^a, p^b] = i\hbar\delta_{ab}$. Then,

$$\langle n\mathbf{k}|[r^a, v^{\text{LDA},b}]|m\mathbf{k}'\rangle = \langle n\mathbf{k}|\tau^{ab}|m\mathbf{k}'\rangle = \tau_{nm}^{ab}(\mathbf{k})\delta(\mathbf{k} - \mathbf{k}'), \quad (\text{A.93})$$

so

$$\langle n\mathbf{k}|[r_i^a, v^{\text{LDA},b}]|m\mathbf{k}'\rangle + \langle n\mathbf{k}|[r_e^a, v^{\text{LDA},b}]|m\mathbf{k}'\rangle = \tau_{nm}^{ab}(\mathbf{k})\delta(\mathbf{k} - \mathbf{k}'), \quad (\text{A.94})$$

where the matrix elements of $\tau_{nm}^{ab}(\mathbf{k})$ are calculated in Sec. A.8. From Eq. (A.18) and (A.19)

$$\langle n\mathbf{k}|[r_i^a, v_{\text{LDA}}^b]|m\mathbf{k}'\rangle = i\delta(\mathbf{k} - \mathbf{k}')(v_{nm}^{\text{LDA},b})_{;k^a} \quad (\text{A.95})$$

$$(v_{nm}^{\text{LDA},b})_{;k^a} = \nabla_{k^a} v_{nm}^{\text{LDA},b}(\mathbf{k}) - iv_{nm}^{\text{LDA},b}(\mathbf{k})(\xi_{nn}^a(\mathbf{k}) - \xi_{mm}^a(\mathbf{k})), \quad (\text{A.96})$$

and

$$\begin{aligned} \langle n\mathbf{k}|[r_e^a, v^{\text{LDA},b}]|m\mathbf{k}'\rangle &= \sum_{\ell\mathbf{k}''} \left(\langle n\mathbf{k}|r_e^a|\ell\mathbf{k}''\rangle \langle \ell\mathbf{k}''|v^{\text{LDA},b}|m\mathbf{k}'\rangle - \langle n\mathbf{k}|v^{\text{LDA},b}|\ell\mathbf{k}''\rangle \langle \ell\mathbf{k}''|r_e^a|m\mathbf{k}'\rangle \right) \\ &= \sum_{\ell\mathbf{k}''} \left((1 - \delta_{n\ell})\delta(\mathbf{k} - \mathbf{k}'')\xi_{n\ell}^a\delta(\mathbf{k}'' - \mathbf{k}')v_{\ell m}^{\text{LDA},b} \right. \\ &\quad \left. - \delta(\mathbf{k} - \mathbf{k}'')v_{n\ell}^{\text{LDA},b}(1 - \delta_{\ell m})\delta(\mathbf{k}'' - \mathbf{k}')\xi_{\ell m}^a \right) \\ &= \delta(\mathbf{k} - \mathbf{k}') \sum_{\ell} \left((1 - \delta_{n\ell})\xi_{n\ell}^a v_{\ell m}^{\text{LDA},b} - (1 - \delta_{\ell m})v_{n\ell}^{\text{LDA},b}\xi_{\ell m}^a \right) \\ &= \delta(\mathbf{k} - \mathbf{k}') \left(\sum_{\ell} \left(\xi_{n\ell}^a v_{\ell m}^{\text{LDA},b} - v_{n\ell}^{\text{LDA},b}\xi_{\ell m}^a \right) + v_{nm}^{\text{LDA},b}(\xi_{mm}^a - \xi_{nn}^a) \right). \end{aligned} \quad (\text{A.97})$$

Using Eqs. (A.95) and (A.97) into Eq. (A.94) gives

$$i\delta(\mathbf{k} - \mathbf{k}') \left((v_{nm}^{\text{LDA},b})_{;k^a} - i \sum_{\ell} \left(\xi_{n\ell}^a v_{\ell m}^{\text{LDA},b} - v_{n\ell}^{\text{LDA},b}\xi_{\ell m}^a \right) - iv_{nm}^{\text{LDA},b}(\xi_{mm}^a - \xi_{nn}^a) \right) = \tau_{nm}^{ab}(\mathbf{k})\delta(\mathbf{k} - \mathbf{k}'), \quad (\text{A.98})$$

then

$$(v_{nm}^{\text{LDA},b})_{;k^a} = -i\tau_{nm}^{ab} + i \sum_{\ell} \left(\xi_{n\ell}^a v_{\ell m}^{\text{LDA},b} - v_{n\ell}^{\text{LDA},b}\xi_{\ell m}^a \right) + iv_{nm}^{\text{LDA},b}(\xi_{mm}^a - \xi_{nn}^a), \quad (\text{A.99})$$

and from Eq. (A.96),

$$\nabla_{k^a} v_{nm}^{\text{LDA},b} = -i\tau_{nm}^{ab} + i \sum_{\ell} \left(\xi_{n\ell}^a v_{\ell m}^{\text{LDA},b} - v_{n\ell}^{\text{LDA},b}\xi_{\ell m}^a \right). \quad (\text{A.100})$$

Now, there are two cases. We use Eq. (2.45).

A.7.1 Case $n = m$

$$\begin{aligned}
\nabla_{k^a} v_{nn}^{\text{LDA},b} &= -i\tau_{nn}^{ab} + i \sum_{\ell} \left(\xi_{n\ell}^a v_{\ell n}^{\text{LDA},b} - v_{n\ell}^{\text{LDA},b} \xi_{\ell n}^a \right) \\
&= -i\tau_{nn}^{ab} - \sum_{\ell \neq n} \left(r_{n\ell}^a \omega_{\ell n}^{\text{LDA}} r_{\ell n}^b - \omega_{n\ell}^{\text{LDA}} r_{n\ell}^b r_{\ell n}^a \right) \\
&= -i\tau_{nn}^{ab} - \sum_{\ell \neq n} \omega_{\ell n}^{\text{LDA}} \left(r_{n\ell}^a r_{\ell n}^b - r_{n\ell}^b r_{\ell n}^a \right), \tag{A.101}
\end{aligned}$$

since the $\ell = n$ cancels out. This would give the generalization for the inverse effective mass tensor $(m_n^{-1})_{ab}$ for nonlocal potentials. Indeed, if we neglect the commutator of \mathbf{v}^{nl} in Eq. (A.92), we obtain $-i\tau_{nn}^{ab} = \hbar/m_e \delta_{ab}$ thus obtaining the familiar expression of $(m_n^{-1})_{ab}$ [164].

A.7.2 Case $n \neq m$

$$\begin{aligned}
(v_{nm}^{\text{LDA},b})_{;k^a} &= -i\tau_{nm}^{ab} + i \sum_{\ell \neq m \neq n} \left(\xi_{n\ell}^a v_{\ell m}^{\text{LDA},b} - v_{n\ell}^{\text{LDA},b} \xi_{\ell m}^a \right) + i \left(\xi_{nm}^a v_{mm}^{\text{LDA},b} - v_{nm}^{\text{LDA},b} \xi_{mm}^a \right) \\
&\quad + i \left(\xi_{nn}^a v_{nm}^{\text{LDA},b} - v_{nn}^{\text{LDA},b} \xi_{nm}^a \right) + i v_{nm}^{\text{LDA},b} (\xi_{mm}^a - \xi_{nn}^a) \\
&= -i\tau_{nm}^{ab} - \sum_{\ell} \left(\omega_{\ell m}^{\text{LDA}} r_{n\ell}^a r_{\ell m}^b - \omega_{n\ell}^{\text{LDA}} r_{n\ell}^b r_{\ell m}^a \right) + i \xi_{nm}^a (v_{mm}^{\text{LDA},b} - v_{nn}^{\text{LDA},b}) \\
&= -i\tau_{nm}^{ab} - \sum_{\ell} \left(\omega_{\ell m}^{\text{LDA}} r_{n\ell}^a r_{\ell m}^b - \omega_{n\ell}^{\text{LDA}} r_{n\ell}^b r_{\ell m}^a \right) + i r_{nm}^a \Delta_{mn}^b, \tag{A.102}
\end{aligned}$$

where we use Δ_{mn}^a of Eq. (2.77). Now, for $n \neq m$, Eqs. (2.45), (A.72) and (A.102) and the chain rule, give

$$\begin{aligned}
(r_{nm}^b)_{;k^a} &= \left(\frac{v_{nm}^{\text{LDA},b}}{i\omega_{nm}^{\text{LDA}}} \right)_{;k^a} = \frac{1}{i\omega_{nm}^{\text{LDA}}} (v_{nm}^{\text{LDA},b})_{;k^a} - \frac{v_{nm}^{\text{LDA},b}}{i(\omega_{nm}^{\text{LDA}})^2} (\omega_{nm}^{\text{LDA}})_{;k^a} \\
&= -i\tau_{nm}^{ab} + \frac{i}{\omega_{nm}^{\text{LDA}}} \sum_{\ell} \left(\omega_{\ell m}^{\text{LDA}} r_{n\ell}^a r_{\ell m}^b - \omega_{n\ell}^{\text{LDA}} r_{n\ell}^b r_{\ell m}^a \right) + \frac{r_{nm}^a \Delta_{mn}^b}{\omega_{nm}^{\text{LDA}}} - \frac{r_{nm}^b}{\omega_{nm}^{\text{LDA}}} (\omega_{nm}^{\text{LDA}})_{;k^a} \\
&= -i\tau_{nm}^{ab} + \frac{i}{\omega_{nm}^{\text{LDA}}} \sum_{\ell} \left(\omega_{\ell m}^{\text{LDA}} r_{n\ell}^a r_{\ell m}^b - \omega_{n\ell}^{\text{LDA}} r_{n\ell}^b r_{\ell m}^a \right) + \frac{r_{nm}^a \Delta_{mn}^b}{\omega_{nm}^{\text{LDA}}} - \frac{r_{nm}^b}{\omega_{nm}^{\text{LDA}}} \frac{v_{nn}^{\text{LDA},a} - v_{mm}^{\text{LDA},a}}{m_e} \\
&= -i\tau_{nm}^{ab} + \frac{r_{nm}^a \Delta_{mn}^b + r_{nm}^b \Delta_{mn}^a}{\omega_{nm}^{\text{LDA}}} + \frac{i}{\omega_{nm}^{\text{LDA}}} \sum_{\ell} \left(\omega_{\ell m}^{\text{LDA}} r_{n\ell}^a r_{\ell m}^b - \omega_{n\ell}^{\text{LDA}} r_{n\ell}^b r_{\ell m}^a \right), \tag{A.103}
\end{aligned}$$

where the $-i\tau_{nm}^{ab}$ term, generalizes the usual expression of $\mathbf{r}_{nm;k}$ for local Hamiltonians, [65, 66, 80, 81] to the case of a nonlocal potential in the Hamiltonian.

A.7.3 Layer Case

To obtain the generalized derivative expressions for the case of the layered matrix elements are required by Eq. (2.69), we could start from Eq. (A.92) again, and replace $\hat{\mathbf{v}}^{\text{LDA}}$ by \mathbf{V}^{LDA} , to

obtain the equivalent of Eqs. (A.101) and (A.102), for which we need to calculate the new τ_{nm}^{ab} , that is given by

$$\begin{aligned}
\mathcal{T}_{nm}^{ab} &= [r^a, \mathcal{V}^{\text{LDA},b}]_{nm} = [r^a, \mathcal{V}^b]_{nm} + [r^a, \mathcal{V}^{\text{nl},b}]_{nm} \\
&= \frac{1}{2} [r^a, v^b C^\ell(z) + C^\ell(z) v^b]_{nm} + \frac{1}{2} [r^a, v^{\text{nl},b} C^\ell(z) + C^\ell(z) v^{\text{nl},b}]_{nm} \\
&= ([r^a, v^b] C^\ell(z))_{nm} + ([r^a, v^{\text{nl},b}] C^\ell(z))_{nm} \\
&= \sum_p [r^a, v^b]_{np} C_{pm}^\ell + \sum_p [r^a, v^{\text{nl},b}]_{np} C_{pm}^\ell \\
&= \frac{i\hbar}{m_e} \delta_{ab} C_{nm}^\ell + \sum_p [r^a, v^{\text{nl},b}]_{np} C_{pm}^\ell. \tag{A.104}
\end{aligned}$$

For a full-slab calculation, that would correspond to a bulk calculation as well, $C^\ell(z) = 1$ and then, $C_{nm}^\ell = \delta_{nm}$, and from above expression $\mathcal{T}_{nm}^{ab} \rightarrow \tau_{nm}^{ab}$. Thus, the layered expression for $\mathcal{V}_{nm}^{\text{LDA},a}$ becomes

$$(\mathcal{V}_{nm}^{\text{LDA},a})_{;k^b} = \frac{\hbar}{m_e} \delta_{ab} C_{nm}^\ell - i \sum_p [r^b, v^{\text{nl},a}]_{np} C_{pm}^\ell + i \sum_\ell \left(r_{n\ell}^b \mathcal{V}_{\ell m}^{\text{LDA},a} - \mathcal{V}_{n\ell}^{\text{LDA},a} r_{\ell m}^b \right) + i r_{nm}^b \tilde{\Delta}_{mn}^a, \tag{A.105}$$

where

$$\tilde{\Delta}_{mn}^a = \mathcal{V}_{nn}^{\text{LDA},a} - \mathcal{V}_{mm}^{\text{LDA},a}. \tag{A.106}$$

As mentioned before, the term $[r^b, v^{\text{nl},a}]_{nm}$ calculated in Sec. A.8, is small compared to the other terms, thus we neglect it throughout this work. [118] The expression for C_{nm}^ℓ is calculated in Sec. A.3.

A.8 Matrix elements of $\tau_{nm}^{ab}(\mathbf{k})$

To calculate τ_{nm}^{ab} , we first need to calculate

$$\mathcal{L}_{nm}^{ab}(\mathbf{k}) = \frac{1}{i\hbar} \langle n\mathbf{k} | [\hat{r}^a, \hat{v}^{\text{nl},b}] | m\mathbf{k}' \rangle \delta(\mathbf{k} - \mathbf{k}') = \frac{1}{\hbar^2} \langle n\mathbf{k} | [\hat{r}^a, [\hat{V}^{\text{nl}}(\hat{\mathbf{r}}, \hat{\mathbf{r}}'), \hat{r}^b]] | m\mathbf{k}' \rangle \delta(\mathbf{k} - \mathbf{k}'), \tag{A.107}$$

for which we need the following triple commutator

$$[\hat{r}^a, [\hat{V}^{\text{nl}}(\hat{\mathbf{r}}, \hat{\mathbf{r}}'), \hat{r}^b]] = [\hat{r}^b, [\hat{V}^{\text{nl}}(\hat{\mathbf{r}}, \hat{\mathbf{r}}'), \hat{r}^a]], \tag{A.108}$$

where the right hand side follows from the Jacobi identity, since $[\hat{r}^a, \hat{r}^b] = 0$. We expand the triple commutator as

$$\begin{aligned}
[\hat{r}^a, [\hat{V}^{\text{nl}}(\hat{\mathbf{r}}, \hat{\mathbf{r}}'), \hat{r}^b]] &= [\hat{r}^a, \hat{V}^{\text{nl}}(\hat{\mathbf{r}}, \hat{\mathbf{r}}') \hat{r}^b] - [\hat{r}^a, \hat{r}^b \hat{V}^{\text{nl}}(\hat{\mathbf{r}}, \hat{\mathbf{r}}')] \\
&= [\hat{r}^a, \hat{V}^{\text{nl}}(\hat{\mathbf{r}}, \hat{\mathbf{r}}')] \hat{r}^b - \hat{r}^b [\hat{r}^a, \hat{V}^{\text{nl}}(\hat{\mathbf{r}}, \hat{\mathbf{r}}')] \\
&= \hat{r}^a \hat{V}^{\text{nl}}(\hat{\mathbf{r}}, \hat{\mathbf{r}}') \hat{r}^b - \hat{V}^{\text{nl}}(\hat{\mathbf{r}}, \hat{\mathbf{r}}') \hat{r}^a \hat{r}^b - \hat{r}^b \hat{r}^a \hat{V}^{\text{nl}}(\hat{\mathbf{r}}, \hat{\mathbf{r}}') + \hat{r}^b \hat{V}^{\text{nl}}(\hat{\mathbf{r}}, \hat{\mathbf{r}}') \hat{r}^a. \tag{A.109}
\end{aligned}$$

Then,

$$\begin{aligned}
& \frac{1}{\hbar^2} \langle n\mathbf{k}| \left[\hat{r}^a, \left[\hat{V}^{nl}(\hat{\mathbf{r}}, \hat{\mathbf{r}}'), \hat{r}^b \right] \right] |m\mathbf{k}'\rangle = \frac{1}{\hbar^2} \int \langle n\mathbf{k}| |\mathbf{r}\rangle \langle \mathbf{r}| \left[\hat{r}^a, \left[\hat{V}^{nl}(\hat{\mathbf{r}}, \hat{\mathbf{r}}'), \hat{r}^b \right] \right] |\mathbf{r}'\rangle \langle \mathbf{r}'| |m\mathbf{k}'\rangle \delta(\mathbf{k} - \mathbf{k}') d\mathbf{r} d\mathbf{r}' \\
&= \frac{1}{\hbar^2} \int \psi_{n\mathbf{k}}^*(\mathbf{r}) \left(r^a V^{nl}(\mathbf{r}, \mathbf{r}') r'^b \right. \\
&\quad \left. - V^{nl}(\mathbf{r}, \mathbf{r}') r'^a r'^b - r^b r^a V^{nl}(\mathbf{r}, \mathbf{r}') + r^b V^{nl}(\mathbf{r}, \mathbf{r}') r'^a \right) \psi_{m\mathbf{k}}(\mathbf{r}') \delta(\mathbf{k} - \mathbf{k}') d\mathbf{r} d\mathbf{r}' \\
&= \frac{1}{\hbar^2 \Omega} \sum_{\mathbf{K}, \mathbf{K}'} C_{n\mathbf{k}}^*(\mathbf{K}) C_{m\mathbf{k}}(\mathbf{K}') \int e^{-i\mathbf{K}\cdot\mathbf{r}} \left(r^a V^{nl}(\mathbf{r}, \mathbf{r}') r'^b - V^{nl}(\mathbf{r}, \mathbf{r}') r'^a r'^b \right. \\
&\quad \left. - r^b r^a V^{nl}(\mathbf{r}, \mathbf{r}') + r^b V^{nl}(\mathbf{r}, \mathbf{r}') r'^a \right) e^{i\mathbf{K}'\cdot\mathbf{r}'} \delta(\mathbf{k} - \mathbf{k}') d\mathbf{r} d\mathbf{r}'.
\end{aligned} \tag{A.110}$$

We use the following identity,

$$\begin{aligned}
& \left(\frac{\partial^2}{\partial K^a \partial K'^b} + \frac{\partial^2}{\partial K'^a \partial K'^b} + \frac{\partial^2}{\partial K^a \partial K^b} + \frac{\partial^2}{\partial K^b \partial K'^a} \right) \int e^{-i\mathbf{K}\cdot\mathbf{r}} V^{nl}(\mathbf{r}, \mathbf{r}') e^{i\mathbf{K}'\cdot\mathbf{r}'} d\mathbf{r} d\mathbf{r}' \\
&= \int e^{-i\mathbf{K}\cdot\mathbf{r}} \left(r^a V^{nl}(\mathbf{r}, \mathbf{r}') r'^b - V^{nl}(\mathbf{r}, \mathbf{r}') r'^a r'^b - r^b r^a V^{nl}(\mathbf{r}, \mathbf{r}') + r^b V^{nl}(\mathbf{r}, \mathbf{r}') r'^a \right) e^{i\mathbf{K}'\cdot\mathbf{r}'} d\mathbf{r} d\mathbf{r}' \\
&= \left(\frac{\partial^2}{\partial K^a \partial K'^b} + \frac{\partial^2}{\partial K'^a \partial K'^b} + \frac{\partial^2}{\partial K^a \partial K^b} + \frac{\partial^2}{\partial K^b \partial K'^a} \right) \langle \mathbf{K} | V^{nl} | \mathbf{K}' \rangle,
\end{aligned} \tag{A.111}$$

to write

$$\mathcal{L}_{nm}^{ab}(\mathbf{k}) = \frac{1}{\hbar^2 \Omega} \sum_{\mathbf{K}, \mathbf{K}'} C_{n\mathbf{k}}^*(\mathbf{K}) C_{m\mathbf{k}}(\mathbf{K}') \left(\frac{\partial^2}{\partial K^a \partial K'^b} + \frac{\partial^2}{\partial K'^a \partial K'^b} + \frac{\partial^2}{\partial K^a \partial K^b} + \frac{\partial^2}{\partial K^b \partial K'^a} \right) \langle \mathbf{K} | V^{nl} | \mathbf{K}' \rangle. \tag{A.112}$$

The double derivatives with respect to \mathbf{K} and \mathbf{K}' can be worked out as shown in Sec. A.2, to obtain the matrix elements of $[\hat{V}^{nl}(\hat{\mathbf{r}}, \hat{\mathbf{r}}'), \hat{r}^b]$ [121]. Therefore, we can obtain the value of the matrix elements of the triple commutator [118].

With above results we can proceed to evaluate the matrix elements $\tau_{nm}(\mathbf{k})$. From Eq. (A.92)

$$\begin{aligned}
\langle n\mathbf{k} | \tau^{ab} | m\mathbf{k}' \rangle &= \langle n\mathbf{k} | \frac{i\hbar}{m_e} \delta_{ab} | m\mathbf{k}' \rangle + \langle n\mathbf{k} | \frac{1}{i\hbar} [r^a, v^{nl,b}] | m\mathbf{k}' \rangle \\
\mathcal{L}_{nm}^{ab}(\mathbf{k}) \delta(\mathbf{k} - \mathbf{k}') &= \delta(\mathbf{k} - \mathbf{k}') \left(\frac{i\hbar}{m_e} \delta_{ab} \delta_{nm} + \mathcal{L}_{nm}^{ab}(\mathbf{k}) \right) \\
\tau_{nm}^{ab}(\mathbf{k}) &= \tau_{nm}^{ba}(\mathbf{k}) = \frac{i\hbar}{m_e} \delta_{ab} \delta_{nm} + \mathcal{L}_{nm}^{ab}(\mathbf{k}),
\end{aligned} \tag{A.113}$$

which is an explicit expression that can be numerically calculated.

A.9 Scissors renormalization for \mathcal{V}_{nm}^Σ

We derive the scissors renormalization for \mathcal{V}_{nm}^Σ . For the scissors case, we have

$$\begin{aligned}\langle n\mathbf{k}|\mathcal{C}(z)\mathbf{r}|m\mathbf{k}\rangle(E_m^\Sigma - E_n^\Sigma) &= \int d\mathbf{r} \psi_{n\mathbf{k}}^*(\mathbf{r})\mathcal{C}(z)\mathbf{r}(E_m^\Sigma - E_n^\Sigma)\psi_{m\mathbf{k}}(\mathbf{r}) \\ &= \int d\mathbf{r} \psi_{n\mathbf{k}}^*(\mathbf{r})\mathcal{C}(z)[\mathbf{r}, H^\Sigma]\psi_{m\mathbf{k}}(\mathbf{r}) \\ &= -i \int d\mathbf{r} \psi_{n\mathbf{k}}^*(\mathbf{r})\mathcal{C}(z)\mathbf{v}^\Sigma\psi_{m\mathbf{k}}(\mathbf{r}) = \mathcal{V}_{nm}^\Sigma \\ \langle n\mathbf{k}|\mathcal{C}(z)\mathbf{r}|m\mathbf{k}\rangle &= \frac{\mathcal{V}_{nm}^\Sigma}{\omega_{nm}^\Sigma}. \end{aligned} \tag{A.114}$$

For the LDA case, we have

$$\begin{aligned}\langle n\mathbf{k}|\mathcal{C}(z)\mathbf{r}|m\mathbf{k}\rangle(E_m^{\text{LDA}} - E_n^{\text{LDA}}) &= \int d\mathbf{r} \psi_{n\mathbf{k}}^*(\mathbf{r})\mathcal{C}(z)\mathbf{r}(E_m^{\text{LDA}} - E_n^{\text{LDA}})\psi_{m\mathbf{k}}(\mathbf{r}) \\ &= \int d\mathbf{r} \psi_{n\mathbf{k}}^*(\mathbf{r})\mathcal{C}(z)[\mathbf{r}, H^{\text{LDA}}]\psi_{m\mathbf{k}}(\mathbf{r}) \\ &= -i \int d\mathbf{r} \psi_{n\mathbf{k}}^*(\mathbf{r})\mathcal{C}(z)\mathbf{v}^{\text{LDA}}\psi_{m\mathbf{k}}(\mathbf{r}) = \mathcal{V}_{nm}^{\text{LDA}} \\ \langle n\mathbf{k}|\mathcal{C}(z)\mathbf{r}|m\mathbf{k}\rangle &= \frac{\mathcal{V}_{nm}^{\text{LDA}}}{\omega_{nm}^{\text{LDA}}}. \end{aligned} \tag{A.115}$$

Then, using the previous two equations, it follows that

$$\mathcal{V}_{nm}^\Sigma = \frac{\omega_{nm}^\Sigma}{\omega_{nm}^{\text{LDA}}} \mathcal{V}_{nm}^{\text{LDA}}. \tag{A.116}$$

Appendix B

Complete Derivations for the SSHG yield

Outline

B.1	Some useful expressions	96
B.1.1	2 ω terms	96
B.1.2	1 ω terms	97
B.1.3	Nonzero components of $\chi(-2\omega; \omega, \omega)$	98
B.2	\mathcal{R}_{pP}	99
B.2.1	For the (111) surface	100
B.2.2	For the (110) surface	103
B.2.3	For the (001) surface	104
B.3	\mathcal{R}_{ps}	105
B.3.1	For the (111) surface	106
B.3.2	For the (110) surface	107
B.3.3	For the (001) surface	107
B.4	\mathcal{R}_{sP}	107
B.4.1	For the (111) surface	108
B.4.2	For the (110) surface	109
B.4.3	For the (001) surface	110
B.5	\mathcal{R}_{ss}	110
B.5.1	For the (111) surface	111
B.5.2	For the (110) surface	111
B.5.3	For the (001) surface	111

B.1 Some useful expressions

We are interested in finding

$$\Upsilon = \mathbf{e}_\ell^{2\omega} \cdot \boldsymbol{\chi} : \mathbf{e}_\ell^\omega \mathbf{e}_\ell^\omega$$

for each different polarization case. We choose the plane of incidence along the κz plane, and define

$$\hat{\kappa} = \cos \phi \hat{\mathbf{x}} + \sin \phi \hat{\mathbf{y}}, \quad (\text{B.1})$$

and

$$\hat{\mathbf{s}} = -\sin \phi \hat{\mathbf{x}} + \cos \phi \hat{\mathbf{y}}, \quad (\text{B.2})$$

where ϕ the angle with respect to the x axis.

B.1.1 2ω terms

Including multiple reflections, the $\mathbf{e}_\ell^{2\omega}$ term is

$$\mathbf{e}_\ell^{2\omega} = \hat{\mathbf{e}}^{\text{out}} \cdot \left[\hat{\mathbf{s}} T_s^{v\ell} R_s^{M+} \hat{\mathbf{s}} + \hat{\mathbf{P}}_{v+} \frac{T_p^{v\ell}}{N_\ell} \left(\sin \theta_0 R_p^{M+} \hat{\mathbf{z}} - W_\ell R_p^{M-} \hat{\kappa} \right) \right], \quad (\text{B.3})$$

and neglecting the multiple reflections reduces this expression to

$$\mathbf{e}_\ell^{2\omega} = \hat{\mathbf{e}}^{\text{out}} \cdot \left[\hat{\mathbf{s}} T_s^{v\ell} T_s^{\ell b} \hat{\mathbf{s}} + \hat{\mathbf{P}}_{v+} \frac{T_p^{v\ell} T_p^{\ell b}}{N_\ell^2 N_b} \left(N_b^2 \sin \theta_0 \hat{\mathbf{z}} - N_\ell^2 W_b \hat{\kappa} \right) \right]. \quad (\text{B.4})$$

We first expand these equations for clarity. Substituting Eqs. (B.1) and (B.2) into Eq. (B.3),

$$\begin{aligned} \mathbf{e}_\ell^{2\omega} = & \hat{\mathbf{e}}^{\text{out}} \cdot \left[\hat{\mathbf{s}} T_s^{v\ell} R_s^{M+} (-\sin \phi \hat{\mathbf{x}} + \cos \phi \hat{\mathbf{y}}) \right. \\ & \left. + \hat{\mathbf{P}}_{v+} \frac{T_p^{v\ell}}{N_\ell} \left(\sin \theta_0 R_p^{M+} \hat{\mathbf{z}} - W_\ell R_p^{M-} \cos \phi \hat{\mathbf{x}} - W_\ell R_p^{M-} \sin \phi \hat{\mathbf{y}} \right) \right]. \end{aligned}$$

We now have $\mathbf{e}_\ell^{2\omega}$ in terms of $\hat{\mathbf{P}}_{v+}$,

$$\mathbf{e}_\ell^{2\omega} = \frac{T_p^{v\ell}}{N_\ell} \left(\sin \theta_0 R_p^{M+} \hat{\mathbf{z}} - W_\ell R_p^{M-} \cos \phi \hat{\mathbf{x}} - W_\ell R_p^{M-} \sin \phi \hat{\mathbf{y}} \right), \quad (\text{B.5})$$

and in terms of $\hat{\mathbf{s}}$,

$$\mathbf{e}_\ell^{2\omega} = T_s^{v\ell} R_s^{M+} (-\sin \phi \hat{\mathbf{x}} + \cos \phi \hat{\mathbf{y}}). \quad (\text{B.6})$$

If we wish to neglect the effects from the multiple reflections, we do the exact same for Eq. (B.4), and get the following term for $\hat{\mathbf{P}}_{v+}$,

$$\mathbf{e}_\ell^{2\omega} = \frac{T_p^{v\ell} T_p^{\ell b}}{N_\ell^2 N_b} \left(N_b^2 \sin \theta_0 \hat{\mathbf{z}} - N_\ell^2 W_b \cos \phi \hat{\mathbf{x}} - N_\ell^2 W_b \sin \phi \hat{\mathbf{y}} \right), \quad (\text{B.7})$$

and $\hat{\mathbf{s}}$,

$$\mathbf{e}_\ell^{2\omega} = T_s^{v\ell} T_s^{\ell b} [-\sin \phi \hat{\mathbf{x}} + \cos \phi \hat{\mathbf{y}}]. \quad (\text{B.8})$$

B.1.2 1ω terms

We have that the \mathbf{e}_ℓ^ω term is

$$\mathbf{e}_\ell^\omega = \left[\hat{\mathbf{s}} t_s^{v\ell} r_s^{M+} \hat{\mathbf{s}} + \frac{t_p^{v\ell}}{n_\ell} \left(r_p^{M+} \sin \theta_0 \hat{\mathbf{z}} + r_p^{M-} w_\ell \hat{\boldsymbol{\kappa}} \right) \hat{\mathbf{p}}_{v-} \right] \cdot \hat{\mathbf{e}}^{\text{in}}.$$

We are interested in finding $\mathbf{e}_\ell^\omega \mathbf{e}_\ell^\omega$ for both polarizations. For $\hat{\mathbf{e}}^{\text{in}} = \hat{\mathbf{p}}_{v-}$ we have

$$\mathbf{e}_\ell^\omega = \frac{t_p^{v\ell}}{n_\ell} \left(r_p^{M+} \sin \theta_0 \hat{\mathbf{z}} + r_p^{M-} w_\ell \cos \phi \hat{\mathbf{x}} + r_p^{M-} w_\ell \sin \phi \hat{\mathbf{y}} \right),$$

so

$$\begin{aligned} \mathbf{e}_\ell^\omega \mathbf{e}_\ell^\omega &= \left(\frac{t_p^{v\ell}}{n_\ell} \right)^2 \left(\left(r_p^{M-} \right)^2 w_\ell^2 \cos^2 \phi \hat{\mathbf{x}} \hat{\mathbf{x}} + 2 \left(r_p^{M-} \right)^2 w_\ell^2 \sin \phi \cos \phi \hat{\mathbf{x}} \hat{\mathbf{y}} \right. \\ &\quad + 2 r_p^{M+} r_p^{M-} w_\ell \sin \theta_0 \cos \phi \hat{\mathbf{x}} \hat{\mathbf{z}} + \left(r_p^{M-} \right)^2 w_\ell^2 \sin^2 \phi \hat{\mathbf{y}} \hat{\mathbf{y}} \\ &\quad \left. + 2 r_p^{M+} r_p^{M-} w_\ell \sin \theta_0 \sin \phi \hat{\mathbf{z}} \hat{\mathbf{y}} + \left(r_p^{M+} \right)^2 \sin^2 \theta_0 \hat{\mathbf{z}} \hat{\mathbf{z}} \right), \end{aligned} \quad (\text{B.9})$$

and for $\hat{\mathbf{e}}^{\text{in}} = \hat{\mathbf{s}}$,

$$\mathbf{e}_\ell^\omega \mathbf{e}_\ell^\omega = \left(t_s^{v\ell} r_s^{M+} \right)^2 \left(\sin^2 \phi \hat{\mathbf{x}} \hat{\mathbf{x}} + \cos^2 \phi \hat{\mathbf{y}} \hat{\mathbf{y}} - 2 \sin \phi \cos \phi \hat{\mathbf{x}} \hat{\mathbf{y}} \right). \quad (\text{B.10})$$

Neglecting the effects of the multiple reflections for the \mathbf{e}_ℓ^ω term yields

$$\mathbf{e}_\ell^\omega = \left[\hat{\mathbf{s}} t_s^{v\ell} t_s^{\ell b} \hat{\mathbf{s}} + \frac{t_p^{v\ell} t_p^{\ell b}}{n_\ell^2 n_b} \left(n_b^2 \sin \theta_0 \hat{\mathbf{z}} + n_\ell^2 w_b \hat{\boldsymbol{\kappa}} \right) \hat{\mathbf{p}}_{v-} \right] \cdot \hat{\mathbf{e}}^{\text{in}}.$$

For all cases, we require a $\mathbf{e}_\ell^\omega \mathbf{e}_\ell^\omega$ product. For brevity, we will directly list these terms for both polarizations. For $\hat{\mathbf{e}}^{\text{in}} = \hat{\mathbf{p}}_{v-}$,

$$\begin{aligned} \mathbf{e}_\ell^\omega \mathbf{e}_\ell^\omega &= \left(\frac{t_p^{v\ell} t_p^{\ell b}}{n_\ell^2 n_b} \right)^2 \left(n_\ell^4 w_b^2 \cos^2 \phi \hat{\mathbf{x}} \hat{\mathbf{x}} + 2 n_\ell^4 w_b^2 \sin \phi \cos \phi \hat{\mathbf{x}} \hat{\mathbf{y}} \right. \\ &\quad + 2 n_\ell^2 n_b^2 w_b \sin \theta_0 \cos \phi \hat{\mathbf{x}} \hat{\mathbf{z}} + n_\ell^4 w_b^2 \sin^2 \phi \hat{\mathbf{y}} \hat{\mathbf{y}} \\ &\quad \left. + 2 n_\ell^2 n_b^2 w_b \sin \theta_0 \sin \phi \hat{\mathbf{y}} \hat{\mathbf{z}} + n_b^4 \sin^2 \theta_0 \hat{\mathbf{z}} \hat{\mathbf{z}} \right), \end{aligned} \quad (\text{B.11})$$

and for $\hat{\mathbf{e}}^{\text{in}} = \hat{\mathbf{s}}$,

$$\mathbf{e}_\ell^\omega \mathbf{e}_\ell^\omega = \left(t_s^{v\ell} t_s^{\ell b} \right)^2 \left(\sin^2 \phi \hat{\mathbf{x}} \hat{\mathbf{x}} + \cos^2 \phi \hat{\mathbf{y}} \hat{\mathbf{y}} - 2 \sin \phi \cos \phi \hat{\mathbf{x}} \hat{\mathbf{y}} \right). \quad (\text{B.12})$$

We summarize these expressions in Table B.1. In order to derive the equations for a given polarization case, we refer to the equations listed there. Then it is simply a matter of multiplying the terms correctly and obtaining the appropriate components of $\chi(-2\omega; \omega, \omega)$.

B.1.3 Nonzero components of $\chi(-2\omega; \omega, \omega)$

For a (111) surface with C_{3v} symmetry, we have the following nonzero components:

$$\begin{aligned}\chi^{xxx} &= -\chi^{xyy} = -\chi^{yyx}, \\ \chi^{xxz} &= \chi^{yyz}, \\ \chi^{zxx} &= \chi^{zyy}, \\ \chi^{zzz}.\end{aligned}\tag{B.13}$$

For a (110) surface with C_{2v} symmetry, we have the following nonzero components:

$$\chi^{xxz}, \chi^{yyz}, \chi^{zxx}, \chi^{zyy}, \chi^{zzz}.\tag{B.14}$$

Lastly, for a (001) surface with C_{4v} symmetry, we have the following nonzero components:

$$\begin{aligned}\chi^{xxz} &= \chi^{yyz}, \\ \chi^{zxx} &= \chi^{zyy}, \\ \chi^{zzz}.\end{aligned}\tag{B.15}$$

Case	$\hat{\mathbf{e}}^{\text{out}}$	$\hat{\mathbf{e}}^{\text{in}}$	$\mathbf{e}_\ell^{2\omega}$	$\mathbf{e}_\ell^\omega \mathbf{e}_\ell^\omega$
\mathcal{R}_{pP}	$\hat{\mathbf{P}}_{v+}$	$\hat{\mathbf{p}}_{v-}$	Eq. (B.5) or (B.7)	Eq. (B.9) or Eq. (B.11)
\mathcal{R}_{pS}	$\hat{\mathbf{s}}$	$\hat{\mathbf{p}}_{v-}$	Eq. (B.6) or (B.8)	Eq. (B.9) or Eq. (B.11)
\mathcal{R}_{sP}	$\hat{\mathbf{P}}_{v+}$	$\hat{\mathbf{s}}$	Eq. (B.5) or (B.7)	Eq. (B.10) or Eq. (B.12)
\mathcal{R}_{sS}	$\hat{\mathbf{s}}$	$\hat{\mathbf{s}}$	Eq. (B.6) or (B.8)	Eq. (B.10) or Eq. (B.12)

Table B.1: Polarization unit vectors for $\hat{\mathbf{e}}^{\text{out}}$ and $\hat{\mathbf{e}}^{\text{in}}$, and equations describing $\mathbf{e}_\ell^{2\omega}$ and $\mathbf{e}_\ell^\omega \mathbf{e}_\ell^\omega$ for each polarization case. When there are two equations to choose from, the former includes the effects of multiple reflections, and the latter neglects them.

B.2 \mathcal{R}_{pP}

Per Table B.1, \mathcal{R}_{pP} requires Eqs. (B.5) and (B.9). After some algebra, we obtain that

$$\begin{aligned}
\Upsilon_{pP}^{\text{MR}} = \Gamma_{pP}^{\text{MR}} & \left[-R_p^{M-} \left(r_p^{M-} \right)^2 w_\ell^2 W_\ell \cos^3 \phi \chi^{xxx} \right. \\
& - 2R_p^{M-} \left(r_p^{M-} \right)^2 w_\ell^2 W_\ell \sin \phi \cos^2 \phi \chi^{xxy} \\
& - 2R_p^{M-} r_p^{M+} r_p^{M-} w_\ell W_\ell \sin \theta_0 \cos^2 \phi \chi^{xxz} \\
& - R_p^{M-} \left(r_p^{M-} \right)^2 w_\ell^2 W_\ell \sin^2 \phi \cos \phi \chi^{xyy} \\
& - 2R_p^{M-} r_p^{M+} r_p^{M-} w_\ell W_\ell \sin \theta_0 \sin \phi \cos \phi \chi^{xyz} \\
& - R_p^{M-} \left(r_p^{M+} \right)^2 W_\ell \sin^2 \theta_0 \cos \phi \chi^{xzz} \\
& - R_p^{M-} \left(r_p^{M-} \right)^2 w_\ell^2 W_\ell \sin \phi \cos^2 \phi \chi^{yxx} \\
& - 2R_p^{M-} \left(r_p^{M-} \right)^2 w_\ell^2 W_\ell \sin^2 \phi \cos \phi \chi^{yxy} \\
& - 2R_p^{M-} r_p^{M+} r_p^{M-} w_\ell W_\ell \sin \theta_0 \sin \phi \cos \phi \chi^{yxz} \\
& - R_p^{M-} \left(r_p^{M-} \right)^2 w_\ell^2 W_\ell \sin^3 \phi \chi^{yyg} \\
& - 2R_p^{M-} r_p^{M+} r_p^{M-} w_\ell W_\ell \sin \theta_0 \sin^2 \phi \chi^{yyz} \\
& - R_p^{M-} \left(r_p^{M+} \right)^2 W_\ell \sin^2 \theta_0 \sin \phi \chi^{yzz} \\
& + R_p^{M+} \left(r_p^{M-} \right)^2 w_\ell^2 \sin \theta_0 \cos^2 \phi \chi^{zxx} \\
& + 2R_p^{M+} r_p^{M+} r_p^{M-} w_\ell \sin^2 \theta_0 \cos \phi \chi^{zxz} \\
& + 2R_p^{M+} \left(r_p^{M-} \right)^2 w_\ell^2 \sin \theta_0 \sin \phi \cos \phi \chi^{zxy} \\
& + R_p^{M+} \left(r_p^{M-} \right)^2 w_\ell^2 \sin \theta_0 \sin^2 \phi \chi^{zyy} \\
& + 2R_p^{M+} r_p^{M+} r_p^{M-} w_\ell \sin^2 \theta_0 \sin \phi \chi^{zzy} \\
& \left. + R_p^{M+} \left(r_p^{M+} \right)^2 \sin^3 \theta_0 \chi^{zzz} \right], \tag{B.16}
\end{aligned}$$

We take this opportunity to introduce a quantity that will be repeated throughout this section,

$$\Gamma_{pP}^{\text{MR}} = \frac{T_p^{v\ell}}{N_\ell} \left(\frac{t_p^{v\ell}}{n_\ell} \right)^2. \tag{B.17}$$

If we neglect the multiple reflections, as described in the manuscript, we have that

$$\begin{aligned}
\Upsilon_{pP} = \Gamma_{pP} & \left[-N_\ell^2 W_b \left(+ n_\ell^4 w_b^2 \cos^3 \phi \chi^{xxx} + 2n_\ell^4 w_b^2 \sin \phi \cos^2 \phi \chi^{xxy} \right. \right. \\
& + 2n_b^2 n_\ell^2 w_b \sin \theta_0 \cos^2 \phi \chi^{xxz} + n_\ell^4 w_b^2 \sin^2 \phi \cos \phi \chi^{xyy} \\
& \left. \left. + 2n_b^2 n_\ell^2 w_b \sin \theta_0 \sin \phi \cos \phi \chi^{xyz} + n_b^4 \sin^2 \theta_0 \cos \phi \chi^{xzz} \right) \right. \\
& - N_\ell^2 W_b \left(+ n_\ell^4 w_b^2 \sin \phi \cos^2 \phi \chi^{yxx} + 2n_\ell^4 w_b^2 \sin^2 \phi \cos \phi \chi^{yxy} \right. \\
& + 2n_b^2 n_\ell^2 w_b \sin \theta_0 \sin \phi \cos \phi \chi^{yxz} + n_\ell^4 w_b^2 \sin^3 \phi \chi^{yyy} \\
& \left. \left. + 2n_b^2 n_\ell^2 w_b \sin \theta_0 \sin^2 \phi \chi^{yyz} + n_b^4 \sin^2 \theta_0 \sin \phi \chi^{yzz} \right) \right. \\
& + N_b^2 \sin \theta_0 \left(+ n_\ell^4 w_b^2 \cos^2 \phi \chi^{zxx} + 2n_\ell^4 w_b^2 \sin \phi \cos \phi \chi^{zxy} \right. \\
& + n_\ell^4 w_b^2 \sin^2 \phi \chi^{zyy} + 2n_\ell^2 n_b^2 w_b \sin \theta_0 \cos \phi \chi^{zxx} \\
& \left. \left. + 2n_\ell^2 n_b^2 w_b \sin \theta_0 \sin \phi \chi^{zzy} + n_b^4 \sin^2 \theta_0 \chi^{zzz} \right) \right], \tag{B.18}
\end{aligned}$$

and again we introduce a quantity that will be repeated throughout this section,

$$\Gamma_{pP} = \frac{T_p^{v\ell} T_p^{\ell b}}{N_\ell^2 N_b} \left(\frac{t_p^{v\ell} t_p^{\ell b}}{n_\ell^2 n_b} \right)^2. \tag{B.19}$$

B.2.1 For the (111) surface

We take Eqs. (B.16) and (B.13), eliminate the components that do not contribute, and apply the symmetry relations as follows,

$$\begin{aligned}
\Upsilon_{pP}^{\text{MR},(111)} = \Gamma_{pP}^{\text{MR}} & \left[-R_p^{M-} \left(r_p^{M-} \right)^2 w_\ell^2 W_\ell \cos^3 \phi \chi^{xxx} \right. \\
& + R_p^{M-} \left(r_p^{M-} \right)^2 w_\ell^2 W_\ell \sin^2 \phi \cos \phi \chi^{xxx} \\
& + 2R_p^{M-} \left(r_p^{M-} \right)^2 w_\ell^2 W_\ell \sin^2 \phi \cos \phi \chi^{xxx} \\
& - 2R_p^{M-} r_p^{M+} r_p^{M-} w_\ell W_\ell \sin \theta_0 \cos^2 \phi \chi^{xxz} \\
& - 2R_p^{M-} r_p^{M+} r_p^{M-} w_\ell W_\ell \sin \theta_0 \sin^2 \phi \chi^{xxz} \\
& + R_p^{M+} \left(r_p^{M-} \right)^2 w_\ell^2 \sin \theta_0 \cos^2 \phi \chi^{zxx} \\
& + R_p^{M+} \left(r_p^{M-} \right)^2 w_\ell^2 \sin \theta_0 \sin^2 \phi \chi^{zxx} \\
& \left. + R_p^{M+} \left(r_p^{M+} \right)^2 \sin^3 \theta_0 \chi^{zzz} \right].
\end{aligned}$$

We reduce terms,

$$\begin{aligned}
\Upsilon_{pP}^{\text{MR},(111)} &= \Gamma_{pP}^{\text{MR}} \left[R_p^{M-} \left(r_p^{M-} \right)^2 w_\ell^2 W_\ell (3 \sin^2 \phi \cos \phi - \cos^3 \phi) \chi^{xxx} \right. \\
&\quad - 2R_p^{M-} r_p^{M+} r_p^{M-} w_\ell W_\ell \sin \theta_0 (\sin^2 \phi + \cos^2 \phi) \chi^{xxz} \\
&\quad + R_p^{M+} \left(r_p^{M+} \right)^2 w_\ell^2 \sin \theta_0 (\sin^2 \phi + \cos^2 \phi) \chi^{zxx} \\
&\quad \left. + R_p^{M+} \left(r_p^{M+} \right)^2 \sin^3 \theta_0 \chi^{zzz} \right] \\
&= \Gamma_{pP}^{\text{MR}} \left[R_p^{M+} \sin \theta_0 \left(\left(r_p^{M+} \right)^2 \sin^2 \theta_0 \chi^{zzz} + \left(r_p^{M-} \right)^2 w_\ell^2 \chi^{zxx} \right) \right. \\
&\quad \left. - R_p^{M-} w_\ell W_\ell \left(2r_p^{M+} r_p^{M-} \sin \theta_0 \chi^{xxz} + \left(r_p^{M-} \right)^2 w_\ell \chi^{xxx} \cos 3\phi \right) \right] \\
&= \Gamma_{pP}^{\text{MR}} r_{pP}^{\text{MR},(111)},
\end{aligned}$$

where

$$\begin{aligned}
r_{pP}^{\text{MR},(111)} &= R_p^{M+} \sin \theta_0 \left(\left(r_p^{M+} \right)^2 \sin^2 \theta_0 \chi^{zzz} + \left(r_p^{M-} \right)^2 w_\ell^2 \chi^{zxx} \right) \\
&\quad - R_p^{M-} w_\ell W_\ell \left(2r_p^{M+} r_p^{M-} \sin \theta_0 \chi^{xxz} + \left(r_p^{M-} \right)^2 w_\ell \chi^{xxx} \cos 3\phi \right). \tag{B.20}
\end{aligned}$$

If we wish to neglect the effects of the multiple reflections, we follow the exact same procedure but starting with Eq. (B.18),

$$\begin{aligned}
\Upsilon_{pP}^{(111)} &= \Gamma_{pP} \left[+ n_b^4 N_b^2 \sin^3 \theta_0 \chi^{zzz} \right. \\
&\quad + n_\ell^4 N_b^2 w_b^2 \sin \theta_0 \cos^2 \phi \chi^{xxx} \\
&\quad + n_\ell^4 N_b^2 w_b^2 \sin \theta_0 \sin^2 \phi \chi^{zxx} \\
&\quad - 2n_b^2 n_\ell^2 N_\ell^2 w_b W_b \sin \theta_0 \cos^2 \phi \chi^{xxz} \\
&\quad - 2n_b^2 n_\ell^2 N_\ell^2 w_b W_b \sin \theta_0 \sin^2 \phi \chi^{xxz} \\
&\quad - n_\ell^4 N_\ell^2 w_b^2 W_b \cos^3 \phi \chi^{xxx} \\
&\quad + n_\ell^4 N_\ell^2 w_b^2 W_b \sin^2 \phi \cos \phi \chi^{xxx} \\
&\quad \left. + 2n_\ell^4 N_\ell^2 w_b^2 W_b \sin^2 \phi \cos \phi \chi^{xxx} \right],
\end{aligned}$$

and reduce,

$$\begin{aligned}
\Upsilon_{pP}^{(111)} &= \Gamma_{pP} \left[+ n_b^4 N_b^2 \sin^3 \theta_0 \chi^{zzz} \right. \\
&\quad + n_\ell^4 N_b^2 w_b^2 \sin \theta_0 (\sin^2 \phi + \cos^2 \phi) \chi^{zxx} \\
&\quad - 2n_b^2 n_\ell^2 N_\ell^2 w_b W_b \sin \theta_0 (\sin^2 \phi + \cos^2 \phi) \phi \chi^{xxz} \\
&\quad \left. + n_\ell^4 N_\ell^2 w_b^2 W_b (3 \sin^2 \phi \cos \phi - \cos^3 \phi) \chi^{xxx} \right] \\
&= \Gamma_{pP} [N_b^2 \sin \theta_0 (n_b^4 \sin^2 \theta_0 \chi^{zzz} + n_\ell^4 w_b^2 \chi^{zxx}) \\
&\quad - n_\ell^2 N_\ell^2 w_b W_b (2n_b^2 \sin \theta_0 \chi^{xxz} + n_\ell^2 w_b \chi^{xxx} \cos 3\phi)] \\
&= \Gamma_{pP} r_{pP}^{(111)},
\end{aligned}$$

where

$$\begin{aligned}
r_{pP}^{(111)} &= N_b^2 \sin \theta_0 (n_b^4 \sin^2 \theta_0 \chi^{zzz} + n_\ell^4 w_b^2 \chi^{zxx}) \\
&\quad - n_\ell^2 N_\ell^2 w_b W_b (2n_b^2 \sin \theta_0 \chi^{xxz} + n_\ell^2 w_b \chi^{xxx} \cos 3\phi).
\end{aligned} \tag{B.21}$$

B.2.2 For the (110) surface

We take Eqs. (B.16) and (B.14), eliminate the components that do not contribute, and apply the symmetry relations as follows,

$$\begin{aligned}
\Upsilon_{pP}^{\text{MR},(110)} &= \Gamma_{pP}^{\text{MR}} \left[R_p^{M+} \left(r_p^{M+} \right)^2 \sin^3 \theta_0 \chi^{zzz} \right. \\
&\quad + R_p^{M+} \left(r_p^{M-} \right)^2 w_\ell^2 \sin \theta_0 \sin^2 \phi \chi^{zyy} \\
&\quad + R_p^{M+} \left(r_p^{M-} \right)^2 w_\ell^2 \sin \theta_0 \cos^2 \phi \chi^{zxx} \\
&\quad - 2R_p^{M-} r_p^{M+} r_p^{M-} w_\ell W_\ell \sin \theta_0 \sin^2 \phi \chi^{yyz} \\
&\quad \left. - 2R_p^{M-} r_p^{M+} r_p^{M-} w_\ell W_\ell \sin \theta_0 \cos^2 \phi \chi^{xxz} \right] \\
&= \Gamma_{pP}^{\text{MR}} \left[R_p^{M+} \sin \theta_0 \left(\left(r_p^{M+} \right)^2 \sin^2 \theta_0 \chi^{zzz} \right. \right. \\
&\quad + \left(r_p^{M-} \right)^2 w_\ell^2 \left(\frac{1}{2}(1 - \cos 2\phi) \chi^{zyy} + \frac{1}{2}(\cos 2\phi + 1) \chi^{zxx} \right) \left. \right) \\
&\quad - 2R_p^{M-} r_p^{M+} r_p^{M-} w_\ell W_\ell \sin \theta_0 \left(\frac{1}{2}(1 - \cos 2\phi) \chi^{yyz} \right. \\
&\quad \left. \left. + \frac{1}{2}(\cos 2\phi + 1) \chi^{xxz} \right) \right] \\
&= \Gamma_{pP}^{\text{MR}} \left[R_p^{M+} \sin \theta_0 \left(\left(r_p^{M+} \right)^2 \sin^2 \theta_0 \chi^{zzz} \right. \right. \\
&\quad + \left(r_p^{M-} \right)^2 w_\ell^2 \left(\frac{\chi^{zyy} + \chi^{zxx}}{2} + \frac{\chi^{zyy} - \chi^{zxx}}{2} \cos 2\phi \right) \left. \right) \\
&\quad - 2R_p^{M-} r_p^{M+} r_p^{M-} w_\ell W_\ell \sin \theta_0 \left(\frac{\chi^{yyz} + \chi^{xxz}}{2} + \frac{\chi^{yyz} - \chi^{xxz}}{2} \cos 2\phi \right) \left. \right] \\
&= \Gamma_{pP}^{\text{MR}} r_{pP}^{\text{MR},(110)},
\end{aligned}$$

where

$$\begin{aligned}
r_{pP}^{\text{MR},(110)} &= R_p^{M+} \sin \theta_0 \left(\left(r_p^{M+} \right)^2 \sin^2 \theta_0 \chi^{zzz} \right. \\
&\quad + \left(r_p^{M-} \right)^2 w_\ell^2 \left(\frac{\chi^{zyy} + \chi^{zxx}}{2} + \frac{\chi^{zyy} - \chi^{zxx}}{2} \cos 2\phi \right) \left. \right) \\
&\quad - 2R_p^{M-} r_p^{M+} r_p^{M-} w_\ell W_\ell \sin \theta_0 \left(\frac{\chi^{yyz} + \chi^{xxz}}{2} + \frac{\chi^{yyz} - \chi^{xxz}}{2} \cos 2\phi \right). \tag{B.22}
\end{aligned}$$

If we wish to neglect the effects of the multiple reflections, we follow the exact same procedure

but starting with Eq. (B.18),

$$\begin{aligned}
\Upsilon_{pP}^{(110)} &= \Gamma_{pP} \left[N_b^2 \sin \theta_0 \left(n_b^4 \sin^2 \theta_0 \chi^{zzz} + n_\ell^4 w_b^2 (\sin^2 \phi \chi^{zyy} + \cos^2 \phi \chi^{zxz}) \right) \right. \\
&\quad \left. - 2n_b^2 n_\ell^2 N_\ell^2 w_b W_b \sin \theta_0 (\sin^2 \phi \chi^{yyz} + \cos^2 \phi \chi^{xxz}) \right] \\
&= \Gamma_{pP} \left[N_b^2 \sin \theta_0 \left(n_b^4 \sin^2 \theta_0 \chi^{zzz} \right. \right. \\
&\quad \left. + n_\ell^4 w_b^2 \left(\frac{\chi^{zyy} + \chi^{zxz}}{2} + \frac{\chi^{zyy} - \chi^{zxz}}{2} \cos 2\phi \right) \right) \\
&\quad \left. - 2n_b^2 n_\ell^2 N_\ell^2 w_b W_b \sin \theta_0 \left(\frac{\chi^{yyz} + \chi^{xxz}}{2} + \frac{\chi^{yyz} - \chi^{xxz}}{2} \cos 2\phi \right) \right] \\
&= \Gamma_{pP} r_{pP}^{(110)},
\end{aligned}$$

where

$$\begin{aligned}
r_{pP}^{(110)} &= N_b^2 \sin \theta_0 \left[n_b^4 \sin^2 \theta_0 \chi^{zzz} + n_\ell^4 w_b^2 \left(\frac{\chi^{zyy} + \chi^{zxz}}{2} + \frac{\chi^{zyy} - \chi^{zxz}}{2} \cos 2\phi \right) \right] \\
&\quad - 2n_b^2 n_\ell^2 N_\ell^2 w_b W_b \sin \theta_0 \left(\frac{\chi^{yyz} + \chi^{xxz}}{2} + \frac{\chi^{yyz} - \chi^{xxz}}{2} \cos 2\phi \right).
\end{aligned} \tag{B.23}$$

B.2.3 For the (001) surface

We take Eqs. (B.16) and (B.14), eliminate the components that do not contribute, and apply the symmetry relations as follows,

$$\begin{aligned}
\Upsilon_{pP}^{\text{MR},(001)} &= \Gamma_{pP}^{\text{MR}} [R_p^{M+} (r_p^{M+})^2 \sin^3 \theta_0 \chi^{zzz} \\
&\quad + R_p^{M+} (r_p^{M-})^2 w_\ell^2 \sin \theta_0 \sin^2 \phi \chi^{zxz} \\
&\quad + R_p^{M+} (r_p^{M-})^2 w_\ell^2 \sin \theta_0 \cos^2 \phi \chi^{zxz} \\
&\quad - 2R_p^{M-} r_p^{M+} r_p^{M-} w_\ell W_\ell \sin \theta_0 \sin^2 \phi \chi^{xxz} \\
&\quad - 2R_p^{M-} r_p^{M+} r_p^{M-} w_\ell W_\ell \sin \theta_0 \cos^2 \phi \chi^{xxz}] \\
&= \Gamma_{pP}^{\text{MR}} [R_p^{M+} \sin \theta_0 \left((r_p^{M+})^2 \sin^2 \theta_0 \chi^{zzz} + (r_p^{M-})^2 w_\ell^2 \chi^{zxz} \right) \\
&\quad - 2R_p^{M-} r_p^{M+} r_p^{M-} w_\ell W_\ell \sin \theta_0 \chi^{xxz}] \\
&= \Gamma_{pP}^{\text{MR}} r_{pP}^{\text{MR},(001)},
\end{aligned}$$

where

$$\begin{aligned} r_{pP}^{\text{MR},(001)} = & R_p^{M+} \sin \theta_0 \left(\left(r_p^{M+} \right)^2 \sin^2 \theta_0 \chi^{zzz} + \left(r_p^{M-} \right)^2 w_\ell^2 \chi^{zxx} \right) \\ & - 2R_p^{M-} r_p^{M+} r_p^{M-} w_\ell W_\ell \sin \theta_0 \chi^{xxz}, \end{aligned} \quad (\text{B.24})$$

If we wish to neglect the effects of the multiple reflections, we follow the exact same procedure but starting with Eq. (B.18),

$$\begin{aligned} \Upsilon_{pP}^{(001)} = & \Gamma_{pP} [N_b^2 \sin \theta_0 (n_b^4 \sin^2 \theta_0 \chi^{zzz} + n_\ell^4 w_b^2 \chi^{zxx}) \\ & - 2n_b^2 n_\ell^2 N_\ell^2 w_b W_b \sin \theta_0 \chi^{xxz}] \\ = & \Gamma_{pP} r_{pp}^{(001)}, \end{aligned}$$

where

$$\begin{aligned} r_{pP}^{(001)} = & N_b^2 \sin \theta_0 (n_b^4 \sin^2 \theta_0 \chi^{zzz} + n_\ell^4 w_b^2 \chi^{zxx}) \\ & - 2n_b^2 n_\ell^2 N_\ell^2 w_b W_b \sin \theta_0 \chi^{xxz}. \end{aligned} \quad (\text{B.25})$$

B.3 \mathcal{R}_{pS}

Per Table B.1, \mathcal{R}_{pS} requires Eqs. (B.6) and (B.9). After some algebra, we obtain that

$$\begin{aligned} \Upsilon_{pS}^{\text{MR}} = & \Gamma_{pS}^{\text{MR}} [- \left(r_p^{M-} \right)^2 w_\ell^2 \sin \phi \cos^2 \phi \chi^{xxx} - 2 \left(r_p^{M-} \right)^2 w_\ell^2 \sin^2 \phi \cos \phi \chi^{xxy} \\ & - 2r_p^{M+} r_p^{M-} w_\ell \sin \theta_0 \sin \phi \cos \phi \chi^{xxz} - \left(r_p^{M-} \right)^2 w_\ell^2 \sin^3 \phi \chi^{xyy} \\ & - 2r_p^{M+} r_p^{M-} w_\ell \sin \theta_0 \sin^2 \phi \chi^{xzy} - \left(r_p^{M+} \right)^2 \sin^2 \theta_0 \sin \phi \chi^{xzz} \\ & + \left(r_p^{M-} \right)^2 w_\ell^2 \cos^3 \phi \chi^{yxx} + 2 \left(r_p^{M-} \right)^2 w_\ell^2 \sin \phi \cos^2 \phi \chi^{yxy} \\ & + 2r_p^{M+} r_p^{M-} w_\ell \sin \theta_0 \cos^2 \phi \chi^{yxz} + \left(r_p^{M-} \right)^2 w_\ell^2 \sin^2 \phi \cos \phi \chi^{yyy} \\ & + 2r_p^{M+} r_p^{M-} w_\ell \sin \theta_0 \sin \phi \cos \phi \chi^{yzy} + \left(r_p^{M+} \right)^2 \sin^2 \theta_0 \cos \phi \chi^{yzz}]. \end{aligned} \quad (\text{B.26})$$

We take this opportunity to introduce a quantity that will be repeated throughout this section,

$$\Gamma_{pS}^{\text{MR}} = T_s^{v\ell} R_s^{M+} \left(\frac{t_p^{v\ell}}{n_\ell} \right)^2 \quad (\text{B.27})$$

If we neglect the multiple reflections, as described in the manuscript, we have that

$$\begin{aligned} \Upsilon_{pS} = & \Gamma_{pS} [- n_\ell^4 w_b^2 \sin \phi \cos^2 \phi \chi^{xxx} - 2n_\ell^4 w_b^2 \sin^2 \phi \cos \phi \chi^{xxy} \\ & - 2n_\ell^2 n_b^2 w_b \sin \theta_0 \sin \phi \cos \phi \chi^{xxz} - n_\ell^4 w_b^2 \sin^3 \phi \chi^{xyy} \\ & - 2n_\ell^2 n_b^2 w_b \sin \theta_0 \sin^2 \phi \chi^{xzy} - n_b^4 \sin^2 \theta_0 \sin \phi \chi^{xzz} \\ & + n_\ell^4 w_b^2 \cos^3 \phi \chi^{yxx} + 2n_\ell^4 w_b^2 \sin \phi \cos^2 \phi \chi^{yxy} \\ & + 2n_\ell^2 n_b^2 w_b \sin \theta_0 \cos^2 \phi \chi^{yxz} + n_\ell^4 w_b^2 \sin^2 \phi \cos \phi \chi^{yyy} \\ & + 2n_\ell^2 n_b^2 w_b \sin \theta_0 \sin \phi \cos \phi \chi^{yzy} + n_b^4 \sin^2 \theta_0 \cos \phi \chi^{yzz}], \end{aligned} \quad (\text{B.28})$$

and again we introduce a quantity that will be repeated throughout this section,

$$\Gamma_{pS} = T_s^{v\ell} T_s^{\ell b} \left(\frac{t_p^{v\ell} t_p^{\ell b}}{n_\ell^2 n_b} \right)^2. \quad (\text{B.29})$$

B.3.1 For the (111) surface

We take Eqs. (B.26) and (B.13), eliminate the components that do not contribute, and apply the symmetry relations as follows,

$$\begin{aligned} \Upsilon_{pS}^{\text{MR},(111)} &= \Gamma_{pS}^{\text{MR}} [2r_p^{M+} r_p^{M-} w_\ell \sin \theta_0 \sin \phi \cos \phi \chi^{xxz} \\ &\quad - 2r_p^{M+} r_p^{M-} w_\ell \sin \theta_0 \sin \phi \cos \phi \chi^{xxz} \\ &\quad - (r_p^{M-})^2 w_\ell^2 \sin \phi \cos^2 \phi \chi^{xxx} \\ &\quad - 2(r_p^{M-})^2 w_\ell^2 \sin \phi \cos^2 \phi \chi^{xxx} \\ &\quad + (r_p^{M-})^2 w_\ell^2 \sin^3 \phi \chi^{xxx}]. \end{aligned}$$

We reduce terms,

$$\begin{aligned} \Upsilon_{pS}^{\text{MR},(111)} &= \Gamma_{pS}^{\text{MR}} [(r_p^{M-})^2 w_\ell^2 (\sin^3 \phi - 3 \sin \phi \cos^2 \phi) \chi^{xxx}] \\ &= \Gamma_{pS}^{\text{MR}} [- (r_p^{M-})^2 w_\ell^2 \chi^{xxx} \sin 3\phi] \\ &= \Gamma_{pS}^{\text{MR}} r_{pS}^{\text{MR},(111)}, \end{aligned}$$

where

$$r_{pS}^{\text{MR},(111)} = - (r_p^{M-})^2 w_\ell^2 \chi^{xxx} \sin 3\phi. \quad (\text{B.30})$$

If we wish to neglect the effects of the multiple reflections, we follow the exact same procedure but starting with Eq. (B.28),

$$\begin{aligned} \Upsilon_{pS} &= \Gamma_{pS} [n_\ell^4 w_b^2 (\sin^3 \phi - 3 \sin \phi \cos^2 \phi) \chi^{xxx}] \\ &= \Gamma_{pS} [-n_\ell^4 w_b^2 \chi^{xxx} \sin 3\phi] \\ &= \Gamma_{pS} r_{pS}^{(111)}, \end{aligned} \quad (\text{B.31})$$

where

$$r_{pS}^{(111)} = -n_\ell^4 w_b^2 \chi^{xxx} \sin 3\phi, \quad (\text{B.32})$$

and we use Γ_{pS} instead of Γ_{pS}^{MR} .

B.3.2 For the (110) surface

We take Eqs. (B.26) and (B.14), eliminate the components that do not contribute, and apply the symmetry relations as follows,

$$\begin{aligned}\Upsilon_{pS}^{\text{MR},(110)} &= \Gamma_{pS}^{\text{MR}} [2r_p^{M+}r_p^{M-}w_\ell \sin \theta_0 \sin \phi \cos \phi (\chi^{yyz} - \chi^{xxz})] \\ &= \Gamma_{pS}^{\text{MR}} [r_p^{M+}r_p^{M-}w_\ell \sin \theta_0 (\chi^{yyz} - \chi^{xxz}) \sin 2\phi] \\ &= \Gamma_{pS}^{\text{MR}} r_{pS}^{\text{MR},(110)}.\end{aligned}$$

where

$$r_{pS}^{\text{MR},(110)} = r_p^{M+}r_p^{M-}w_\ell \sin \theta_0 (\chi^{yyz} - \chi^{xxz}) \sin 2\phi. \quad (\text{B.33})$$

If we neglect the effects of the multiple reflections as mentioned above, we have

$$r_{pS}^{(110)} = n_\ell^2 n_b^2 w_b \sin \theta_0 (\chi^{yyz} - \chi^{xxz}) \sin 2\phi, \quad (\text{B.34})$$

and we use Γ_{pS} instead of Γ_{pS}^{MR} .

B.3.3 For the (001) surface

We take Eqs. (B.26) and (B.14), eliminate the components that do not contribute, and apply the symmetry relations as follows,

$$\begin{aligned}\Upsilon_{pS}^{\text{MR},(001)} &= \Gamma_{pS}^{\text{MR}} [-2r_p^{M+}r_p^{M-}w_\ell \sin \theta_0 \sin \phi \cos \phi \chi^{xxz} \\ &\quad + 2r_p^{M+}r_p^{M-}w_\ell \sin \theta_0 \sin \phi \cos \phi \chi^{xxz}] = 0.\end{aligned}$$

Neglecting the effects of multiple reflections will obviously yield the same result, thus

$$\Upsilon_{pS}^{\text{MR},(001)} = \Upsilon_{pS}^{(001)} = 0. \quad (\text{B.35})$$

B.4 \mathcal{R}_{sP}

Per Table B.1, \mathcal{R}_{sP} requires Eqs. (B.5) and (B.10). After some algebra, we obtain that

$$\begin{aligned}\Upsilon_{sP}^{\text{MR}} &= \Gamma_{sP}^{\text{MR}} \left[R_p^{M-} W_\ell (-\sin^2 \phi \cos \phi \chi^{xxx} + 2 \sin \phi \cos^2 \phi \chi^{xxy} - \cos^3 \phi \chi^{xyy}) \right. \\ &\quad + R_p^{M-} W_\ell (-\sin^3 \phi \chi^{yxx} + 2 \sin^2 \phi \cos \phi \chi^{yyx} - \sin \phi \cos^2 \phi \chi^{yyy}) \\ &\quad \left. + R_p^{M+} \sin \theta_0 (\sin^2 \phi \chi^{zxx} - 2 \sin \phi \cos \phi \chi^{zxy} + \cos^2 \phi \chi^{zyy}) \right].\end{aligned} \quad (\text{B.36})$$

We take this opportunity to introduce a quantity that will be repeated throughout this section,

$$\Gamma_{sP}^{\text{MR}} = \frac{T_p^{v\ell}}{N_\ell} \left(t_s^{v\ell} r_s^{M+} \right)^2 \quad (\text{B.37})$$

If we neglect the multiple reflections, as described in the manuscript, we have that

$$\begin{aligned}\Upsilon_{sP} = \Gamma_{sP} & \left[N_\ell^2 W_b (-\sin^2 \phi \cos \phi \chi^{xxx} + 2 \sin \phi \cos^2 \phi \chi^{xxy} - \cos^3 \phi \chi^{xyy}) \right. \\ & + N_\ell^2 W_b (-\sin^3 \phi \chi^{yxx} + 2 \sin^2 \phi \cos \phi \chi^{yxy} - \sin \phi \cos^2 \phi \chi^{yy}) \\ & \left. + N_b^2 \sin \theta_0 (+\sin^2 \phi \chi^{zxx} - 2 \sin \phi \cos \phi \chi^{zxy} + \cos^2 \phi \chi^{zyy}) \right],\end{aligned}\quad (\text{B.38})$$

and again we introduce a quantity that will be repeated throughout this section,

$$\Gamma_{sP} = \frac{T_p^{v\ell} T_p^{\ell b}}{N_\ell^2 N_b} \left(t_s^{v\ell} t_s^{\ell b} \right)^2. \quad (\text{B.39})$$

B.4.1 For the (111) surface

We take Eqs. (B.36) and (B.13), eliminate the components that do not contribute, and apply the symmetry relations as follows,

$$\begin{aligned}\Upsilon_{sP}^{\text{MR},(111)} = \Gamma_{sP}^{\text{MR}} & [+ R_p^{M-} W_\ell \cos^3 \phi \chi^{xxx} \\ & - R_p^{M-} W_\ell \sin^2 \phi \cos \phi \chi^{xxx} \\ & - 2 R_p^{M-} W_\ell \sin^2 \phi \cos \phi \chi^{xxx} \\ & + R_p^{M+} \sin \theta_0 \sin^2 \phi \chi^{zxx} \\ & + R_p^{M+} \sin \theta_0 \cos^2 \phi \chi^{zxx}].\end{aligned}$$

We reduce terms,

$$\begin{aligned}\Upsilon_{sP}^{\text{MR},(111)} = \Gamma_{sP}^{\text{MR}} & [R_p^{M-} W_\ell (\cos^3 \phi - 3 \sin^2 \phi \cos \phi) \chi^{xxx} \\ & + R_p^{M+} \sin \theta_0 (\sin^2 \phi + \cos^2 \phi) \chi^{zxx}] \\ & = \Gamma_{sP}^{\text{MR}} [R_p^{M-} W_\ell \chi^{xxx} \cos 3\phi + R_p^{M+} \sin \theta_0 \chi^{zxx}] \\ & = \Gamma_{sP}^{\text{MR}} r_{sP}^{\text{MR},(111)},\end{aligned}$$

where

$$r_{sP}^{\text{MR},(111)} = R_p^{M+} \sin \theta_0 \chi^{zxx} + R_p^{M-} W_\ell \chi^{xxx} \cos 3\phi. \quad (\text{B.40})$$

If we wish to neglect the effects of the multiple reflections, we follow the exact same procedure but starting with Eq. (B.38),

$$\begin{aligned}\Upsilon_{sP}^{(111)} = \Gamma_{sP} & [- N_\ell^2 W_b \sin^2 \phi \cos \phi \chi^{xxx} \\ & + N_\ell^2 W_b \cos^3 \phi \chi^{xxx} \\ & - 2 N_\ell^2 W_b \sin^2 \phi \cos \phi \chi^{yyx} \\ & + N_b^2 \sin \theta_0 \sin^2 \phi \chi^{zxx} \\ & + N_b^2 \sin \theta_0 \cos^2 \phi \chi^{zxx}],\end{aligned}$$

and reduce,

$$\begin{aligned}
\Upsilon_{sP}^{(111)} &= \Gamma_{sP} [N_\ell^2 W_b (\cos^3 \phi - 3 \sin^2 \phi \cos \phi) \chi^{xxx} \\
&\quad + N_b^2 \sin \theta_0 (\sin^2 \phi + \cos^2 \phi) \chi^{zxx}] \\
&= \Gamma_{sP} [N_\ell^2 W_b \chi^{xxx} \cos 3\phi + N_b^2 \sin \theta_0 \chi^{zxx}] \\
&= \Gamma_{sP} r_{sP}^{(111)},
\end{aligned}$$

where

$$r_{sP}^{(111)} = N_b^2 \sin \theta_0 \chi^{zxx} + N_\ell^2 W_b \chi^{xxx} \cos 3\phi. \quad (\text{B.41})$$

B.4.2 For the (110) surface

We take Eqs. (B.36) and (B.14), eliminate the components that do not contribute, and apply the symmetry relations as follows,

$$\begin{aligned}
\Upsilon_{sP}^{\text{MR},(110)} &= \Gamma_{sP}^{\text{MR}} [R_p^{M+} \sin \theta_0 (\sin^2 \phi \chi^{zxx} + \cos^2 \phi \chi^{zyy})] \\
&= \Gamma_{sP}^{\text{MR}} \left[R_p^{M+} \sin \theta_0 \left(\frac{1}{2}(1 - \cos 2\phi) \chi^{zxx} + \frac{1}{2}(\cos 2\phi + 1) \chi^{zyy} \right) \right] \\
&= \Gamma_{sP}^{\text{MR}} \left[R_p^{M+} \sin \theta_0 \left(\frac{\chi^{zyy} + \chi^{zxx}}{2} + \frac{\chi^{zyy} - \chi^{zxx}}{2} \cos 2\phi \right) \right] \\
&= \Gamma_{sP}^{\text{MR}} r_{sP}^{\text{MR},(110)},
\end{aligned}$$

where

$$r_{sP}^{\text{MR},(110)} = R_p^{M+} \sin \theta_0 \left(\frac{\chi^{zxx} + \chi^{zyy}}{2} + \frac{\chi^{zyy} - \chi^{zxx}}{2} \cos 2\phi \right). \quad (\text{B.42})$$

If we wish to neglect the effects of the multiple reflections, we follow the exact same procedure but starting with Eq. (B.38),

$$\begin{aligned}
\Upsilon_{sP}^{(110)} &= \Gamma_{sP} [N_b^2 \sin \theta_0 (\sin^2 \phi \chi^{zxx} + \cos^2 \phi \chi^{zyy})] \\
&= \Gamma_{sP} \left[N_b^2 \sin \theta_0 \left(\frac{1}{2}(1 - \cos 2\phi) \chi^{zxx} + \frac{1}{2}(\cos 2\phi + 1) \chi^{zyy} \right) \right] \\
&= \Gamma_{sP} \left[N_b^2 \sin \theta_0 \left(\frac{\chi^{zxx} + \chi^{zyy}}{2} + \frac{\chi^{zyy} - \chi^{zxx}}{2} \cos 2\phi \right) \right] \\
&= \Gamma_{sP} r_{sP}^{(110)},
\end{aligned}$$

where

$$r_{sP}^{(110)} = N_b^2 \sin \theta_0 \left(\frac{\chi^{zxx} + \chi^{zyy}}{2} + \frac{\chi^{zyy} - \chi^{zxx}}{2} \cos 2\phi \right). \quad (\text{B.43})$$

B.4.3 For the (001) surface

We take Eqs. (B.36) and (B.14), eliminate the components that do not contribute, and apply the symmetry relations as follows,

$$\begin{aligned} \Upsilon_{sP}^{\text{MR},(001)} &= \Gamma_{sP}^{\text{MR}} [R_p^{M+} \sin \theta_0 (\sin^2 \phi + \cos^2 \phi) \chi^{zxx}] \\ &= \Gamma_{sP}^{\text{MR}} [R_p^{M+} \sin \theta_0 \chi^{zxx}] \\ &= \Gamma_{sP}^{\text{MR}} r_{sP}^{\text{MR},(001)}. \end{aligned}$$

where

$$r_{sP}^{\text{MR},(001)} = R_p^{M+} \sin \theta_0 \chi^{zxx}. \quad (\text{B.44})$$

If we wish to neglect the effects of the multiple reflections, we follow the exact same procedure but starting with Eq. (B.38),

$$\begin{aligned} \Upsilon_{sP}^{(001)} &= \Gamma_{sP} [N_b^2 \sin \theta_0 (\sin^2 \phi + \cos^2 \phi) \chi^{zxx}] \\ &= \Gamma_{sP} [N_b^2 \sin \theta_0 \chi^{zxx}] \\ &= \Gamma_{sP} r_{sP}^{(001)}, \end{aligned}$$

where

$$r_{sP}^{(001)} = N_b^2 \sin \theta_0 \chi^{zxx}. \quad (\text{B.45})$$

B.5 \mathcal{R}_{sS}

Per Table B.1, \mathcal{R}_{sS} requires Eqs. (B.6) and (B.10). After some algebra, we obtain that

$$\begin{aligned} \Upsilon_{sS}^{\text{MR}} &= \Gamma_{sS}^{\text{MR}} [-\sin^3 \phi \chi^{xxx} + 2 \sin^2 \phi \cos \phi \chi^{xxy} - \sin \phi \cos^2 \phi \chi^{xyy} \\ &\quad + \sin^2 \phi \cos \phi \chi^{yxx} - 2 \sin \phi \cos^2 \phi \chi^{yxy} + \cos^3 \phi \chi^{yyy}]. \end{aligned} \quad (\text{B.46})$$

We take this opportunity to introduce a quantity that will be repeated throughout this section,

$$\Gamma_{sS}^{\text{MR}} = T_s^{v\ell} R_s^{M+} \left(t_s^{v\ell} r_s^{M+} \right)^2. \quad (\text{B.47})$$

If we neglect the multiple reflections, as described in the manuscript, we have that

$$\begin{aligned} \Upsilon_{sS} &= \Gamma_{sS} [-\sin^3 \phi \chi^{xxx} + 2 \sin^2 \phi \cos \phi \chi^{xxy} - \sin \phi \cos^2 \phi \chi^{xyy} \\ &\quad + \sin^2 \phi \cos \phi \chi^{yxx} - 2 \sin \phi \cos^2 \phi \chi^{yxy} + \cos^3 \phi \chi^{yyy}], \end{aligned} \quad (\text{B.48})$$

and again we introduce a quantity that will be repeated throughout this section,

$$\Gamma_{sS} = T_s^{v\ell} T_s^{\ell b} \left(t_s^{v\ell} t_s^{\ell b} \right)^2. \quad (\text{B.49})$$

We note that both Eqs. (B.46) and (B.48) are identical save for the different Γ_{sS} terms. Therefore, we can safely derive the equations only once, and then use Γ_{sS}^{MR} when we wish to include multiple reflections, or Γ_{sS} when we do not.

B.5.1 For the (111) surface

We take Eqs. (B.46) and (B.13), eliminate the components that do not contribute, and apply the symmetry relations as follows,

$$\begin{aligned} \Upsilon_{sS}^{\text{MR}} &= \Gamma_{sS}^{\text{MR}} [(3 \sin \phi \cos^2 \phi - \sin^3 \phi) \chi^{xxx}] \\ &= \Gamma_{sS}^{\text{MR}} [\chi^{xxx} \sin 3\phi] \\ &= \Gamma_{sS}^{\text{MR}} r_{sS}^{\text{MR},(111)}, \end{aligned}$$

where

$$r_{sS}^{\text{MR},(111)} = \chi^{xxx} \sin 3\phi. \quad (\text{B.50})$$

As mentioned above,

$$r_{sS}^{(111)} = r_{sS}^{\text{MR},(111)}, \quad (\text{B.51})$$

so if we wish to neglect the effects of the multiple reflections, we simply use Γ_{sS} instead of Γ_{sS}^{MR} .

B.5.2 For the (110) surface

When considering Eqs. (B.46) and (B.14), we see that there are no nonzero components that contribute. Therefore,

$$\Upsilon_{pS}^{\text{MR},(110)} = \Upsilon_{pS}^{(110)} = 0. \quad (\text{B.52})$$

B.5.3 For the (001) surface

When considering Eqs. (B.46) and (B.14), we see that there are no nonzero components that contribute. Therefore,

$$\Upsilon_{sS}^{\text{MR},(001)} = \Upsilon_{sS}^{(001)} = 0. \quad (\text{B.53})$$

Bibliography

- [1] J. E. Sipe, D. J. Moss, and H. M. van Driel. Phenomenological theory of optical second- and third-harmonic generation from cubic centrosymmetric crystals. *Phys. Rev. B*, 35(3):1129–1141, January 1987.
- [2] U. Höfer. Nonlinear optical investigations of the dynamics of hydrogen interaction with silicon surfaces. *Appl. Phys. A*, 63(6):533–547, December 1996.
- [3] J. E. Mejía, B. S. Mendoza, M. Palummo, G. Onida, R. Del Sole, S. Bergfeld, and W. Daum. Surface second-harmonic generation from si (111)(1x1) h: Theory versus experiment. *Phys. Rev. B*, 66(19):195329, 2002.
- [4] S. A. Mitchell, M. Mehendale, D. M. Villeneuve, and R. Boukherroub. Second harmonic generation spectroscopy of chemically modified Si(1 1 1) surfaces. *Surf. Sci.*, 488(3):367–378, August 2001.
- [5] A.L. Schawlow and C.H. Townes. Infrared and optical masers. *Physical Review*, 112(6):1940–1949, Dec 1958.
- [6] P.A. Franken, A.E. Hill, C.W. Peters, and G. Weinreich. Generation of optical harmonics. *Physical Review Letters*, 7(4):118–119, Aug 1961.
- [7] J.A. Armstrong, N. Bloembergen, J. Ducuing, and P.S. Pershan. Interactions between light waves in a nonlinear dielectric. *Physical Review*, 127(6):1918–1939, Sep 1962.
- [8] N. Bloembergen and P.S. Pershan. Light waves at the boundary of nonlinear media. *Physical Review*, 128(2):606–622, Oct 1962.
- [9] R.W. Terhune, P.D. Maker, and C.M. Savage. Optical harmonic generation in calcite. *Physical Review Letters*, 8(10):404–406, May 1962.
- [10] B. Lax, J.G. Mavroides, and D.F. Edwards. Nonlinear interband and plasma effects in solids. *Physical Review Letters*, 8(4):166–168, 1962.
- [11] N. Bloembergen, R.K. Chang, S.S. Jha, and C.H. Lee. Optical second-harmonic generation in reflection from media with inversion symmetry. *Physical Review*, 174(3):813–822, Oct 1968.
- [12] C. Flytzanis and J. Ducuing. Second-order optical susceptibilities of III-V semiconductors. *Physical Review*, 178(3):1218–1228, Feb 1969.
- [13] A.E. Siegman. *Lasers*. University Science Books, 1986.

- [14] C.K. Chen, A.R.B. de Castro, and Y.R. Shen. Surface-enhanced second-harmonic generation. *Physical Review Letters*, 46(2):145–148, Jan 1981.
- [15] P. Guyot-Sionnest and Y.R. Shen. Bulk contribution in surface second-harmonic generation. *Physical Review B*, 38(12):7985–7989, Oct 1988.
- [16] Y.R. Shen. Surface properties probed by second-harmonic and sum-frequency generation. *Nature*, 337(6207):519–525, February 1989.
- [17] J.L.P. Hughes and J.E. Sipe. Calculation of second-order optical response in semiconductors. *Physical Review B*, 53(16):10751–10763, Apr 1996.
- [18] B.S. Mendoza and W.L. Mochán. Exactly solvable model of surface second-harmonic generation. *Physical Review B*, 53(8):4999–5006, Feb 1996.
- [19] B.S. Mendoza, W.L. Mochán, and J.A. Maytorena. Visible-infrared sum and difference frequency generation at adsorbate-covered Au. *Physical Review B*, 60(20):14334–14340, Nov 1999.
- [20] B.S. Mendoza and W.L. Mochán. Polarizable-bond model for second-harmonic generation. *Physical Review B*, 55(4):2489–2502, Jan 1997.
- [21] J.A. Maytorena, B.S. Mendoza, and W.L. Mochán. Theory of surface sum frequency generation spectroscopy. *Physical Review B*, 57(4):2569–2579, Jan 1998.
- [22] M.C. Downer, Y. Jiang, D. Lim, L. Mantese, P.T. Wilson, B.S. Mendoza, and V.I. Gavrilenko. Optical second harmonic spectroscopy of silicon surfaces, interfaces and nanocrystals. *Physica Status Solidi A*, 188(4):1371–1381, 2001.
- [23] G. Lüpke. Characterization of semiconductor interfaces by second-harmonic generation. *Surface Science Reports*, 35(3-4):75 – 161, 1999.
- [24] P.F. Moulton. Spectroscopic and laser characteristics of Ti:Al₂O₃. *Journal of the Optical Society of America B*, 3(1):125–133, Jan 1986.
- [25] D. Strickland and G. Mourou. Compression of amplified chirped optical pulses. *Optics Communications*, 55(6):447 – 449, 1985.
- [26] R.W. Boyd. *Nonlinear Optics*. Academic Press, 2003.
- [27] A.M. Janner. *Second-Harmonic Generation, a Selective Probe for Excitons*. PhD thesis, University of Groningen, 1998.
- [28] J. D. Jackson. *Classical Electrodynamics, 3rd Edition*. Wiley-VCH, 3rd edition edition, July 1998.
- [29] N. Bloembergen. Surface nonlinear optics: A historical overview. *Applied Physics B: Lasers and Optics*, 68(3):289–293, 1999.
- [30] J.E. Sipe, V. Mizrahi, and G.I. Stegeman. Fundamental difficulty in the use of second-harmonic generation as a strictly surface probe. *Physical Review B*, 35(17):9091–9094, 1987.

- [31] Y.R. Shen. Surface contribution versus bulk contribution in surface nonlinear optical spectroscopy. *Applied Physics B: Lasers and Optics*, 68(3):295–300, 1999.
- [32] A. Aktsipetrov, I. M. Baranova, and A. Il'inskii. Surface contribution to the generation of reflected second-harmonic light for centrosymmetric semiconductors. *J. Exp. Theor. Phys.*, 91:297, 1986.
- [33] Z. Xu, X. F. Hu, D. Lim, J. G. Ekerdt, and M. C. Downer. Second harmonic spectroscopy of Si(001) surfaces: Sensitivity to surface hydrogen and doping, and applications to kinetic measurements. *J. Vac. Sci. Technol. B*, 15(4):1059–1064, July 1997.
- [34] P. Guyot-Sionnest and Y. R. Shen. Bulk contribution in surface second-harmonic generation. *Phys. Rev. B*, 38(12):7985–7989, October 1988.
- [35] M. C. Downer, B. S. Mendoza, and V. I. Gavrilenko. Optical second harmonic spectroscopy of semiconductor surfaces: advances in microscopic understanding. *Surf. Interface Anal.*, 31(10):966–986, 2001.
- [36] Y. R. Shen. Surface contribution versus bulk contribution in surface nonlinear optical spectroscopy. *Appl. Phys. B*, 68(3):295–300, 1999.
- [37] J.F. McGilp. A review of optical second-harmonic and sum-frequency generation at surfaces and interfaces. *Journal of Physics D: Applied Physics*, 29:1812, 1996.
- [38] J.F. McGilp. Second-harmonic generation at semiconductor and metal surfaces. *Surface Review and Letters*, 6(3-4):529–558, 1999.
- [39] O.A. Aktsipetrov, A.A. Fedyanin, A.V. Melnikov, J.I. Dadap, X.F. Hu, M.H. Anderson, M.C. Downer, and J.K. Lowell. D.C. electric field induced second-harmonic generation spectroscopy of the Si(001)-SiO₂ interface: Separation of the bulk and surface non-linear contributions. *Thin Solid Films*, 294(1-2):231–234, 1997.
- [40] O. A. Aktsipetrov, I. M. Baranova, and K. N. Evtyukhov. *Second Order Non-linear Optics of Silicon and Silicon Nanostructures*. CRC Press, February 2016.
- [41] T. Scheidt, E.G. Rohwer, H.M. von Bergmann, and H. Stafast. Optical second harmonic imaging: A versatile tool to investigate semiconductor surfaces and interfaces. *The European Physical Journal Applied Physics*, 27(1-3):393–397, 2004.
- [42] W. Daum, H. J. Krause, U. Reichel, and H. Ibach. Identification of strained silicon layers at si-SiO₂ interfaces and clean si surfaces by nonlinear optical spectroscopy. *Phys. Rev. Lett.*, 71(8):1234–1237, August 1993.
- [43] J. F. McGilp, M. Cavanagh, J. R. Power, and J. D. O'Mahony. Probing semiconductor interfaces using nonlinear optical spectroscopy. *Opt. Eng.*, 33(12):3895–3900, 1994.
- [44] C. Meyer, G. Lüpke, U. Emmerichs, F. Wolter, H. Kurz, C. H. Bjorkman, and G. Lucovsky. Electronic transitions at si(111)/SiO₂ and si(111)/s3n4 interfaces studied by optical second-harmonic spectroscopy. *Phys. Rev. Lett.*, 74(15):3001–3004, April 1995.

- [45] J. R. Power, J. D. O'Mahony, S. Chandola, and J. F. McGilp. Resonant optical second harmonic generation at the steps of vicinal si(001). *Phys. Rev. Lett.*, 75(6):1138–1141, August 1995.
- [46] P. Godefroy, W. De Jong, C. W. Van Hasselt, M. A. C. Devillers, and T. Rasing. Electric field induced second harmonic generation spectroscopy on a metal-oxide-silicon structure. *Appl. Phys. Lett.*, 68(14):1981–1983, 1996.
- [47] J. I. Dadap, Z. Xu, X. F. Hu, M. C. Downer, N. M. Russell, J. G. Ekerdt, and O. A. Aktsipetrov. Second-harmonic spectroscopy of a Si (001) surface during calibrated variations in temperature and hydrogen coverage. *Phys. Rev. B*, 56(20):13367, 1997.
- [48] N. Bloembergen. Surface nonlinear optics: a historical overview. *Appl. Phys. B-Lasers O.*, 68(3):289–293, 1999.
- [49] J. F. McGilp. Second-harmonic generation at semiconductor and metal surfaces. *Surf. Rev. Lett.*, 6(03n04):529–558, 1999.
- [50] T. Suzuki, D. E. Milovzorov, S. Kogo, M. Tsukakoshi, and M. Aono. Surface second-harmonic generation spectra of si (111)-7x7 in the Å 1.0 1.7 eV fundamental photon energy. *Appl. Phys. B*, 68(3):623–627, 1999.
- [51] J. L. P. Hughes and J. E. Sipe. Calculation of second-order optical response in semiconductors. *Phys. Rev. B*, 53(16):10751, 1996.
- [52] M. C. Downer, Y. Jiang, D. Lim, L. Mantese, P. T. Wilson, B. S. Mendoza, and V.I. Gavrilenko. Optical second harmonic spectroscopy of silicon surfaces, interfaces and nanocrystals. *Phys. Status Solidi A*, 188(4):1371–1381, 2001.
- [53] Y. R. Shen. Surface properties probed by second-harmonic and sum-frequency generation. *Nature*, 337(6207):519–525, February 1989.
- [54] C. K. Chen, A. R. B. de Castro, and Y. R. Shen. Surface-enhanced second-harmonic generation. *Phys. Rev. Lett.*, 46(2):145–148, January 1981.
- [55] B. S. Mendoza, A. Gaggiotti, and R. Del Sole. Microscopic theory of second harmonic generation at si (100) surfaces. *Phys. Rev. Lett.*, 81(17):3781–3784, 1998.
- [56] A. M. Zheltikov, G. Ferrante, and M. Zarcone. On the far-and near-field optical microscopy of microelectronics structures using second-harmonic and sum-frequency generation. *Laser Phys.*, 10(2):600–602, 2000.
- [57] G. Lüpke. Characterization of semiconductor interfaces by second-harmonic generation. *Surf. Sci. Rep.*, 35(3):75–161, 1999.
- [58] J. J. Dean, C. Lange, and H. M. van Driel. Ultrafast surface strain dynamics in MnAs thin films observed with second harmonic generation. *Phys. Rev. B*, 89(2):024102, January 2014.
- [59] L. M. Malard, T. V. Alencar, A. P. M. Barboza, K. F. Mak, and A. M. de Paula. Observation of intense second harmonic generation from $\text{MoS}_{\{2\}}$ atomic crystals. *Phys. Rev. B*, 87(20):201401, May 2013.

- [60] M. Cazzanelli, F. Bianco, E. Borga, G. Pucker, M. Ghulinyan, E. Degoli, E. Luppi, V. Véniard, S. Ossicini, D. Modotto, S. Wabnitz, R. Pierobon, and L. Pavesi. Second-harmonic generation in silicon waveguides strained by silicon nitride. *Nature Materials*, 11:148, 2014.
- [61] P. N. Butcher and T. P. McLean. The non-linear constitutive relation in solids at optical frequencies. *Proc. Phys. Soc.*, 81(2):219, 1963.
- [62] D. E. Aspnes. Energy-band theory of the second-order nonlinear optical susceptibility of crystals of zinc-blende symmetry. *Phys. Rev. B*, 6(12):4648–4659, December 1972.
- [63] J. E. Sipe and E. Ghahramani. Nonlinear optical response of semiconductors in the independent-particle approximation. *Phys. Rev. B*, 48(16):11705–11722, 1993.
- [64] Z. H. Levine. Optical second-harmonic susceptibilities: Frequency-dependent formulation with results for GaP and GaAs. *Phys. Rev. B*, 49(7):4532–4538, February 1994.
- [65] C. Aversa and J. E. Sipe. Nonlinear optical susceptibilities of semiconductors: Results with a length-gauge analysis. *Phys. Rev. B*, 52(20):14636–14645, 1995.
- [66] S. N. Rashkeev, W. R. L. Lambrecht, and B. Segall. Efficient ab initio method for the calculation of frequency-dependent second-order optical response in semiconductors. *Phys. Rev. B*, 57(7):3905–3919, 1998.
- [67] For bulk calculations schemes of the SH susceptibility tensor beyond the independent particle approximation, see Refs. [72, 146–148, 161, 165–167].
- [68] N. Arzate and B. S. Mendoza. Microscopic study of surface second-harmonic generation from a clean si(100) c(4×2) surface. *Phys. Rev. B*, 63(12):125303, 2001.
- [69] B. S. Mendoza, M. Palummo, G. Onida, and R. Del Sole. Ab initio calculation of second-harmonic-generation at the si(100) surface. *Phys. Rev. B*, 63(20):205406, 2001.
- [70] H. Sano, G. Mizutani, W. Wolf, and R. Podloucky. Ab initio study of linear and nonlinear optical responses of si(111) surfaces. *Phys. Rev. B*, 66(19):195338, November 2002.
- [71] J. E. Mejía, B. S. Mendoza, and C. Salazar. Layer-by-layer analysis of second harmonic generation at a simple surface. *Revista Mexicana de Física*, 50(2):134–139, 2004.
- [72] Mads L. Trolle, Gotthard Seifert, and Thomas G. Pedersen. Theory of excitonic second-harmonic generation in monolayer MoS₂. *Phys. Rev. B*, 89(23):235410, June 2014.
- [73] W. Kohn and L. J. Sham. Self-consistent equations including exchange and correlation effects. *Phys. Rev.*, 140(4A):A1133–A1138, November 1965.
- [74] G. Onida, L. Reining, and A. Rubio. Electronic excitations: density-functional versus many-body green's-function approaches. *Rev. Mod. Phys.*, 74(2):601, 2002.
- [75] M. J. Lucero, T. M. Henderson, and G. E. Scuseria. Improved semiconductor lattice parameters and band gaps from a middle-range screened hybrid exchange functional. *J. Phys. Condens. Mat.*, 24(14):145504, April 2012.

- [76] Z. H. Levine and D. C. Allan. Linear optical response in silicon and germanium including self-energy effects. *Phys. Rev. Lett.*, 63(16):1719–1722, October 1989.
- [77] Z. H. Levine and D. C. Allan. Quasiparticle calculation of the dielectric response of silicon and germanium. *Phys. Rev. B*, 43(5):4187–4207, February 1991.
- [78] R. Del Sole and R. Girlanda. Optical properties of semiconductors within the independent-quasiparticle approximation. *Phys. Rev. B*, page 11789, 1993.
- [79] L. Kipp, D. Biegelsen, J. Northrup, L.-E. Swartz, and R. Bringans. Reflectance difference spectroscopy: Experiment and theory for the model system Si(001):As and application to si(001). *Phys. Rev. Lett.*, 76(15):2810–2813, April 1996.
- [80] F. Nastos, B. Olejnik, K. Schwarz, and J. E. Sipe. Scissors implementation within length-gauge formulations of the frequency-dependent nonlinear optical response of semiconductors. *Phys. Rev. B*, 72(4):045223, 2005.
- [81] J. Cabellos, B. Mendoza, M. Escobar, F. Nastos, and J. Sipe. Effects of nonlocality on second-harmonic generation in bulk semiconductors. *Phys. Rev. B*, 80(15):155205, 2009.
- [82] L. Reining, R. Del Sole, M. Cini, and J. G. Ping. Microscopic calculation of second-harmonic generation at semiconductor surfaces: As/Si(111) as a test case. *Phys. Rev. B*, 50(12):8411–8422, 1994.
- [83] S. Ismail-Beigi, E. K. Chang, and S. G. Louie. Coupling of nonlocal potentials to electromagnetic fields. *Phys. Rev. Lett.*, 87(8):087402, August 2001.
- [84] Eleonora Luppi, Hans-Christian Weissker, Sandro Bottaro, Sottile Francesco, Valérie Véniard, Lucia Reining, and Giovanni Onida. Accuracy of the pseudopotential approximation in *ab initio* theoretical spectroscopies. *Phys. Rev. B*, 78:245124, 2008.
- [85] S. M. Anderson, N. Tancogne-Dejean, B. S. Mendoza, and V. Véniard. Theory of surface second-harmonic generation for semiconductors including effects of nonlocal operators. *Phys. Rev. B*, 91(7):075302, February 2015.
- [86] S. M. Anderson and B. S. Mendoza. Derivation of the three-layer model for surface second-harmonic generation, 2016.
- [87] S. Bergfeld, B. Braunschweig, and W. Daum. Nonlinear Optical Spectroscopy of Suboxides at Oxidized Si(111) Interfaces. *Phys. Rev. Lett.*, 93(9):097402, August 2004.
- [88] A.K. Geim and K.S. Novoselov. The rise of graphene. *Nat. Mater.*, 6(3):183–191, 2007.
- [89] A. Reina, X. Jia, J. Ho, D. Nezich, H. Son, V. Bulovic, M.S. Dresselhaus, and J. Kong. Large area, few-layer graphene films on arbitrary substrates by chemical vapor deposition. *Nano Lett.*, 9(1):30–35, 2008.
- [90] K. S. Novoselov, Z. Jiang, Y. Zhang, S. V. Morozov, H. L. Stormer, U. Zeitler, J. C. Maan, G. S. Boebinger, P. Kim, and A. K. Geim. Room-temperature quantum hall effect in graphene. *Science*, 315(5817):1379–1379, 2007.

- [91] A. A. Balandin, S. Ghosh, W. Bao, I. Calizo, D. Teweldebrhan, F. Miao, and C. N. Lau. Superior thermal conductivity of single-layer graphene. *Nano Lett.*, 8(3):902–907, 2008.
- [92] M.Y. Han, B. Özyilmaz, Y. Zhang, and P. Kim. Energy band-gap engineering of graphene nanoribbons. *Phys. Rev. Lett.*, 98(20):206805, 2007.
- [93] Y. Zhang, T.T. Tang, C. Girit, Z. Hao, M.C. Martin, A. Zettl, M.F. Crommie, Y.R. Shen, and F. Wang. Direct observation of a widely tunable bandgap in bilayer graphene. *Nature*, 459(7248):820–823, 2009.
- [94] Z.H. Ni, T. Yu, Y.H. Lu, Y.Y. Wang, Y. P. Feng, and Z.X. Shen. Uniaxial strain on graphene: Raman spectroscopy study and band-gap opening. *ACS Nano*, 2(11):2301–2305, 2008.
- [95] Beidou Guo, Liang Fang, Baohong Zhang, and Jian Ru Gong. Graphene doping: a review. *Ins. J.*, 1(2):80–89, 2011.
- [96] D. C. Elias, R. R. Nair, T. M. G. Mohiuddin, S. V. Morozov, P. Blake, M. P. Halsall, A. C. Ferrari, D. W. Boukhvalov, M. I. Katsnelson, A. K. Geim, and K. S. Novoselov. Control of graphene’s properties by reversible hydrogenation: evidence for graphane. *Science*, 323(5914):610–613, 2009.
- [97] N. P. Guisinger, G. M. Rutter, J. N. Crain, P. N. First, and J. A. Stroscio. Exposure of epitaxial graphene on sic (0001) to atomic hydrogen. *Nano Lett.*, 9(4):1462–1466, 2009.
- [98] D. K. Samarakoon and X. Q. Wang. Tunable band gap in hydrogenated bilayer graphene. *ACS Nano*, 4(7):4126–4130, 2010.
- [99] D. W. Boukhvalov, M. I. Katsnelson, and A. I. Lichtenstein. Hydrogen on graphene: Electronic structure, total energy, structural distortions and magnetism from first-principles calculations. *Phys. Rev. B*, 77:035427, Jan 2008.
- [100] R. Zapata-Peña, S. M. Anderson, B. S. Mendoza, and A. I. Shkrebtii. Nonlinear optical responses in hydrogenated graphene structures. *physica status solidi (b)*, 253(2):408, December 2016.
- [101] I. Žutić, J. Fabian, and S. D. Sarma. Spintronics: Fundamentals and applications. *Rev. Mod. Phys.*, 76(2):323, 2004.
- [102] A. Fert. Nobel lecture: Origin, development, and future of spintronics. *Rev. Mod. Phys.*, 80(4):1517, 2008.
- [103] G. Lampel. Nuclear dynamic polarization by optical electronic saturation and optical pumping in semiconductors. *Phys. Rev. Lett.*, 20:491–493, Mar 1968.
- [104] M. I. Dyakonov and V. I. Perel. *Theory of optical spin orientation of electrons and nuclei in semiconductors*. Elsevier, New York, 1984. edited by F. Meier and B. P. Zakharchenya.
- [105] F. Nastos, J. Rioux, M. Strimas-Mackey, B. S. Mendoza, and J. Sipe. Full band structure LDA and k·p calculations of optical spin-injection. *Phys. Rev. B*, 76(20), November 2007.

- [106] B. S. Mendoza and J. L. Cabellos. Optical spin injection at semiconductor surfaces. *Phys. Rev. B*, 85(16):165324, 2012.
- [107] N. Arzate, R. A. Vázquez-Nava, and B. S. Mendoza. Optical spin- and current-injection study on si (111)-in surfaces. *Phys. Rev. B*, 90(20):205310, 2014.
- [108] R. D. R. Bhat and J. E. Sipe. Excitonic effects on the two-color coherent control of interband transitions in bulk semiconductors. *Phys. Rev. B*, 72(7):075205, 2005.
- [109] J. M. Fraser, A. I. Shkrebtii, J. E. Sipe, and H. M. Van Driel. Quantum interference in electron-hole generation in noncentrosymmetric semiconductors. *Phys. Rev. Lett.*, 83(20):4192, 1999.
- [110] A. Haché, Y. Kostoulas, R. Atanasov, J. L. P. Hughes, J. E. Sipe, and H. M. van Driel. Observation of coherently controlled photocurrent in unbiased, bulk gaas. *Phys. Rev. Lett.*, 78:306–309, Jan 1997.
- [111] N Laman, AI Shkrebtii, JE Sipe, and HM Van Driel. Quantum interference control of currents in cdse with a single optical beam. *App. Phys. Lett.*, 75(17):2581–2583, 1999.
- [112] P. J. Sturman. *Photovoltaic and Photo-refractive Effects in Noncentrosymmetric Materials*, volume 8. CRC Press, 1992.
- [113] J. E. Sipe and A. I. Shkrebtii. Second-order optical response in semiconductors. *Phys. Rev. B*, 61(8):5337, 2000.
- [114] E. J. Mele, P. Král, and D. Tománek. Coherent control of photocurrents in graphene and carbon nanotubes. *Phys. Rev. B*, 61(11):7669, 2000.
- [115] J. L. Cabellos, B. S. Mendoza, and A. I. Shkrebtii. Optical coherent current control at surfaces: Theory of injection current. *Phys. Rev. B*, 84(19):195326, 2011.
- [116] N. Bloembergen and P. S. Pershan. Light Waves at the Boundary of Nonlinear Media. *Physical Review*, 128(2):606–622, October 1962.
- [117] M. S. Hybertsen and S. G. Louie. Electron correlation in semiconductors and insulators: Band gaps and quasiparticle energies. *Phys. Rev. B*, 34(8):5390–5413, October 1986.
- [118] Valérie Véniard, E. Luppi, and H. Hübener. unpublished.
- [119] E. N. Adams. The crystal momentum as a quantum mechanical operator. *J. Chem. Phys.*, 21(11):2013–2017, November 1953.
- [120] E. I. Blount, F. Seitz, and D. Turnbull. Formalisms of band theory. *Solid State Phys.*, 13:305, 1962.
- [121] Valerio Olevano. Private communication.
- [122] C. Motta, M. Giantomassi, M. Cazzaniga, K. Gaál-Nagy, and X. Gonze. Implementation of techniques for computing optical properties in 0-3 dimensions, including a real-space cutoff, in ABINIT. *Comput. Mater. Sci.*, 50(2):698–703, 2010.

- [123] L. Kleinman and D. M. Bylander. Efficacious form for model pseudopotentials. *Phys. Rev. Lett.*, 48(20):1425–1428, 1982.
- [124] B. Adolph, V. I. Gavrilenko, K. Tenelsen, F. Bechstedt, and R. Del Sole. Nonlocality and many-body effects in the optical properties of semiconductors. *Phys. Rev. B*, 53(15):9797–9808, 1996.
- [125] B. S. Mendoza, F. Nastos, N. Arzate, and J. Sipe. Layer-by-layer analysis of the linear optical response of clean and hydrogenated si(100) surfaces. *Phys. Rev. B*, 74(7):075318, 2006.
- [126] In Ref. [127], a non hermitian operator was used in the context of linear optical response.
- [127] C. Hogan, R. Del Sole, and G. Onida. Optical properties of real surfaces from microscopic calculations of the dielectric function of finite atomic slabs. *Phys. Rev. B*, 68(3):035405, 2003.
- [128] C. Castillo, B. S. Mendoza, W. G. Schmidt, P. H. Hahn, and F. Bechstedt. Layer-by-layer analysis of surface reflectance anisotropy in semiconductors. *Phys. Rev. B*, 68(4):041310, 2003.
- [129] N. Tancogne-Dejean, B. S. Mendoza, and V. Véniard. Effect of material properties on the accuracy of antiresonant approximation: Linear and second-order optical responses. *Phys. Rev. B*, 90(3):035212, July 2014.
- [130] R.W. Boyd. *Nonlinear Optics*. Academic Press, New York, 2003.
- [131] Richard L. Sutherland. *Handbook of Nonlinear Optics*. CRC Press, April 2003.
- [132] Michele Cini. Simple model of electric-dipole second-harmonic generation from interfaces. *Phys. Rev. B*, 43(6):4792–4802, February 1991.
- [133] V. Mizrahi and J. E. Sipe. Phenomenological treatment of surface second-harmonic generation. *J. Opt. Soc. Am. B*, 5(3):660–667, 1988.
- [134] J. E. Sipe. New Green-function formalism for surface optics. *Journal of the Optical Society of America B*, 4(4):481–489, 1987.
- [135] S. V. Popov, Y. P. Svirko, and N. I. Zheludev. *Susceptibility tensors for nonlinear optics*. CRC Press, 1995.
- [136] X. Gonze, B. Amadon, P. . M. Anglade, J. . M. Beuken, F. Bottin, P. Boulanger, F. Bruneval, D. Caliste, R. Caracas, M. Cote, T. Deutsch, L. Genovese, Ph. Ghosez, M. Giantomassi, S. Goedecker, D. R. Hamann, P. Hermet, F. Jollet, G. Jomard, S. Leroux, M. Mancini, S. Mazeved, M. J. T. Oliveira, G. Onida, Y. Pouillon, T. Rangel, G. . M. Rignanese, D. Sangalli, R. Shaltaf, M. Torrent, M. J. Verstraete, G. Zerah, and J. W. Zwanziger. ABINIT: First-principles approach to material and nanosystem properties. *Comput. Phys. Commun.*, 180(12):2582–2615, December 2009.
- [137] The ABINIT code is a common project of the Université Catholique de Louvain, Corning Incorporated, and other contributors (URL <http://www.abinit.org>).

- [138] N. Troullier and J. L. Martins. Efficient pseudopotentials for plane-wave calculations. *Phys. Rev. B*, 43(3):1993–2006, January 1991.
- [139] V. Olevano, L. Reining, and F. Sottile. <http://dp-code.org>.
- [140] Bernardo Mendoza Santoyo, José Luis Cabellos Quiroz, and Tonatiuh Rangel Gordillo. Tiniba: Programas para el cálculo en paralelo de respuestas ópticas en semiconductores usando un cluster de computo. Registrado ante el Instituto Nacional de Derechos de Autor (INDAUTOR-México) con número de registro 03-2009-120114033400-01.
- [141] L. Caramella, C. Hogan, G. Onida, and R. Del Sole. High-resolution electron energy loss spectra of reconstructed si(100) surfaces: First-principles study. *Phys. Rev. B*, 79:155447, Apr 2009.
- [142] The half-slab layer extends to the middle of the vacuum region between consecutive (front-back or back-front) surfaces of the repeated super cell scheme.
- [143] M. Rohlfing, P. Krüger, and J. Pollmann. Efficient scheme for GW quasiparticle band-structure calculations with applications to bulk si and to the si(001)-(2x1) surface. *Phys. Rev. B*, 52(3):1905–1917, July 1995.
- [144] P. García-González and R. W. Godby. GW self-energy calculations for surfaces and interfaces. *Comput. Phys. Commun.*, 137(1):108–122, June 2001.
- [145] R. Asahi, W. Mannstadt, and A. J. Freeman. Screened-exchange lda methods for films and superlattices with applications to the si(100)2x1 surface and inas_{1-x}ns_x superlattices. *Phys. Rev. B*, 62:2552, 2000.
- [146] E. Luppi, H. Hübener, and V. Véniard. Ab initio second-order nonlinear optics in solids: Second-harmonic generation spectroscopy from time-dependent density-functional theory. *Phys. Rev. B*, 82:235201, 2010.
- [147] R. Leitsmann, W. Schmidt, P. Hahn, and F. Bechstedt. Second-harmonic polarizability including electron-hole attraction from band-structure theory. *Phys. Rev. B*, 71(19):195209, 2005.
- [148] B. Adolph and F. Bechstedt. Influence of crystal structure and quasiparticle effects on second-harmonic generation: Silicon carbide polytypes. *Phys. Rev. B*, 62:1706, 2000.
- [149] Nicolas Tancogne-Dejean. *Ab initio description of second-harmonic generation from crystal surfaces*. PhD thesis, Ecole polytechnique, September 2015.
- [150] E. Kaxiras and J. D. Joannopoulos. Hydrogenation of semiconductor surfaces: Si and Ge (111). *Phys. Rev. B*, 37(15):8842–8848, May 1988.
- [151] F. Jona, W. A. Thompson, and P. M. Marcus. Experimental determination of the atomic structure of a H-terminated Si111 surface. *Phys. Rev. B*, 52(11):8226–8230, September 1995.
- [152] D. R. Alfonso, C. Noguez, D. A. Drabold, and S. E. Ulloa. First-principles studies of hydrogenated Si(111)-7x7. *Phys. Rev. B*, 54(11):8028–8032, September 1996.

- [153] F. Cargnoni, C. Gatti, E. May, and D. Narducci. Geometrical reconstructions and electronic relaxations of silicon surfaces. I. An electron density topological study of H-covered and clean Si(111)(1×1) surfaces. *J. Chem. Phys.*, 112(2):887–899, January 2000.
- [154] R. C. Weast, M. J. Astle, and W. H. Beyer. *CRC handbook of chemistry and physics*, volume 69. CRC press Boca Raton, FL, 1988.
- [155] Y. Li and G. Galli. Electronic and spectroscopic properties of the hydrogen-terminated Si(111) surface from ab initio calculations. *Phys. Rev. B*, 82(4):045321, July 2010.
- [156] N. Tancogne-Dejean, C. Giorgetti, and V. Véniard. Optical properties of surfaces with supercell *ab initio* calculations: Local-field effects. *Phys. Rev. B*, 92(24):245308, July 2015.
- [157] P. Yu and M. Cardona. *Fundamentals of Semiconductors: Physics and Materials Properties*. Springer Science & Business Media, third edition, March 2005.
- [158] The size of the excitonic Hamiltonian scales as $(N_k^3 \times N_v \times N_c)^2$, where N_k is the total number of \mathbf{k} -points, and N_v and N_c are the number of valence and conduction states, respectively. For these values, the size of the Hamiltonian for the Si(111)(1×1):H surface of this article would be over 1 petabyte, which far exceeds conventional computing capabilities.
- [159] M. Palummo, G. Onida, R. Del Sole, and B. S. Mendoza. Ab initio optical properties of Si(100). *Phys. Rev. B*, 60(4):2522–2527, July 1999.
- [160] K. Gaál-Nagy, A. Incze, G. Onida, Y. Borensztein, N. Witkowski, O. Pluchery, F. Fuchs, F. Bechstedt, and R. Del Sole. Optical spectra and microscopic structure of the oxidized Si(100) surface: Combined *in situ* optical experiments and first principles calculations. *Phys. Rev. B*, 79(4):045312, January 2009.
- [161] E. Luppi, H. Hübener, and V. Véniard. Communications: Ab initio second-order nonlinear optics in solids. *J. Chem. Phys.*, 132(24):241104, 2010.
- [162] A. B. Gordienko and A. S. Poplavnoi. Influence of the pseudopotential nonlocality on the calculated optical characteristics of crystals. *Russian Physics Journal*, 47(7):687–691, July 2004.
- [163] M. Fuchs and M. Scheffler. Ab initio pseudopotentials for electronic structure calculations of poly-atomic systems using density-functional theory. *Comput. Phys. Commun.*, 119(1):67–98, June 1999.
- [164] N. W. Ashcroft and N. D. Mermin. *Solid State Physics*. Brooks Cole, Saunders College, Philadelphia, 1976.
- [165] H. Hübener, E. Luppi, and V. Véniard. Ab initio calculation of many-body effects on the second-harmonic generation spectra of hexagonal sic polytypes. *Phys. Rev. B*, 83:115205, 2011.
- [166] C. Attaccalite and M. Grüning. Nonlinear optics from an ab initio approach by means of the dynamical berry phase: Application to second- and third-harmonic generation in semiconductors. *Phys. Rev. B*, 88:235113, 2013.

- [167] M. Grüning and C. Attaccalite. Second harmonic generation in *h*-bn and mos₂ monolayers: Role of electron-hole interaction. *Phys. Rev. B*, 89:081102, 2014.